University of Huddersfield Repository

Martin, Haydn

Investigations into a multiplexed fibre interferometer for on-line, nanoscale, surface metrology

Original Citation

Martin, Haydn (2010) Investigations into a multiplexed fibre interferometer for on-line, nanoscale, surface metrology. Doctoral thesis, University of Huddersfield.

This version is available at http://eprints.hud.ac.uk/8797/

The University Repository is a digital collection of the research output of the University, available on Open Access. Copyright and Moral Rights for the items on this site are retained by the individual author and/or other copyright owners. Users may access full items free of charge; copies of full text items generally can be reproduced, displayed or performed and given to third parties in any format or medium for personal research or study, educational or not-for-profit purposes without prior permission or charge, provided:

- The authors, title and full bibliographic details is credited in any copy;
- A hyperlink and/or URL is included for the original metadata page; and
- The content is not changed in any way.

For more information, including our policy and submission procedure, please contact the Repository Team at: E.mailbox@hud.ac.uk.

http://eprints.hud.ac.uk/

INVESTIGATIONS INTO A MULTIPLEXED FIBRE INTERFEROMETER FOR ON-LINE, NANOSCALE, SURFACE METROLOGY

HAYDN PAUL MARTIN

A thesis submitted to The University of Huddersfield in partial fulfilment of the requirements for the degree of Doctor of Philosophy

The University of Huddersfield in collaboration with Taylor Hobson Ltd.

April 2010

ABSTRACT

Current trends in technology are leading to a need for ever smaller and more complex featured surfaces. The techniques for manufacturing these surfaces are varied but are tied together by one limitation; the lack of useable, on-line metrology instrumentation. Current metrology methods require the removal of a workpiece for characterisation which leads to machining down-time, more intensive labour and generally presents a bottle neck for throughput.

In order to establish a new method for on-line metrology at the nanoscale investigation are made into the use of optical fibre interferometry to realise a compact probe that is robust to environmental disturbance. Wavelength tuning is combined with a dispersive element to provide a moveable optical stylus that sweeps the surface. The phase variation caused by the surface topography is then analysed using phase shifting interferometry.

A second interferometer is wavelength multiplexed into the optical circuit in order to track the inherent instability of the optical fibre. This is then countered using a closed loop control to servo the path lengths mechanically which additionally counters external vibration on the measurand. The overall stability is found to be limited by polarisation state evolution however.

A second method is then investigated and a rapid phase shifting technique is employed in conjunction with an electro-optic phase modulator to overcome the polarisation state evolution. Closed loop servo control is realised with no mechanical movement and a step height artefact is measured. The measurement result shows good correlation with a measurement taken with a commercial white light interferometer.

ACKNOWLEDGEMENTS

I would first like to thank my supervisor Jane Jiang for her guidance and belief in me throughout this project. Her dedication to her students and work goes far beyond the norm.

Secondly, thanks to all my colleagues in the Centre of Precision Technologies including the director Liam Blunt. You have all made for a pleasant and enjoyable place to work.

To those colleagues at Taylor Hobson, thank you for allowing me access to your knowledge and expertise and also for your humour which helped to make my short stay so enjoyable.

Thanks to Mum, Dad and Maria for getting me this far.

Finally, thank you to my partner Sarah without whose unbounded patience, understanding and support I could never have completed this work.

This work is dedicated to the memory of my grandmothers, Muriel Martin and Malvina Petravicius, both of whom sadly passed during its conception.

TABLE OF CONTENTS

LIST OF FIGURES

LIST OF TABLES

LIST OF ABBREVIATIONS

AC	Alternating Current
ADC	Analogue to Digital Converter
AFM	Atomic Force Microscope
AM	Amplitude Modulation
APTH	Active Phase Tracking Homodyne
CCD	Charge Coupled Device
CCI	Coherence Correlation Interferometer
CLTF	Closed Loop Transfer Function
CMM	Coordinate Measurement Machine
CMOS	Complementary Metal Oxide Semiconductor
DAC	Digital to Analogue Converter
DAQ	Data Acquisition
DBR	Distributed Bragg Reflector
DC	Direct Current
DFB	Gain Bandwidth Product
DOF	Depth Of Field
GPIB	General Purpose Interface Bus
GPIO	General Purpose Input Output
GRIN	Graded Index
HWP	Half Wave Plate
IC	Integrated Circuit
IDE	Integrated Development Environment
IID	Independently Identically Distributed
IR	Infrared
ISO	International Standards Organisation
ISR	Interrupt Service Routine
JTAG	Joint Test Action Group
LAN	Local Area Network
LCP	Left Circularly Polarised
LED	Light Emitting Diode
LP	Linearly Polarised
LTI	Linear Time Invariant
LVDT	Linear Variable Differential Transformer
MEMS	Micro-Electro-Mechanical System
MEOMS	Micro-Electro-Opto-Mechanical System
MFD	Mode Field Diameter
MFI	Multiplexed Fibre Interferometer
MSPS	Mega Samples Per Second
N.A.	Numerical Aperture
NEP	Noise Equivalent Power
OCT	Optical Coherence Tomography
OLTF	Open Loop Transfer Function
OPD	Optical Path Difference
PC	Personal Computer
PCB	Printed Circuit Board
PDF	Probability Density Function
PGI	Phase Grating Interferometer
PI	Proportional Integral
PID	Proportional Integral Differential
PM	Polarisation Maintaining
PSD	Power Spectral Density
PSI	Phase Shifting Interferometry
PZT	Piezo-electric Transducer
QWP	Quarter Wave Plate
RAM	Random Access Memory

RCP	Right Circularly Polarised
RIN	Relative Intensity Noise
RMS	Root Mean Square
RPS	Rapid Phase Shifting
SLED	Super-luminescent Light Emitting Diode
SM	Single Mode
SNR	Signal to Noise Ratio
SOP	State Of Polarisation
SPI	Serial Peripheral Interface
STM	Scanning Tunnelling Microscope
TE	Transverse Electric
TEM	Transverse Electromagnetic
TIR	Total Internal Reflection
TM	Transverse Magnetic
TTL	Transistor-Transistor Logic
VI	Virtual Instrument
VSWLI	Vertical Scanning White Light Interferometry
WDM	Wavelength Division Multiplexing
WLSI	White Light Scanning Interferometer

1 Introduction

1.1 Overview

High precision manufacture covers a variety of tools and techniques for producing both the structured and stochastic surfaces that are becoming more and more prevalent in today's technologies. While manufacturing technologies have advanced in their ability to produce high-precision surfaces, the metrology needed for their characterisation has progressed at a slower rate. Certainly, a level of maturity has been reached in one sense; instrumentation with the ability to measure surfaces on the sub-nanoscale and upwards is available and well established.

The specific techniques used to carry out metrology are dependent upon the application with contact based methods using styli providing the largest potential range to resolution ratio. Non-contact methods are preferred when surface characteristics are such that contact methods would be destructive. Although various optical approaches have been developed it is interferometry that has seen the greatest success, mainly due to its high vertical resolution, traceability and areal capture ability. This has been initially through the development of phase shifting interferometry, which became a powerful tool with the advent of cheap computer processing and CCD arrays. After this the development of vertical scanning white light interferometry (VSWLI) further extended capabilities in terms of range. In addition, its ability to acquire fast areal data makes it an attractive proposition for the types of surface to which it is suited.

Both optical and stylus based instruments suffer from a number of limitations. They tend to be large in size and heavy in order to provide the environmental stability required for reliable sub-nanometre resolution measurement. During a manufacturing process, it is necessary to be able to characterise the workpiece to ensure it meets specification. Current high precision metrology instrumentation has a major disadvantage in this sense, it generally requires the removal of the workpiece for characterisation. While this is clearly time and labour intensive, resulting in a drop in throughput, it is also often very problematic due to the difficulty of precisely realigning the machine tool and/or workpiece. In general, a method for measuring the

process with the workpiece holds great advantage in terms of labour and manufacturing throughput.

1.2 Measurement Process Types

Vacharanukul and Mekid (2005) neatly divide the act of measurement during the manufacturing process in three ways; in-process, on-line and post-process.

1.2.1 In-process

In-process measurement is the act of measuring the workpiece during the process of manufacture, that is while the machining actually takes place. This is generally the most challenging area for measurement in that any metrology technique must deal with added difficulties of vibration and the presence of lubricants or debris.

1.2.2 On-line

On-line (alternatively on-machine or in-situ) measurement is that which takes place without the removal of a workpiece from the machine tool. Unlike in-process measurement however, the manufacturing is actually halted during the measurement period. This relaxes significantly some of the challenges for implementation while also providing the advantages associated with not having to remove/refit the workpiece.

1.2.3 Post-process

Post-process measurement is the standard method for inspection in high precision manufacturing. It requires the physical removal of the workpiece after which the measurement takes place on a separate, dedicated instrument. Not only does the measurement normally require time consuming and skilful alignment procedures, any further alteration to be made in light of the results require the re-alignment of the workpiece on the machine tool. Typically measurement is not automated and as such throughput tends to be decreased substantially.

1.3 Instrumentation for On-line Surface Metrology

There are specific requirements for metrology instrumentation that is more suited for integration or retrofit into manufacturing technology in order to provide an on-line

surface metrology role. Such devices would require a small, compact probe that could be flexibly mounted close to the machine tool/workpiece without fouling any of the workings. Non-contact measurement would also be advantageous in this situation as the probe could be placed away from the surface to some degree. While in general the machining used for high precision manufacture is by necessity well stabilised against environmental disturbance, any retrofit device will not necessarily be within the physical metrology frame, hence some robustness against temperature drift and stability would be beneficial.

Optical fibres, with their ability to move light into places very easily, provide interesting prospects for application to online surface metrology. The concept of a small optical probe, mounting at the head of a fibre is an attractive one from the point of view installing onto a machine tool. With such a device, the interrogation optics and associated electronics could be placed separately and conveniently, away from the probe head.

1.4 Aim, Objectives and Contribution

1.4.1 Aim

To investigate the potential for applying optical fibre interferometry in on-line nanoscale surface measurement applications.

1.4.2 Objectives

- To develop a fibre optic interferometer capable of measuring nanoscale surface texture.
- Present a small, compact and remote mountable probe head.
- Feature an optical stylus utilising wavelength scanning and a dispersive element to provide fast profile measurement without mechanical movement.
- Be robust against environmental perturbation.

1.4.3 Contribution

The work contained in this thesis has made the following novel contributions:

- Development and demonstration of a rapid phase shifting technique, using an integrated optic electro-optic modulator, to obtain real-time phase information from a fibre interferometer which is insensitive to polarisation state evolution.
- Development and demonstration of active vibration compensation using real-time calculated phase feedback to stabilise the all-fibre interferometer path length by the use of a separate reference wavelength.
- Demonstration of a stabilised multiplexed fibre interferometer to resolve a step height of several hundred nanometres using a compact, remote mountable fibre probe.

1.5 Thesis Structure

This study relates work done on the development of a fibre optic interferometer for use in surface measurement applications, with the aim of producing an instrument capable of producing robust nanoscale measurement in a compact form.

This study comprises a number of components to fulfil the overall aim:

- Chapter 2 presents a brief description of the development of surface metrology and provides introduction to some of the terminology used in the field. There is also an appraisal of current metrology capabilities and instrumentation and a consideration of their application to online measurement.
- Chapter 3 introduces some basic concepts and terminology describing the nature of light. The chapter concentrates on those areas relating to interferometry and fibre-optics.
- Chapter 4 gives an overview of interferometry for surface metrology and describes established techniques and methodologies. By the end of the chapter, the methodologies suitable for implementing a fibre interferometer sensor for surface metrology are identified.
- Chapter 5 describes initial investigations into the use of a fibre interferometer for surface measurement in order to determine the feasibility of such an

approach. The operation of the instrument is confirmed and its performance with regard to measurement stability evaluated.

- Chapter 6 identifies the main theoretical noise sources present in fibre interferometers and associated electronic subsystems. Noise sources are grouped by type and an analysis of each type's effects is performed. A theoretical noise floor is presented and the likely main noise sources (and their magnitudes) are identified.
- Chapter 7 investigates a second fibre interferometer apparatus with a different design to attempt to overcome some of the limitations in the first instrument. Here a novel methodology of rapid phase shifting is implemented in order to improve performance. In addition the all-fibre design allows for the realisation of a much more compact probe.
- Chapter 8 presents an appraisal of the investigated apparatus and implemented methodologies.
- Chapter 9 considers some potential avenues for further investigation and improvement.

The results of the first investigation into a fibre interferometer design (see chapter 5) highlighted many of the weaknesses and difficulties with using fibre interferometers for surface metrology. This included the problem of polarisation state evolution in the fibre, which resulted in low frequency drift when using closed loop feedback. In addition the physical size of the optical probe was such that it was not very suitable for online mounting. These issues were taken into consideration and a new optical design and alternative interrogation method was developed and investigated in chapter 7.

Proof of concept for the idea was obtained through this second investigation. The theoretical noise study suggests with some additional engineering, a viable surface metrology instrument may be developed using the proposed methodology.

1.6 Publications

The work in this thesis has produced three peer reviewed journal papers, one international patent and 3 conference papers. A full publication list may be found in the Publications and Awards section at the end of this thesis.

2 Surface Metrology

2.1 Introduction

This chapter introduces surface metrology and gives a brief overview of its development. Concepts are introduced in a rough historical context in order to make clear the way the science has developed. Terminology used within the field is introduced and explained.

The wide range of instrumentation used for the retrieval of surface topographic information is described. Reference is also given to the physical location and the point in time during the process at which the metrology takes place within the manufacturing cycle. Finally, a description of metrology needs for the future with regard to online methods is made.

2.2 Surface Metrology

2.2.1 Overview

Jiang et al. (2007a) give the definition of surface metrology as, 'the science of measuring small-scale geometrical features on surfaces: the topography of the surface.'

The measurement of surfaces comprises two essential elements; the physical retrieval of surface topography information by instrumentation, and the subsequent analysis of that information (characterisation). Surface metrology is a relatively recent scientific field and has historically been driven by technological developments in other fields. For instrumentation this has been through the development of sensors, optics and digitisation techniques. Characterisation has been driven by advances in computing and the application of mathematical techniques such as digital filtering, wavelet theory and region detection.

As the need for more and more precise engineering has evolved, the enabling technologies and techniques for surface metrology have also done so. So too has the understanding of the importance of surface characteristics on the function of a surface in a given application.

2.2.2 Initial Development

At the turn of the 19th century the measurement of surface texture was confined to the subjective inspection by eye (with or without a microscope) or the running of a fingernail across a machined surface. In this way a skilled operator could gauge the approximate roughness of the surface to some degree. The main concern was in the height of the surface roughness normal to the surface as this had an understood effect on assembly tolerances. Also of interest was the geometry of the roughness because of its impact in contact applications. It was not until 1919 that the first instrument was designed by Tomlinson at National Physical Laboratory (NPL) to specifically measure the height of the surface roughness. The real development of instrumentation however did not really begin until the 1930s when stylus based methods became quickly established through the work of several companies worldwide. These instruments allowed the recording of a profile of the surface topography along one lateral axis.

2.2.3 Characterisation

With the advent of instrumentation to provide a profile of surface topography there was another issue to be considered; what to do with the profile data. There were two polarised viewpoints on how to characterise a surface; to use a simple number on a scale (which relates to some definable surface attribute), or to use the complete profile. Neither of these methods where very suitable for linking surface texture with function; one is too simple, the other overly complex. The first step toward modern characterisation of surface texture was given by Abbott and Firestone (1933) whose material to air ratio curve provided a means of linking function (for the case of contact) with simple numerical parameters. Such was the success of the method that it is still in use today in assessing the manufacture of bearing and sealing surfaces.

As surface metrology matured as a discipline throughout the 1940s and 50s it became apparent that the spatial frequencies contained in a surface profile could be usefully separated into three ranges, named roughness, waviness and form. The definitions of these ranges result from their origin in the manufacturing process (Whitehouse 2002, ch. 1).

- Roughness is the texture imparted due to the machining process. It is inevitable and unavoidable result of the manufacturing process.
- Waviness is the result of problems in the machine tool, possibly a lack of stiffness or some form of harmonic disturbance. It is often periodic in nature and occurs at longer wavelengths than the underlying roughness. It may also occur as a slow moving random type wave.
- Form is the underlying surface geometry and comprises the longest wavelengths of the surface. Form errors may be introduced by into the surface geometry by longer term effects such as thermal changes.

So these three terms result from the manufacturing process, machine tool and design respectively. Once this had been established the potential uses were obvious, analysis of waviness for instance could yield information about machine tool problems such as excess chatter. The separation and characterisation of the surface roughness allowed a direct assessment of the manufacturing process.

2.2.4 Filtering

Throughout the 1950s the problem of effectively separating roughness from waviness was considered. Mechanical and electrical methods were both investigated but by 1963, the way forward was clear. Electronic filtering could simply and easily simulate the filtering of the real profile and acted directly upon the analogue output produced by stylus instruments. Initially the filtering was provided by a simple cascaded 2RC filter but further improvements soon came along in the form of phase corrected filters, although these were difficult to implement in analogue electronics.

The advent of computers and digital techniques in the late 60s provided the next great leap forward, allowing the accurate modelling of filters in software and enabling more complex analysis. Digital storage meant the chart recorder had seen its day and data could now be analysed at leisure using a multitude of different filters. Digital storage and analysis meant that characterisation was for the first time separable from the instrumentation.

The actual definitions (and the cut off wavelengths) for roughness, waviness and form are extremely dependent on the surface being characterised. However roughness

is ultimately bounded at its upper frequency by the stylus tip size (or resolving power in optical applications). Form is bounded by the size of the workpiece. The frequency breakpoints that bind waviness are rather more ambiguous however; a watch spindle a few millimetres in length and an axle in a motor vehicle will have substantially different cut-offs frequencies.

Generally a sampling length over which a parameter is to be computed must be defined. The sampling length chosen is dependent on the process being examined; the values differ between periodic and non-periodic profiles for instance. A suitable sampling length is iteratively arrived at from an initial estimation of a parameter combined with several measurements at different sample lengths (Whitehouse 2002, ch.2).

For the case of profile measurements, three cut-off wavelengths are defined for use extracting roughness and waviness profiles:

λ_s is the short cut-off wavelength for the roughness profile. This is to separate the low pass filtering of the stylus from the roughness profile. This is important to ensure that any stylus wear or damage does not alter the roughness profile.

λ_c defines the cut-off wavelength separating the roughness and waviness profiles.

λ_f is the longest cut-off wavelength and separates the waviness profile and the form of the workpiece.

The usual filter type used to extract the roughness and waviness profiles is the Gaussian filter, chosen because it is easily generated digitally, phase corrected and symmetrical. The cut-off wavelengths are defined as being at the 50 % amplitude transmission points of the filter characteristic.

There are occasions when it is not strictly necessary to separate waviness and roughness when trying to evaluate the surface function.

2.2.5 Parameterisation

The link between a surface function and its topography is one of the key reasons for carrying out measurements on surfaces. Another is to enable the control of the manufacturing process and to isolate issues in materials, tooling and the manufacturing environment. Having suitably filtered a profile the obvious question is

what to do with the data. In some way it is necessary to link the data to a functional prediction or process control. The aim of parameterising the data is to provide tools for making that link. Early instrumentation yielded only simple parameters such as R_a which is the average height deviation of roughness from the mean line. These simple parameters came about because they could easily be ascertained from the chart readouts produced by early instrumentation. The advent of computers and digital storage allowed for the expansion of the number of available parameters as well as the complexity of those parameters. One upshot of all this was the so-called 'parameter rash' (Whitehouse 1982) as researchers were now able to develop parameters at will. The result was a large number of parameters having significant redundancy and overlap.

Profile parameters fall into four base categories: amplitude, spatial, hybrid and statistical.

Amplitude parameters are those which consider only the height variation of surface roughness. Examples include:

- R_q the root mean square (RMS) deviation of height from the mean line
- R_z the height difference between the five highest peaks and the five lowest valleys

Spatial parameters are those that consider the spacing of surface features. They include the average distance between mean line crossing and the average peak density. Generally spatial parameters are found most useful in conjunction with amplitude parameters in the form of a hybrid parameter.

Hybrid parameters incorporate amplitude and spacing information. Examples include:

- Δ_q is the RMS slope of the profile.
- ρ is the average curvature of the profile.

Historically, these parameters proved difficult to access because of the difficulty obtaining the reliable differentials required using analogue electronics. Even with digital methods the act of differentiation conspires to amplify noise on the result and as such care must be taken.

Statistical parameters often appear in the form of curves such as material ratio (Abbott-Firestone curve), autocorrelation and amplitude distribution which are generally of use for random process analysis. They essentially remove positional dependence, thus suppressing any localised random effects. This means that such curves tend to be more stable across a surface and can reveal underlying information that may be not be apparent when using other parameters. The power spectrum can also reveal underlying harmonic information produced by tool feed in, for instance, turned surfaces.

This brief overview is intended only to give a feel for parameter use and derivation in surface metrology. Whitehouse (2002) gives a detailed description of parameters in his exhaustive work on the subject of surface metrology.

2.2.6 Areal Characterisation

Historically, profile measurement has always been the main tool in surface analysis. However surfaces, and their interactions, are by nature areal (3D). As such better functional determination might be anticipated if a surface is analysed in this way.

The term ‘areal’ is used in surface metrology to make a clear distinction from true 3D measurement methods, as carried out by devices such as coordinate measurement machines (CMM). Most surface metrology instrumentation takes a plan view of a surface and presents height data over an area. The measurement of sidewalls, for instance, is not possible so the information obtained is 2½D, or areal.

In recent times, areal surface analysis and characterisation has become more widespread. This major change in approach to surface measurement and characterisation rode upon the increasing availability of computing power in the 1980s. Areal measurement was first investigated in the late 1960s in the form of stylus instruments with a translation stage for stepping the workpiece in the second lateral dimension. However it was increasing computing power that allowed the processing of the vast increase in data taken from such instruments that made areal characterisation feasible. Commercial stylus instruments for areal surface measurement were becoming available in the early 1990s. The development of other instrumentation such as scanning white light interferometers (SWLI), phase shifting

interferometers and atomic force microscopes (AFM) also pushed forward areal measurement.

The gradual shift to areal measurement has required some conceptual changes in surface characterisation. The development of 14 parameters for the quantifying of areal surface texture was initially made by Stout et al. (1994a and 1994b). These so called 'Birmingham 14' parameters were somewhat theoretical and in some instances ill defined mathematically, especially in regard to defining hills, valleys and how they interconnect. They did however supply a solid basis from which to derive a more rigorous and practical parameter set. The European Surfstand project (E.C. Contract No SMT4-CT98-22561, 1998) produced this more rigorous set of parameters which is made up of field and feature parameters.

The field parameters consist of 12 S-parameters and 13 V-parameters. The S-parameters are 'surface' parameters and are made up of amplitude, spacing, hybrid, fractal and other parameters.

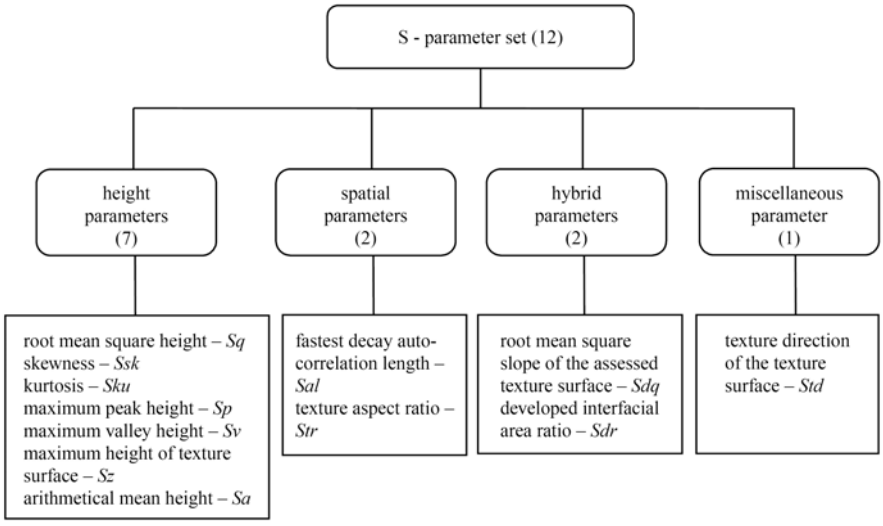

Figure 2.1 The S-parameter set (Jiang et al. 2007b)

V-parameters are 'volume' parameters and are made up of linear areal material ratio curve, void volume and material volume parameters (Blunt & Jiang, 2003).

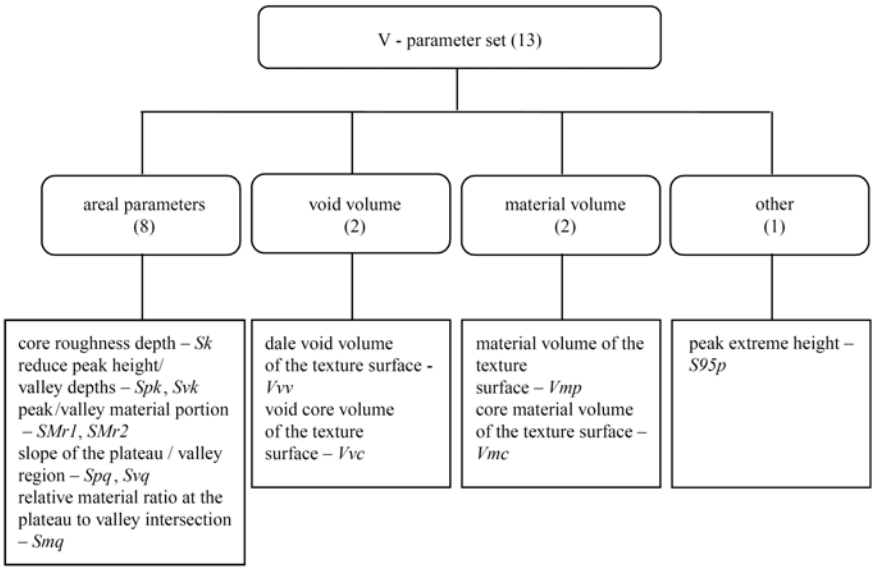

Figure 2.2 The V-parameter set (Jiang et al. 2007b)

S-parameters require the exact location of valleys and peaks and this is provided by the use of feature extraction by Wolf pruning in avoiding false peaks/pits due to noise (Scott 2003). This feature extraction method has been used to provide the segmentation of surface topographic features and derive a set of 9 feature parameters (Scott 2009). These features parameters are anticipated to be become very important in the analysis of deterministic (as opposed to stochastic) surfaces that are becoming more and more economically important. A deterministic surface is one that has a definable pattern. Examples are tessellated surfaces (e.g. road signs, golf balls), Fresnel lenses and diffraction gratings.

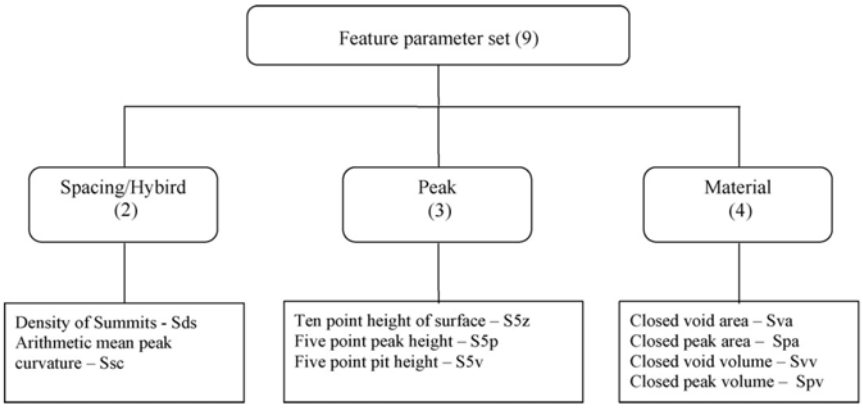

Figure 2.3 The feature parameter set (Jiang et al. 2007b)

At the time of writing the new areal surface texture parameters are in the process of being committed to the international standard ISO 25178 series.

2.2.7 Filtering for Areal Surface Characterisation

Advancements in filtering have been concurrent with the development of areal surface parameters. The standard filter for separating roughness, waviness and form from the primary profile was a Gaussian filter in 2D analysis. However the application of new mathematical techniques, in particular wavelet decomposition, has refined the separation of scales in addition to being faster (Jiang & Blunt, 2004). Other filters that have been investigated and authorised for ISO standard use are spline, robust Gaussian and morphological filters.

Because of the expansion of filtering methods for areal surfaces the vernacular for describing filtering has also been consciously altered. The terminology of roughness and waviness has been superseded by the concept of scale limited surfaces. The areal surface is scale limited by the application of some combination of an S-filter, L-filter and F-operator. The F-operator is defined as an operator because both form fitting and removal is performed. The S/L-filters and F-operators are now defined by a nesting index, which is equivalent to the filter cut-off for linear filters, but extends generality to allow for the parameter definition for other filtering methods such as wavelet transforms.

2.2.8 Freeform Surfaces

Manufacturing technology has begun to move away from simple geometries for surfaces and is now capable of producing surfaces with more complex geometries. One prime example is in optics manufacture where freeform geometries can produce smaller optics with less glass and improved performance. The scope of freeform optics is wide and the potential production quantities large; mobile phone cameras, laser printers, biomedical and telecommunications are some example applications of freeform optics.

Freeform surfaces have no axes of rotation and present a major problem for characterisation due to the difficulty of fitting the form. Work is ongoing in

developing optimised fitting algorithms to provide more accurate and consistent surface fitting (Jiang et al., 2007b).

2.3 Instrumentation for Surface Metrology

2.3.1 Introduction

When grouping surface metrology methods it is useful to consider two factors; the method employed and the location relative to the manufacturing process at which it is carried out.

The usual way is to group measurement methods into two basic camps; the contact based methods (using a stylus of some description) and the non-contact methods.

2.3.2 Stylus Based Methods

The stylus method was the original method of profiling a surface and is still very prevalent today. The resulting profile obtained is a convolution of the geometry of the stylus tip and the surface. As such the shape and size of the stylus tip is an important parameter. Stylus based methods often use inductive type sensors such as linear variable displacement transformer (LVDT) which are coupled to the vertical movement of the stylus. For more accurate work optical methods are employed to gauge the stylus deviation, the Taylor Hobson PGI range being an important example of such a method which delivers a large vertical range and high resolution.

The stylus method is limited inherently by the fact it makes contact with the surfaces, the resulting pressures generated by the stylus as it traverses the surface can damage it if it is soft. Conversely, the stylus can be worn down by particularly abrasive surfaces resulting in inconsistency of measured data for any given measurement run. Song & Vorburger (1991) give a good overview of the stylus method emphasising the importance of low stylus force and a small tip size. Several methods have been investigated to lower the stylus force, Weckenmann et al. (2006) reviews several methods with reference to contact probing for micro-electrical mechanical systems (MEMS). Low force optical fibre based contact probes have been devised which provide good access to high aspect ratio features and very low contact force, one example is given by Muralikrishnan et al. (2006). Another technique is the servo-driven stylus, where a piezoelectric transducer is used to actively maintain a constant

stylus force. This has the advantage of reducing stylus force as well as allowing faster measurement without skipping (Bauza et al., 2006).

Another major disadvantage of contact methods are their slowness, this being especially the case when multiple passes of a stylus must be made over a surface in order to create a full 3D (or areal) topography of the surface. Speed is limited by the mechanical motion required and the need to prevent the stylus skipping, this being a problem that increases with the reduction of applied stylus force.

Another set of methods that falls uncomfortably into the stylus bracket are those of scanning tunnelling microscopy (STM) and atomic force microscopy (AFM). While a stylus is present, it is not a pre-requisite that it actually makes contact with the surface. The STM method monitors the tunnelling current flowing between a minute stylus tip and a conductive surface. By either monitoring the current variation or adjusting the tip height to keep it constant, the surface topography may be obtained. The AFM method relies on the deflection of a cantilever by atomic forces at the surface; the tip need not be in physical contact with the surface, although it may be in some modes of operation. The deflection of the cantilever is usually assessed by laser beam deflection or interferometry. Both techniques can provide exceptionally high lateral resolutions due to extremely small tip dimensions, enabling measurements to be made down to the atomic and molecular scales. Using these devices however is in general complex and time consuming; in addition, the equipment is expensive (Whitehouse, 1997). The lateral range is usually very limited, only a few tens of microns, although there is ongoing work to increase this (Mazzeo et al., 2009).

2.3.3 Non-contact Methods

It is possible to separate non-contact methods into two main camps; those utilising optics and those that apply some other technique.

Non-optical methods include capacitive, inductive (eddy-current), ultrasonic and pneumatic. In general it is found that these methods do not provide the lateral resolution required for surface roughness at the micro and nano-scales. Generally these methods are resigned to larger macro-scale consideration. In the case of inductive techniques they are also very material dependent.

Optical methods are inherently much faster than the stylus methods and have obvious advantages in their non-contact nature for delicate samples. In areal measurements they really come into their own over stylus techniques with regard to acquisition speed; this may also have knock on benefits for the measurement stability.

They do require a certain amount of reflectivity in the surface which can lead to problems for the measurement of specular surfaces with steep gradients (high aspect ratios) as more light is reflected away from the probe. Another issue is that the optical surface is not the same as the tactile surface and the differences become more prevalent at nanometric measurement levels. One example of the difference has been highlighted by Rhee et al. (2005) and relates to the discrepancy between roughness results obtained with a stylus method and a vertical scanning white light interferometer (VWLSI).

Vorburger and Teague (1981) give a good summary of optical techniques for the evaluation of surface topography. Optical devices may be divided into profiling and parametric methods. Profiling is where the topology is derived point by point and the parameters then deduced from the raw data. Of course stylus based methods are also profiling, and one may also consider full-field interferometric measurement a profiling technique even though it captures a whole area at once.

Parametric

Parametric methods are those techniques which derive a given surface parameter such as the R_q directly. Such methods analyse the properties of light reflecting off a rough surface. Some examine the total intensities of either the diffuse or specular radiation. With increasing R_q the diffuse radiance increases, while at the same time, the specular component decreases. Others measure the diffuseness or the actual angular distribution of the reflected radiation. All these scattering methods rely heavily on empirical data and curve fitting since deriving the results from optical theory is intractable for a surface of any complexity.

Other parametric methods to have been investigated include diffractometry, ellipsometry and speckle interferometry. The diffractometer is interesting in that it produces a real-time power spectral density of the surface for smooth surfaces (R_q <

λ/6). It is quite insensitive to position and surface speed and is thus a good candidate for fitting in-process.

Ellipsometry is a technique well associated with the measurement of the refractive index of solids and films, as well as thickness in the case of the latter. Ellipsometry considers the change of the polarisation state of light being reflected from the surface. Unfortunately the change in polarisation may be imparted by many factors besides the surface topography including material composition, temperature and strain. Generally no monotonic relationship between surface roughness and any ellipsometric parameter has been convincingly found (Whitehouse 2002, ch. 8).

Speckle interferometry has been a fruitful path for the investigation of surface roughness. It relies on the examination of the localised intensity variation (speckle) created by the scattering of coherent light. Either the Fraunhofer or Fresnel patterns can be investigated; the names being analogous to the observation of diffraction phenomena. There are two basic types of observation that are made; speckle contrast and speckle pattern decorrelation.

Speckle contrast measurements are performed by detecting the variation in intensity of a speckle field as the surface (or detector) moves. This is done by ensuring the aperture of the detector is smaller than the speckle grain size. This method has clear benefits for on-line manufacturing as it requires the movement of the surface to operate. A good linearity is found for speckle contrast and roughness for R_q values less than the coherence length (or spatial coherence) of light source used. Speckle contrast with a short-coherence source was first investigated by Sprague (1972) as a way to increase the operating range. The speckle contrast was found to increase monotonically (though not linearly) with the R_q value of the surface. More recent work such as that by Lehmann et al. (1997) has involved more complex analysis of speckle grain shape.

In speckle correlation, separate speckle patterns are obtained by either altering wavelength or the angle of incidence of the source light. The cross correlation between the obtained speckle patterns can be related to the R_q results obtained from a stylus instrument. This method can determine R_q values of much larger than the wavelength of the illuminating light; this is its main advantage over speckle contrast (Dhanasekar et al. 2008).

The limitations of speckle interferometry lie in assumptions that the surface height distribution is Gaussian and only a single scattering takes place in the theoretical evaluations. In reality, there are usually deviations in experimental results because of these assumptions.

In general light scattering methods are attractive for on-line measurement of surface roughness parameters. This is because of their insensitivity to alignment and vibration. Unfortunately light scattering methods require a theoretical model of a surface in order to gauge roughness and as such they often fall down practically especially when applied over a range of sample types. Moreover, the information they provide is too limited, only an area averaged parameter is obtained. A true profile of the surface heights is not obtainable so it is not possible to examine structured surfaces, provide graphical information or perform any complex analysis.

Profiling

Non-contact profiling may be grouped as interferometric and non-interferometric. Interferometric devices are many and varied and this thesis will deal with a few of the major variants of such devices in more detail in chapters 3 and 4. Suffice to say that that in recent times it is the vertical scanning white light interferometer that has proved the most fruitful commercially, providing sub-nanometre resolution over several hundred microns of range (Taylor Hobson 2009a, Veeco 2009) with capture times taking several tens of seconds for a full-field. Other interferometric methods such as shearing interferometry and phase shifting interferometry see more specific use in the field of surface metrology, particularly in optics manufacture.

Non-interferometric options for profiling are fairly restricted. There are some methods based on confocal and beam scanning (or flying spot) microscopy. One example is the focus detection follower first suggested by Depuy (1967). Here the objective lens is servoed to keep the object image in focus above the surface; the control signal from the servo then relates to the surface height profile. Zhang and Lilong (1997) expanded upon this technique by measuring the servoed displacement with an interferometer.

Another method is the chromatic aberration surface profiler first suggested by Molesini and Quercioli (1986). Here an objective lens, purposefully produced with

large longitudinal chromatic aberration, is used with a white light source to generate a set of focal points which have a distance to wavelength dependence. The reflected light from the surface is inspected by a spectrometer, the wavelength of the intensity peak then relates to a known focal distance. This method has seen some commercial success as it is relatively fast.

An interesting technique has been investigated by Taguchi et al. (2003) in which the power spectrum of a surface is derived from the Fraunhofer diffraction intensity. Using this and the object intensity from the surface the phase is retrieved and the surface reconstructed. While this method is fast, it is currently restricted to those surfaces having a specific and periodic structure.

2.3.4 Summary

A large array of available surface measurement techniques have been examined in this section. They have been assessed for their suitability for implementation for on-line surface measurement. Contact (stylus) based methods are found to be too slow and cumbersome. Non-contact, parametric methods such as light scattering are not information rich enough, providing only an averaged area value for surface roughness. Non-contact profiling methods such as white light interferometry are able to provide the full profile information required but are generally too bulky implement on-line.

2.4 The Requirements for Online Measurement

The work in this thesis aims at making progress in the direction of producing a viable on-line surface measurement at the micro and nanoscale. Modern manufacturing techniques such as lithography and fast tool servo diamond turning are enabling the productions of complex surface micro-features for applications such as MEMS, MEOMS (Micro Electro-Optical-Mechanical System) and micro-fluidics. In order to characterise these structured surfaces a profiling (as opposed to a parametric) method is required. While there is no shortage of profiling techniques available at any given operating range; the critical difficulty is the devising of an approach that is suitable for on-line application.

A viable instrument for high precision manufacture needs to provide sub-nanometre resolution with nanometre repeatability. The measurement time should ideally be less than 60 seconds. The measurement range for very high precision surfaces should be at least 0.5 μm, with the potential for extending this for smooth, low gradient surfaces.

The requirement for an online profiling method is that it is reasonably robust to vibration and temperature as machining does not necessarily take place in an isolated environment. The probing mechanism must be compact because it must fit around any tooling without fouling its operation. Reasonable speed is also another necessity, even though it need not be strictly real-time (unlike in-process measurement). The delicate nature of many devices containing micro-features precludes traditional stylus based techniques and so a non-contact method is to be preferred.

Once stylus based approaches and parametric light scattering techniques have been removed from the list of possible ways forward, the list is found to be somewhat reduced. A specially designed on-line AFM head mounted upon a diamond turning machine has been investigated by Gao et al. (2007). The speed of such a method must be severely limited and the probe not particularly compact or robust. Full-field interferometric methods in general are extremely bulky and cannot realistically be integrated into on-line. The same argument can be extended to other optical profiling methods such as focus detection and chromatic aberration probing.

In this thesis a method is investigated that uses optical fibre interferometry which is combined with a compact probe head that can measure a profile using wavelength tuning with no moving parts. In addition to this, the multiplexing of multiple wavelengths into one fibre leads to the ability to actively keep the fibre paths compensated for temperature and at the same time provides some robustness against vibration. A detailed account of this is given in chapter 5.

2.5 Conclusion

This chapter has given brief coverage to the historical development of surface metrology as well as the main aspects of measurement, filtering and characterisation. The current common methodologies and instrumentation for carrying out surface metrology were introduced. Consideration was given to the point in the production

process that surface metrology may take place. Here the concept of on-line surface metrology was introduced and the requirements for its implementation explained. Current methods are found to be severely lacking in one or more key areas such as robustness, speed and compactness. Fibre interferometry was highlighted as having several useful attributes for the potential application to on-line surface measurement.

Inteferometry in general can provide the sub-nanometre resolution over the 0.5 μm range required. It is theoretically able to provide high measurement speed, only the rate of data capture limits this. Fibre interferometry can provide the remote mountable probe head which makes it feasible to implement such an instrument on-line.

The next chapter will introduce the basic concepts surrounding light propagation with specific reference to interferometry.

3 Light in Interferometers

3.1 Introduction

The aim of this chapter is to give an overview of the physical nature of light and a consideration of the approximations which must often be applied to make the study of its interaction with an instrument simpler and more manageable. It is not intended to be fully rigorous, but to define the theory and terminology that will be used in this thesis to describe the physical interactions being studied. The basic aspects of scalar optics, wave propagation, beam propagation, interference, spatial and temporal coherence as well as polarisation are all explained within this chapter and will provide the basis for further expansion later in the work.

3.2 Wave Propagation

3.2.1 Scalar Optics

The true nature of light as an electromagnetic wave is fully and rigorously described by Maxwell's equations. However in reality much optical engineering does not require such a detailed representation, often the scalar or ray optic approximations are enough to provide the level of insight needed to design optical instrumentation.

The scalar optics approximation substitutes the six field vectors associated with an electromagnetic wave with a scalar that represents the magnitude of the electric field vector. One of the main reasons why this is a feasible approximation is that for many areas of optics, the main interaction of an electromagnetic wave with a dielectric material is through the electric field vector.

Scalar optics describes light in the form of a transverse wave and as such it is a function of position, $\mathbf{r} = (x, y, z)$ and time, t. The resulting wavefunction $u(\mathbf{r}, t)$ must satisfy the wave equation in order to be valid;

$$\nabla^2 u - \frac{1}{c^2}\frac{\partial^2 u}{\partial t^2} = 0 \tag{3.1}$$

where ∇^2 is the Laplacian operator. Any function which satisfies the wave equation represents a possibly existing optical wave. c represents the propagation speed of the

wave which is the speed of light, c_0 in free space. This reduces to $c = c_0 / n$ in a transparent, homogenous medium where n is the refractive index of that medium.

For a monochromatic wave the wavefunction may be represented as

$$u(\mathbf{r},t) = a(\mathbf{r})\cos\left[\omega t + \varphi(\mathbf{r})\right] \tag{3.2}$$

where $a(\mathbf{r})$ and $\varphi(\mathbf{r})$ are the amplitude and phase of the wavefunction, while ω is the angular frequency (rad/s). This wave function has a single frequency of oscillation, while its phase and amplitude vary depending on position.

3.2.2 Complex Amplitude

Due to the imposed complexity of the cosine term in (3.2) we may represent the wavefunction in phasor form which will be seen to simplify algebra later on. This more convenient notation is the called the complex wavefunction,

$$U(\mathbf{r},t) = a(\mathbf{r})e^{j\varphi(\mathbf{r})}e^{j\omega t} \tag{3.3}$$

which also satisfies the wave equation.

Realistically any measurements of a light wave will be taken over many cycles of the time dependent term due to the response time of available optical detectors. What is actually observed is the averaging out of the time dependent term. With this in mind, often for the purpose of describing physical observations, the time dependent term can be neglected and only the complex amplitude considered,

$$U(\mathbf{r}) = a(\mathbf{r})e^{j\varphi(\mathbf{r})} \tag{3.4}$$

This is apparent if one considers light having a wavelength of 1500 nm in free space has a period of approximately 5 fs.

In this representation the original wavefunction is related to the complex amplitude by;

$$u(\mathbf{r},t) = \mathrm{Re}\left[U(\mathbf{r})e^{j\omega t}\right] = \frac{1}{2}\left[U(\mathbf{r})e^{j\omega t} + U^*(\mathbf{r})e^{j\omega t}\right] \tag{3.5}$$

with $U^*(\mathbf{r})$ representing the complex conjugate of $U(\mathbf{r})$.

3.2.3 Intensity

The observed optical intensity, $I(\mathbf{r})$ may be shown to be related to the complex amplitude, bearing in mind the effect of time averaging over many cycles of the optical period as,

$$I(\mathbf{r}) = \left|U(\mathbf{r})\right|^2 \tag{3.6}$$

The observed intensity of a monochromatic wave is the absolute square of its complex amplitude and is non-time varying. This is also true of a polychromatic wave.

3.2.4 The Gaussian Beam

While the plane wave represents a theoretical ideal of a wave that does not spread angularly, the reality is that all physical waves must have some expansion due to their wave nature. It is however possible for light waves to be locally confined into a beam, whereby the spread is minimised over the area of interest.

One important example of such a beam is the Gaussian beam which forms the basis for many other variations. The Gaussian beam is also of particular importance when considering the light beam output by a single mode fibre which is to a good approximation Gaussian in its nature.

A beam by definition must have a low angular spread which means it must deviate minimally from its axis of propagation. The associated wavefronts must therefore be paraxial in nature and as such need to satisfy the paraxial Helmholtz equation in order to produce a physical realisable beam.

The solutions for the paraxial Helmholtz equation require that the complex envelope must be a slowly varying function of the propagation vector. This has the effect of modulating the underlying wavefunction as it travels through space. The slowly varying requirement means that this modulation must occur over many optical cycles of the wavefunction so that its complex amplitude is locally constant over several wavefronts.

While the simplest solution of the paraxial Helmholtz equation is the paraboloidal wave, which is itself a paraxial approximation of a spherical wave, the Gaussian beam is the most important from an analytical point of view. It is essentially a shifted

version of the paraboloidal wave but where the shift constant is imaginary in nature and its complex envelope function in Cartesian form is

$$A(\mathbf{r}) = \frac{A_1}{q(z)} e^{-jk\frac{x^2+y^2}{q(z)}q(z)} \tag{3.7}$$

where the axis of propagation is z. In addition, $q(z) = z + jz_0$ where z_0 is called the Rayleigh range.

The resulting complex wavefunction can then be shown to be,

$$U(\mathbf{r}) = A_0 \frac{W_0}{W(z)} e^{\frac{-x^2+y^2}{W^2(z)}} \cdot e^{-jkz - jk\frac{x^2+y^2}{2R(z)} + j\zeta(z)} \tag{3.8}$$

where the constant $A_0 = A_1 / jz_0$. In this form the complex wavefunction describes the Gaussian beam in terms of physically observable elements thus presenting an empirically useful format from which the following beam parameters in table 3.1 may be defined.

Beam Radius	$W(z) = W_0\sqrt{1+\left(\frac{z}{z_0}\right)^2}$
Beam Waist Radius	$W_0 = \sqrt{\left(\frac{\lambda z_0}{\pi}\right)}$
Wavefront Radius of Curvature	$R(z) = z\left[1+\left(\frac{z_0}{z}\right)^2\right]$
Excess phase retardation	$\zeta(z) = \tan^{-1}\left(\frac{z}{z_0}\right)$

Table 3.1 Gaussian beam parameters in relation to the Rayleigh range

- The beam radius is the distance from the centre of the beam to the point at which the intensity drops to $1/e^2$ of the central intensity. The beam radius increases away from it narrowest point, the beam waist.

- The beam waist radius refers to the minimum point of the beam radius, and may be thought of as the focal point of the beam. The beam radius defines the smallest spot size that may be created by any given beam.
- The wavefront radius curvature varies from that of a plane wave at the beam waist, when $z = 0$, and gradually transforms to that of a spherical wave as z tends to infinity.
- The excess phase retardation parameter describes the excess phase delay experienced by a Gaussian beam wavefront in comparison to an equivalent plane or spherical wave originating from the same point.

For beam scanning applications such as those being considered in this thesis, the primary interest is in the spot size parameters and specifically the minimal spot size and depth of field achievable for a given imaging setup.

The intensity of the Gaussian beam unsurprisingly forms a Gaussian profile with radial distance ρ from its centre. The width of the beam, $W(z)$ increases monotonically with the axial distance either side of the focal point at $z = 0$. Far from the beam waist the intensity, $I(\mathbf{r})$ falls off with the inverse-square of the axial distance. The peak intensity is in the centre of the beam and at the focal plane, when $z = 0$ and $\rho = 0$.

Beams are usually described by the total power they carry, so it is useful to determine the intensity at a point in terms of this,

$$I(\rho, z) = \frac{2P}{\pi W^2(z)} e^{\frac{-2\rho^2}{W^2(z)}} \tag{3.9}$$

The Gaussian relationship between the radial distance and the inverse-square law dependence on the axial displacement of the intensity is clear here. As such, at any point along the propagation axis $1 - 1/e^2$ or approximately 86 % of the optical power is contained within a circle of radius of $W(z)$. The diameter $2W(z)$ is chosen as the standard measure of beam diameter, also known as the $1/e^2$ diameter or more commonly, the spot size. 99 % of the optical power is seen to be contained within the a radius of $1.5W(z)$.

When considering the depth of field (DOF) of such a beam, the same definitions are used as for general optical imaging systems involving lenses. That is the depth of field is the axial distance in which the spot size remains within $\sqrt{2} \cdot W_0$. This may be shown to be half the Rayleigh range z_0 and is defined as,

$$DOF = 2z_0 = \frac{2\pi W_0^2}{\lambda} \tag{3.10}$$

From (3.10) it is clear that that a reduction in depth of field must always occur with the reduction of the spot size for a Gaussian beam; this is an analogous situation to that found with lens imaging where range (or depth of field) reduces with resolution.

Other methods of deriving the complex wavefunction of the fundamental Gaussian beam show that it has the smallest spot size to divergence angle product of any possible beam. In this sense the Gaussian beam may be focussed to a smaller spot size than any other beam for a given numerical aperture, in other words, it is the most focusable (Pamperloni & Enderlein 2004).

One important property of the Gaussian beam is that during transmission through circularly symmetric optical components, it will always remain a Gaussian beam, albeit transformed in some of its parameters, as long as the paraxial conditions hold true. This means that it is possible to alter the parameters of a Gaussian beam by the simple use of lenses. (Saleh & Teich 1991, pp.80-92).

3.3 Interference

Interference occurs due to the principle of superposition between two waves occupying the same point in space. For two monochromatic waves of the same single frequency, the effect of interference may also be most easily described by the superposition of their complex amplitudes.

$$U(\mathbf{r}) = U_1(\mathbf{r}) + U_2(\mathbf{r}) \tag{3.11}$$

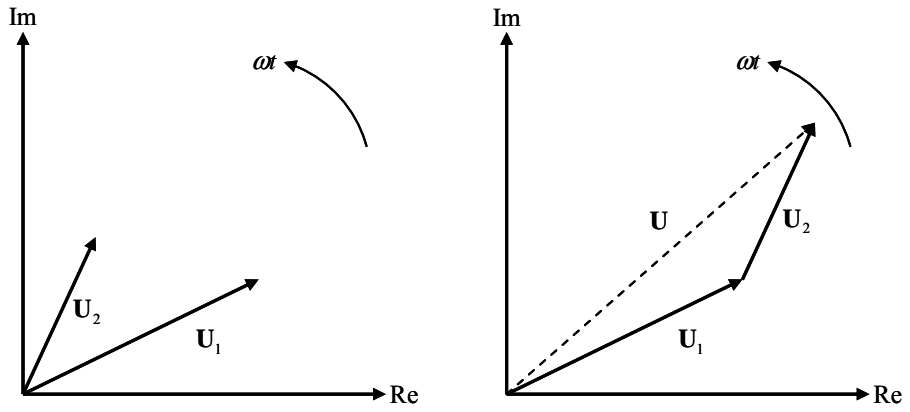

Figure 3.1 The superposition of two complex amplitudes in phasor form

Figure 3.1 represents the complex amplitudes in the complex plane. We may use the Pythagorean relationship to determine the intensity as defined in (3.6). Here the positional dependence, **r** is dropped for clarity yielding

$$|U|^2 = X^2 + Y^2 \tag{3.12}$$

where in general, $X = \sum_1^i \mathrm{Re}\{U_i\}$ and $Y = \sum_1^i \mathrm{Im}\{U_i\}$. In this way the vector sum of the real wavefunctions becomes the algebraic sum of the complex amplitude components. From figure 3.1 it is clear that $|U|^2$ is equivalent to the intensity of the complex amplitude U. For the simple case of two wave superposition this becomes

$$|U|^2 = (a_1 \cos\varphi_1 + a_2 \cos\varphi_2)^2 + (a_1 \sin\varphi_1 + a_2 \sin\varphi_2)^2 \tag{3.13}$$

which after expansion and the use of trigonomic identities reduces to

$$|U|^2 = a_1^{\,2} + a_2^{\,2} + 2a_1 a_2 \cos(\varphi_1 - \varphi_2) \tag{3.14}$$

Finally using the intensity definition in (3.6) an equation may be produced relating only to the intensities of the original waves;

$$I = I_1 + I_2 + 2\sqrt{I_1 I_2}\cos(\varphi) \tag{3.15}$$

where $\varphi = \varphi_1 - \varphi_2$ is the phase difference between the two waves. This is the so called interference equation and relates directly to physical observations in that it is only possible to measure the averaged intensity over many optical cycles.

This is probably the most important equation to be written in this thesis and is one that shall be revisited several times. It forms the basis for the field of interferometry which has many and widely varying applications.

3.4 Coherence

3.4.1 Phase Requirement for Observable Interference

When considering interference occurring between two waves it is necessary introduce the idea of coherence, which defines the statistical relationship of points in an optical field over time and space. The requirement for observable interference is that there must be some correlation between the phases of the interfering waves.

3.4.2 The Superposition of Waves of Random Phase

For instance, take the superposition of several waves having random phases, and for simplicity, equal amplitudes. For N waves, each with a phase φ_n and all with an amplitude a, the superposition may be represented at a point in space $\mathbf{r}$ by a summation of their complex amplitudes,

$$U_T(\mathbf{r}) = \sum_{n=1}^{N} U_n(\mathbf{r}) = \sum_{n=1}^{N} a(\mathbf{r}) e^{j\varphi_n(\mathbf{r})} \tag{3.16}$$

The intensity of the resulting wave, as determined by (3.5) and dropping the dependence on $\mathbf{r}$ for simplicity is then

$$I_T = |U_T|^2 = U_T \cdot U_T^* = a^2 \sum_{n=1}^{N} e^{j\varphi_n} \sum_{n=1}^{N} e^{-j\varphi_n} \tag{3.17}$$

The double summation then yields an answer in the form of

$$I_T = a^2 \left[1 + e^{j(\varphi_1 - \varphi_2)} + e^{-j(\varphi_1 - \varphi_2)} + 1 \ldots \right] \tag{3.18}$$

where each term $e^{-j(\varphi_N - \varphi_N)}$ contributes unity to the overall summation. Using the appropriate identity it is seen that

$$I_T = a^2 \left[N + 2\cos(\varphi_1 - \varphi_2) + \ldots \right] \tag{3.19}$$

If N is large there are many random contributions of phase and as many of them will be negative as positive and so the cosine terms will average out to zero yielding

$$I_T = Na^2 \tag{3.20}$$

The interference term 'washes out' and leaves simply the sum of the time-averaged intensities. This is not to say that interference is not occurring, but that it cannot be observed due to the time averaging process of intensity detection occurring as it does over many optical cycles. (Nussbaum & Phillips, 1976, pp.135-146).

From (3.19) it is clear why there needs to be some amount of correlation or coherence between the beams present in an interferometer; if there is none, no interference will be observed. The degree of coherence between beams determines the contrast, or visibility, of the observed interference fringes.

3.4.3 Types of Coherence

A set of lightwaves as observed may be divided into 3 basic partitions depending on their relationship to each other statistically. They may be coherent, incoherent (random) or partially coherent. In addition, the type of coherency may be separated and defined by the terms spatial coherence and temporal coherence.

The intensity of any particular wavefunction is what we, as observers, are able to comprehend due to the limited frequency responses of the detectors available to us. For random, incoherent light one finds a random wavefunction at any point in time or space and so the intensities of each wave must be time averaged yielding

$$I(\mathbf{r},t) = \left\langle \left| U(\mathbf{r},t) \right|^2 \right\rangle \tag{3.21}$$

For coherent light the act of time averaging has no effect on the obtained result. If this averaged intensity remains constant it may be described as statistically stationary. That is the averaged contributions of all the light waves over the observation period contribute to some constant mean level. One example of where light is not stationary is that of pulsed light, where the intensity varies periodically.

As was mentioned earlier, light may be either coherent, incoherent or somewhere in between. It is thus necessary to describe the degree of coherence and this is done statistically by the use of the autocorrelation function in which a function is compared to a shifted version of itself.

3.4.4 Temporal Coherence

The autocorrelation function for a complex function, in this case the complex wavefunction, $U(\mathbf{r},t)$ is defined as

$$G(\tau)=\lim_{T\to\infty}\frac{1}{2T}\int_{-T}^{T}U^{*}(t)\cdot U(t+\tau)\,dt \tag{3.22}$$

where the dependence on **r** is excluded for brevity and the assumption is made that the function is stationary. τ in this case is the time delay variable as we are considering the temporal autocorrelation and the function $G(\tau)$ is thus termed the temporal coherence function. The peak of $G(\tau)$ is always found to be at $G(0)$.

In general it is rather more useful to remove the dependency of the temporal coherence function on the intensity by normalising it and thus producing the complex degree of coherence,

$$g(\tau)=\frac{G(\tau)}{G(0)}=\frac{\langle U^{*}(t)\cdot U(t+\tau)\rangle}{\langle U^{*}(t)\cdot U(t)\rangle} \tag{3.23}$$

whose absolute value may not exceed unity.

If the value of $|g(\tau)|$ decays monotonically either side of its peak value at $g(0)$, the coherence time of the wavefunction being observed is defined as being the time delay between the points at which the complex degree of temporal coherence has dropped by some prescribed amount. What that amount is exactly is open to interpretation, but often the full-width half-maximum (FWHM) or $1/e^{2}$ points are used depending on the application and the shape of the function $|g(\tau)|$. Figure 3.2 shows a possible example of a complex degree of temporal coherence function with the FWHM labelled.

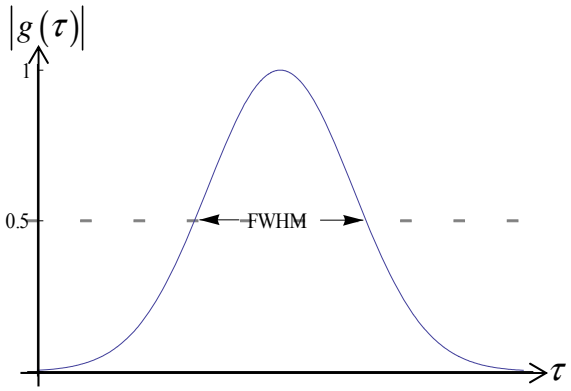

Figure 3.2 An arbitrary complex degree of coherence function

One important observation is that if the coherence time is much longer than any of the time delays being considered in a system, then the temporal coherence function simply becomes

$$|g(\tau)| = 1 \tag{3.24}$$

From the point of view of interferometry it is often more useful to talk about the coherence length which is simply

$$l_c = \frac{c}{n}\tau_c \tag{3.25}$$

The reason for this is because in interferometers the time delay, τ is physically realised by the changing of an optical path length within the instrument.

A light source whose coherence length is much larger than the differences of any of the optical path lengths encountered within an instrument can be considered to be effectively coherent.

3.4.5 Wavetrains

The concept of temporal coherence may be usefully considered in terms of wave trains. An optical source produces light in a set of discreet wave trains with each wave train being self-coherent, but only lasting for a finite period of time. Clearly, the longer the period of the wave trains emitted by the source, the more coherent the source. The physical mechanisms behind the production of wave trains varies

depending on the nature of the source whether it be a laser, light emitting diode (LED) or a thermal source such as a tungsten bulb (Jenkins & White 1976, p.276-279).

3.4.6 Power Spectral Density and Linewidth

The temporal coherence of light is intrinsically connected to its power spectral density (PSD) due to the application of the Weiner-Khinchin theorem which states that

$$S(\omega) = \int_{-\infty}^{\infty} G(\tau) e^{-j\omega\tau} d\tau \tag{3.26}$$

From this it can be seen that there is an inverse relationship between the PSD and the coherence time for an optical wave. In the extreme, a purely monochromatic wave must have an infinite coherence time; that is the length of the wave train must be infinite.

The width of the PSD is known as the linewidth or spectral bandwidth. Its definition, like that of the coherence time is somewhat arbitrary. A popular definition however is the full-width half-maximum (FWHM) of the spectral profile.

The relationship between the PSD of a wave and the complex degree of temporal coherence results has the effect of producing a natural line width upon any spectral line. Any spectral line is effectively broadened due to the finite duration of the wave train. This is distinct to other types of spectral line broadening that are due to mechanisms within the source itself such as Doppler shift broadening or pressure broadening. (Elmore & Heald, pp. 445-447).

In general, the wider the linewidth, the shorter the coherence time due to the Fourier transform relationship, and there is of course a dependence on the shape of the PSD function. It is therefore possible to increase the coherence time of light by using an optical filter to reduce its spectral width, at the expense of reducing intensity. For certain common PSD profiles it is useful to know the relationship between the FWHM spectral widths and the coherence time;

PSD Profile	FWHM Spectral Width , Δ_v
Lorentzian	$\frac{1}{\pi\tau_c}$
Gaussian	$\frac{\sqrt{2\ln 2/\pi}}{\tau_c}$

Table 3.2 FWHM spectral widths for common PSD profiles

In summary, the temporal coherence of light may be viewed in terms of wavetrains, or the Fourier decomposition of its spectral components. Light having a long coherence length must conversely feature a very narrow spectral bandwidth compared to its centre frequency and may be described as quasi-monochromatic. The concept of a purely monochromatic wave is theorectical as this would require an infinite coherence length.

3.4.7 Spatial Coherence

In the previous section the terminology describing the temporal coherence of a light source was arrived at. In that description the dependence on the position vector **r** was dropped and the interaction of waves at only one single point in space was considered. To fully describe the coherence of a complete wave it is necessary to re-introduce the position vector **r** and consider the coherence between two points $U(\mathbf{r}_1,t)$ and $U(\mathbf{r}_2,t)$ of a random wavefunction in space. The temporal coherence function in (3.22) then extends to become the mutual coherence function,

$$G(\mathbf{r}_1,\mathbf{r}_2,\tau)=\left\langle U^*(\mathbf{r}_1,t)\cdot U(\mathbf{r}_2,t+\tau)\right\rangle \tag{3.27}$$

Its peak is at $G(\mathbf{r}_1,\mathbf{r}_2,0)$ and so the normalised form is

$$g(\mathbf{r}_1,\mathbf{r}_2,\tau)=\frac{G(\mathbf{r}_1,\mathbf{r}_2,\tau)}{\left[I(\mathbf{r}_1)I(\mathbf{r}_2)\right]^{1/2}} \tag{3.28}$$

where $g(\mathbf{r}_1,\mathbf{r}_2,\tau)$ is the complex degree of coherence and its absolute magnitude is bounded between zero and unity. It is clear that at the same position in space, when

$\mathbf{r}_1 = \mathbf{r}_2$ then (3.28) reduces to the complex degree of temporal coherence shown in (3.23).

The spatial coherence of a random wave may be considered by examining the complex degree of mutual coherence at specific time delay, generally $\tau = 0$. If the light is quasi-monochromatic then we may consider the light to be completely temporally coherent. The complex degree of coherence then reduces to the harmonic function

$$G(\mathbf{r}_1, \mathbf{r}_2, \tau) = G(\mathbf{r}_1, \mathbf{r}_2) e^{jk\tau} \tag{3.29}$$

The complex degree of spatial coherence may now be defined as,

$$g(\mathbf{r}_1, \mathbf{r}_2) = \frac{G(\mathbf{r}_1, \mathbf{r}_2)}{\left[I(\mathbf{r}_1) I(\mathbf{r}_2) \right]^{1/2}} \tag{3.30}$$

The coherence area in a given plane is then defined by a predetermined drop in the value of the function $\left| g(\mathbf{r}_1, \mathbf{r}_2) \right|$ with the distance on the plane $\left| \mathbf{r}_1 - \mathbf{r}_2 \right|$. The coherence area is important when considering the passing of waves through apertures and also determining the coherence of light with regard to the resolution of an optical system. If the coherence area of a wave is smaller than the resolution of the optical system it may be considered to be effectively incoherent. Conversely if a light wave passes through a pinhole smaller than its coherence area at that point, spatial coherence is imparted upon the wave.

The coherence area should not be confused with the coherence length defined in (3.25) which is in fact a parameter relating to the temporal coherence.

3.4.8 Longitudinal Coherence

The concept of coherence in a transverse wave having wavefronts of equal phase is usefully described by longitudinal coherence. In Cartesian coordinates a wave propagating along the z-axis will be entirely spatially coherent on any position on a given wavefront. However, it is only partially coherent in the axial (longitudinal) direction. The temporal coherence has a one to one relationship with the longitudinal coherence.

3.4.9 Interference of Partially Coherent Light

With the coherence of light now defined in the previous sections, it is now possible to expand upon the definition of the superposition of two waves. In section 3.3 the intensity resulting from the superposition of two completely coherent waves was derived. In (3.28) the complex degree of coherence was defined for a single wave. It is however equally valid to describe the complex degree of coherence between two different waves having complex wavefunctions $U_1(\mathbf{r},t)$ and $U_2(\mathbf{r},t)$. At a given point in space, the time-averaged intensities of the individual waves are $I_1 = \left\langle |U_1|^2 \right\rangle$ and $I_2 = \left\langle |U_2|^2 \right\rangle$. The cross-correlation function (as opposed to auto-correlation) is then

$$G_{12} = \left\langle U_1^* U_2 \right\rangle \tag{3.31}$$

and in a similar fashion to (3.23) its normalised version is

$$g_{12} = \frac{\left\langle U_1^* U_2 \right\rangle}{\left(I_1 I_2\right)^{1/2}} \tag{3.32}$$

The interference for the two superposed waves, as given in section 3.3, is rewritten here but with the time-averaging made explicit,

$$I = \left\langle |I_1|^2 \right\rangle + \left\langle |I_1|^2 \right\rangle + \left\langle U_1 U_2^* \right\rangle + \left\langle U_1^* U_2 \right\rangle \tag{3.33}$$

By using (3.31) we arrive at an interference equation which relates to the cross-correlation of the two complex wavefunctions,

$$I = I_1 + I_2 + G_{12} + G_{12}^* = I_1 + I_2 + 2\,\mathrm{Re}\left\{G_{12}\right\} \tag{3.34}$$

The normalised version of the cross-correlation function (3.32) may then be usefully substituted into (3.34) since we have the terms I_1 and I_2 present already,

$$I = I_1 + I_2 + G_{12} + G_{12}^* = I_1 + I_2 + 2\sqrt{I_1 I_2}\,\mathrm{Re}\left\{g_{12}\right\} \tag{3.35}$$

The final form is then

$$I = I_1 + I_2 + 2\sqrt{I_1 I_2}\,\left|g_{12}\right|\cos\varphi \tag{3.36}$$

which is similar to the interference equation shown in (3.15) but that the third term is now modulated by the complex degree of coherence where $\varphi = \arg\{g_{12}\}$ and is the phase difference of the two waves. This is a more generalised form of the interference equation. Consider that if the two superposed waves are completely coherent, that is $g_{12} = 1$ then the interference equation defined in (3.15) is recovered (Saleh & Teich 1991, pp.342-375).

From (3.35) it can be seen that the intensity produced by the interference is a sinusoidal pattern which varies as the phase difference between the two waves changes. It is this variation that is measured by an interferometer in order to determine optical path length changes. Figure 3.3 shows a normalised intensity response for the interference between two arbitrary partially coherent waves. The modulation of the interference by some envelope function, $|g_{12}|$ is quite clear.

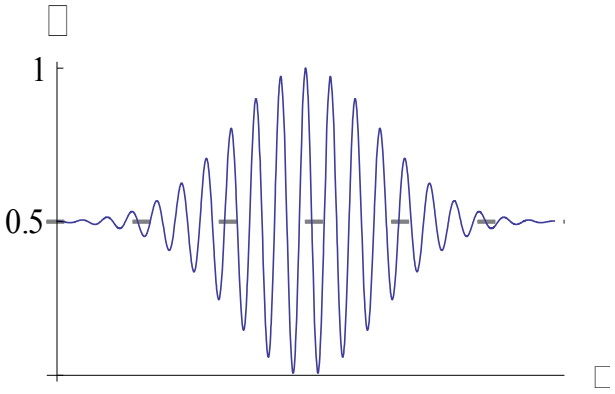

Figure 3.3 Example of Interference between two partially coherent waves

3.5 Polarised Light

3.5.1 The Polarised Nature of Light

The scalar optics approximation has many benefits for the instrument designer, simplifying greatly the concepts of diffraction and interference of a light wave passing through an optical system. It has however one major limitation and that is in the way it approximates the electro-magnetic vector field into a single number that represents the electric field vector along a fixed axis of polarisation. This means it is unable to represent the polarized nature of light in any way. Unfortunately, as will be

shown, the polarisation of light waves is of great consequence to them undergoing coherent interference.

One way to provide for the continued use of the scalar optics approximation is to keep track of the polarisation state of light separately. This allows for a manageable approach for representing an optical system, by the method of recording the polarising effects of components through 'book keeping'. Hobbs states that such an approach is 'inelegant and mathematically unjustified, but works well in practice,' and in reality this is the most applied methodology in the field of optical instrument design (Hobbs 2000, pp.9-10).

The Poincaré sphere gives a method of easily visualising the effect of polarisers, retarders and rotators upon the polarisation state.

3.5.2 The Poincaré Sphere Representation.

A useful and easily visualised representation of polarised light is the projection of the polarisation ellipse onto the Poincare Sphere. It provides a method for plotting the polarisation state and allows the user to visualise easily how polarisation evolution takes place. It is a representation that has gained great favour in the literature relating to polarisation effects in fibre interferometers, so it is essential to gain an understanding of the representation. The derivation of the method relies on spherical trigonometry, however only a basic understanding of the projection is necessary in order to use the Poincaré sphere to map polarisation state transformations. While the method is what appears to be a simplistic and elegant way of looking at polarisation transformation problems it is really only useful as an aide with which to visualise the way polarizing components act upon a polarised beam. In reality most problems are solved using the Jones calculus. Nevertheless it is extremely popular in fibre optics literature. (Collett 2003, pp.46-53)

For a transverse electromagnetic (TEM) wave described as travelling along the optical axis (the z axis), its electric field vector lies in the x-y plane. The tip of the electric field vector on the x-y plane at any chosen point along the z axis traces out an ellipse over one period of oscillation. This polarisation ellipse can be used as a means of describing the propagation of the TEM wave, $E(z,t)$ along a displacement, z and over time, t

The polarisation ellipse is formed by taking two arbitrary, orthogonal components of the electrical field vector in the x-y plane, $E_x\hat{x}$ and $E_y\hat{y}$. Critically, their frequency of oscillation is the same, but they differ in both phase and amplitude. The electric field is described as,

$$E(z,t) = E_x\hat{x} + E_y\hat{y} \tag{3.37}$$

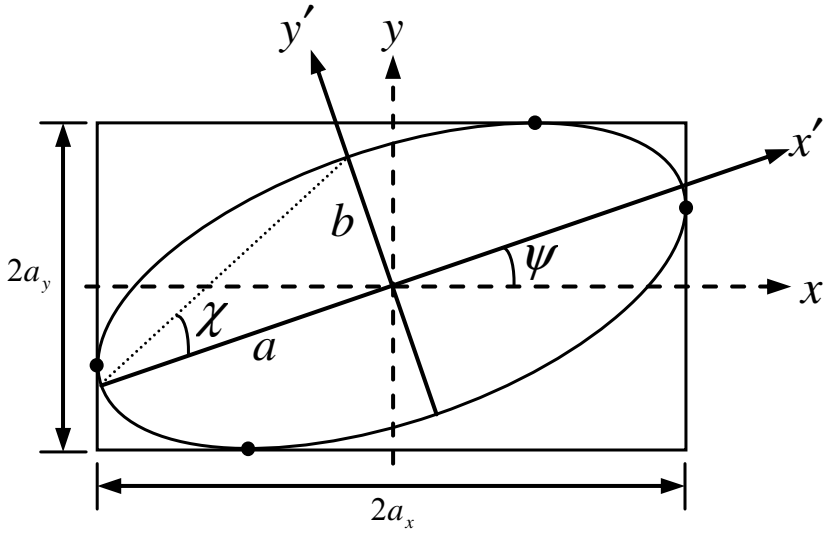

Figure 3.4 The polarisation ellipse and its components

Figure 3.4 shows a representation of the polarisation ellipse. A common alternative way of defining the ellipse is in terms of an angle of rotation, ψ and an angle of ellipticity, χ where,

$$\tan\chi = \frac{\pm b}{a} \quad \text{over the range} \left(-\frac{\pi}{4} \le \chi \le +\frac{\pi}{4}\right) \tag{3.38}$$

Where $2b$ and $2a$ are the minor and major axis lengths of the ellipse respectively ($a > b$). The angle of rotation, ψ is the angle the major axis makes with the x axis.

The Stokes parameters for elliptically polarised light can be related to the spherical coordinate set. First, the Stokes parameters; S_1, S_2 and S_3 are plotted on the x, y and z axes respectively in Cartesian space. By observing the angles formed in the equivalent spherical coordinate space it can be shown that the inclination angle, $\theta = 2\chi$ and the azimuth angle, $\varphi = 2\psi$. Each point on the Poincaré sphere represents a unique polarisation state and all possible polarisation states are represented on the

sphere. The radius of the sphere is proportional to the intensity of the polarised light. The longitude of any point on the sphere represents a specific angle of rotation, while the latitude represents the angle of ellipticity. An arbitrary polarisation state, p is shown in figure 3.5.

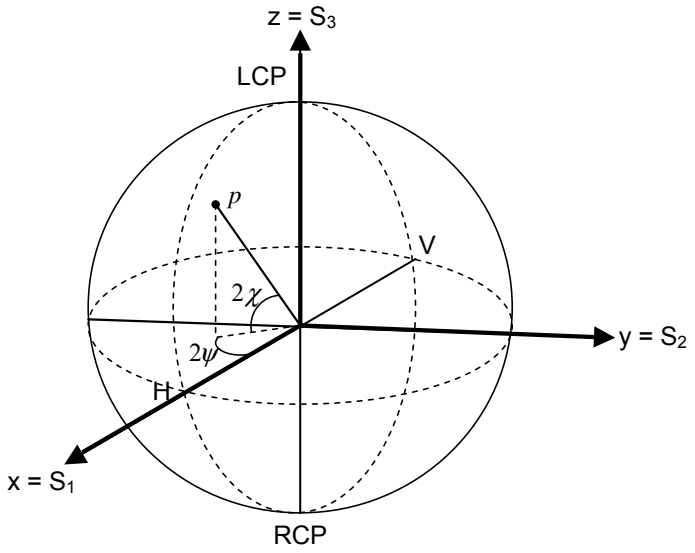

Figure 3.5 A polarisation state p on the Poincaré sphere

For linearly polarised light, the point on the sphere is restricted to the equator, since the angle of ellipticity is zero. Horizontal LP light is represented by the point on the equator along the x axis. For vertical LP the point moves 180º around the equator a point diametrically opposite. A +45º LP, the point will move 90º around the equator clock anticlockwise to a point on the y axis. We can see that the action of any linear polariser is to restrict the polarisation state to equatorial plane.

A rotator changes the orientation angle, ψ of the polarisation ellipse. This is equivalent to a rotation of the Poincaré sphere about the S_3 axis of 2ψ. Essentially it is a migration of the polarisation state point along given latitude. This is shown in figure 3.6.

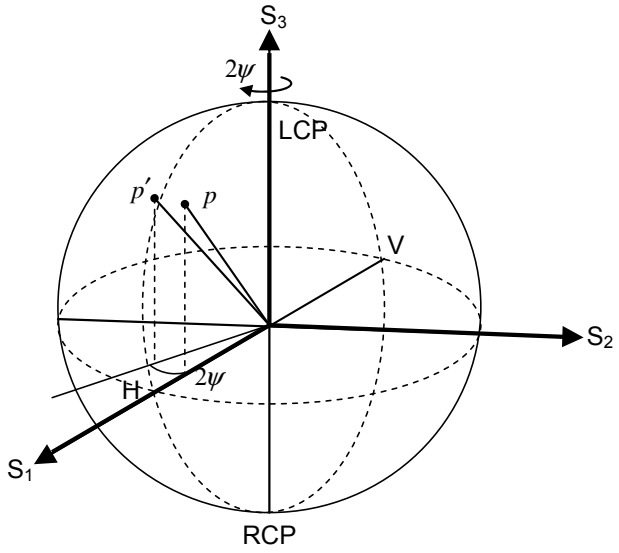

Figure 3.6 Migration if the polarisation state from p to p' as a result of action by a rotator

A linear retarder, changes the angle of ellipticity, χ of the polarisation ellipse, thus we can view it as altering the latitude of the polarisation state point as plotted on the Poincaré sphere. The upper and lower poles of the Poincaré sphere represent left and right circularly polarised light (LCP and RCP) respectively. The behaviour of a linear retarder to the polarisation state can be modelled by a rotation of the Poincaré sphere by an angle of 2φ about an axis on the equator. This axis makes an angle 2ψ with the S_1 axis, where ψ is the orientation angle of the retarders fast axis to the x axis, as shown in figure 3.7 (Goldstein 2003, pp.241-273).

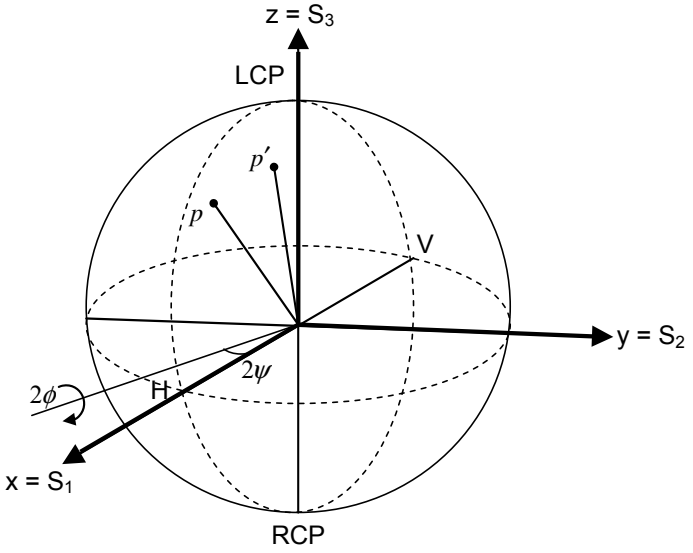

Figure 3.7 Migration of the a polarisation state from point p to point p' as a result of the action of an elliptical retarder with a phase shift of φ and a fast axis orientation of ψ from the horizontal

3.5.3 Modelling polarisation state Evolution in Optical Fibre using Elliptical Retarders

A further optical component shall now be considered, the elliptical retarder, so called because its eigenvectors are both elliptical polarisation states. Such a component can be viewed as the combination a a linear retarder followed by a rotator. Such a device is of great importance to the study of fibre interferometers because it may be used to describe the overall polarisation state evolution of light travelling down an optical fibre. Any length of optical fibre may be viewed as an elliptical retarder for this purpose (Sarma 1977).

From the point of view of the Poincaré sphere, the elliptical retarder may be modelled in a similar fashioned to a linear retarder except that the axis of retardation may now intersect the sphere at any state of polarisation (SOP) point, it is not only restricted to the equator (Johnson 1981).

3.6 Fibre Optics

3.6.1 Historical Overview of Fibre Optics

It is necessary in this work to become familiar with the basic principles of guided wave optics in order to understand the basic operation of an optical fibre interferometer and also to appreciate the limitations and problems associated with such devices. It is not in the scope of this thesis to delve to deeply in the complex underlying theory of guided waves in optical fibres and it is only necessary to be concerned with the operation of telecommunications band single mode fibre to gain an understanding of the instruments outlined herein.

Since their inception in the 1960s fibre optics have been responsible for revolutionising networking across long and short distance runs. This is due to their ability to transmit optical signals over large distances with little attenuation and the corresponding reduction in repeaters. In addition to this, the optical domain carrier

frequencies mean the potential bandwidths of optical fibres are much higher than is possible with traditional metallic cable or microwave links. Such systems are limited to bit rates of approximately 100Mb/s and repeaters are required every few kilometres. Optical fibre technology has seen a steady growth of bit rates since its inception with commercial technologies now providing 40 Gb/s on long distance single mode, single wavelength links. Wavelength division multiplexing (WDM) techniques have demonstrated capacities of 10 Tb/s on a single fibre. Many of the more recent techniques have been directly applicable to currently in-place fibre infrastructure. For instance, a data rate 1 Tb/s over 5 km link was recently demonstrated over a multimode fibre link typical of existing optical local area network (LAN) installations present in buildings (Gasulla and Capmany 2008). One figure of merit used to determine the quality of an optical fibre link is the capacity-distance product which has doubled every year between 1975 and 2000. Another beneficial aspect of optical fibre is that it is made from glass, a material that is both cheap and plentiful especially compared to the copper used in traditional wire links. Optical fibre has been the main reason for the success of the internet revolution and its impact will increase further as fibre to the home (FTTH) technology replaces the bandwidth limit imposed by that final length of copper cable connecting us to the telephone exchanges. (Dutton 1998, pp.1-8)

3.6.2 Structure of Optical Fibre

The simplest fibre structure is the step index fibre which is the fibre type used within instruments discussed in this thesis. Many other fibre profiles exist in order to improve upon the basic properties of step index fibres in terms of intrinsic loss, bending loss, mode field radius and dispersion. Such exotic fibre profiles include gradient index, W-profile, triangular core and Gaussian core, all of which refer to the refractive index profile across the fibre diameter. Exotic core shapes also exist to provide polarisation maintaining properties either through shaping the core elliptically or adding stress rods that exert a birefringence in the core (PANDA or bowtie).

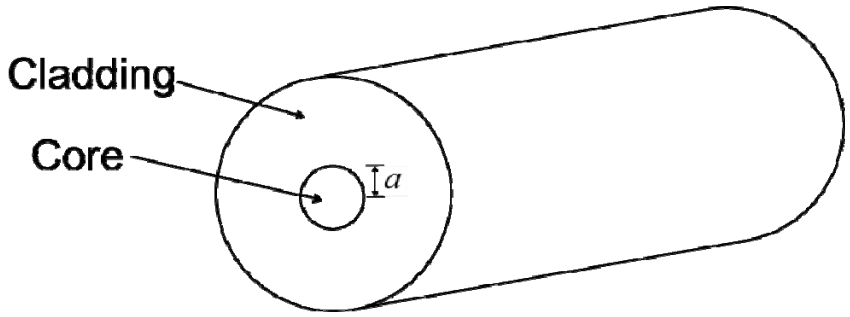

Figure 3.8 Step index fibre structure

The step index fibre consists of two concentric homogenous dielectrics each of a distinct refractive index. The outer material is the cladding and is most commonly found to be 125 μm in diameter. The core diameter $2a$ varies depending on the operating wavelength but for long haul telecommunications fibre it is generally 8-10 μm. The inner core and outer cladding have indices n_1 and n_2 respectively and $n_2 < n_1$ in order to provide for total internal reflection (TIR) of a ray entering the core within the fibre. The indexes are generally very close together in value however so that the fibre satisfies the weakly guiding condition. The key parameters defining a step index fibre are the core diameter, a and the normalised index difference which is defined as

$$\Delta \frac{\left(n_1^2 - n_2^2\right)}{2n_1^2} \approx \frac{n_1 - n_2}{n_1} = \frac{\delta n}{n_1} \tag{3.39}$$

In addition, the numerical aperture (N.A.) is defined as the sine of the maximum half angle at which a ray may enter the core and remain guided by the fibre. The N.A. is found to be

$$\text{N.A.} = \sin\theta = \frac{1}{n_0}\sqrt{n_1^2 - n_2^2} = \frac{n_1}{n_0}\sqrt{2\Delta} \tag{3.40}$$

When considering waves propagating through a fibre, the cylindrical coordinate system is used with the fibre axis coincident with the z axis.

3.6.3 Operating Conditions

Telecommunications fibre has traditionally been operated at three specific transmission bands or windows were attenuation in the fibre material was at its

lowest. The various attenuation mechanisms superpose to present the attenuation profile for a silica waveguide. This is shown in figure 3.9.

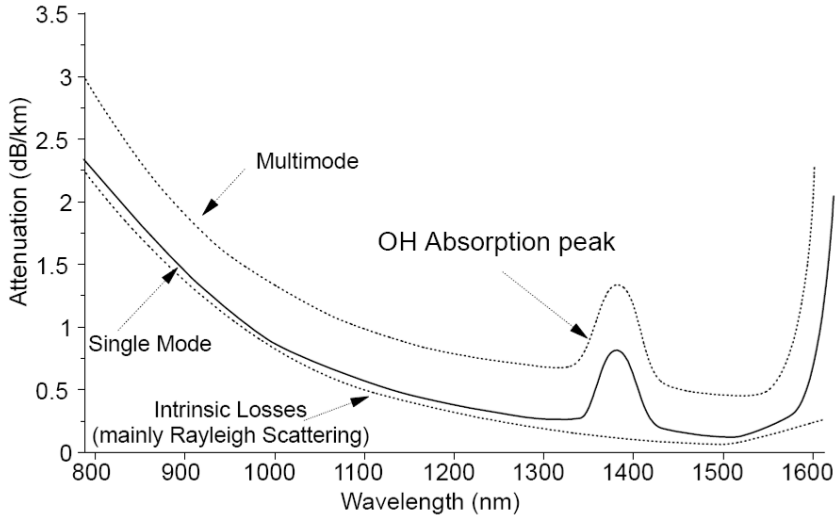

Figure 3.9 Attenuation of optical fibre with wavelength (Dutton 1998, p.31)

Originally, during the 1970s and early 1980s the first transmission window was 800 - 900 nm. Reference to figure 3.9 suggests this is certainly not optimal, but source and detector technology proved to be the limiting factor.

By the mid 1980s improvements in sources and detectors realised the possibility of operating in a window centred around 1310 nm. Within this window the attenuation is only 0.4 dB per km and attractively, dispersion almost zero, thus reducing pulse broadening over long distance runs. This window is the basis for many of the older telecommunications networks still operating today.

In the 1990s further advances still in source and detector technology and specifics of fibre amplifier performance saw the advent of a third transmission window between 1510 nm and 1600 nm which has the lowest attenuation of all. Most newly developed communications systems use this band.

Of course the use of fibre optic interferometry as outlined in this thesis does not have the same stringent requirements for long haul performance as the total fibre length in any given systems is unlikely to be more than several tens of metres. However economies of scale with regard to optical fibre and its associated components, interconnects and so on have a major impact on the cost of any developed instrument.

In general, using standardised telecommunications technology results in a massively reduced cost when compared to an equivalent system constructed from more niche (scientific) market components. As a consequence of these economies of scale, the instrumentation developed in this thesis operates in1510-1600 nm window.

3.6.4 Guided Modes

Various possible guided modes types exist depending on the orientation of the field vector of the guided waves. These are transverse electric (TE), transverse magnetic (TM) or hybrid (EH or HE). In terms of ray paths, TE and TM modes are associated with meridionally guided rays, i.e. those which exist in a plane that crosses the core centre. These modes maintain one field vector (**E** for TE, **H** for TM) in the transverse plane and one which has a small component in the z direction. The hybrid modes are associated with skew rays which never cross the core centre and as such change direction on each bounce, meaning both the **E** and **H** vectors have z components.

The weak-guidance approximation resulting from the very small index difference between the core and cladding allows for the severe limiting of possible guided modes to a set of the so called linearly polarised (LP) modes. These may be considered to have their electric and magnetic field vectors confined to within the transverse plane of the fibre on account of them having such small components in the z direction. They essentially act as a TEM wave and exhibit almost plane wave behaviour. When field analysis is carried out to determine the existence of the various modes, it is done using the weakly guided LP modes approximation.

The field analysis for determining the LP modes of an optical fibre is somewhat complex and arduous and bearing in mind that we are only concerned with single mode operation we can consider directly the requirements for the guiding of a single mode.

The number of guided modes present in an optical fibre depends on the normalised frequency parameter,

$$V_m = ak_0\left(n_1^2 - n_2^2\right)^{1/2} = n_1 ak_0\sqrt{2\Delta} \tag{3.41}$$

where $k_0 = \frac{2\pi}{\lambda}$ is the free space wavenumber. The normalised frequency parameter, V-number or mode volume as it is variously named determines the number of modes that will be guided in any given fibre for a given operating wavelength range. Solutions to the wave equation under the boundary conditions specified for the fibre and taking into account the weakly guiding TEM approximation yield a single guided mode when the V-number is in the range $0 < V < 2.405$.

This mode results from a hybrid mode and is known as the LP_{01} mode. With this in mind we can rewrite (3.41) in terms of a cut-off wavelength above which single mode operation occurs,

$$\lambda_{cutoff} = \frac{2\pi}{2.405} a n_1 \sqrt{2\Delta} \tag{3.42}$$

At this point it is worthwhile evaluating (3.42) for some common scenarios.

Consider that the index difference for single mode fibres is typically about 0.2% for single mode fibres and the index of the doped silica core around 1.5. The second transmission window used for long distance telecommunications ranges from wavelengths of 1250 – 1350 nm. If we take the shortest wavelength end of the band we find that for single mode operation in this region the maximum core radius must be 5.04 μm. Clearly such a core size also provides for single mode operation at the upper low attenuation window, which ranges from wavelengths of 1530 – 1565 nm, without any change in physical fibre parameters (Buck 2004 pp. 51-79).

The V-number, as well as defining the cut off wavelength for a given core radius, it also determines the so called mode field diameter (MFD) of the guided wave. The electric field profile of the LP_{01} mode is very well approximated by a Gaussian profile centred on the fibre axis. The MFD is thus determined by the points at which the consequent intensity drops to $1/e^2$ from the core centre. For single mode operation the MFD is always larger than the core diameter, hence some of the field is carried in the cladding. The approximate relationship between the MFD (determined by the best fit Gaussian) and the V-number is given by

$$w_0 = a\left(\frac{1}{3} + \sqrt{\frac{2.6}{V_m^3}}\right) \tag{3.43}$$

for the single mode situation. From (3.43) we can determine that as the V-number decreases the MFD increases resulting in a larger proportion of the field being carried in the cladding. Such a situation results in the guided mode being more susceptible to bending losses but at the same time relaxes alignment tolerance for efficient coupling of light to and from the fibre. In general a compromise must be struck and the V-number is kept between 1.8 and 2.4. For this reason, the core diameter of single mode fibre for telecommunications use generally varies between 8 – 10 μm (Hobbs 2000, pp.239-245).

From the above results we can anticipate that the core size for single mode fibre operating in the visible spectrum must be smaller and this is indeed the case. Single mode operation of a fibre at $\lambda = 633$ nm requires a maximum core radius of 2.55 μm.

3.7 Conclusion

In this chapter the essential terminology and mathematics needed to describe the propagation of light in interferometers was defined. The scalar optics concepts of beam propagation, interference and coherence were introduced. The Poincaré sphere was introduced as a common way of describing the polarisation of light in optical fibre. The basic operation of optical fibre was then described with the onus placed upon single mode (SM) fibres. General considerations for the use of optical fibres were also covered.

These basic concepts will be used to describe the operation of the interferometer in general in Chapter 4. The concepts of beam propagation, interference and coherence are central to describing interferometric devices. Futhermore, the concept of the fibre optic interferometer will be looked at in detail and importantly, the effect of polarisation states on the operation of such instruments.

The next chapter will go on to describe the specific operation of several interferometer types used in surface metrology and provide a basis for the practical investigations further on.

4 Interferometry

4.1 Introduction

This chapter intends to provide a general introduction to the interferometer and then study closely two specific types; the Michelson and Fabry-Perot. The importance of the Michelson interferometer and its variants in the field of surface metrology will be discussed. Next the creation of sensors using fibre optic interferometers will be considered along with advantages and difficulties of implementing such techniques.

4.2 The Interferometer

4.2.1 Background

Interference and thus the validation of the wave like character of light was first observed by Young in his single and double slit experiments in 1801. Since then a bewildering array of instruments have been developed in order to harness the phenomenon and they are known collectively as interferometers. The scope of optical interferometry to enable measurement of a wide variety of parameters is huge.

The measurement of the angular diameter of stars using Michelson's stellar interferometer (not to be confused with the Michelson interferometer) mounted on a telescope was arranged in 1921. This was then superseded by Hanbury-Brown and Twiss using a long baseline correlation interferometer having even greater sensitivity. The refractive index of gases may be measured using a Mach-Zehnder interferometer, one of its paths travelling through a transparent gas cell.

Perhaps the most famous interferometer is the Michelson interferometer, invented by A.A. Michelson and used in the Michelson-Morley experiment which proved the non-existence of ether. Michelson's research resulted directly in the application of light in the field of metrology. In 1892, Michelson succeeded in measuring the International Metre bar standard using the red band of cadmium as a light source. Using this light source he determined that the International Metre Bar had a length which was equal to 1,533,164.13 wavelengths of red cadmium at 760 mm atmospheric pressure. For the first time a link was made between the metre standard and the speed of light.

The interferometer has since found a host of other uses and has many variants on its design. For instance the Twyman-Green interferometer, which is essentially Michelson interferometer illuminated with collimated light, is still often used in the testing the accuracy of optical components and enabled for the first time, the manufacture of virtually perfect lenses and prisms (Jenkins & White 1974, pp.349 – 353).

The Mirau interferometer allows a compact form suitable for integrating with a microscope objective and features an in-line structure making it relatively robust to vibration pickup. As such, the Mirau has enabled interference microscopy which is the basis for many surface measurement profilers such as vertical scanning white light interferometry (VWLSI) (Hariharan 1992, p.110).

The Fabry-Perot cavity, which makes use of multiple beam interference can act as a narrow band filter, one use is in the selection of a single mode from a multiple set of longitudinal modes in a laser cavity. The SI unit for the metre is realised by the combination of an iodine-stabilised helium-neon laser and a fringe counting interferometer. In addition the Fabry-Perot interferometer works well as a spectrometer especially for low light situations as less light is lost than with traditional diffractive methods (Hariharan 1992, pp.67-68).

In general it is the ability of an interferometer to convert a very small change (in the phase of an optical wave) into a relatively large and thus observable change in intensity that makes it such a useful tool.

4.2.2 Fringes

All interferometers produce bands of varying intensity called fringes that occur as the result of the coherent superposition of waves. There are many categories of fringes such as Newton, Brewster and Fizeau, the names usually being derived from the instrument or method by which they are produced. They may be circular, parallel or anything in between and may also be coloured in the case of white light fringes. Interferometry concerns itself with the production of interference fringes (or interferograms) and there subsequent analysis. Fringe spacing, shape, deviation, rate of translation and colour are all used to determine a variation in a measurand depending on the specific application.

While interference fringes have many uses and provide the capability to measure certain parameters to a high degree of accuracy, a second class of interference fringes also exists which often conspire to cause problems. This class of fringes are known as etalon fringes, being that they are created by any cavity in an optical instrument shorter than the coherence length of the light illuminating it. These unwanted fringes can play havoc with measurements made if we are not careful to ensure unwanted back reflected light from surfaces is not minimised by using suitable alignment techniques and anti-reflection coatings.

4.2.3 Division Type

Interferometers fall into one of two distinct categories depending on how they derive the wave sources they interfere. Wavefront division interferometers split a single wavefront into two or more wavefronts using apertures, Michelson's stellar interferometer being one example. The other type of interferometer splits an incoming beam by amplitude to create two separate beams. This may be done by a variety of methods such as a partially reflective surface, diffraction grating of polarizing prism. The Michelson is an important interferometer that falls into this class. It will feature heavily in the material presented in the remainder of this thesis as it is this configuration that forms the basis for the instrumentation developed.

4.3 The Michelson Interferometer

4.3.1 Apparatus

The Michelson Interferometer is an apparatus which makes use of two beam amplitude division to produce interference fringes. Invented by A. A. Michelson an American physicist, it allows the precise measurement of wavelength, length or refractive index. It relies on the fact that two partially or fully coherent light waves will interfere either constructively or destructively, dependent on their relative phases.

Figure 4.1 describes the setup of a Michelson interferometer consisting of two mirrors, one fixed and one adjustable along the same optical axis as the incident light rays. The tilt of the mirrors is adjustable with the aid of fine pitched screws to ensure

that the return path is exactly coincident with the forward path. Fresnel reflections have been omitted from this figure for simplicity.

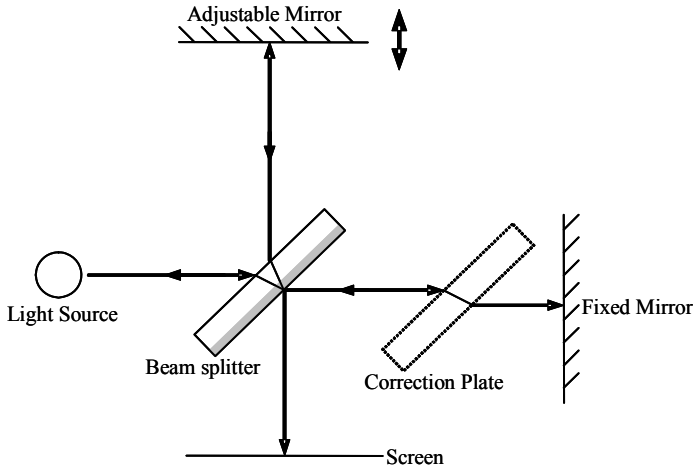

Figure 4.1 The Michelson interferometer

Precise translational adjustment is required on the adjustable mirror and is carried out by fine threaded screws or often a piezo-electric translator (PZT). Between the two mirrors and a light source lies a beam splitter, partially mirrored and orientated such that half the light incident is transmitted through and half is reflected at 90º to the angle of incidence.

The individual paths between the respective mirrors and the beam splitter are called the arms of the interferometer. Generally the reference arm is the arm containing the adjustable mirror while the measurement arm contains the fixed mirror. This is the definition that will be applied throughout this thesis. The light waves travel the lengths of their respective arms before recombining at the beam splitter. The resulting interfered wave is then cast onto a screen/detector or viewed directly with the eye or a telescope. It is at this recombination point that the interference occurs.

4.3.2 Analysis

The basic theory regarding the interference of coherent waves has been considered in section 3.3. However it is worthwhile expanding on the particular details involving the Michelson interferometer. For simplicity it is useful to consider the interferometer illuminated with a collimated wavefront as is found in the Twyman-Green variant. figure 4.2 shows the setup up of such an interferometer.

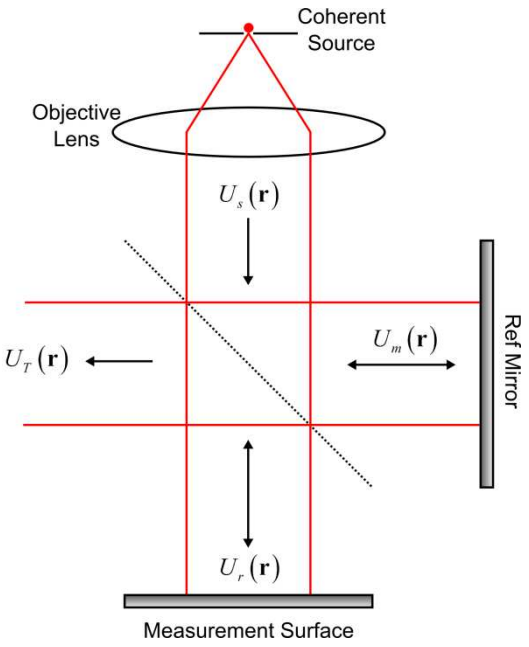

Figure 4.2 The Twyman-Green interferometer

If we consider a plane wave of complex amplitude $U_s(\mathbf{r})$ incident on the beam splitter, it is separated into two orthogonal beams, one reflected along the measurement arm direction and one transmitted through to the reference arm. Assuming a perfect, lossless 50/50 beam splitter, there is no aberration of the wavefronts and the amplitude of the waves is halved exactly producing two waves

$$U_r(\mathbf{r}) = \frac{1}{2}U_s(\mathbf{r}) \tag{4.1}$$

$$U_m(\mathbf{r}) = \frac{1}{2}U_s(\mathbf{r}) \tag{4.2}$$

as notated in figure 4.2. After reflection from their respective mirrors they recombine upon the beam splitter. The intensity of the wave arriving at the detector is then

$$I(\mathbf{r}) = \left|U_T(\mathbf{r})\right|^2 = \left|U_r(\mathbf{r})U_s(\mathbf{r})\right|^2 \tag{4.3}$$

At a single point, $\mathbf{r}$ and dropping that notation for brevity, the output intensity is as was shown in section 3.4.9,

$$I = I_1 + I_2 + 2\sqrt{I_1 I_2}\,|g_{12}|\cos\varphi \tag{4.4}$$

where $\cos\varphi$ is the argument of the degree of complex coherence with φ being the phase difference between in two waves, which is in turn due to the different optical paths travelled in each arm of the interferometer, and the phase change on reflection from the respective mirrors.

Equation (4.4) shows that the intensity of the light projected onto the screen is dependent on the phase difference between the waves in the two arms. When φ is an odd multiple of π the interference is destructive and the observed intensity is at a minimum. Conversely even multiples of π will lead to constructive interference and maxima are observed.

One important point to note is that an equivalent light wave (but 180º out of phase with $U_T(\mathbf{r})$) travels back toward the light source and is lost to the observer. This is an important consequence required for the conservation of energy. In the case of a fringe minimum occurring at the output, a maximum will be occurring at an equivalent point in the wave travelling back to the source. This is a matter of importance when dealing with laser sources, as light entering the cavity can cause instability in the source.

The fringe contrast, modulation depth or visibility is determined by the magnitude of the complex degree of coherence. If the waves are fully coherent and in phase then the visibility is unity. Generally however it is more useful to relate the visibility in terms of an observable quantity, the intensity. The visibility of the fringes is defined as

$$V = \frac{I_{\max} - I_{\min}}{I_{\max} + I_{\min}} \tag{4.5}$$

Clearly $I_{\max}$ and $I_{\min}$ occur when the $\cos\varphi$ term is at +1 and -1 respectively. The visibility is then seen to be

$$V = \frac{2\sqrt{I_1 I_2}}{I_1 + I_2}\left|g_{12}\right| \tag{4.6}$$

Thus the modulation depth is proportional to the magnitude of the complex degree of coherence. In the case of equal intensities in the arms where $I_1 = I_2 = I_0$ then the visibility is simply, $V = |g_{12}|$.

Equation (4.4) may now be compactly rewritten as

$$I = I_0 [1 + V \cos \varphi] \tag{4.7}$$

where $I_0 = I_1 I_2$ and is the DC intensity.

In the following discussion the usual form of illumination is assumed, that of quasi-monochromatic light. The relationship between the optical path difference and the phase difference is linear in a Michelson interferometer. Moving the mirror in the reference arm a distance l will result in a change in the optical path length $2l$ due to the double pass of the light in the arms. In general we can say that the phase difference is related to the distance moved by

$$\varphi = 2kx = \frac{4\pi l}{\lambda} \tag{4.8}$$

With reference to (4.7) it can be seen that φ changes modulo 2π every time the reference arm moves by a distance $\lambda/2$. Maxima are observed every time the mirror moves by a half wavelength.

It is therefore possible to accurately measure distances by moving the mirror slowly and counting the number of maxima that are displayed. By setting the mirrors to a known distance, the wavelength of the source may be calculated.

Of course since a wavelength term is also present in (4.8) a phase change may also be effected by a change in refractive index, for instance by the introduction of a gas into one of the paths. Indeed, interferograms may be seen to be disturbed by the refractive index fluctuation of air due to density and temperature variation. This can be especially problematic in long path length interferometers.

4.4 Interferometry for Surface Profiling

4.4.1 Overview

For the measurement of large areas of surface deviation the Twyman-Green interferometer is the most useful tool as it can image a large area limited only by the aperture of the beam splitter and collimating lens in use. This is of particular use for the high precision polishing of optics, where small deviations in form are compared in an optical component. The requirements for the analysis of high precision surfaces are somewhat different however.

Surface profiling operates over a range of dimensional scales depending on the type of manufacturing being undertaken. At each scale the filter ranges and cut-off wavelengths that define surface roughness, waviness and form vary, as do the physically limited parameters like the sampling interval.

The analysis of surface texture on the micro and nano scales requires lateral resolutions down to microns. For optical techniques to image at these resolutions microscopy techniques must be used. The lateral resolution achievable by using an optical approach is always diffraction limited. The only way to increase the resolving power at a given wavelength is to image a smaller area using a higher N.A. lens. In general microscopy the Abbé approximated limit for two resolved points is

$$R = \frac{\lambda}{2N.A.} \tag{4.9}$$

for the case of external illumination.

Generally as lens N.A. and magnification increases, there is a resulting shortening of the working distance. This creates substantial difficulties in the design of objectives for interference microscopy. There are thus three essential interferometer designs that are implemented depending on the magnification used.

The relationship between the phase φ at any imaged point and the height h above the surface above some reference is $\varphi = 2h$ due to the double pass of light in Michelson interferometers and its variants (Wyant & Creath 1992)

4.4.2 Michelson

Low magnification but large area imaging is suited to Michelson based interferometric objectives. A large field of view is possible but the presence of a beam splitter after the objective severely limits the working distance and is not

feasible at higher N.A. Generally this lens type is seen at x1.5, x2.5 and x5 magnifications.

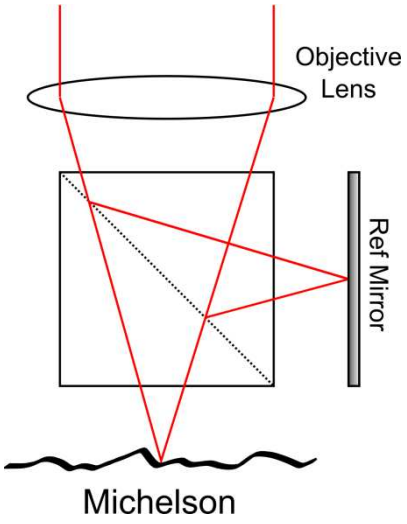

Figure 4.3 The Michelson interferometric objective

4.4.3 Mirau

This interferometer layout circumnavigates the issue of the bulky beam splitter by using a semi reflective element orthogonal to the transmitted lightwave. A small mirror is used as the reference and the whole design much more compact. In fact the inline construction of the reference and sample mean that the Mirau interferometer features decreased sensitivity to vibration, making it a popular choice for many applications. Disadvantages are the obfuscation in the centre of the field caused by the presence of the mirror and also the difficulty in applying phase shifting techniques through the translation of the reference mirror. Magnifications of x10 to x50 are possible until the working distance restriction proves limiting.

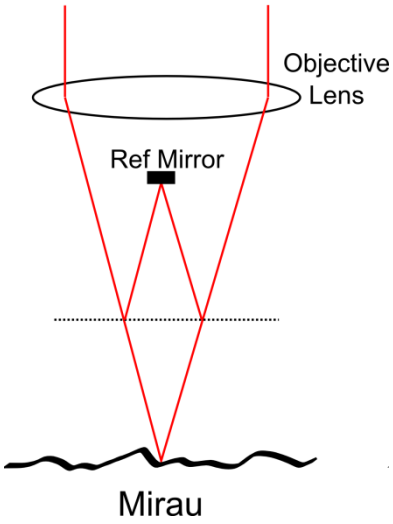

Figure 4.4 The Mirau interferometer objective

4.4.4 Linnik

This interferometer makes use of matched objectives to remove all obstruction between the lens and the sample, thus removing working distance restrictions. Such a method is exceptionally expensive as not only are two objectives required, they must also be exceptionally well matched. The expense means that the Linnik interferometer objective is only found in those situations where the working distance restriction needs to be removed, magnifications of up to x100 (0.95 N.A. in air) are possible.

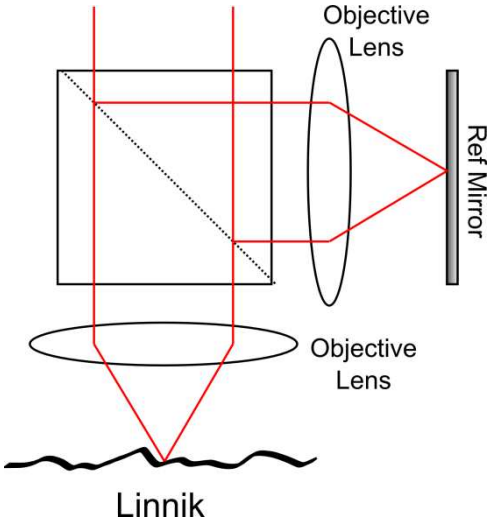

Figure 4.5 The Linnik interferometer objective

4.4.5 Limitations of Monochromatic Interferometry

One major limitation of monochromatic interferometry is the limited unambiguous range encountered due to the fact that the intensity relation to the phase is modulo 2π. For a smoothly varying surface such as a lens it is possible unwrapping algorithms are available to increase this range. However they are limited to gradients that change the phase by less than π over adjacent pixels which in the case of a Michelson interferometer running at $\lambda = 633$ nm would be 158.25 nm. Various algorithms have been designed to minimise the effects of noise and bad data which can cause incorrect phase unwrapping (Charlette & Hunter, 1996; Herraez et al., 2002).

Techniques have been developed to extend the measurement range including the method of synthetic wavelength where two narrowband sources are used to illuminate the interferometer. This produces an effective, or synthetic, wavelength of

$$\lambda_{syn} = \frac{\lambda_1 \lambda_2}{|\lambda_1 - \lambda_2|} \tag{4.10}$$

which has the effect of extending the range. Unfortunately the degree of certainty to which the fringe position may be identified in any given setup does not alter, so the resolution of the system scales with the range increase. The technique was first developed by Polhemus (1973) and was then applied to phase shifting interferometry by Cheng and Wyant (1985a). A further advance of this technique was made by Cheng and Wyant (1985b) using a third wavelength to improve range while reducing the loss of resolution.

The major leap forward in optical surface profiling came with the advent of the vertical scanning white light interferometer (VSWLI) which solved the phase ambiguity problem. Here, the lens-interferometer is scanned vertically above the surface and the intensity is tracked synchronously with the distance moved. The intensity forms a pattern similar to that shown in figure 3.3 which is shaped by the absolute complex degree of coherence of the source, $|g_{12}|$. The peak of the envelope function is then derived using a suitable algorithm and corresponds to the point of zero optical path difference (OPD), which is non-ambiguous. By simultaneously tracking the phase of the signal contained within the envelope function it is possible

to discern the point of zero OPD to accuracies of a nanometre or so. Although white light interferometry was being considered quite early by Wyant (1974) among others, the first white light interferometer for surface profiling in its modern form was developed by Dresel et al. (1992) who first applied the envelope detection method to rough surfaces. White light interferometry techniques have effectively revolutionised optical surface profiling by providing high resolution over a reasonable range. Companies producing commercial VSWLI claim repeatable measurements down to 0.1 nm over ranges of 100 μm. The vertical range may be extended using z-axis stitching techniques although with a resulting loss of accuracy and increased acquisition time (Taylor Hobson, 2009a; Veeco, 2009).

4.4.6 Interrogating Interferometers

Because of the cosinusoidal relationship of the phase and intensity of an interferometer, extraction of the phase is a non-trivial matter. The techniques for extracting such information are as varied as the applications in which interferometers are implemented. A discussion of the various techniques within the specific context of fibre interferometers will be given in section 4.7.

4.5 Optical Fibre Sensors

4.5.1 Background

The use of optical fibres holds great advantage in the convenience of moving light from the source to where it is needed. Fibre sensing technology covers a wide range of techniques; the fibre itself may be used as the sensing element, or it may simply be used to transport light to a sensing element. The methods of interrogating the fibre tend to fall into four main categories; intensity, wavelength, polarisation and interferometry.

Intensity based schemes are numerous, for instance small displacements may be measured by allowing the displacement to effect the coupling of a fibre, by acting upon the coupling laterally. Micro-bending methods place a section of fibre in a corrugated deformer; when force is exerted on the deformer it results in intensity loss as light is coupled into the cladding (Mitchell, 1991).

Wavelength based sensing methods are now very established and popular, especially when based around fibre Bragg grating (FBG) methods. Here, an FBG (written into the fibre core itself) produces a narrowband filter due to its high reflectivity over a small wavelength range. The narrowband of peak reflectivity depends on the spacing of the etched fibre grating which in turn varies with strain applied to the fibre. Compared with many alternative methods, wavelength sensing is relatively stable to drifting parameters such as polarisation (Hobbs 2000, pp.271-273).

Polarisation dependent schemes work on the fact that an optical fibre is able to carry two orthogonal, degenerate polarisation states and disturbances to the fibre can results in coupling between these modes which may be harnessed to produce sensors. The results have been somewhat mixed due the intrinsic instability found in optical fibres (Spillman, 1991).

Interferometry using optical fibres may be produced in several ways; most of the structures are analogous to their bulk optic counterparts and are referred to by the same nomenclature e.g. Fabry-Perot, Mach-Zehnder and Sagnac.

Fibre interferometers have extremely high sensitivity to optical path length change, whether that be through strain or refractive index change, and this is what is harnessed to produce sensor elements. In this study we are concerned solely with fibre optic interferometric sensors, however many of the interrogation methods cross over to bulk interferometers.

4.5.2 Fibre Interferometers

The arms of an interferometer themselves may actually comprise optical fibres, forming a fibre interferometric sensor such that the fibre itself forms part of the sensing element. This has produced a large array of sensor types where the fibre actually forms part of the sensing element. Many such sensors rely on path length changes caused by strain induced by physical interactions with the fibre. One fibre arm (the sensing arm) is exposed to the environment to be measured and the other kept in a benign (static with regard to the measurand) environment to act as a reference. The differential path difference imposed by variation in the measurement arm can then be interrogated using suitable techniques. Often such devices are rendered more sensitive to a particular parameter by using a coating to enhance the

strain induced by the particular physical parameter to be observed. An example of this is a magnetostrictive coating applied to the fibre to render it sensitive to a magnetic field (Bucholtz 1991). In a fibre optic hydrophone, the bare fibre may be coated with a material having a high Young's modulus, the increased 'stiffness' being more effective at converting acoustic waves in to strain.

Interferometers maybe fashioned from optical fibres quite easily using a variety of different methods. Their configurations are generally named with regard to the bulk optics interferometers they are equivalent to. Common configurations of fibre interferometers are the Mach-Zehnder, Michelson and Sagnac.

4.5.3 Advantages

Interferometric fibre sensors can be made to be very sensitive to many of the environmental parameters one might hope to measure. They are also very inert which makes them attractive for use in difficult environments. Very small phase differences may be measured and measurement sensitivity often scales with the length of fibre used in the sensing arm.

The flexible nature of optical fibre and its ability to be coiled around small form factors mean sensors may be very compact. Robustness comes from the fact that the fibre is extremely inert and thus resistant to contaminants.

Many fibre interferometric sensors rely on the measurand affecting the fibre itself in some way. This means it is often not necessary for the light to enter free space, meaning alignment is much more convenient due to the lack of bulk optics such as lenses and mirrors. The ability of optical to guide light easily to where it is needed also means that the construction of an optical circuit is often much easier than for the bulk optic equivalent.

Lowered cost is not always a given when using optical fibre based techniques but often individual components created using all-fibre or integrated optics construction and operating within popular wavelength bands (telecommunications) can conspire to produce a relatively cheap overall system.

4.5.4 Issues

The same attributes of fibre interferometric sensors that prove attractive are also often their undoing however; the sensitivity of fibre is not very selective and path length changes can be induced by a whole host of different physical sources.

For instance, a fibre optic interferometric hydrophone is extremely sensitive to temperature variation (which induces path length change though thermal stress) as well as the disturbances caused by acoustic pickup. This low frequency drift is prevalent in all fibre interferometric setups and occurs due to path length alteration. It causes major problems, not just in the inability to perform effective measurements within the drift frequency bandwidth, but also in the variation of the operating point caused by the drift. In the case of the fibre interferometric hydrophone, the majority of the temperature induced variation is found to be in a lower frequency band than that of interest and so it is simply filtered out of the final output.

Operating point drift in fibre interferometers results in the signal fading, which at best alters the sensitivity and signal-to-noise (SNR) parameters of the interferometer and at worst, causes the signal to disappear completely. There are a wide range of techniques used for preventing the signal from an interferometer from fading completely, thus always ensuring that a signal is present. These techniques are covered in detail in section 4.7.

The ease of alignment gained with an optical fibre setup can also present problems due to etalons being created between connection points in the optical circuit. As there is no control over alignment there is no option to alter it slightly in order to mitigate these effects. In single mode fibre setups the light is very well spatially correlated, so there is no washing out of these effects over area and the full etalon fringes are seen at the output.

4.6 The Michelson Fibre Interferometer

4.6.1 Apparatus

In order to realise fibre interferometers several components in addition to the fibre itself are necessary. In order to present a contextual description of these various components it is instructive to consider the construction of a simple Michelson Fibre interferometer and discuss the components involved individually.

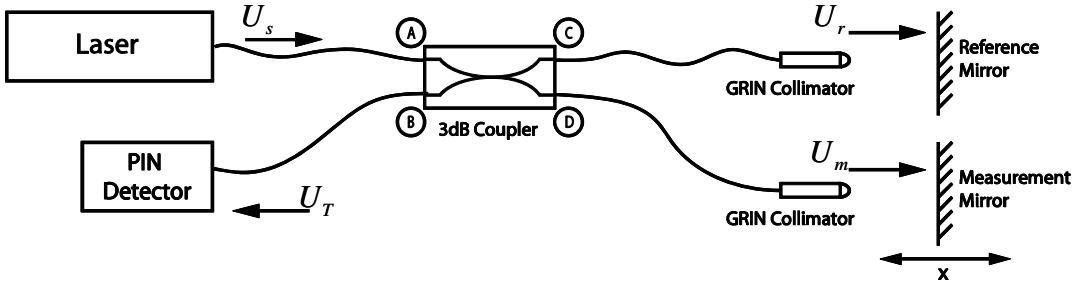

Figure 4.6 A Michelson fibre interferometer

Figure 4.6 shows a Michelson interferometer setup using single mode optical fibre. Several of the individual elements are the same as for the bulk optic equivalent. There is a light source and a suitable detector element of some sort to analyse the fringes produced. There is also a mirror at the end of each arm to retro-reflect the light back into the fibre. In addition to these components there is a directional coupler, which provides a function analogous to the beam splitter in a bulk interferometer, as well as a pair of graded index (GRIN) collimators.

4.6.2 The Directional Coupler

A directional coupler provides means of transferring the wave energy from one waveguide to another. Directional couplers were originally developed using integrated optics techniques and are based on the phenomenon of evanescent wave coupling. This relies on the fact that a guided wave does not exist exclusively in the waveguide, the mode field extends out into the cladding (see section 3.6.4). By placing two waveguides close together energy may be transferred from one waveguide to another. The use of coupled-mode theory can be used to simplify analysis when weak coupling between the waveguides is being studied. Coupled-mode theory relies on the approximation that only the amplitudes of the waves are altered in the coupling process, the transverse spatial distributions and the propagation constants remain constant.

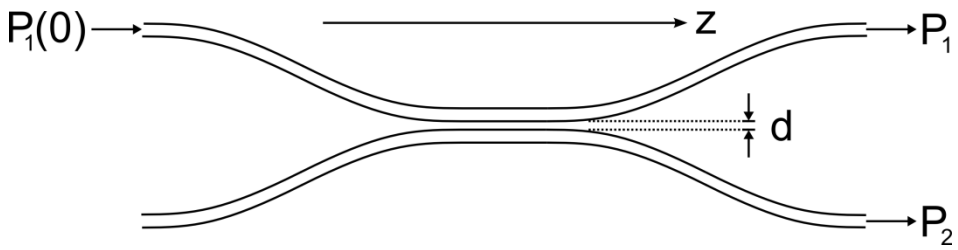

Figure 4.7 A 4 port directional coupler

With reference to figure 4.7 the optical powers in the two waveguides, assuming their refractive indexes are matched and the wave is injected into the upper waveguide is

$$P_1(z) = P_1(0)\cos^2(\zeta z) \tag{4.11}$$

$$P_2(z) = P_1(0)\sin^2(\zeta z) \tag{4.12}$$

where ς is the coupling coefficient between the two waveguides which is dependent on the mode or modes being considered and the physical parameters of the waveguide including the separation distance, d and the refractive index. From (4.11) and (4.12) it is seen that the power in the each waveguide varies along the length z of the coupler.

At a certain length $z = \pi/2\varsigma$ the power is completely transferred from one waveguide to the other. For the common case of the 3dB coupler which is analogous to a 50/50 beamsplitter then $z = \pi/\varsigma$. For any given coupler, by varying the coupling length it is possible to acquire any required coupling ratio. Examination of (4.12) also reveals that the power in the cross-coupled component P_2 is delayed by $\pi/2$ in relation to the straight-through component P_1, for the case of a 3dB coupler.

Adjustability may be obtained by enabling a simple mechanical translation along the longitudinal waveguide direction which effectively changes the coupling length. Also in the case of integrated optics couplers, it is possible to use a heating element to alter the waveguide characteristics to produce a similar effect.

All-fibre techniques have since been developed that allow coupling between two fibres by simultaneously fusing and stretching them. The fused portion then tapers

reducing the diameter of the fibre and producing coupling between the two fibres. These have the benefit of low return and insertion loss and minimal expense.

The system shown in figure 4.6 is analogous to the Michelson interferometer if one considers the 3dB directional coupler acting as a type of beam splitter. After reflection from their respective mirrors U_r and U_m interfere within the 3dB coupler and emerge at ports 1 and 2. Only the light from port 2 is captured by the PIN detector so half of the interfering light wave is lost.

A lossless 3dB coupler can be modelled as a two-port device using a transformation matrix,

$$\begin{pmatrix} C \\ \\ D \end{pmatrix} = \begin{pmatrix} \frac{1}{\sqrt{2}} & \frac{-j}{\sqrt{2}} \\ \frac{-j}{\sqrt{2}} & \frac{1}{\sqrt{2}} \end{pmatrix} \begin{pmatrix} A \\ \\ B \end{pmatrix} \tag{4.13}$$

where A, B, C and D are the port of the directional coupler as labelled on figure 4.7. In this representation the A and B are input ports, the 2 x 2 matrix is the transfer function. The resulting outputs are then found to be C and D.

In the setup identified in figure 4.6 there is only one input to the 3dB coupler so $B = 0$ and $A = U_0(\mathbf{r})$ is the complex amplitude of the input wave from the source. Considering an ideal and lossless component the output vector is,

$$\begin{pmatrix} C \\ \\ D \end{pmatrix} = \frac{1}{\sqrt{2}} \begin{pmatrix} 1 & -j \\ -j & 1 \end{pmatrix} \begin{pmatrix} U_0 \\ \\ 0 \end{pmatrix} = \frac{1}{\sqrt{2}} \begin{pmatrix} U_0 \\ \\ -jU_0 \end{pmatrix} \tag{4.14}$$

The light then exits the fibre and after reflection from their respective mirrors the light re-enters ports C and D of the coupler. There is a phase shift induced into each wave which is produced by the round trip optical path length traversed, $2l$ and an unknown phase shift ψ induced by the reflection from the mirror; this results from the fact that it is a non-dielectric surface (Medicus et al., 2007). The phase change on reflection varies with material type, depth, angle of incidence and wavelength. For the situation of monochromatic source illumination the relationship describing the induced phase shift is

$$\alpha = \frac{2l}{\lambda}(\bmod 2\pi) + \psi \tag{4.15}$$

In addition to this there will be some attenuation of the amplitude of the wave due to absorption and the reflectance of the mirror or surface. This may be represented as a simple scalar, ρ where $0 \le \rho \le 1$.

The overall phase shift and attenuation may be combined as a phasor, $\rho e^{j\alpha}$ which in a suitable matrix form acts upon the original output vector in (4.13),

$$\begin{pmatrix} C' \\ \\ D' \end{pmatrix} = \begin{pmatrix} \rho_r e^{j\alpha_r} & 0 \\ 0 & \rho_m e^{j\alpha_m} \end{pmatrix} \begin{pmatrix} C \\ \\ D \end{pmatrix} = \frac{U_s}{\sqrt{2}} \begin{pmatrix} \rho_r e^{j\alpha_r} \\ \\ \rho_m e^{j\alpha_m} \end{pmatrix} \tag{4.16}$$

where the subscripts r and m refer to the properties considered in the reference and measurement arms respectively. C' and D' represent the transformed lightwaves C and D respectively returning to the coupler.

The transfer function of the coupler of as outlined in (4.13) is identical regardless of the orientation of the directional coupler. It is thus possible to simply reverse the input and output port vectors in equation (4.13) so the output vector is now

$$\begin{pmatrix} A' \\ \\ B' \end{pmatrix} = \frac{1}{\sqrt{2}} \begin{pmatrix} 1 & -j \\ -j & 1 \end{pmatrix} \begin{pmatrix} C' \\ \\ D' \end{pmatrix} = \frac{U_s}{2} \begin{pmatrix} 1 & -j \\ -j & 1 \end{pmatrix} \begin{pmatrix} \rho_r e^{j\alpha_r} \\ \\ \rho_m e^{j\alpha_m} \end{pmatrix} = \frac{U_s}{2} \begin{pmatrix} \rho_r e^{j\alpha_r} - j\rho_m e^{j\alpha_m} \\ \\ -j\rho_r e^{j\alpha_r} - j\rho_m e^{j\alpha_m} \end{pmatrix} \tag{4.17}$$

At this point it is worthwhile defining a phase difference $\alpha = \alpha_r - \alpha_m$ yielding,

$$\begin{pmatrix} A' \\ \\ B' \end{pmatrix} = \frac{U_s}{2} \begin{pmatrix} \rho_r e^{j(\alpha+\alpha_m)} - j\rho_m e^{j\alpha_m} \\ \\ -j\rho_r e^{j(\alpha+\alpha_m)} - j\rho_m e^{j\alpha_m} \end{pmatrix} \tag{4.18}$$

The output intensities can now be examined separately to yield,

$$I_A = A'A'^* = \frac{U_s^{\,2}}{4}\left(\rho_r e^{j(\alpha+\alpha_m)} - j\rho_m e^{j\alpha_m}\right)\left(\rho_r e^{-j(\alpha+\alpha_m)} - j\rho_m e^{-j\alpha_m}\right) \tag{4.19}$$

$$I_B = B'B'^* = \frac{U_s^{\,2}}{4}(-j\cdot j)\left(\rho_r e^{j(\alpha+\alpha_m)} + \rho_m e^{j\alpha_m}\right)\left(\rho_r e^{-j(\alpha+\alpha_m)} + j\rho_m e^{-j\alpha_m}\right) \quad (4.20)$$

After multiplying out and simplifying it is seen that,

$$I_A = \frac{U_s^{\,2}}{4}\left[\rho_r^{\,2} + \rho_m^{\,2} - \rho_m\rho_r\left(e^{j\alpha} + e^{-j\alpha}\right)\right] = \frac{U_s^{\,2}}{4}\left[\rho_r^{\,2} + \rho_m^{\,2} + 2\rho_m\rho_r\cos(-\alpha)\right] \quad (4.21)$$

$$I_B = \frac{U_s^{\,2}}{4}\left[\rho_r^{\,2} + \rho_m^{\,2} + \rho_m\rho_r\left(e^{j\alpha} + e^{-j\alpha}\right)\right] = \frac{U_s^{\,2}}{4}\left[\rho_r^{\,2} + \rho_m^{\,2} + 2\rho_m\rho_r\cos(\alpha)\right] \quad (4.22)$$

The result shows that the outputs from each port of the coupler are identical but 180° out of phase. The fibre optic coupler in a fibre interferometer is shown to be analogous to the beam splitter in a bulk interferometer (Kashyap & Nayar, 1983).

One important observation is that, like a bulk interferometer, when a fringe at the output is at a minimum, the fringe of the input port must be at a maximum. In this case a large amount of power is incident upon the laser source. For this reason it is essential in interferometric applications that the source is isolated in some way from light returning from the instrument or source instabilities are likely to ensue. This situation causes particular concern for fibre interferometry because the inherent alignment of all components means that all the power is coupled back to the source. In order to overcome this problem, an isolator must be placed in front of the source.

4.6.3 GRIN Collimators

The GRIN (GRaded INdex) lenses serve to collimate the light output from the fibre. GRIN lens are produced from a rod of glass having a refractive index profile that is parabolic across its diameter. Rays propagating within such a material are confined to the rod and oscillate with a certain period. They form a sinusoidal ray pattern as the propagate which has a particular periodicity or beat. Altering the length of the rod so the rays exit at different points along the beat length allows the beam to be focused at will.

Setting the length of the GRIN rod to exactly a quarter of a pitch focuses the rays at infinity thus collimating the beam. GRIN lens are generally butt coupled to a single mode fibre using index matched epoxy resin and the pitch used is often 0.23/0.24 to allow some working distance at the imaged side.

Many other viable methods are available for collimating the output of a fibre such as microscope objectives, Thermal Core Expansion (lens less) and spherical lens, the latter being probably the most common.

4.6.4 Mirrors

The mirrors must be adjusted so their planes are exactly normal to the incident beam. This ensures as much of the return light is coupled back into the fibre as possible. Alignment adjustments are made by fine screws on the back of each mirror's mounting. Mounting one mirror on a translation stage having an axis such that the beam distance travelled is adjustable is useful to alter the optical path length.

As well as using external bulk mirrors it is possible to use the fact that a clean cleave of a bare fibre in air will send approximately 4% of the light power back into the fibre producing the effect of a weak mirror. The cleaved fibre end may also be mirrored directly using a solution of silver nitrate and the appropriate amount of warming (Kashyap & Nayar, 1983). Such a method produces an effective and compact mirror but with a corresponding loss of path length adjustability.

The phase change on reflection from a non-dielectric surface such as an aluminium coated mirror differs from the 180° case seen for a dielectric surface. The relationship is complicated and the exact value depends on material, angle of incidence, thickness of material and wavelength. However in general it is of little consequence in monochromatic interferometry as the value will manifest itself as a constant phase term assuming the measurand is a homogenous material. If the material changes however, for instance in the situation of a step height being comprised of two different materials, the different constant phase term can cause an error in the measurement of that step height. There is some scope for correcting this in post processing if the materials are known (Medicus et al., 2007).

4.6.5 Detector

An electro-optical detector has the role of converting the photons incident on it into electrical charge carriers. Many different devices have been created with this in mind and most fall into two broad categories, quantum or thermal. The former of the two includes semiconductor based devices such as photodiodes, CCDs and solar cells.

The prevalent technology for detecting light in telecommunications fibre optic systems is the photodiode as it provides fast performance, low cost, linearity, ruggedness and a reasonable noise performance at 300K. The specifications for photodiodes mean that they are the detector type of choice for many optical applications and as such the technology is well developed and documented.

The photodiode is essentially a doped p-n junction where the p-type layer is transparent thus allowing incident light to reach the junction. The doping around the junction creates a depletion layer and any photon incident on that area will create an electron-hole pair. The transit of these charge carriers to their respective conductors contributes to generated photocurrent.

The operational wavelength defines the material used in the p-n junction, with silicon (Si) being the usual choice for the visible up to about 1.1 μm. Above this wavelength indium-gallium-arsenide (InGaAs) is used which can provide detection over the range of 1 μm to 1.65 μm (Stotlar 2000, pp.593 – 596).

Figures of merit for establishing the effectiveness of a particular detector in an application include quantum efficiency, responsivity, noise-equivalent power (NEP), capacitance and spectral response. These parameters determine not only whether the device is suitable for a particular application, but also influence how the front end electronics are to be designed.

The detectors employed in the instruments studied in this thesis are all PIN photodiodes so called because they are comprised of a standard PN junction with a low-doped intrinsic layer in the middle. This layer decreases the capacitance of the junction which in turn increases the speed substantially. Another important way to reduce the junction capacitance is to reduce the area of a junction. In order to do this without reducing light capturing capacity some focussing optics are required in front of a photodiode. Conveniently in the case of fibre optics the mode field diameter emitted from single mode fibre is only a few microns depending on the operating wavelength. This means a fibre can be butt coupled straight onto a small area photodiode thus realising good performance easily. Photodiodes can be bought ready pigtailed to single mode optical fibre providing a very convenient solution.

The photodiodes used in the instruments in this thesis are Wuhan Telecommunications PDDM981. They were chosen due to their low price and more than adequate performance in terms of bandwidth. The responsivity of the photodiode is shown in figure 4.8.

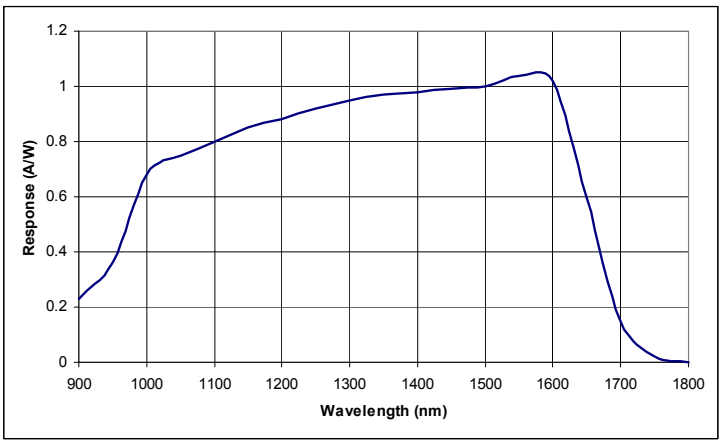

Figure 4.8 Wavelength response of the PDDM981 photodiode (Wuhan Telecommunications)

The PIN photodiode produces a current proportional to the light power incident upon the active junction. In this sense it acts as a current source, and electronics must be used to convert this into a voltage signal. Discussion on the practical application of photodiodes and the design of suitable interrogation electronics is in given in appendix A.

4.6.6 Laser Source

The choice of laser source is of upmost importance; the linewidth, power output and noise parameters must be considered carefully if the interferometer is to function optimally. Furthermore, parameters that may appear to be beneficial, for instance a very narrow linewidth from a good single mode laser which should provide a very sharp fringe visibility, can worsen etalon effects in a fibre setup due to its long coherence length.

Laser sources come in three basic types which are categorised by the kind of gain medium used; gas, solid state and semiconductor. It should be noted that term solid state differs from the definition found in the field of electronics and refers specially to

a gain medium held within a crystal or glass structure. The choice of a laser source is dependent on the operating wavelength and power required for the application.

In the arena of optical fibre telecommunications it is found that semiconductor lasers predominate. Two types of laser source are used in the instruments developed in this thesis, a fixed wavelength laser diode and a tuneable laser.

Clearly the coupling requirements for single mode fibre are very stringent, the coupling of a free space laser beam requires the use of a microscope objective and fibre launch stage, which provides fine 3 axis alignment. All the laser sources used in the research described in this thesis are purpose designed for single mode fibre use however. The laser diodes used are ready pigtailed to single mode fibre, the required collimation optics are already integrated within the package. In addition the tuneable laser sources have adaptors fitted to allow the connection of a standard FC-PC connector thus providing problem free light launching.

Laser Diode

Laser diodes are the cheapest laser type by a long margin. In addition, their monolithic structure makes them very robust in terms of physical handling and alignment. Various types of structures exist including such as quantum well and double heterostructure. They all work by generating photons at a heavily doped p-n junction which when biased on the p side acts as the population inverted gain medium required for lasing to occur.

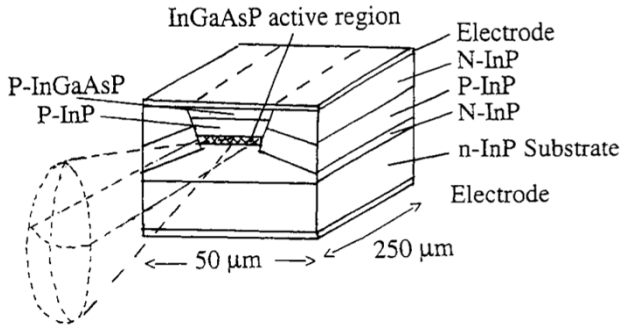

Figure 4.9 A typical heterostructure laser diode for telecommunications (Bass & Stryland 2001)

Stimulated light is confined to within an area of the diode by constructing a wave guide around the active area. Generally this area is defined such that only a single

lateral mode is supported, except in those laser diode designs that maximise power output. The output of the diode is elliptical as the waveguide is generally several tens of microns wide but only 1-2 μm tall which causes difficulties for collimation. Only the central portion of the ellipse tends to be collimated, reducing the efficiency as light in the wings is vignetted.

In addition to creating a waveguide channel in the lasing medium it is necessary to form a cavity for lasing to occur successfully. This is fairly straightforward in diode lasers as the high refractive index of the semiconductor medium means that Fresnel reflection on its own can produce reflectivities of up to 30 %. All that is required is for the material on both sides to be cleaved cleanly and parallel. One facet is usually coated to increase reflectivity and a photodiode placed behind it to monitor the intensity produced directly. (Bass & Stryland, 2001).

As a rule, laser diodes are quite difficult to use due to their sensitivity to junction temperature and injection current (mainly as a result of current heating) and also optical feedback into the cavity. Their output will tune with changes in all those parameters over a short range after which mode hops will occur (Dandridge & Goldberg 1982). This can lead to a sudden jump in output intensity and wavelength, which could have a catastrophic effect on interferometry resulting in unstable and jumping fringes.

The advent of distributed feedback (DFB) laser diodes has resulted in the ability to provide a stable single mode output with few or no mode hops over small variations in operating parameters. This relaxes the stringent requirements for driving the laser diode significantly.

DFB lasers use a Bragg grating etched into the gain medium of the laser diode. This produces a highly selective etalon which ensures only a single longitudinal mode can exist at any one time. The method is analogous to the placing of an etalon in a gas laser to select a single mode. DBR diodes still tune with junction temperature though as heating effects the periodicity of the DBR grating, thus changing the selection wavelength. For this reason they need temperature control with a peltier element or similar in order to provide stable wavelength over long periods.

Telecommunications grade DFB diodes can provide linewidths down to 1 MHz at operating wavelengths of 1310 nm or 1550 nm and can provide several mW of optical power. It is this type of laser diode that is used as the reference interferometer source in the instruments described in this thesis. This is because it provides a stable, narrow linewidth thus yielding the long coherence length required (Yu & Yang 141-167).

Tuneable Laser Sources

Tuneable laser sources provide the ability to alter the wavelength of the source at will. Various types of laser are found to be tuneable including dye lasers and some types of solid state lasers. The devices used in the instruments described in this thesis are external cavity diode lasers. Two commercial standalone devices have been investigated; the Ando AQ4320D and the Hewlett-Packard HP8168F. The reason for the use of two different devices is due to the unfortunate malfunction of the former during the course of study, it being a machine of some age.

Both the lasers used have a similar mode of operation in which an external cavity is created, containing a variable tuning element, which allows the selection of a specific longitudinal mode. While the basic specifications for tuning range, power output and linewidth are roughly comparable for both devices, the details of each implementation affect the way the devices act toward the end user, so it is worth considering them briefly here.

Ando AQ4320D

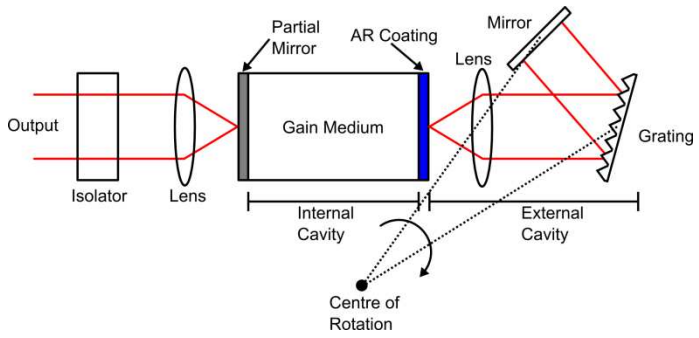

Figure 4.10 Ando AQ4320D Laser Cavity Schematic

Figure 4.10 shows a schematic layout of the AQ4320D. A standard laser diode forms the gain element, but here one surface is AR coated in order to allow the light to pass

through it with minimal reflection. This light then passes into an external cavity containing grating and mirror configuration. The angle at which the light is incident on the grating results in the selection of one particular wavelength diffracted at an angle normal to the mirror. A particular cavity mode may be selected by rotating mirror/grating assembly together (Ando Electric Co., 1999)

Light at the single longitudinal mode then exits the gain medium through the other facet and exits the device through a magneto-optical isolator which provides 60 dB return loss in order to safeguard the cavity from external sources.

HP8168F

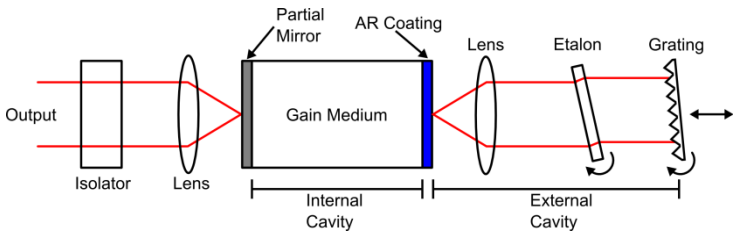

Figure 4.11 Hewlett-Packard HP8168F laser cavity schematic

This laser functions in a very similar manner to the AQ4320D however the setup is somewhat more complex (see figure 4.11). The external cavity is formed using a grating in the Littrow configuration so that light at the selected wavelength is diffracted normal to its incidence. Rotating the grating selects the wavelength of interest, but in this configuration it is not possible to isolate a single mode. For this reason an etalon is present in the cavity which itself may be tilted and essentially provides a more finely tuning filter to select the single longitudinal mode from a set of modes roughly filtered by the grating. It addition to the two rotating axes of movement, the grating itself must be translated back and forth to shorten and lengthen the cavity in order to fulfil the selection criteria (Muller et al. 1993).

It is fairly obvious that the tuning method employed in the HP8168F is far more complicated than in the AQ430D requiring as it does the independent movement of two separate components, one of which must be translated on two axes. This is compared to the AQ430D which tunes with just a single rotation of an assembly with a grating and mirror fixed in place. It is anticipated that this is the basic reason why the AQ430D can provide a continuously swept tuning over 100 nm in 1 second. The

HP8168F on the other hand can only step wavelengths discretely with each wavelength step regardless of size, taking about 200 ms and during each shift the laser power is switched off. It shall be seen later in this thesis this has a big impact in the way interrogation of the interferometer is performed.

4.6.7 Fibre Connections

Fibre components require connecting together in some way. In a laboratory setup it is found that ready built push fit connectors provide a fast and convenient way of connecting components and altering configurations easily. In our case the majority of the connectors are of the standard FC type. These connectors house 125 μm outside diameter fibre in a ceramic ferrule and are cheap and readily available. They make physical contact to reduce transmission losses to 0.4 dB per connection, although this may degrade over time with multiple mating cycles. The FC connectors come in three basic types which are:

PC – Polished. 40 dB return loss.

UPC – Ultra polished (lower return loss). 50 dB return loss.

APC – Angled connector. Here the ferrule is at an 8° angle which ensures that most of the Fresnel reflected light is angled back into the cladding and not guided. 60 dB return loss.

For each of the three basic types seen above there is also a polarisation maintaining (PM) version which provides a closer tolerance keying slot to ensure the fibre cores are aligned with enough rotational accuracy.

Most of the fibre connections were made using FC-PC connectors in the instruments to be considered in this thesis however, the higher return losses were mitigated to some degree by the addition of a small amount of index matching gel between the connector ferrules before mating. This has the effect of lowering Fresnel reflections substantially.

Other methods for joining fibres include mechanical splicing and fusion splicing. Mechanical splicing is the joining of the two fibres in a housing of some form, usually with index matching gel placed between the ends to aid efficient coupling. The fibres are then set in an epoxy resin to hold them permanently in place. It is a

cheap if time consuming method of connecting two fibres, the outlay for the housing being minimal. Fusion coupling on the other hand requires an expensive one-off outlay on a fusion splicer, but once obtained no other raw materials are required. In a fusion splice, the two fibre ends are brought close together and carefully aligned before being fused together in a high temperature arc. Fusion splicing machines generally automate much of this process, the result being quick and convenient splicing while also providing the best performance in terms of coupling and return loss (Chomycz 2000, pp. 115-118).

Fusion coupling was used where possible in the apparatus described in this work in order to minimise return loss.

4.7 Phase Retrieval for Fibre Interferometers

4.7.1 Nonlinear Phase-Intensity Relationship

A major difficulty for any interferometer system is the accurate retrieval of the phase information. The output of an interferometer is related sinusoidally to the optical path length difference, Δl between its arms so that the output intensity is

$$I = I_r I_m + V\sqrt{I_r I_m}\cos\left(\frac{2\pi\Delta l}{\lambda}\right) \tag{4.23}$$

Any detection scheme must analyse the intensity of the interferometer in order to deduce the change in phase and hence the parameter being studied. In addition, those instruments that operate over long ranges longer than the unambiguous range $2\pi/\lambda$ must also provide for some method for keeping track of the integer multiples. One example of this is commonly seen in zero-crossing detection which enables fringe counting in absolute distance measurement applications.

4.7.2 Operating Point Drift

Whatever the parameter being analysed by an interferometric fibre optic sensor, and no matter what methods are used to try and enhance the sensitivity of such a sensor, it is found that optical fibre is very sensitive to temperature drift and mechanical (acoustic) perturbation. Temperature induced noise induced in fibre sections longer than fibre thermal coherence length are responsible for low frequency path length

drift in the optical fibre. Generally the rms value of the thermal disturbance scales with the square root of the fibre length (Musha et al 1982).

The interference equation may be re-written to include an error term, $\varepsilon(t)$ that is due to the unwanted phase variation induced in an interferometer.

$$I = I_r I_m + V\sqrt{I_r I_m}\cos\left(\frac{2\pi l}{\lambda} + \varepsilon(t)\right) \tag{4.24}$$

This effect is one of the main obstacles to overcome when designing fibre optic interferometers and any phase retrieval method must overcome this in some way. For small signal operation within one fringe, the interferometer is seen to be most sensitive around an operating point at quadrature (where the cosine term is $\pi/2$) due the steepest phase-intensity gradient. The other reason for operating at the quadrature point is that the phase to intensity relationship is approximately linear over this range which can prove useful in simplifying interrogation. The error term $\varepsilon(t)$ can result in an interferometer drifting away from this ideal operating point resulting in what is termed signal fade. As the interferometer operating point is pushed toward the peaks of the cosine function sensitivity tends to zero. Any effective interrogation method must successfully deal with this.

Various methods for the retrieval of the phase information have been created and many variations on each of the methods are to be found in the literature. The methods may be categorised into 5 main types however; passive homodyne, active phase tracking homodyne, heterodyne, synthetic heterodyne and phase shifting. These methods are outlined briefly below. In the following section, $S(t)$ refers to an AC small signal riding on a DC phase operating point, φ.

4.7.3 Passive Homodyne

Passive homodyne aims to overcome the signal fading issue by acquiring two outputs I_1 and I_2 from an interferometer that are 90° apart in phase.

$$I_1 \propto \cos[S(t) + \varphi] \tag{4.25}$$

$$I_2 \propto \sin[S(t) + \varphi] \tag{4.26}$$

As the two signals never fade simultaneously it may always be recovered. One simple method is by cross-multiplication with their respective differentials;

$$I_1 \dot{I}_2 - I_2 \dot{I}_1 = \cos^2\left[S(t)+\varphi\right]\cdot\frac{d}{dt}\left[S(t)+\varphi\right] + \sin^2\left[S(t)+\varphi\right]\cdot\frac{d}{dt}\left[S(t)+\varphi\right]$$
$$= \frac{d}{dt}\left[S(t)+\varphi\right] \tag{4.27}$$

where the dots denote differentiation with respect to time. This process may be easily carried out by analogue or using digital methods. The required phase shifted signal can be obtained from a 3 x 3 directional coupler (Koo et al. 1982) or by using a switched twin wavelength method (Sheem et al. 1982). Ho et al. (2000) also used a four-quadrant Ronchi grating and PIN detector to create the required two differential phase shifted outputs and also reduced common-mode laser noise.

4.7.4 Heterodyne

The heterodyne method was first used in the development of fibre optic gyroscopes; this was one of the first commercially successful examples of the emerging technology. They rely on two light beams, one in each arm of the interferometer, whose frequencies are offset from each other in frequency by a few MHz. Upon interfering, the two light waves (amplitudes E_{sig} and E_{ref} produce the following output.

$$I \propto {E_{sig}}^2 \cos^2\left[\omega_{sig} t + \varphi\right] + {E_{ref}}^2 \cos^2(\omega_{sig} + \Delta\omega)t$$
$$+E_{sig}E_{ref}\cos\left[(2\omega_{sig} + \Delta\omega)t + \varphi\right] + E_{sig}E_{ref}\cos\left[\Delta\omega t + \varphi\right] \tag{4.28}$$

Beat frequencies are present in the original signal, one of which is at the offset frequency (the last term shown). This beat frequency can be resolved directly by a photo-detector and the phase tracked with a phase locked loop or similar. The frequency offset light beams can be produced by a Bragg cell or dual frequency Zeeman laser. This technique has been used as a demodulation scheme for Sagnac based fibre optic gyroscopes (Culshaw and Giles 1982).

4.7.5 Synthetic Heterodyne

Synthetic heterodyne detection works by applying a sinusoidal carrier, ω_c to the interferometer by modulating the source light phase with a single frequency sine wave. This yields a signal of the form,

$$I \propto \cos\left[A \sin \omega_c t + S(t)\right] \tag{4.29}$$

Using Bessel functions, this may be expanded again to yield;

$$I \propto J_0(A) - J_1(A)\sin(\omega_c t)\sin S(t) + J_2(A)\cos(2\omega_c t)\cos S(t) \tag{4.30}$$

where the J terms are the Bessel coefficients. Suitable mixing with local oscillators and lowpass filtering results in two signals;

$$I_1 \propto -J_1(A)\sin S(t) \tag{4.31}$$

$$I_2 \propto J_2(A)\cos S(t) \tag{4.32}$$

These may then be processed using the passive homodyne technique shown in equation (4.27) to yield a non fading phase term. A precursor to this technique was the pseudo-heterodyne which use a ramped waveform. This has the disadvantage of inducing high harmonics and being a difficult waveform with which to modulate a PZT (Jackson et al. 1982).

4.7.6 Active Phase Tracking Homodyne

Active Phase Tracking Homodyne (APTH) uses an active stabilisation method in order to oppose any change in the optical path lengths. A feedback control system is used to control the phase of the interferometer by modulating either the optical path length or the operating wavelength. Whatever the method employed the concept is to create a phase change to oppose that caused by the drift thus stabilising an interferometer at a single operating point, usually at quadrature (Jackson et al. 1982).

Possibilities for altering the optical path length include the movement of a PZT mounted mirror or fibre wrapped PZT cylinder in one of the arms (Jackson et al. 1980). If the interferometer is unbalanced, so that $l \neq 0$ in (4.23), then the phase may be altered by modulating the source wavelength (Dandridge & Tveten, 1982). Methods investigated have included modulating the length of a laser cavity by mounting the rear reflector on a PZT and also tuning laser diodes over a small

frequency range by modulating either temperature or injection current (Kashyap & Nayar, 1983). One issue for the use of APTH is the fact that it stabilises the interferometer for all frequencies up to a limit defined by the dynamics of the control method employed. The effective use of such a system usually revolves around the low pass filtering of the feed back signal so that the low frequency drift from temperature is stabilised while allowing the higher frequency band of interest to pass un-attenuated (Fritsch & Adamovsky, 1982)

4.7.7 Phase Retrieval Issues Specific to Height Measurement

All the above methods deal with dynamic AC small signals where the parameter being measured modulates the fringe only slightly. Such methods rely on filtering to separate the drift signal from the wanted signal. In surface measurement however, the phase value relating to a spot height is absolute and static i.e. DC. The effect of the low frequency drift term cannot be eliminated and superimposes itself additively on the measurement data.

To resolve a surface height measurement completely, the phase must be resolved absolutely and across the full range of the sinusoid. These issues throw up a slightly different set of challenges which must be overcome in the development of a fibre interferometer used for surface measurement.

4.7.8 Phase Shifting Interferometry

One well established technique that has long been used in bulk optic interferometry for wavefront analysis is that of phase shifting. Phase shifting interferometry (PSI) is a solution to retrieving the absolute phase value from an interferogram. This method can determine the exact phase value of the interferogram detected by the photo-detector. The essence of the principle is that any phase from any interferogram contains three unknowns. From (4.7),

$$I = I_0\left[1 + V\cos\varphi\right] \tag{4.33}$$

the three unknowns are the DC intensity, the visibility and the phase.

By shifting the interferogram by a known constant phase term α and doing this n number of times it is possible to create n simultaneous equations

$$
\begin{aligned}
I_1 &= I_0\left[1+V\cos\left(\varphi+\alpha_1\right)\right] \\
I_2 &= I_0\left[1+V\cos\left(\varphi+\alpha_2\right)\right] \\
&\vdots \\
I_n &= I_0\left[1+V\cos\left(\varphi+\alpha_n\right)\right]
\end{aligned}
\tag{4.34}
$$

which may then be solved in some manner to derive the all unknown terms. Clearly, three phase shifts is the minimum required to provide a solution.

The phase is manually shifted to various points and the output interferogram recorded at each point. This may be done by a variety of methods including rotating half-wave plates, tilted glass windows, moving a diffraction grating and most commonly a moveable reference mirror mounted on a PZT. In addition to methods using physical movement, and unbalanced interferometer may have its phase shifted by changing wavelength. This method was investigated by Ishii et al. (1987) using a tuned laser diode. The shifting may also be performed continuously over a range as opposed to in steps, a method which is known as the integrating-bucket method. It holds some advantages in that the mechanical dynamics, especially in regard to settling times, are of less importance however a reduction of visibility is also experienced.

There exist a wide variety of algorithms for the determination of the original phase from a set of phase shifted interferograms. Algorithms for this technique have been well researched and a multitude have been developed with the first reported being by Carré (1966). Advantages vary between algorithms with some being designed to reduce random errors, other being more robust to systematic errors. In general it is found that the more phase shifts taken the more accurate the result, up until the point where parameter variation becomes significant because of the excess time required, usually when $n > 7$.

A three step method was reported by Wyant et al. (1984), and several four-step methods have also been developed, of which the Carré algorithm has the unique attribute in all phase shifting algorithms in that it does not need the value of the phase shifts to be known, requiring only that they are equal.

One important method is the simple 5-step method reported by Schwider et al. (1983) where the final step is equal to the same value as the first step. This algorithm is very robust against deviations from the ideal 90° shift as may be encountered by an

uncalibrated PZT. It took Hariharan et al. (1987) to point this particular benefit out thus the algorithm is known as the Schwider-Hariharan.

Work has continued in the development of phase shifting algorithms and an interesting example is a fast three step method based around a look up table, resulting in extremely fast microprocessor implementation (Huang & Zhang, 2006). A pseudo two step method has also been developed by using fast sinusoidal modulation mush faster than the integration time, and over a large phase range (NG 1996).

Phase shifting has problems associated with it however; the speed of movement of a PZT mounted mirror to create the phase shift and the associated settling time for the mechanical system reduces if step wise shifts are taken. This increases the length of time taken to make a measurement which directly influences the accuracy of that measurement. In addition, PZT effects such as non-linearity and hysteresis will always introduce some error into the actual value of the phase shift which will also affect the accuracy of the results. These may be mitigated somewhat by the use of a good calibration routine (Cheng & Wyant, 1985c).

4.7.9 Phase Retrieval Methods for a Fibre Interferometer applied to Surface Measurement.

It should be clear from the preceding sections that the requirements for a monochromatic interferometric sensor in a surface metrology context are twofold. First, it is necessary to derive the phase of the interferometer over the full unambiguous 2π range. This requires that a phase shifting methodology be applied to the interferometer. Second, due to the inherent path length instabilities in optical fibre arms it is necessary to provide some way of stabilising the arms and avoiding signal fading. Here the use of PSI means that that the path lengths must remain stable at DC over the period of measurement so it is clear that the only methodology that is suitable is APTH which actively servos out any disturbance. All the other methods described in section 4.7 are essentially AC techniques.

4.8 Conclusion

This chapter presented the basic concept of interferometry and expanded upon the specific operation of several interferometer types that are commonly used in surface

metrology. The use of an optical fibre based interferometer was examined and some of the associated challenges divulged. A description of the various methodologies for obtaining phase information from fibre interferometers was given. Appraisal of these methods suggested that phase shifting interferometry, an already well established technique in surface metrology, was well suited for phase extraction where absolute phase was required.

The material in this chapter forms the basis for the inital development of a fibre interferometer for surface metrology applications in chapter 5. The material on the fibre optic Michelson interferometer will be directly applied. The optical components described in this chapter will form the basis of the interferometer investigated. The examination of phase retrieval techniques leads to the application of phase shifting specifically to this instrument.

In the next chapter and initial experimental investigation into a real fibre optic interferometer is described. The instrument is applied to a surface measurement application and its performance and suitability is evaluated.

5 Initial Investigations into a Multiplexed Fibre Interferometer

5.1 Introduction

This chapter introduces a fibre interferometer apparatus for surface profiling. Some previous work in this area is reported upon and its limitations discussed. A new method to overcome these limitations is then proposed and investigated. A theoretical appraisal of the concepts behind the multiplexed fibre interferometer is first given. Then the method and its implementation are described in detail and experiments to test performance are reported and appraised.

Before designing an instrument for high precision surface metrology applications it is necessary to first consider the performance targets that are required. Table 5.1 summarises these targets which were first outlined in section 2.4.

Performance Target	Value
Measurement Time	< 60 s
Vertical Uncertainty	<0.5 nm rms
Vertical Range	> 0.5 µm
Lateral Resolution	Diffraction Limited
Lateral Resolution	Diffraction Limited

Table 5.1 Performance specification for a high precision surface metrology instrument

5.2 Previous Work

5.2.1 Description

The work in this thesis is a continuation and progression of the work first reported by Lin et al. (2004) which had the aim of producing a surface profiling instrument using a fibre Michelson interferometer. In order to make such a system feasible it is necessary to stabilise the fibre interferometer in order to negate the effects of acoustic and thermal disturbance. This was performed using a wavelength division

multiplexing (WDM) method in which one wavelength acted as a reference and provided feedback for an active phase tracking homodyne (APTH) technique. Figure 5.1 shows the basic setup.

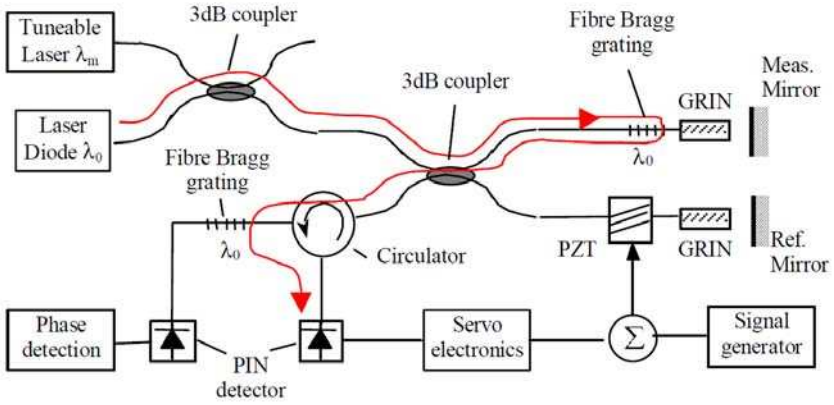

Figure 5.1 Multiplexed fibre interferometer from Lin et. al. 2004

A fibre wrapped piezo cylinder was used to alter the fibre path length. Such piezo cylinders have a frequency response up around 50 kHz and optical path length change to applied voltage ratio may be altered by the number of fibre turns wound onto the cylinder. The principle is to alter the optical path length, using the reference wavelength sourced by the laser diode as part of a servo loop. The measurement wavelength, supplied by the tuneable laser, then exists in a stable environment and is able to measure phase change without being affected by any environmental perturbation.

Along with the initial investigations into the instrument shown in figure 5.1, Lin et al. (2004) also proposed an optical stylus technique involving a diffraction grating and tuneable laser in order to sweep a beam across a profile and thus obtain phase information pertaining to surface topography. Although it was proposed, the method was not actually implemented in this system.

5.2.2 Limitations

The system proposed by Lin et al. has one essential limitation and that is the fibre Bragg grating (FBG) placed before the GRIN lens. This has the role of reflecting the reference wavelength while allowing the measurement wavelength to pass out onto the measurand. The result is that the optical paths of the two interferometers,

measurement and reference, are not identical. In this situation, the APTH method can only stabilise the reference path, and as such disturbance in the measurement path between the FBG and the measurand is unattenuated. This issue is compounded because of the short length of fibre between the FBG and the GRIN lens, which is uncompensated and much more sensitive to any environmental perturbation than an air path of the same length.

The resulting system proposed cannot provide enough stability for accurate measurement of surface topography. In order to develop such an instrument a better method for stabilising the interferometer must be found, and in addition, the optical stylus concept needs to be further investigated.

5.2.3 An Improved Method

In order to improve on the method described in section 5.2.1 it is necessary to reduce the non-commonality of the reference and measurement optical paths. Figure 5.2 shows an experimental setup devised to improve performance by removing the FBG from the measurement arm and allowing the reference beam to be incident upon the surface. The device shall be henceforth known as a multiplexed fibre interferometer (MFI) in the course of this thesis.

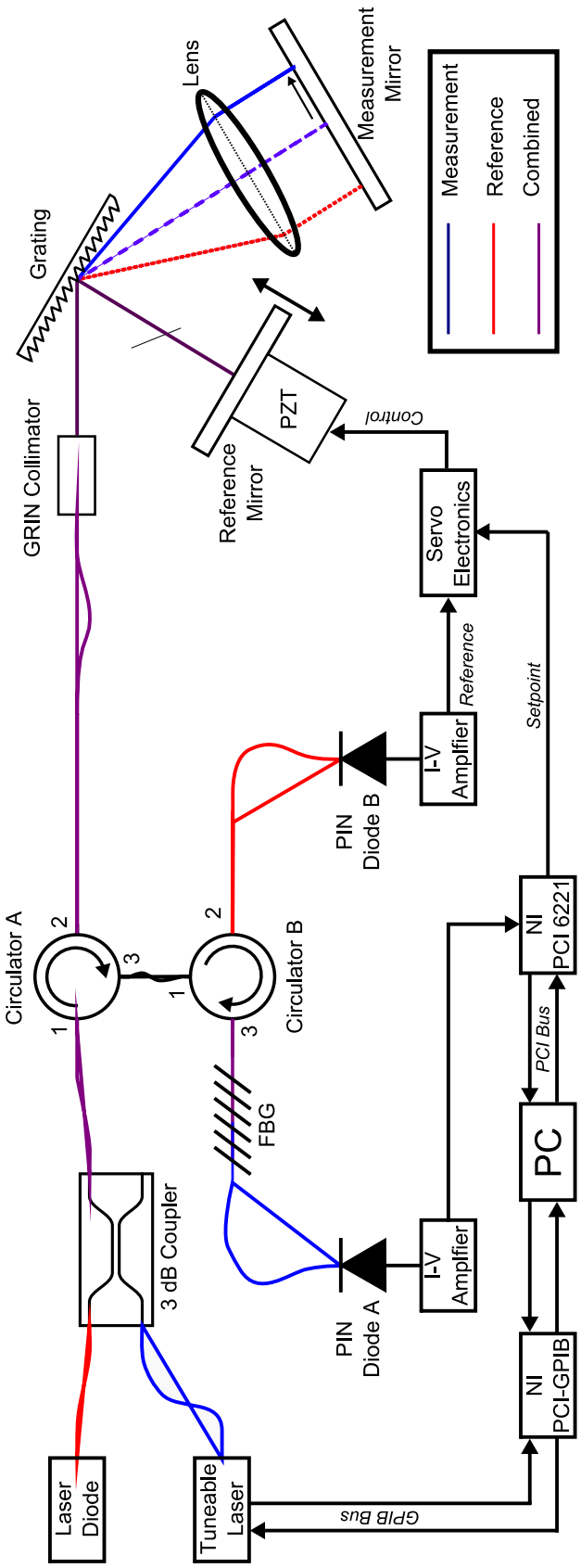

Figure 5.2 Multiplexed Fibre Interferometer Schematic

With this technique the only section at which the reference and measurement interferometer paths are separate is at the diffraction grating. As such the different optical paths cover only a short distance in air or the glass of the objective lens; both these mediums are much more stable than optical fibre.

It can be seen in figure 5.2 that the instrument is not in actual fact a true all-fibre interferometer given that the interference occurs upon the diffraction grating between the retro-reflected first and zero order diffracted beams. In may be more correctly termed a fibre sourced interferometer. The system is also inherently more stable as it is essentially a bulk interferometer, but it maintains the advantages of a fibre link allowing it to be remotely placed.

The over-arching methodology for the instrument shown in figure 5.2 is that twin interferometers, running at different wavelengths, are near-common path throughout the whole of the optical circuit. The next section considers the experimental setup in some detail.

5.3 Apparatus

5.3.1 Overview

There are many elements to the experimental setup shown in figure 5.2, both of an optical and electronic nature. This section gives an overall view of the path of optical and electrical signals through the instrument. Detailed studies of the component parts will be presented in subsequent sections. The optical path will first be considered and the roles of the various components explained. Following that will be an overview of the electronic part of the instrument.

For the initial investigations and proof of concept work, a mirror was used to represent a surface. In optical terms this may be considered the 'ideal' surface, having maximum reflectivity and minimal surface texture as the surface is polished to within $\lambda/20$ at 632.8 nm.

5.3.2 Optical

Figure 5.2 highlights the various wavelengths present in the optical circuit by colour. The reference interferometer wavelength ($\lambda_r = 1550$ nm) is supplied by a laser diode

(Wuhan Telecommunications PDDM981) and enters port 1 of a 3 dB coupler. Light from a tuneable laser source (Ando AQ4320D) provides the measurement interferometer source ($\lambda_m = 1555 - 1575$ nm) and enters port 2 of the coupler. In this way, the light exiting ports 3 and 4 of coupler A is wavelength division multiplexed (WDM). The light exiting port 4 is dumped by placing the cleaved fibre end into index matching gel to disperse the light harmlessly and minimise return loss. This method of multiplexing results in approximately half of the source light power being lost.

The multiplexed light is then incident on port 1 of circulator A and exits port 2, where it exits the fibre. A GRIN lens then serves to collimate the light exiting the fibre into free space where it is then incident on a blazed diffraction grating (Yvon Jobin 5109720). This grating then diffracts the incident beam into a zero order (reflected) beam and two first order beams. The zero-order beam is comprised of both the reference and measurement interferometer wavelengths. First order diffraction produces two angularly separated beams, consisting of the reference and measurement wavelengths respectively.

The zero order beam is normally incident on the reference mirror and is thus retro-reflected back to the same point on the grating from which it emerged. The angularly dispersed first order beams are collimated using an achromatic doublet (Melles Griot 06 LAI007) upon the measurement mirror. The beams are reflected back from the measurement mirror and then re-trace their path back to the grating where they interfere with the returning zero order beam and are incident upon the GRIN lens afterwhich they re-enter the fibre.

Interference takes place where the retro-reflected zero and first order beams recombine at the grating. The resulting interfered beam then re-enters the GRIN lens where it is focused back into the fibre.

The incident beam, containing both interfered multiplexed wavelengths, re-enters circulator A at port 2 and exits at port 3. Here it enters circulator B at port 1, exiting at port 2 where it is incident on the fibre Bragg grating (FGB). The FBG acts to separate the reference and measurement wavelengths.

The reference wavelength ($\lambda_r = 1550$ nm) coincides with the peak reflectivity wavelength of the FBG and as such is reflected back in to circulator B at port 2 where it exits at port 3 and is incident on PIN diode B. The measurement interferometer wavelengths are passed by the FBG, with some attenuation, where they are then incident on PIN diode A.

It is seen that circulator B and the FBG form a wavelength de-multiplexer which separates the measurement and reference interferometer outputs onto PIN diodes A and B respectively.

5.3.3 Electronics

The instrument contains numerous electronic modules which may be addressed in any particular order. Signal flow is marked by the arrows in figure 5.2 from which the labels in the following list are also taken.

I-V Amplifier

These are current to voltage converters, commonly known as transimpedance amplifiers. They convert the photocurrents generated by their respective PIN photodiodes into a voltage. The voltage output of the transimpedance amplifier is proportional to the intensity of light exiting the fibre.

Servo Electronics

This module forms the basis for the active phase tracking homodyne (APTH) method implemented to stabilise the instrument (see section 4.7.6). It is essentially a proportional-integral (PI) controller which takes the voltage output from the reference interferometer and compares it to a setpoint (or demand) voltage. It then applies a voltage to the piezoelectric translator (PZT) stage in order to move the reference mirror until the error is zero.

PC

The PC is used as the host for National Instruments Labview software.

NI PCI-GPIB

This is a National Instruments NI PCI-GPIB provides a GPIB (IEEE 488.2) interface and controller on the host PC. This is used primarily for communication with the AQ

4320D and HP 8168F tunable lasers, as well as the Ando AQ6317 optical spectrum analyser.

NI PCI-6221

This is another National Instruments multifunction data acquisition (DAQ) card. It provides a means of acquiring analogue voltage signals at up to 250 kS/s, shared over 16 input channels with 16 bit resolution. In addition it can supply two analogue voltage waveforms with an update rate of up to 833 kS/s at 16 bit resolution. It also feature digital inputs/outputs. The NI PCI-6221 is used to provide the setpoint voltage to the servo electronics and acquire the analogue voltage data from the measurement interferometer.

PZT

The PZT serves to translate the reference mirror along the optical axis in order to create a path length change in the both the reference and measurement interferometers. It is actuated by a voltage applied to it from the servo electronics module. The PZT model used is of the low voltage stack type having multiple, parallel wired piezo elements whose individual translations are additive. This creates a relatively large translation for small applied voltages at the expense of some other attributes such as capacitance (which is increased). The model used is the PI 810.10 which has a translation of 15 μm over 100 V with a resolution of 0.15 nm.

5.4 Analysis of Instrument Performance

The operation of the multiplexed fibre interferometer may be understood by considering it in four distinct sections. There is the surface to phase relationship, the optical probe operation, the active stabilisation and the phase shifting method. This next section will go through to analyse each element individually.

5.4.1 Surface Height to Phase Relationship

The aim of the instrument is to derive height data from the measurement surface using an optical stylus. The response of the interferometer at a point x along a profile on the surface is

$$I(x) = I_1(x) + I_2(x) + V\cos\varphi(x) \tag{5.1}$$

where I_1 and I_2 are the intensities of the light returing from the reference and measureand mirrors respectively. Taking the phase in the reference arm to be constant it is found that the phase in the measurement arm is dependent only on the surface height, h such that,

$$\varphi(x) = \varphi(0) + \frac{4\pi\left[h(x) - h(0)\right]}{\lambda} \tag{5.2}$$

where $\varphi(0)$ is the initial phase difference at the starting point on the profile and $h(x) - h(0)$ is the surface height difference at a point x also relative to that starting point. The visibility term from (4.6) is

$$V = \frac{2\sqrt{I_1 I_2}}{I_1 + I_2}\left|g_{12}\right| \tag{5.3}$$

which assuming the coupler has a perfect 50/50 splitting ratio, may be expanded to take into account the various losses encountered within the optical circuit of which the reflectivity of the measurand is of particular importance as this may vary substantially between materials. The overall attenuation of the returning light intensity is the product of twice the forward absorption coefficients, σ in each arm , the reflectivity, r of the measurand/reference mirror and the grating efficiency, g_{eff} of the diffracted order.

$$I_1 = I_0 \cdot 2\sigma_1 r_1 \cdot g_{eff} \tag{5.4}$$

$$I_2 = I_0 \cdot 2\sigma_2 r_2 \cdot g_{eff} \tag{5.5}$$

All the coefficients in (5.4) and (5.5) will vary depending on the current position of the optical stylus on the profile.

5.4.2 Optical Stylus by Wavelength Tuning

The optical stylus method relies on the tuning of the measurement interferometer wavelength in order to sweep the light beam across the surface to take a profile of the height variation. The method is very similar to that found in spectrometers whereby a

grating is used to angularly disperse an incoming light beam which is then collimated onto a sensor. In the case of the optical probe in this instrument a tuneable laser is used to change the wavelength over time meaning that the full laser power is available at each profile position measured. Figure 5.3 shows a schematic of the optical probe.

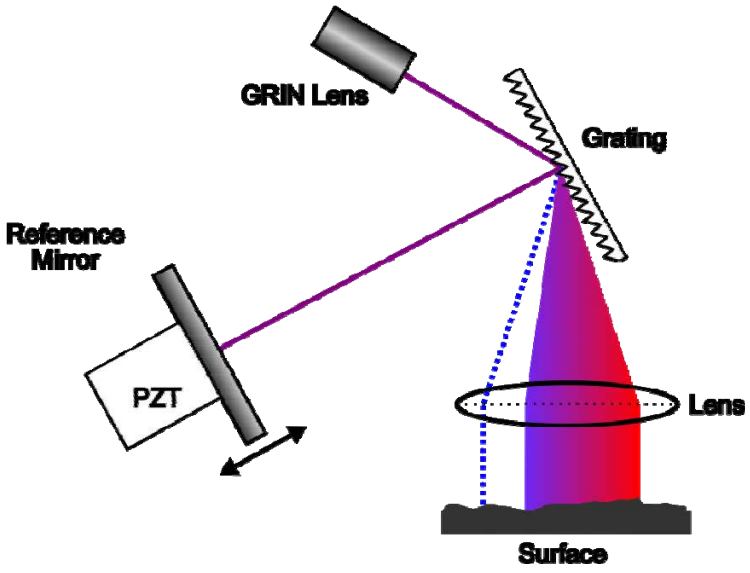

Figure 5.3 Optical probe schematic

The grating in the optical probe creates an angular dispersion which has a wavelength dependence. This is a direct consequence of the grating equation

$$\beta = \sin^{-1}\left(\frac{m\lambda}{d} - \sin\alpha\right) \tag{5.6}$$

where β is the diffracted angle, d the grating spacing, m the grating order and α the angle of incidence. All angles are measured in relation to the grating normal as shown in figure 5.4, the sign of the angle being dependent on which side of the grating normal the angle is.

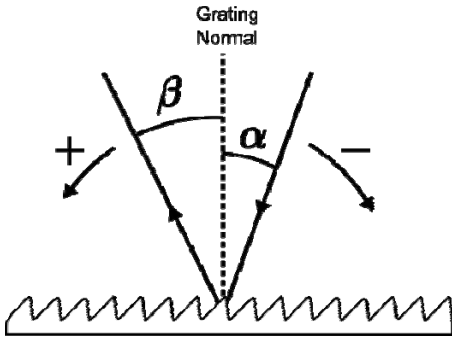

Figure 5.4 Angle sign definition for gratings

The collimating lens in the optical probe has the effect of collimating the angularly dispersed light. The relationship between the angular dispersion and the length of the scanned profile is given by the linear dispersion, which is commonly found in spectrometer design equations. The magnitude of the linear dispersion of the beam along the profile is given by

$$\frac{\Delta x}{\Delta \lambda} = f \cdot \frac{m}{d \cos \beta} \tag{5.7}$$

where f is the effective focal length of the lens used. The cosine term in the denominator of (5.7) requires that the diffracted angle be kept small in order to maintain the linearity of the scan.

Equations (5.6) and (5.7) show that it is possible to vary the scan width using two methods; by varying the angle of incidence α, or by changing the effective focal length, f of the collimating lens. Clearly f is fixed for a given optical probe as the lens must be physically changed and varying α may only be done over a short range before the onset of non-linearity in scan.

It is worth pointing out that any non-linearity in the scan with wavelength is systematic and there is thus scope for calibrating it out by either altering the wavelength step during the scanning, or using a suitable method for interpolating the scanned data.

The lens used to collimate the light was an achromatic doublet (Melles Griot 06 LAI007) having an effective focal length of 60.8m at an operating wavelength of 1550 nm. An achromatic doublet is used because it forms the smallest possible beam spot size for a simple single element lens. The grating used (Yvon Jobin 5109720) has groove density, $1/d$ of 900 lines/mm which at 1550 nm limited the grating to first order operation thus $m = 1$. The use of a blazed diffraction grating helps direct more optical power in the first order diffraction beam which helps to counter the attenuation caused by the measurand that will likely have a lower reflectivity than the reference mirror.

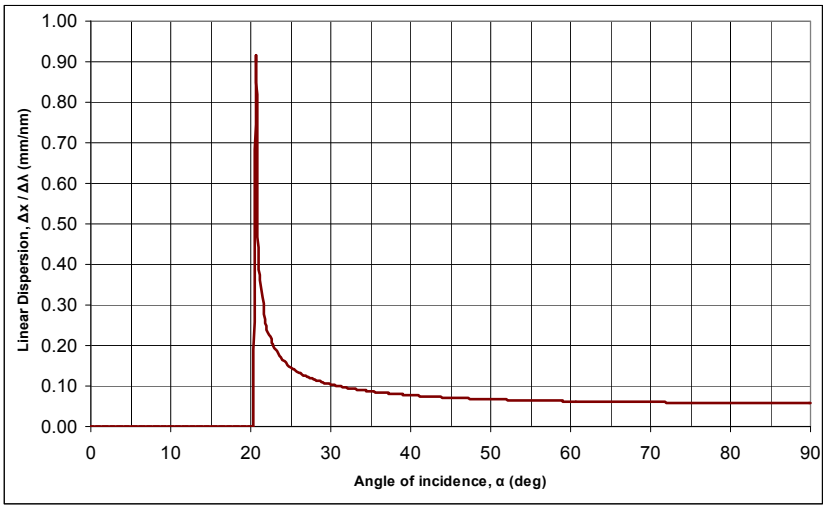

Figure 5.5 Linear dispersion vs. beam angle of incidence, α

Figure 5.5 shows how the linear dispersion changes with the angle of incidence of the grating beam. A numerical analysis of a scan point by point was carried out for a wavelength sweep of 20 nm at various angles of incidence. The result in figure 5.6 shows clearly how the scan range and linearity are related. The scan range may be increased to a degree at the expense of the linearity of the wavelength sweep.

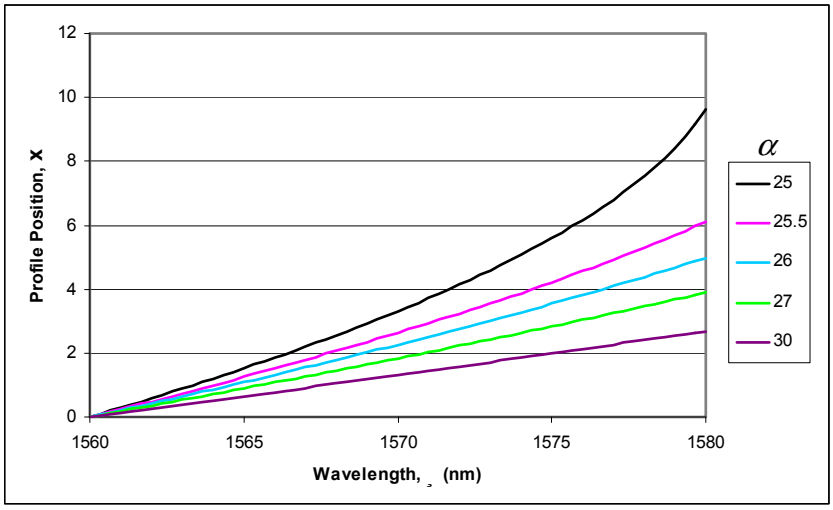

Figure 5.6 Scan path linearity for various angles of incidence

In the initial experiments the incidence angle, α was kept such that the scan range was approximately 3 mm, thus maintaining a good degree of linearity.

The zero order beam which is used to form the reference arm is the special case of the grating equation (5.6) in which $m = 0$. Here we see that the wavelength dependence disappears and only the specular component is left.

$$\beta = -\alpha \tag{5.8}$$

This means that as the wavelength is swept and the first order beam moves across the optical profile, the reference beam will always remain stationary (Palmer 2005, pp. 20-44).

5.4.3 Active Disturbance Rejection

The problems of phase instability in fibre interferometers were outlined at length in section 4.7.2. Here we see that the phase variation creates an error term which maps itself upon the surface height information. This relationship can be described by the addition of a random time varying phase term, $\varepsilon(t)$ as shown in equation (4.24). Considering for a moment the apparatus set up with just the reference wavelength source enabled, the output of the interferometer is

$$I_{ref}(x) = I_0\left\{1 + V\cos\left[\varphi + \varepsilon(t)\right]\right\} \tag{5.9}$$

where an error term, $\varepsilon(t)$ describes the unwanted phase variation due to thermal and acoustic perturbation. The active phase tracking homodyne method (APTH) as described in section 4.7.6 can be used to stabilise the interferometer using the PZT mounted mirror to change the reference arm path length. The PZT is able to translate the mirror along the optical axis of the reference mean with the application of a voltage.

A servo control loop may be considered in which the reference mirror is moved to oppose the time varying error term in the phase. This may be implemented very simply, if not optimally, with a PI controller tuned manually. An analysis of the control loop may be done by first considering the individual elements as shown in figure 5.7.

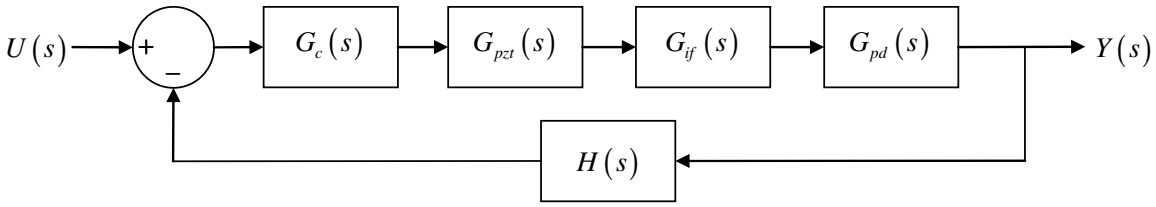

Figure 5.7 Block diagram representation of the closed loop MFI

Control systems analysis is often carried out in terms of Laplace functions, where $s = j\omega$ and is the complex frequency. This has the benefit of converting differential equations in to linear algebra and thus greatly simplifying the analysis.

Figure 5.7 shows the open loop transfer function (OLTF) in the s-domain (complex frequency domain) in the general case of some controller having the transfer function $G_c(s)$ is,

$$G(s) = G_c(s) G_{pzt}(s) G_{if}(s) G_{pd}(s) \tag{5.10}$$

$G_{pzt}(s)$, $G_{if}(s)$, $G_{pd}(s)$ are the transfer functions of the PZT/driver combination, interferometer and photodiode/transimpedance amplifier combination respectively.

Consequently the closed transfer function (CLTF) is given by

$$CLTF = \frac{G(s)}{1 + G(s) H(s)} \tag{5.11}$$

with the feedback path, $H(s)$ being unity as it is a direct connection (Dorf & Bishop 1998, ch. 2).

Interferometer Response

The analysis of a control loop in terms of Laplace transforms may only be realised if the system is linear time invariant (LTI). When considering the response of the interferometer in (5.9) the fact that it is cosinusoidal means that the system is not strictly an LTI system. However one may consider that in the ideal case the feedback in the control loop will keep excursions of phase small. As such, a small signal approximation to the response of the interferometer may be applied which is linear over a small range (about quadrature) and thus LTI. This approximation results in the modelling of $G_{if}(s)$ as a simple gain term.

The maximum gradient appears around the quadrature point and remains approximately constant over small deviations from that point. The magnitude of the gradient is simply the visibility,

$$G_{if} \simeq K_{if} = \frac{2\sqrt{I_1 I_2}}{I_1 + I_2} \tag{5.12}$$

for the small signal case. The complex degree of temporal coherence, $|g_{12}|$ is approximated to unity since the coherence lengths of the sources are far longer than the optical path lengths being considered. K_{if} can be considered to be a conversion gain transforming optical path length in metres to power in Watts.

Piezo-electric Translator

The dynamic response of a PZT is very complex due a combination of inherent non-linearities and the mechanical dynamics involved with moving the mass of the mirror. PZTs exhibit several undesirable characteristics including hysteresis, non-linear voltage-displacement response, drift and creep. They also have an asymmetric force supplying capability, and unless pre-tensioned with a compressive spring force are able to supply much more push than pull. The mass of the mirror mounted upon the PZT results in finite settling times due to the interaction of the mass and the stiffness of the piezo element. This is of particular relevance in phase stepped techniques where the mirror is moved into different positions.

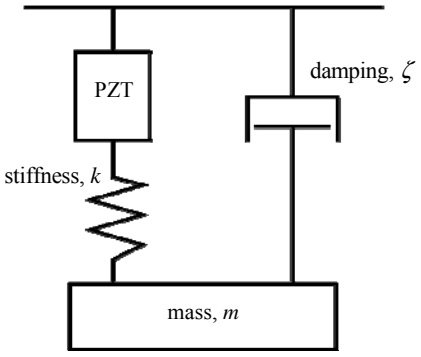

Figure 5.8 Equivalent representation of a PZT

Figure 5.8 shows the approximated equivalent system to be used for the analysis. The mechanical response of the PZT is considered to be a spring-damper system with an attached mass. The s-domain representation is given by,

$$G_{PZT}(s) = \frac{\omega_n^2}{s^2 + \frac{\omega_n}{Q}s + \omega_n^2} \tag{5.13}$$

which is familiar as a second order system with ω_n being the resonant frequency (rad) while Q is the quality factor which describes the sharpness of the resonance. The quality factor is related to the damping ratio, $\xi = 1/2Q$. It is found that the resonant frequency is governed by the mass, m and the stiffness of the piezo material, k such that

$$\omega_n = \sqrt{k/m} \tag{5.14}$$

It is possible to derive an unloaded mass, m_0 from (5.14) for an unloaded PZT with datasheet values for stiffness and resonant frequency (Hicks & Atherton 1997). The effective mass for a PZT loaded with a mass, m is then $m_{eff} = m_0 + m$. It should be noticed that the small scale stiffness values are often larger than the large scale stiffness values so the appropriate value for the situation must be used.

For the PI-810.10 PZT having large signal stiffness, $k = 18.6$ N/μm and resonant frequency of 22 kHz it is found that $m_0 = 0.977 \text{ x } 10^{-1}$ kg.

A Bode plot of the transfer function, $G_{pzt}(s)$ was produced using Matlab for the PI-810.10 PZT investigated and is given in figure 5.9. The mass of the small mounted mirror was found to be $1\text{x}10^{-3}$ kg thus the effective mass, $m_{eff} = 1.977 \text{ x } 10^{-3}$ kg. The quality factor is unknown but it shall be seen that this does not hold too much importance when the device is used well below resonance. Here, an arbitrary value $Q = 10$ is chosen order to make clear the effect on the frequency response (Physik Instrumente 2005).

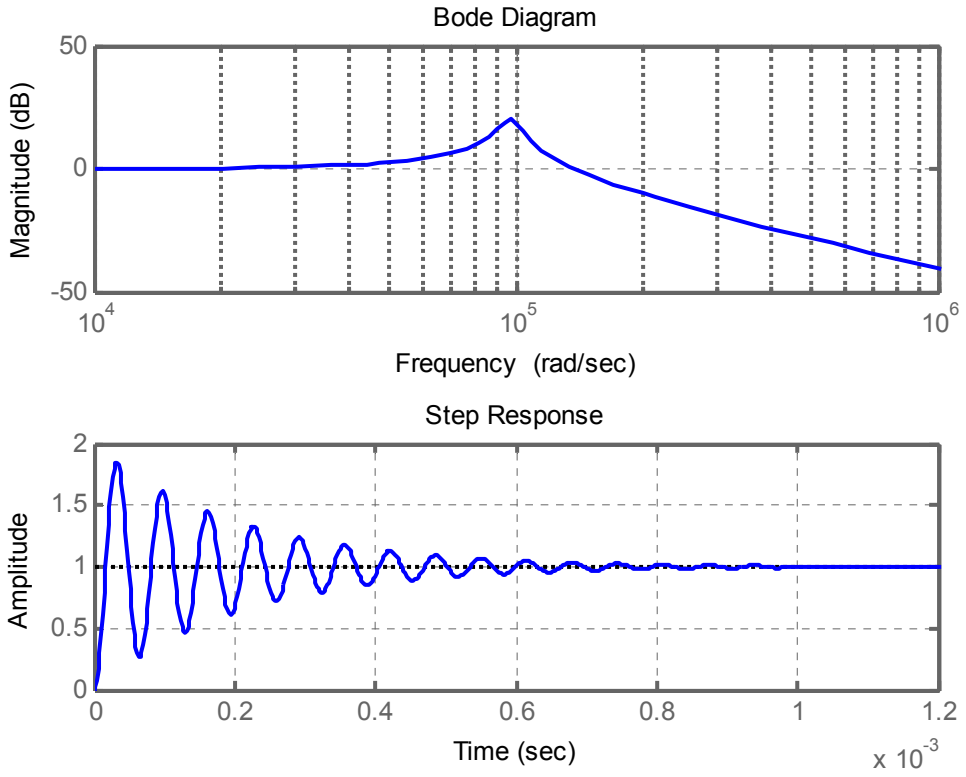

Figure 5.9 Simulated Bode plot and step response for a PZT

It is seen from figure 5.9 that the additional load of the mirror has lowered the resonant frequency from 22 kHz to 15.5 kHz. It may be seen from the normalised step response that the quality factor or degree of resonance has a large effect on the settling time.

Slew Rate Limiting

Another important parameter of PZT performance is the maximum slew rate obtainable in operation. In practice it is this limitation that generally impinges upon the stability of a control loop before the resonant behaviour. Slew rate limitations can arise from two sources, the maximum push/pull force produced by the PZT in order to accelerate the load mass and the current driving (compliance) limits of the drive electronics.

Push/Pull Limiting

The main limitation on the frequency response of the feedback system overall is the limited slew rate of the piezoelectric actuator used to move the mirror. For dynamic

operation, a PZT must provide enough force to create the required acceleration on the mirror mounted upon it. This force is given by,

$$F_{dyn} = \pm 4\pi^2 \cdot m_{eff} \left(\frac{\Delta L}{2} \right) f^2 \tag{5.15}$$

The current PI-810.10 PZT has a maximum stopped push force of 50 N. However, piezo-electric elements are much less efficient at contracting and thus the maximum pull force is found to be much lower at 1 N. The maximum non-slew rate limited sinusoidal frequency is given by,

$$f_{\max} = \sqrt{\frac{F_{dyn}}{2\pi^2 \cdot m_{eff} . \Delta L}} \tag{5.16}$$

The effective mass, $m_{eff} = 1.977$ x 10^{-3} kg was derived earlier, and $F_{dyn} = 1$ N is the lower limit as produced by the maximum pulling force of the PZT. The limit on the peak to peak displacement, $\Delta L = 3.6$ μm is given by the product of the displacement to voltage ratio (0.15 μm/V) and the maximum voltage range (24 V), which is limited by the drive electronics (Physik Instrumente 2009).

An evaluation of equation (5.16) suggests $f_{\max} = 2.67$ kHz as the large signal worst case value. For the small signal case which we can define as being one full fringe, or approximately 775 nm at an operating wavelength of 1550 nm, we might expect a maximum undistorted frequency of about 5.75 kHz.

Current Limiting

The peak sinusoidal frequency that may be obtained by using PZT drive electronics supplying maximum current, $i_{\max}$ over a peak to peak voltage range V_{pk-pk} is given by,

$$f_{\max} = \frac{i_{\max}}{\pi \cdot C_{pzt} \cdot V_{pk-pk}} \tag{5.17}$$

In the PZT drive electronics used in this apparatus, the BUF624T current driver can supply $i_{\max} = 250$ mA which over $V_{pk-pk} = 24$ V (limited by the LF355 op amp operating range) yields the large signal case of $f_{\max} = 9.2$ kHz. The small signal case

is somewhat higher, to move one full fringe at 1550 μm requires a voltage shift of 5.17 V, yielding $f_{\max} = 42.8$ kHz (Burr Brown 1996).

It is clear from these design calculations that the PZT slew rate is not limited by the drive electronics and we may consider the maximum push/pull rate to be the limiting factor. Slew rate limiting is not easily and simply modelled using s-domain methods as it is an inherently non-linear function. In general the effects of slew rate limiting on a control loop can be disastrous and it is usually avoided by ensuring that the slew rates of any controller are smaller, thus avoiding integral windup (Pickelman 2003).

Photodiode Front-end

The photodiode and transimpedance amplifier transfer function, $G_{pd}(s)$ is generally well modelled as a multi-pole response produced by the interaction of shunt impedance at the input and the feedback impedance along with the open loop gain profile of the op amp used. A detailed circuit analysis is involved and as such is given separately in appendix A. Good design will ensure that the response of the photodetector front end is sufficient enough not to limit the performance of the control loop while at the same time ensuring the minimum bandwidth in order to minimise noise on the output. The general transfer function for a transimpedance amplifier and photodiode front end is derived in appendix A.1 and is

$$z_{trans} = \frac{A_{ol}(s)\, z_f(s)}{1 + A_{ol}(s) + {}^{z_f(s)}\!/_{z_{sh}(s)}} \tag{5.18}$$

The voltage produced by a transimpedance amplifier for a photocurrent of i_{ph} from a reverse biased photodiode is given by,

$$V_{out} = i_{ph} R_f \tag{5.19}$$

In other words the value of R_f sets the DC transimpedance.

The responsivity of the PDDM981 PIN photodiode used in this instrument is given as 1.05 A/W at a working wavelength of 1550 nm (Wuhan Telecommunications). The maximum input voltage range of the NI PCI-6221 DAQ card is ±10 V (National Instruments 2007). With the losses of the optical system unknown initially, a suitable value for the transimpedance was required and this was carried out experimentally.

The idea was to present a reasonable voltage range for the normal operating conditions. The reference transimpedance amplifier was initially designed with a 50 k variable resistor and a 10 pF feedback capacitance in which provided fairly heavy damping to the response, ensuring consistent stability over the transimpedance operating range. This resulted in manageable working output voltages of up to 0-5 V in practice.

An analysis using a Matlab script (see appendix C) was carried out, the frequency and step responses are shown in figure 5.10.

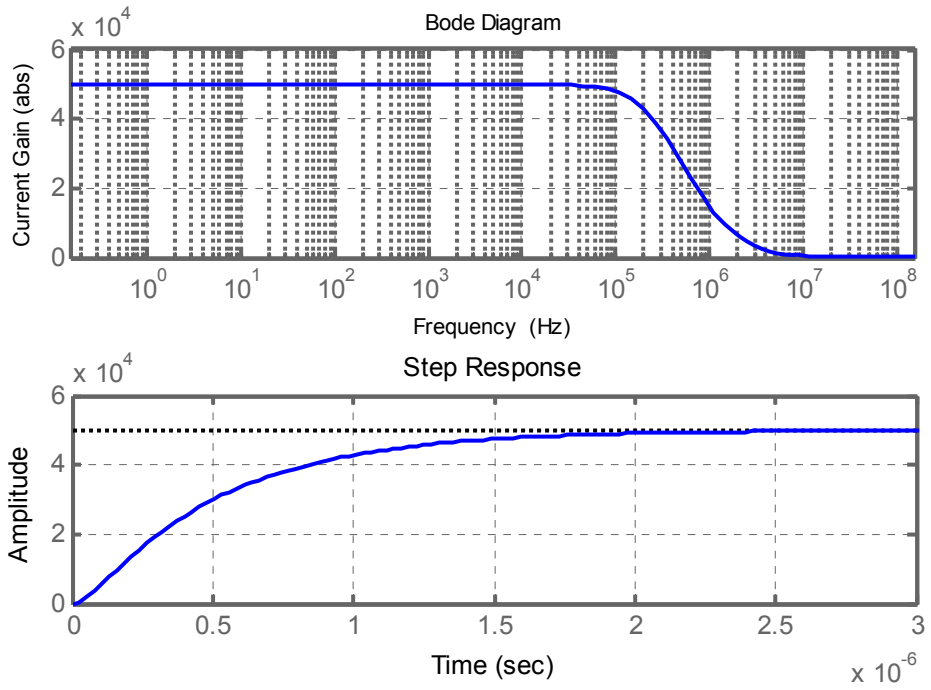

Figure 5.10 Simulated Bode-magnitude plot and step response for a transimpedance amplifier

For the case of the circuit used as a transimpedance amplifier in this apparatus it will be seen that that any poles of the transfer function are at frequencies several orders of magnitude higher than those of the PZT actuator. Hence these poles have negligible effect on the overall system transfer function and as such the transfer function may be usefully modelled as the simple DC transimpedance given in (5.19), in which case,

$$G_{pd} \simeq K_{pd} = R_f \tag{5.20}$$

In this way K_{pd} may be considered as a conversion gain, changing intensity to voltage.

The Controller

With the all the contributing elements in the forward path or plant approximately characterised it is worthwhile revisiting (5.8) and rewriting the forward path

$$G(s) = K_c(s) \cdot K_{pzt}(s) \cdot K_{if} \cdot K_{pd} \tag{5.21}$$

which now includes the approximation of the photodiode front end and small signal interferometer responses as simple gain terms.

The requirement now is to select a controller which when employed in the forward path, will allow for the reduction of external disturbance affecting the closed loop system. Figure 5.11 shows the block diagram of the closed loop system with a disturbance source $D(s)$ representing unwanted optical path length variation in the loop.

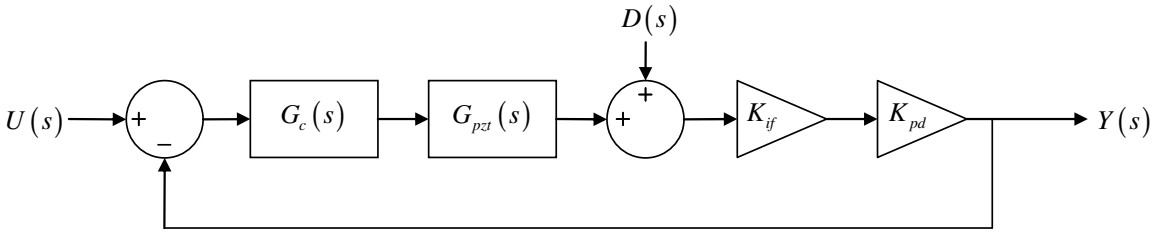

Figure 5.11 Block diagram representation of the closed loop MFI with the addition of an external disturbance

The method for quantifying the level of disturbance rejection in a control loop is by defining a sensitivity transfer function, S_G^D which describes the output response of the system to a given disturbance signal,

$$S_D^G = \frac{Y(s)}{D(s)} \tag{5.22}$$

The open loop transfer function from figure 5.11 is simply $G(s) = K_{if} K_{pd}$ and the feedback path is $H(s) = G_c(s) \cdot G_{pzt}(s)$. With reference to equation (5.22) the closed loop transfer function is then

$$S_D^G = \frac{G(s)}{1+G(s)H(s)} = \frac{K_{if}K_{pd}}{1+K_{if}K_{pd}G_c(s)G_{pzt}(s)} \tag{5.23}$$

The sensitivity, S_G^D is the main figure of merit for analysing the effectiveness of this system to reducing the influence of environmental perturbation. Equation (5.23) shows that increasing the gain of the controller $G_c(s)$ will in general improve the disturbance rejection assuming of course that the closed loop system remains stable.

The obvious initial choice for a controller $G_c(s)$ is that of a proportional-integral controller since it is easy to implement and generally robust in operation if the parameters are correctly chosen. A PI controller can provide effective control which is easily implemented, by virtue of having only two parameters, by analogue electronics.

The PI control is essentially a simplification of the common proportional-integral-differential (PID) controller with the derivative term set to zero. There are various PID controller structures which have varying historical reasoning behind them. These are the ideal (or non-interacting), series and parallel forms. The parallel form is the most general as the three actions are completely separated and as such the integral term to be turned off if necessary. Its transfer function is

$$G_c = K_p + \frac{K_i}{s} + K_d s \tag{5.24}$$

where K_p, K_i and K_d are the gains of the proportional, integral and differential elements respectively. The integration time, τ_i is sometimes used to refer to the integration gain where $K_i = 1/\tau_i$ (Visioli 2006, pp. 1-18). The analogue electronic implementation of the parallel PI controller ($K_d = 0$) used in this apparatus is given in appendix B.2.

Given the implementation of a PI controller as the closed loop compensator it is now possible to analyse the effectiveness of the control loop and load disturbance due to environmental perturbation. For the purpose of this analysis it was decided to set the gain $K_{if} \cdot K_{pd} = 3$ which is equivalent to a 3V peak-to-peak interference fringe and was found to be reasonable in practicality.

5.4.4 Control Loop Analysis

The overall control may be usefully studied in Matlab which eases computation and provides access to useful graphical routines such as bode plots step responses. Appendix D.3 shows the Matlab script used to study the control loop, the variable nomenclature relates to that used in the previous sections.

There are two control parameters to consider, the proportional and integral gains, K_p and K_i respectively and also one unknown parameter Q. It is important that the integral gain is kept equal to or smaller than the maximum slew rate available by the PZT actuator, thus $K_i = 5.75 \text{ x } 10^3$ is the simulation value set which is the maximum to allowable for predictable simulation results.

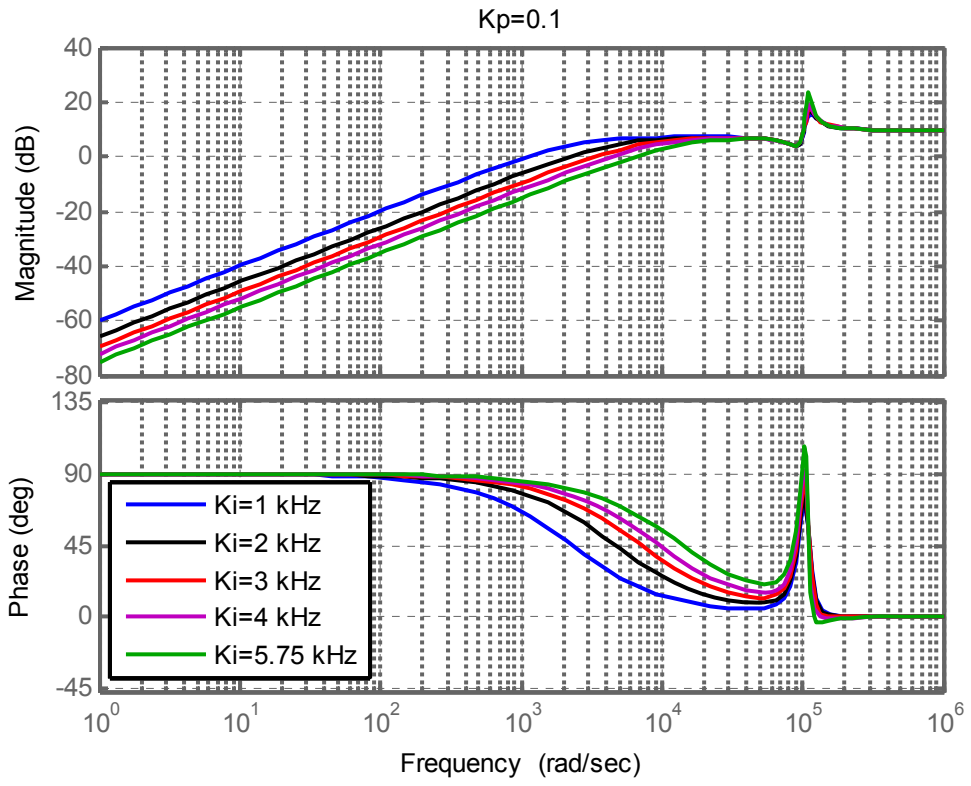

Figure 5.12 Simulated Bode plot of the sensitivity function for varying integration gains

Figure 5.12 shows the frequency response of the sensitivity function, S_D^G with varying amounts of integration gain for a static proportional gain of 0.1. It is very

clear that increasing the integration directly improves the disturbance rejection. It also however appears to amplify any component around the resonant frequency.

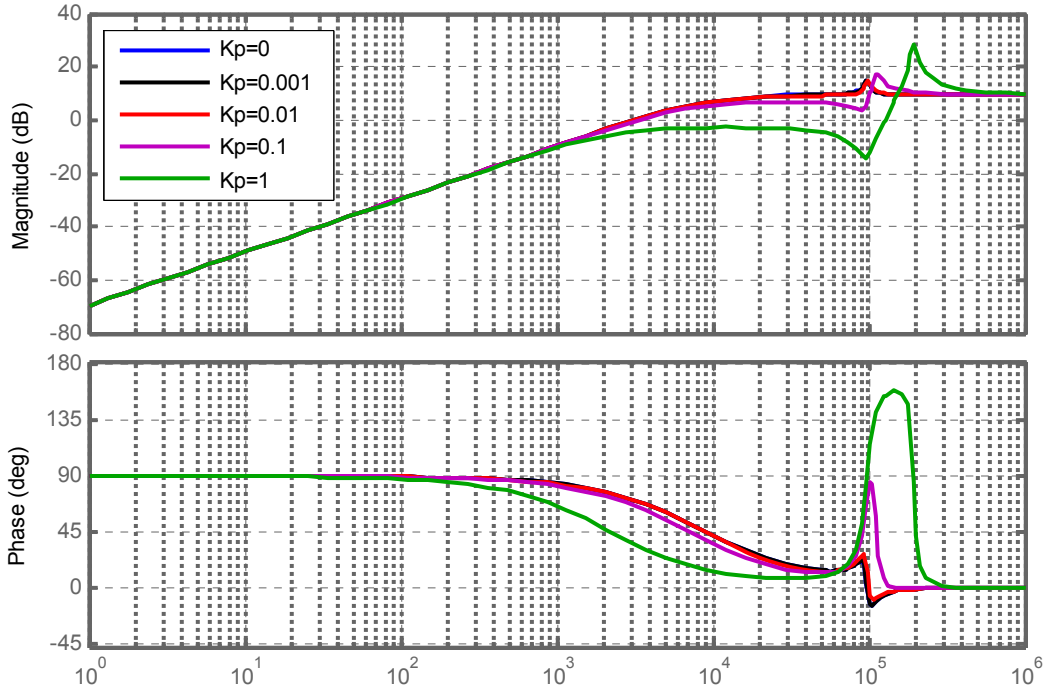

Figure 5.13 For varying proportional gains

Figure 5.13 shows the frequency response of the sensitivity function, S_D^G with varying amounts of proportional gain. It would appear that changing the proportional gain does nothing to alter disturbance rejection at low frequencies, however at high frequencies it appears to help. It also appears to amplify the resonance, although the slew rate limit, not modelled here must also be limiting. It is noticed in the step response that the higher the proportional gain, the more distortion seen in the initial 'kick' of the step response. Too much proportional gain actually appears to slow down the step response.

The consequence of slew rate limiting is not included in the model due to the fact it is not a linear function, nor is it easily linearised. In this sense it is an unknown element and will cause instability if the actuator is driven above the slewing frequency. The best technique for ensuring stability is to ensure the integration gain remains below the slew rate limiting frequency.

The mathematical analysis of the control loop gives a strategy for implementation of the PI settings. The integration gain is the primary method of reducing load disturbance so the critical action is to raise this as high as possible with any improvement possible with the proportional element of the control being secondary.

Obviously all the considerations for improving the disturbance rejection qualities are dependent on the closed loop stability. There are several tests used in control theory to determine whether a closed loop system will be stable including phase/gain margins, Nyquist and root loci plots. Frequency domain methods are intuitive and clear and a gain-phase plot can show clearly the ramifications of parameter variation on a system. In a gain-phase plot, the gain and phase value of the open loop function are plotted with changing frequency (Dorf & Bishop 1998, ch. 9).

The phase margin is defined as the amount of phase shift the will result in a marginally stable closed loop system. A marginally stable closed loop system will occur when the phase of the open loop transfer function is 180° at the unity gain cross over frequency. The critical factor for stability is to ensure that the phase margin does not reach zero, indeed for a system robust to parameter variation in the plant it is preferable that it should be no less than 30°, above this gain peaking will occur and an under damped closed loop response observed.

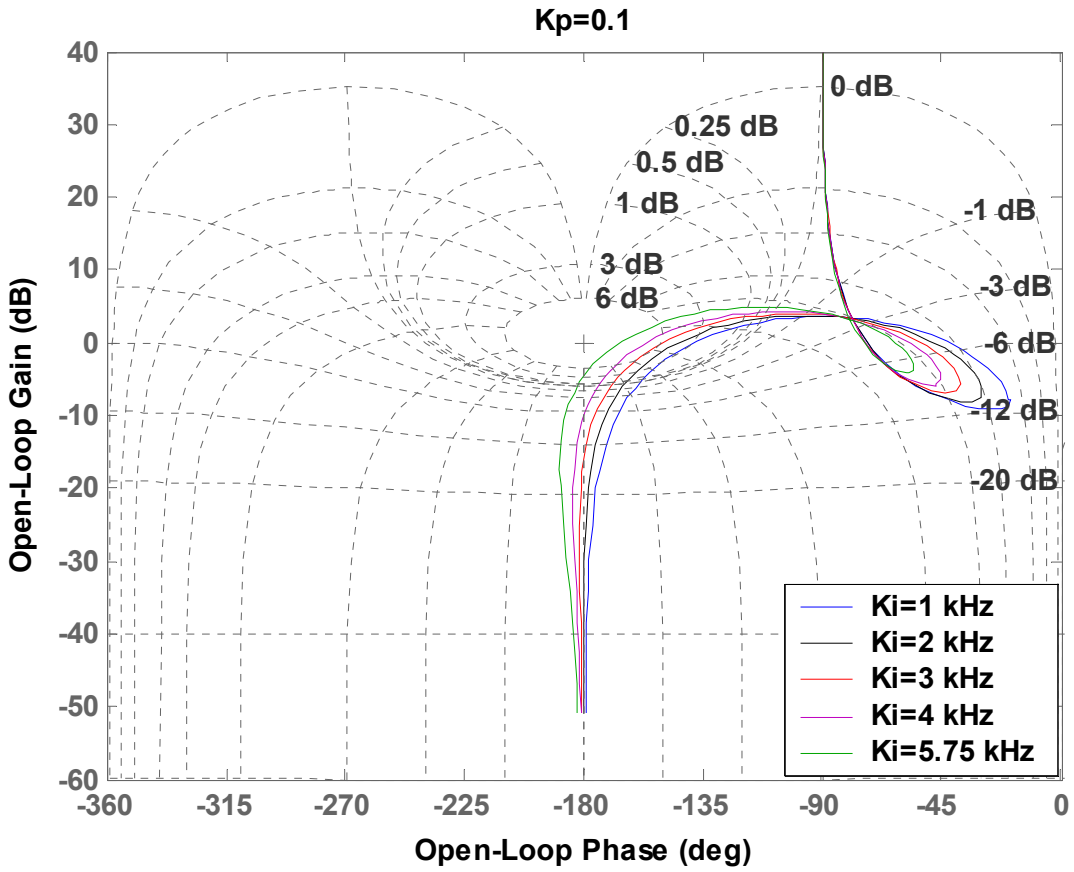

Figure 5.14 Simulated Nichols chart of the open loop response of the MFI for varying values of integration gain.

Figure 5.14 shows a Nichols (gain vs. phase) plot for $G(s)$ for varying levels of integral gain. The phase margin on the plot is given by the horizontal distance between the cross-haired point (where the phase is 180° and the gain 0 dB) and the curve. It is clear that if at any point the curve crosses into the quadrant above and to the left of the cross-haired point and unstable system will result. For the results given in figure 5.14 it can seen that the closed loop system should always be stable even when the integral gain is turned up to the slew rate maximum of 5.75 kHz (as imposed earlier). This is confirmed by examining the closed loop step response shown in figure 5.15. The beginnings of instability (gain peaking) are produced at the highest value of integration gain however indicating a marginal situation.

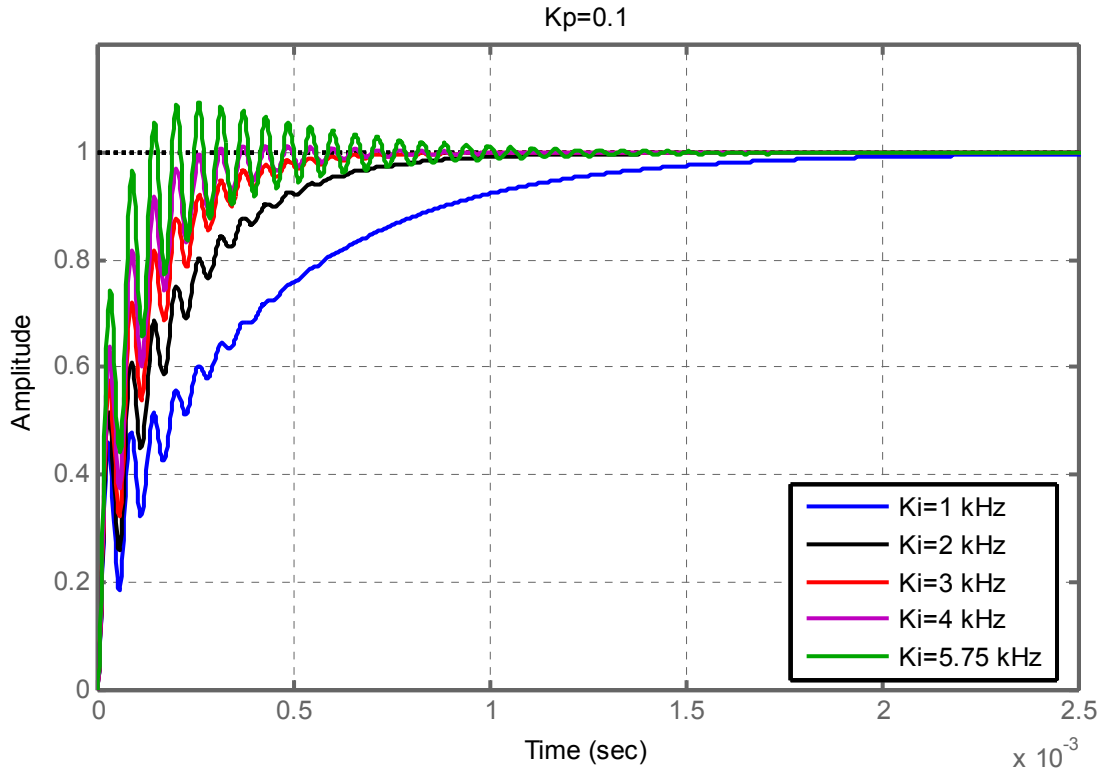

Figure 5.15 Simulated closed loop response of the MFI to a setpoint change

5.4.5 Extraction of Phase Data

Extraction of phase data from the output of an interferometer is non-trivial due to the co-sinusoidal nature of the response. PSI is one solution for retrieving the absolute phase value from an interferogram and is suitable for determining the absolute (DC) phase value (see section 4.7.8). The phase is manually shifted to various points and the output interferogram recorded at each point. A suitable algorithm may then be used to determine the actual value of the original phase (Creath 1988).

For this instrument, PSI techniques were used to retrieve the phase information from the interferometer using the Carré algorithm (Carré 1966). This algorithm was used in preference to others because it is unique in the fact that it does not require a known phase shift to be performed. This is clearly a great advantage in this system as the shifting of the mirror will induce a different magnitude of phase shift in each of the wavelengths scanned to gain the whole scan profile. The only requirement in the use

of the Carré algorithm is to ensure is that each phase step created by the mirror i.e. the distance the mirror is moved, is identical with each phase step.

If $\varphi(x)$ is the original phase at a sampled point x on the scan profile, the phase is altered by 4 equal steps, $-3\alpha, -\alpha, +\alpha$ and $+3\alpha$ around this point and 4 intensity values $I_1(x)$, $I_2(x)$, $I_3(x)$ and $I_4(x)$ respectively are obtained. These are then input into the Carré algorithm to yield the original phase value at each point. The Carré algorithm is given by,

$$\varphi = \tan^{-1}\sqrt{\frac{(3I_2 - 3I_3 - I_1 + I_4)(I_1 + I_2 - I_3 - I_4)}{(I_1 - I_2 - I_3 + I_4)^2}} \tag{5.25}$$

where the dependence on x is dropped for clarity.

5.5 Implementation

5.5.1 Practical Implementation of PI Control

The physical implementation of the PI controller used in this apparatus was done using op amps throughout; the details are given in appendix B.2. The circuit was designed to supply a variation of proportional and integral gains through variable resistors, allowing the circuit to be tuned. The poles of the operational amplifiers formed by feedback impedances, open loop gain roll off etc. are all found at much higher frequencies than the dominant dynamics of the control loop and are thus neglected. The reasons for this are outlined in description of the transimpedance amplifier in section 5.3.3.

Tuning of the PI circuit was done by mounting the measurement mirror on a second PZT and applying a sinusoidal waveform from a signal generator, while the reference interferometer output was observed. The integration and proportional gains were then adjusted to minimise the peak to peak disturbance of the reference interferometer. The setup of the optical probe to facilitate this is shown in figure 5.16.

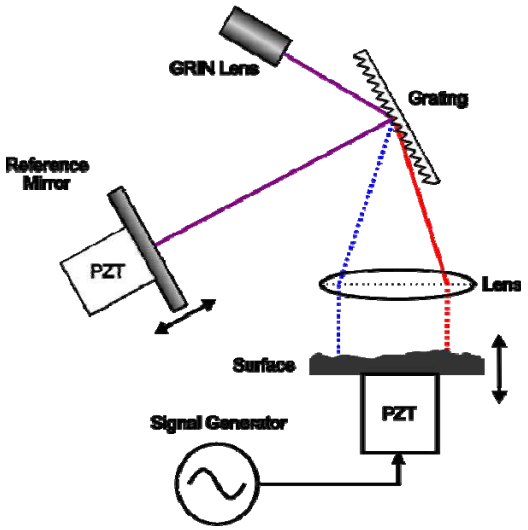

Figure 5.16 Schematic of the optical probe with added PZT to apply disturbance to the measurand

5.5.2 Closed Loop Control to Implement PSI

Along with disturbance rejection, the closed loop PI control was used to shift phase. This is made possible by changing the setpoint voltage applied to the control so that the mirror is moved and another point on the fringe is locked. The resulting path length change due to mirror movement also induces phase shift in the measurement interferometer. By altering the setpoint voltage, it is possible to move the mirror inbetween each profile capture whilst maintaining the disturbance correction. As such a number of phase shifted profiles may be captured in a sequence.

There are two great advantages in using closed loop control for phase shifting. First, the phase shift may be performed very accurately due to the closed loop nature of the system. This also means that the nonlinearities of drift and hysteresis in the PZT do not affect the accuracy of the shift. The other advantage is that that disturbance rejection is continually ongoing during the whole measurement process.

Looking at the Carré algorithm (5.25) it is seen that 4 intensity measurements at different reference mirror positions are required in order to derive the phase encoded height profile of the surface. The literature suggests that the most effective phase shift angle for the rejection of noise induced by phase shifting error is 110º. This is equivalent to setting $\alpha = 55°$ (Kemao et al. 2000).

From equation (5.2) the distance the reference mirror will have to move in produce the required shifting of the phase term is

$$x = \frac{\varphi\lambda}{4\pi} \tag{5.26}$$

The reference interferometer operating wavelength, $\lambda = 1550$ nm requires a mirror shift of 236.8 nm to produce the 110º phase shift. As the measurement wavelength varies during the sweep, the magnitude of the phase step for the measurement interferometer will vary across the profile. This is the reason for using the Carré algorithm. Any other algorithm would require the induced phase step to be mapped across the sweep.

5.5.3 Sequence of Operation

Figure 5.17 shows a functional representation of the non-optical elements of the apparatus. It shows the PC running LabView controlling the Ando AQ4320D tunable laser via a GPIB bus. The NI-PCI 6221 DAQ card is used to sample and digitise the output of the measurement interferometer.

Each of the elements of the PI controller and PZT driver is also represented and detailed circuit diagrams are provided in appendix B.

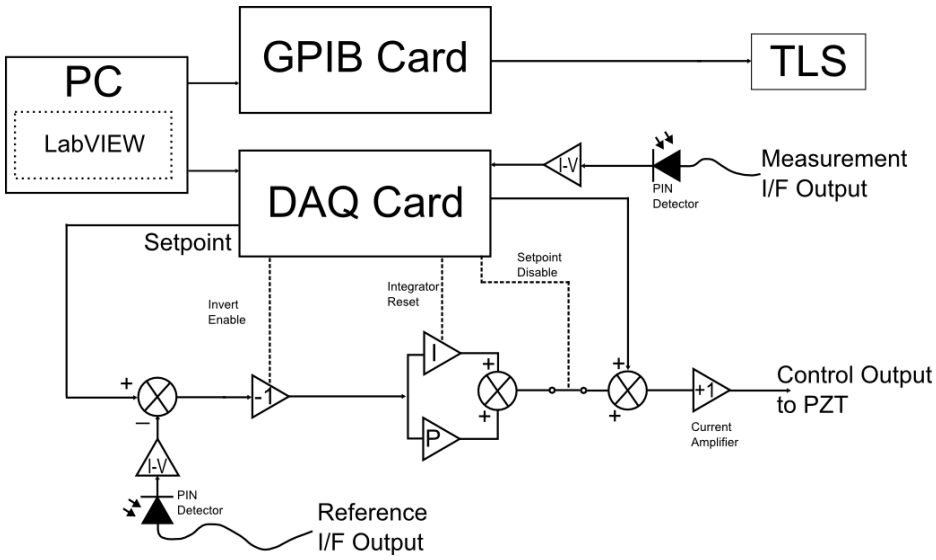

Figure 5.17 Functional diagram of the MFI

The DAQ card provides an analogue setpoint voltage to the PI controller with which to control the phase shifted position. It also supplies TTL compatible logic levels to provide:

Invert Enable - a setpoint inversion function to enable the controller top move to phase shift positions 3 and 4.

Integrator Reset – Allows the integrator to be reset remotely, in the case of full scale range being reached. When activated the integration capacitor is shorted and the interferometer locks back on to the nearest setpoint value when re-enabled.

Setpoint Disable – Disconnects the control signal from the PZT. Used during fringe visibility calibration.

It is useful to consider the flow of events that are taken when the apparatus is used to take a measurement. This is given by the flowchart in figure 5.18, while the following sections explain each element in more detail.

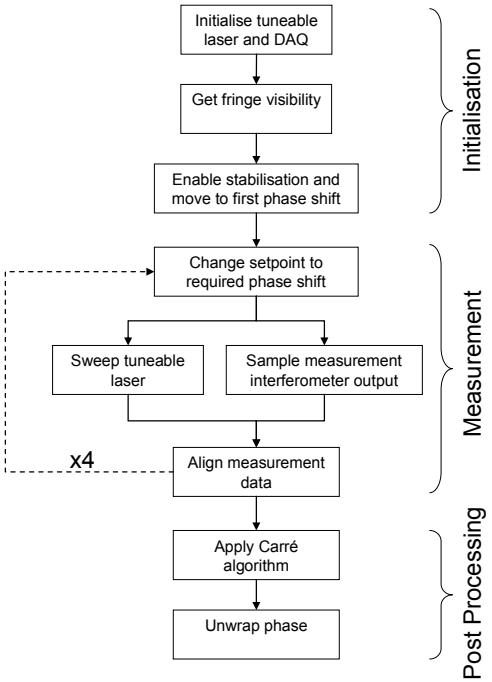

Figure 5.18 Event flow of MFI during the measurement cycle

Initialise Tuneable Laser and DAQ Card.

First the tuneable laser and DAQ are initialised and set to known states ready for wavelength sweeping. At this stage, parameters such as wavelength sweep range, starting wavelength and power may all be selected.

Get Fringe Visibility

In order to apply the correct phase steps using closed loop control it is necessary to determine the setpoint voltages that must be applied. A calibration routine was found to be necessary to determine the visibility of the interferometer and thus determine the correct setpoint voltages.

With reference to equation (5.9) if the visibility, V of the interferometer and the quadrature point intensity are known it is possible to determine the setpoint voltage changes needed to perform the required shift.

This was be done by disabling the closed loop controller and then applying a simple triangle wave to the PZT. The amplitude of triangle wave was such that its peak to peak voltage was sufficiently high enough to move the mirror over several fringe multiples and as such a sinusoidal intensity response was produced at the output of the interferometer. This in turn was registered as a voltage waveform on the DAQ card which was then stored.

The peak values on the recorded response were then calculated by taking an average of the all the low and high values. This act yields the low and high peaks, V_{pk-hi} and V_{pk-lo} respectively. The following formula then describes the voltage to phase relationship of the reference interferometer;

$$V_{out} = V_{pk-lo} + \frac{V_{pk-hi} - V_{pk-lo}}{2}\left[1 + \cos\varphi\right] \tag{5.27}$$

Also the quadrature point voltage, when $\varphi = 90°$ is given by,

$$V_{quad} = \frac{V_{pk-hi} - V_{pk-lo}}{2} + V_{pk-lo} \tag{5.28}$$

V_{out} is the voltage output seen by the DAQ card for any given phase value, φ. The 4 setpoint values, relating to the 4 mirror shift positions were then found by simply calculating V_{out} for $\varphi = $ -110°, -55°, +55°, +110° . These values then relate to the

required shift around the quadrature point, $\varphi = 90°$. The phase step of 55% is found the be the most effective for the reduction of random amplitude due to noise (Qian et al. 2004).

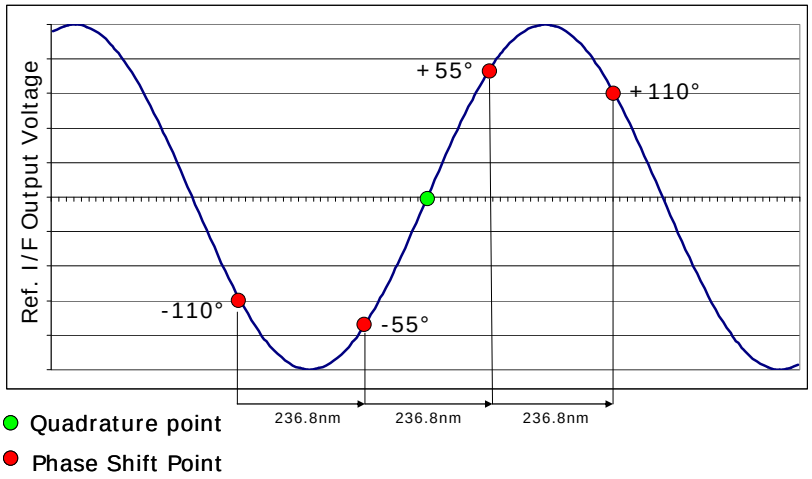

Figure 5.19 Response of the interferometer with the required setpoints shown (angles are relative to the quadrature point)

Figure 5.19 shows a representation of the intensity fringe with the calculated setpoint values as red spots and the mirror shift distance required to step between them. The quadrature voltage point is shown as a green spot.

Phase stepping is thus enabled by changing the setpoint voltage to the relevant calculated value before the wavelength swept intensity profile from the measurement interferometer is taken. This will yield the required 4 sets of intensity samples, relating to the measured profile of the surface.

Changing Setpoint to Required Phase Shift

The setpoint shifting required a combination of hardware and software control (via Labview). The required setpoint voltages are obtained by the visibility routine before the measurement cycle begins. The voltages are output from the DAQ card to the controller circuit (the *setpoint* input on figure 5.17). The actual shift order used is slightly different from figure 5.19 shown previously.

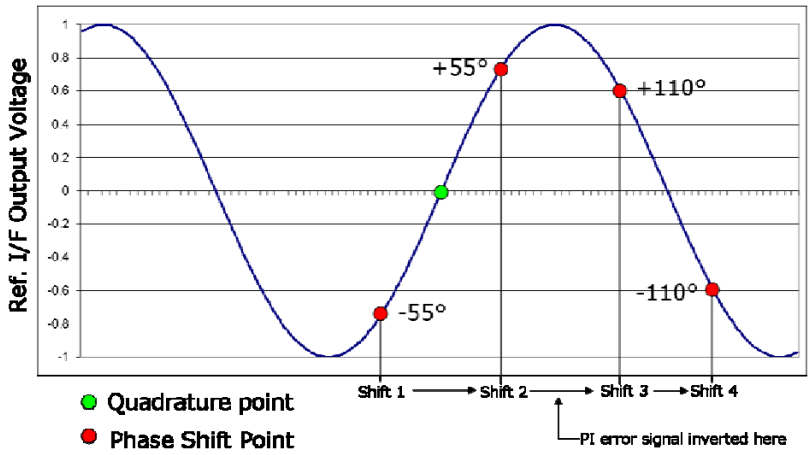

Figure 5.20 Shift order of the setpoints during the measurement cycle

The measurement cycle starts by setting the mirror at the quadrature point. The measurement cycle then proceeds as follows;

Shift 1 - Reduce the setpoint, get $-\alpha$ profile, $I_2(x)$.

Shift 2 - Increase the setpoint, get $+\alpha$ profile, $I_3(x)$.

Shift 3 - Invert error signal, reduce setpoint, get $+3\alpha$ profile, $I_4(x)$.

Shift 4 - Reduce setpoint, get -3α profile, $I_1(x)$.

It should be noted that for shift 4 that the mirror is not actually in the -3α position but 775 nm (one full fringe) in front of it. However as the response is modulo 2π the intensity profile is identical for the purposes of the Carré algorithm.

The inverting of the setpoint is used to 'push' the setpoint over peak onto the opposite side of the response. A unity gain inverter is used to perform this task, it may be switched into the control circuit from a command in the Labview routine.

Align Measurement Data

After the measurement cycle was complete and the 4 intensity profiles were obtained it was found that the sample sets were not precisely aligned. The reason for this is that the start of the tuneable laser wavelength sweep is not precisely synchronised with the start of the sampling. This occurrence stems from the non-deterministic nature of the operating systems of the computer, the laser and the GPIB interface over which the start-sweep command issued. As a result there is a variable time delay

between the start of the sampling and the start of the laser sweep. It was thus necessary to post process the obtained intensity profiles in order to fully synchronise their elements.

An analogue voltage output is available from the Ando AQ4320D tuneable laser that is proportional to the current swept wavelength and this was used as the basis for aligning the scanned data. During a wavelength sweep this output was sampled simultaneously with the measurement interferometer intensity data using the multiplexed input feature of the DAQ card. The resulting sampled data is stored in a 2D array of data, with one row containing the intensity samples from the interferometer and the other containing the analogue voltage output from the tuneable laser (Ando Electric Co 1999). An example of the waveform sampled from the tuneable laser is shown figure 5.21.

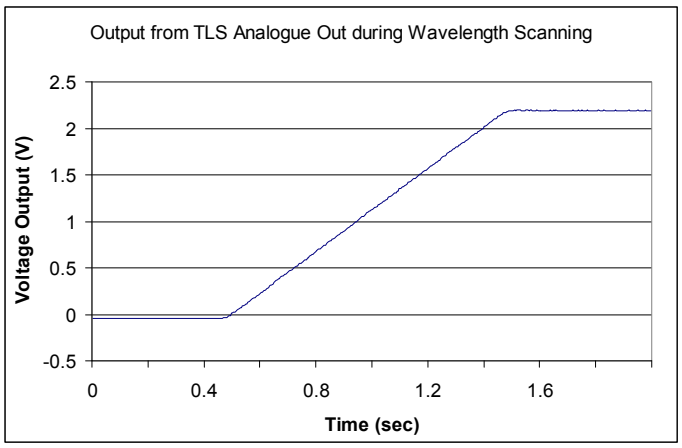

Figure 5.21 Output of the tuneable laser analogue output during wavelength sweeping

The sampling is started before the tuneable laser sweep command is issued and carries on after the sweep finishes in order to ensure a full capture of the sweep. The actual intensity data required occurs only during the ramped section of the output shown in figure 5.21. By aligning the ramps data values of all 4 sample data sets, it is possible to synchronise the intensity sample sets at the same time, as long as the operation is identically performed on both rows of each 2D array. The method used was to cross-correlate the tuneable laser output sampled datasets $I_2(x)$, $I_3(x)$, $I_4(x)$ individually with data set $I_1(x)$. The discrete form of the cross-correlation function is defined as,

$$(f * g)_i = \sum_j f_j^* g_{i+j} \tag{5.29}$$

where f_j^* is the complex conjugate of the sample value f_j which in this case are always real values.

In essence, it moves the dataset $g[j]$ over the dataset $f[j]$ sample wise in steps of i. After each shift, the corresponding sample points are multiplied together and all the results are summated. Clearly, when the two signals are closely matched there will be a peak in the cross-correlation signal at that point. So the value of i at the peak of $(f * g)_i$ provides the number of shifts required to bring the intensity datasets back in line.

After obtaining the number of samples needed to shift each of the datasets $I_2(x)$, $I_3(x)$ and $I_4(x)$ that number were simply removed from the front of the datasets, thus bringing them into line. There must of course be some error associated with this method especially as the analogue output from the tuneable laser is of a low quality, uncalibrated and quite noise prone. Any error will become more relevant as the lateral resolution of the system is increased, by reducing the beam spot size, and this would need to be considered carefully.

The final stage of pre-processing the sampled datasets is to detect the start of the scan by running a threshold detector over the tuneable laser analogue output. When the threshold is exceeded (at the start of the ramp) then this is deemed to be the first sample on the scan. The next 10 000 samples are isolated and retained (10 kHz sample rate with 1 second wavelength sweep duration) from each data set. The result is an aligned set of intensity profiles, in the form of a 4 row array, with which to pass to the Carré algorithm.

Apply Carré Algorithm

The implementation of the Carré algorithm in LabVIEW consists of two parts; the actual phase calculation and a method to remove the phase ambiguity. The phase ambiguity results from the nature of the arctangent calculation in (5.25). The phase can only be determined modulo π using this algorithm on its own. We can determine the phase modulo 2π by examining the signs of the quantities proportional to $\sin\varphi$

and $\cos\varphi$. The rules given in table 5.2 are then used to adjust the original calculated phase value to ensure it lies in the correct quadrant.

$\sin\varphi$	$\cos\varphi$	Adjusted Phase
Positive	Positive	φ
Positive	Negative	$\pi-\varphi$
Negative	Negative	$\pi+\varphi$
Negative	Positive	$2\pi-\varphi$
0	Anything	π
Positive	0	$\pi/2$
Negative	0	$3\pi/2$

Table 5.2 Rules for determining arctangent quadrant for the Carré algorithm

For the Carré algorithm, the quantities that must be examined are:

$$\left(I_2(x)-I_3(x)\right)\propto\sin\varphi \tag{5.30}$$

$$\left(I_2(x)+I_3(x)\right)-\left(I_1(x)+I_4(x)\right)\propto\cos\varphi \tag{5.31}$$

Unwrap Phase

After the Carré algorithm has been executed, a phase unwrapping algorithm was run. This provides a method of increasing the measurement range for slowly varying surface heights (i.e. gentle slopes). It is a commonly used technique in monochromatic phase shifting interferometry, and works by detecting for phase steps values greater than π between adjacent sample values. If such a gap is detected, 2π is added on (of taken off if the difference is negative) all proceeding samples. It is necessary for the phase unwrapping technique to work that there are no actual jumps greater than π between adjacent pixels and thus the technique is limited to gently sloping surfaces. Another problem is sensitivity to measurement noise around the upper and lower (0 and 2π) points on the fringe, where a small amount of noise can trigger a wraparound (Creath 1988).

5.6 Experimental Results

5.6.1 Introduction

Several experiments were carried out with the aim of assessing the performance of the interferometer scheme. First, the disturbance rejection capability of both the reference and measurement interferometers was measured in isolation. Then known displacements of 50 nm where measured with the instrument to assess the uncertainty of the system. A flat mirror was then scanned using the optical stylus several times in order to gauge the repeatability. Finally, two step height samples were measured in order to determine the realistic measurement performance.

5.6.2 Reference Interferometer Disturbance Rejection

The first experiment was designed to test the effectiveness of the disturbance rejection technique. A sinusoidal displacement was applied to the measurement mirror of just over a full fringe (775 nm) in order to ascertain the effectiveness of the control scheme. A second PZT (PI-820.10) was used to move the measurand in order to achieve this.

The experiment was carried out over several frequencies and figure 5.22 shows the observed reference interferometer output. In each of the plots, the active stabilisation is inactive in the left half, and then switched on at about the midpoint. Figure 5.22a, b, c and d show the results at 2, 5, 10 and 20 Hz disturbance frequencies respectively.

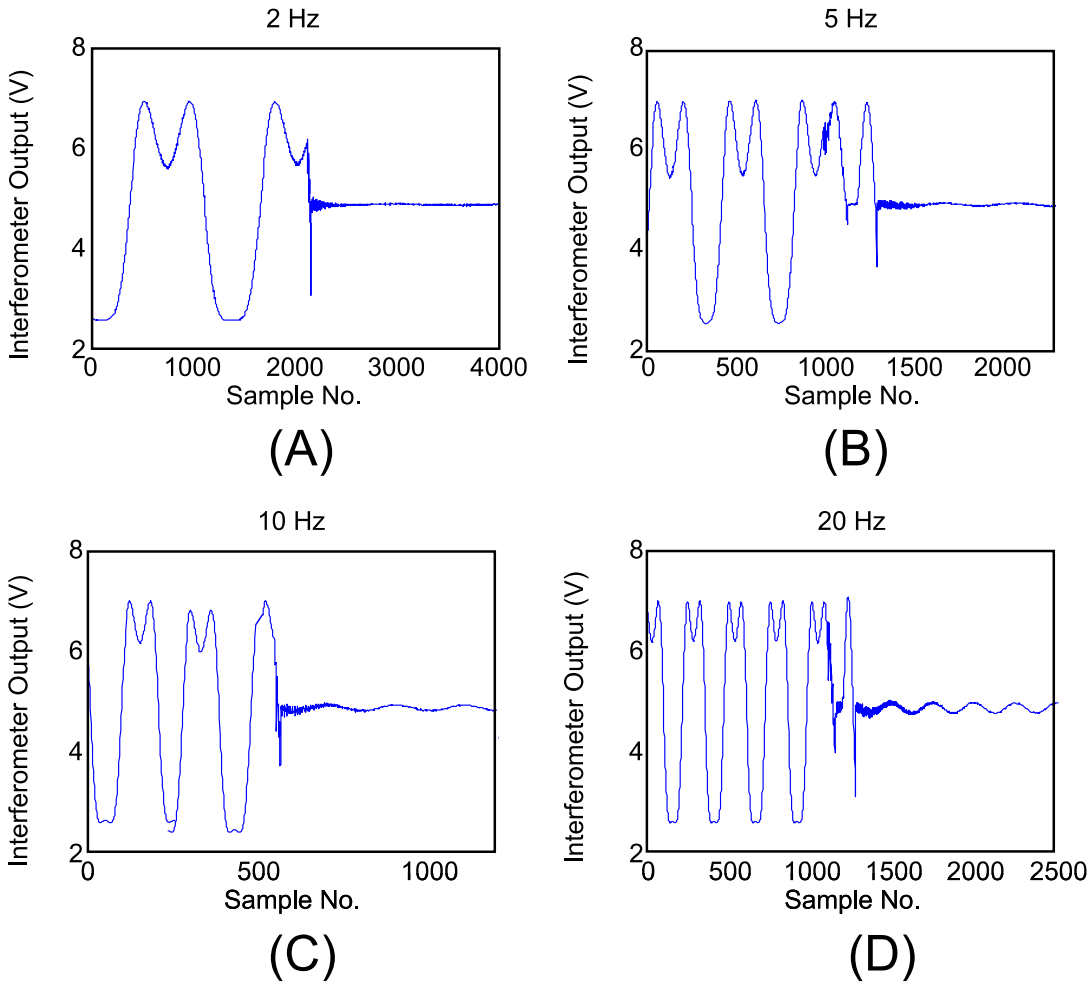

Figure 5.22 The effect of the active stabilisation for varying frequencies

The left hand side of each plot shows the free running interferometer with the stabilisation turned off and examination confirms that the induced sinusoidal disturbance is indeed over a full fringe, the folding over of the fringe is quite clear at the peaks. The righthand side of each plot shows the interferometer output when the stabilisation control turned on.

The results seen in the diagram show quite clearly the effectiveness of the control loop at attenuating load disturbance at the reference interferometer. At the point at which the active stabilisation is enabled there is a transient response, after which the output variation appears to be much diminished.

Qualitative inspection of the stabilised portions for each plot in figure 5.22 suggests that the amount of residual disturbance in the output increases with frequency. This is

to be expected if one considers the analysis given in section 5.4.4 and specifically the results shown in figure 5.12.

Figure 5.23 shows the corresponding control voltage for each of the cases shown in figure 5.22. The square wave on the left hand portion of each graph is the open loop response of the control due to the control loop being open (de-activated).

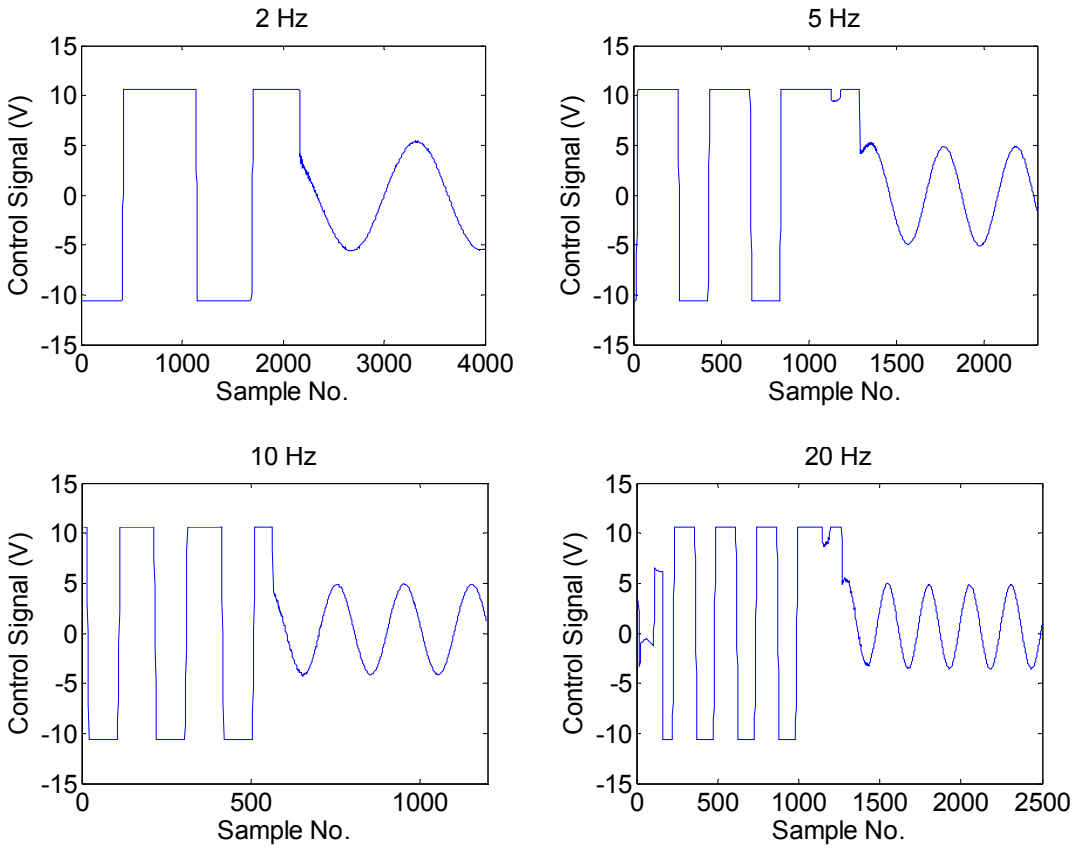

Figure 5.23 Actuating signal from PI controller for varying frequencies

Figure 5.22 and figure 5.23 demonstrate how the control loop works to reduce load disturbance in the reference interferometer. In order to gauge its effectiveness in more quantitative terms an experiment was carried out similar to the previous one in which the measurement mirror was sinusoidally displaced at various frequencies. The peak to peak displacement was approximately 300 nm. At each frequency the free-running peak to peak amplitude, V_f and stabilised peak to peak amplitudes, V_s were recorded. The ratio of these gives the effective attenuation at each frequency where,

$$\text{Attenuation (dB)} = 20\log_{10}\left(V_f / V_s\right) \qquad (5.32)$$

Figure 5.24 shows the results of the experiment in graph format. The trend is of steadily reduced attenuation with increased frequency as anticipated in the analysis in section 5.4.4.

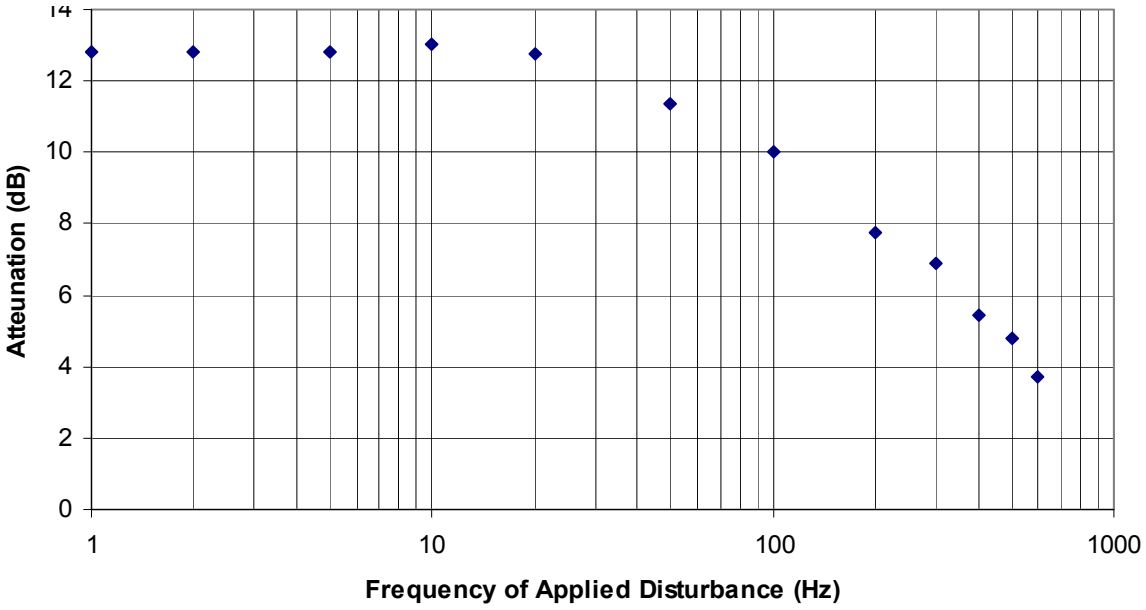

Figure 5.24 Attenuation of sinusoidal disturbance with increasing frequency

This is an important result which verifies the possiblility of stabilising a fibre interferometer using a reference interferometer operating at a separate wavelength. The magnitude of the attenuation represents the effectiveness of the disturbance rejection. The flattening of the response curve at lower frequencies is likely to be due to the noise floor of the interferometer and control loop being reached. Theoretically the response should continue to rise as the frequency goes down.

5.6.3 Measurement Interferometer Disturbance Rejection

It would appear from experimental results in the preceding analysis that the reference interferometer is stabilised by the control loop and that the effectiveness of this stabilisation is, as anticipated, dependent upon the disturbance frequency. It is also necessary however to determine the long term stability of the system and the peak to peak disturbance that might be anticipated. Long term stability in this sense is the stability over a time period of more than one measurement cycle. It is also vital to

assess the quality of the disturbance rejection upon the measurement interferometer, which is what we are ultimately trying to stabilise with the multiplexed interferometer method.

In order to assess the performance the interferometer apparatus was set up on a vibrationally isolated optical table. In this way most of the environmental perturbation can be attributed to air turbulence and temperature drift and as such remained fairly constant in magnitude across the experimental period. The outputs of the measurement and reference interferometers were both sampled at 1 kHz for 6 seconds. This was performed with the control loop first disabled then enabled. At the beginning of each sampling period the PZT was oscillated over a full fringe to determine the visibility. Figure 5.25 shows the results of the experiment, the fringe visibility is clearly seen in the far left hand side of each graph.

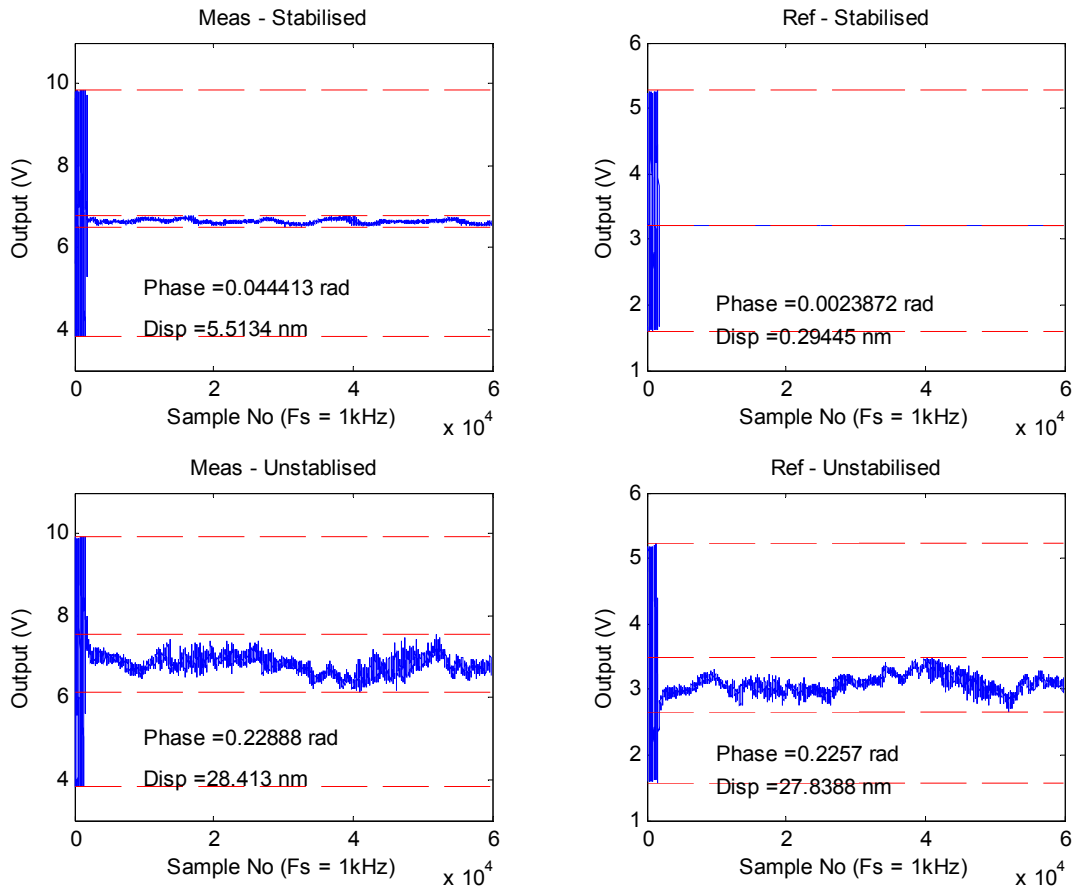

Figure 5.25 Simultaneous measurements of reference and measurement outputs over a 6 second period with active stabilisation on (upper) and off (lower)

5.6.4 Absolute Displacement Accuracy

The aim of this experiment was to determine how accurate the MFI was in terms of absolute displacements. In order to determine this it was necessary to be able to accurately create a known displacement and then subsequently measure it. For the purposes of this a PI-721.CDQ closed loop PZT operated with a PI-E661 controller was obtained upon which the measurement mirror was placed. This high accuracy PZT uses a capacitance sensor and closed loop control to create translations to a resolution of 0.5 nm with a repeatability of 5 nm (Physik Instrumente 2008, 2009b).

The high accuracy PZT was used to move the measurement mirror in 50nm steps over a 250 nm range. The profile of mirror surface was then scanned after each step. The height data for each step measured is shown in figure 5.26.

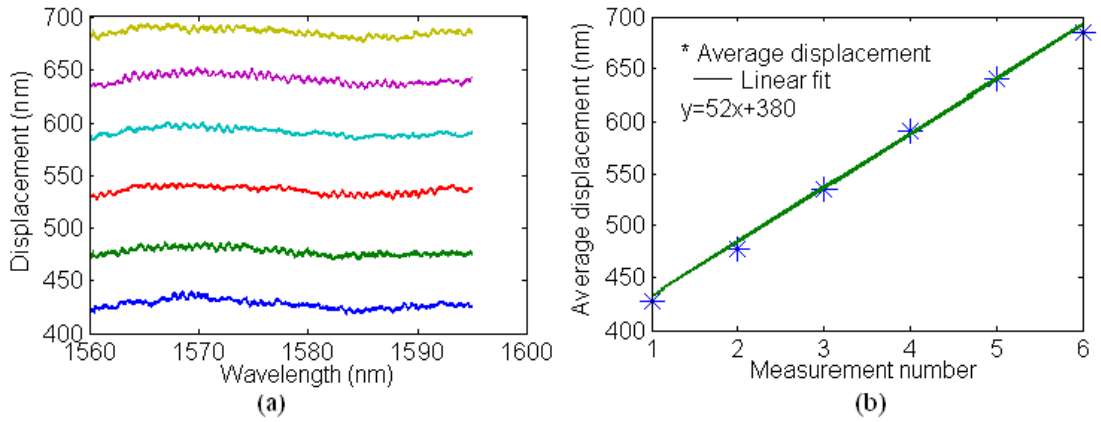

Figure 5.26 Recorded displacements of measurement mirror by MFI and a linear fit of the results

Figure 5.26 also shows the mean value of the surface displacement of each consecutive step and the linear fit for the data, the standard deviation of the measurement data being 4.1 nm.

The same profile of the mirror surface was again measured five times but this time without any stepping of the measurement mirror. The resulting profiles can be seen in the upper part of figure 5.27. The time between measurements was approximately 20 seconds due to lack of full software automation. The peak to peak variation in height value for each profile point was then calculated in order to gauge the repeatability possible. This is shown in the lower trace of figure 5.27.

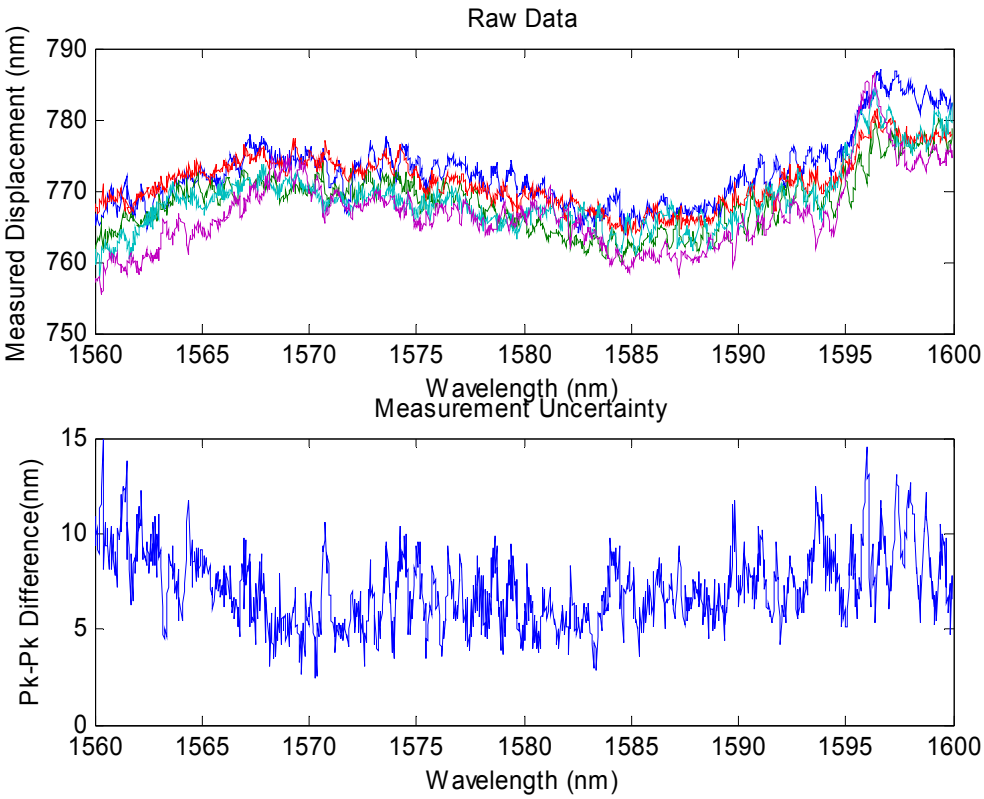

Figure 5.27 Multiple measurements of a flat mirror

What is clear from figure 5.27 is that there appears to be some drift between each profile taken. The peak uncertainty is approximately 16 nm.

In figure 5.28 each of the raw profile measurements were centred around their mean value, thus removing any DC offset. The peak to peak uncertainty now appears improved at around 11 nm besides an obvious spike of 16 nm at a wavelength of about 1596 nm.

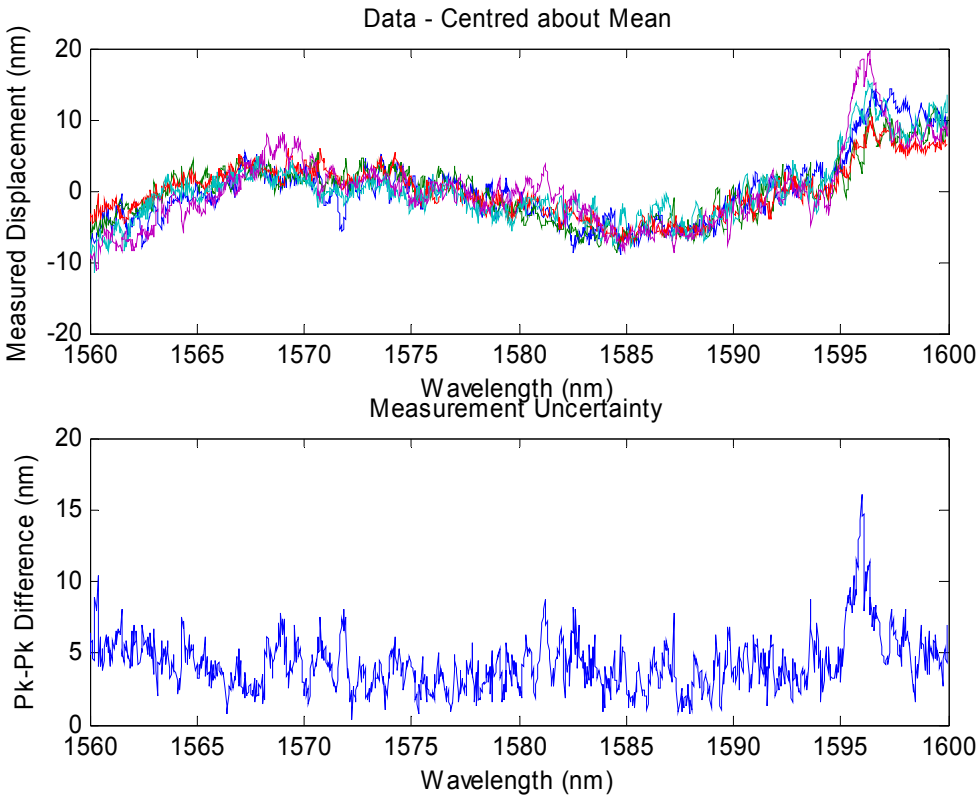

Figure 5.28 Multiple measurements of a flat mirror with DC offsets removed

5.6.5 First Step Height Measurement Result

Although the response of the measurement interferometer is less than ideal it is still good enough to contemplate using the apparatus to perform an actual surface measurement. The interferometer showed a peak to peak uncertainty of 16 nm, while the specification given in section 5.1 required less than 6 nm (1 nm rms). With this aim in mind, a step height sample was obtained to see if the interferometer could distinguish a step feature.

The sample was a glass slide which has raised regions produced by etching away a deposited material layer. A photograph of the sample is shown in figure 5.29.

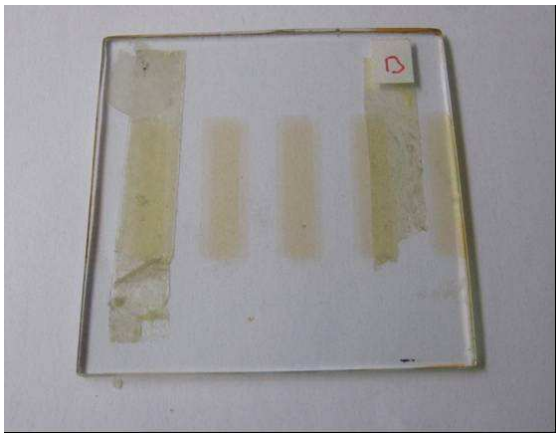

Figure 5.29 First step height artefact

The sample was then placed in the multiplexed fibre interferometer and the phase measurement routine run. The results are shown in figure 5.30.

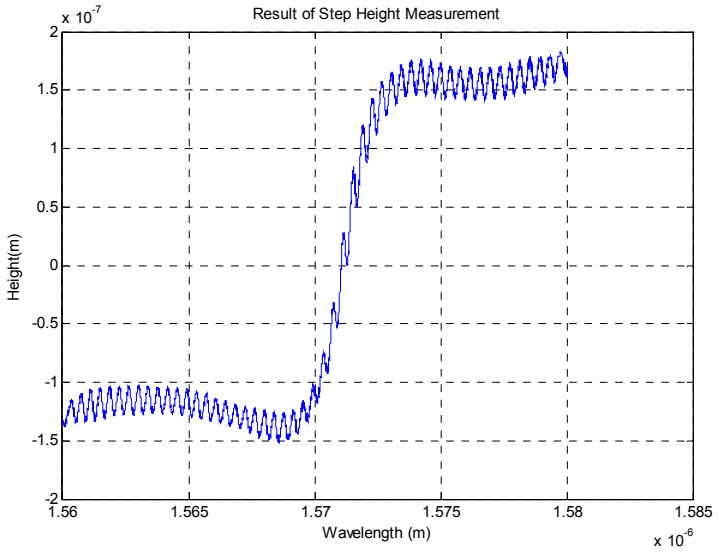

Figure 5.30 Measurement result from MFI

The actual step height recorded is appears to be approximately 0.31 μm as measured by the fibre interferometer. The step height appears to show quite severe oscillation as the wavelength is scanned. This oscillation is approximately 30 nm peak to peak which is clearly a lot larger than the measurement uncertainty derived in section 5.6.3. This leads to the conclusion that it must be related to the properties of the sample.

5.6.6 Second Step Height Measurement Result

The oscillation seen in the sample in the preceding section suggests the instrument is not capable of measuring some sample types. Here it appears that the optical transparency of the material created an secondary etalon. Because of this difficulty, it was decided to investigate another step height sample, this time a sample of various step heights created by an unknown metallic deposition upon a silicon substrate. A photograph of the sample is shown in figure 5.31.

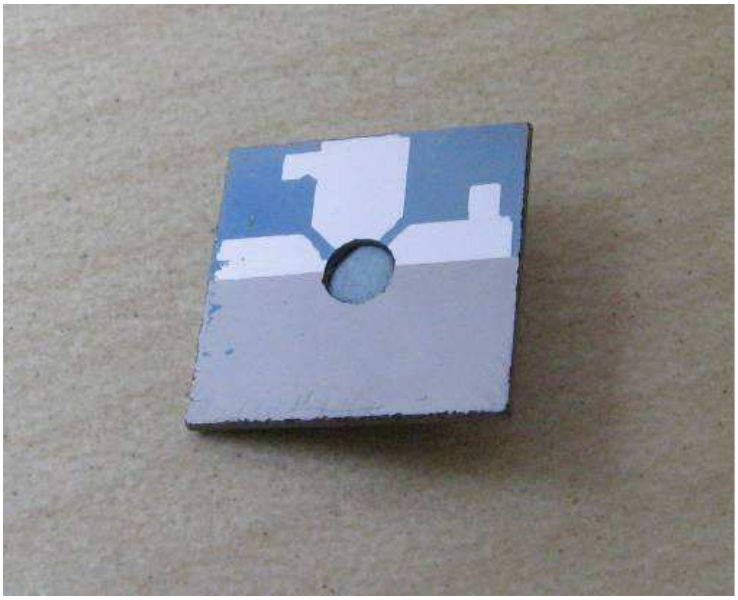

Figure 5.31 Second step height artefact

Examination of the photograph shows that the pattern of the metallic deposition upon the silicon substrate (black) in the upper horizontal half of the artefact. The lower half of the sample as pictured was cold chrome coated to ensure a homogenous surface. The experiment carried out in this section was carried out prior to the cold chrome coating and in fact the sample is 4 fold rotationally symmetric about the central hole. A visible pit defect in the upper left quadrant enabled the orientation of the artefact to be easily determined however.

This experiment was carried out to determine the ability of the system to take measurements in the face of induced disturbance. A step height sample measured with the system. A large scale 50Hz sinusoidal disturbance of 750nm peak to peak was applied to the measurand using a PZT aligned so that the oscillation was along

the optical axis. Such a disturbance accounts for approximately a full fringe of disturbance around the operating wavelength and as such would completely obscure any height data obtained in any uncompensated interferometer.

The step height was first measured by the MFI with no disturbance applied and the resultant phase profile is shown in figure 5.32. It was then measured again with the disturbance applied to the measurand; the results are shown in figure 5.33.

Due to the fact that the phase stepping and the active vibration compensation are both controlled by the same closed loop feedback, it was impossible to make a measurement without also having the vibration compensation active. It is therefore not possible to show the worst case result of the disturbed step height sample with no vibration compensation present.

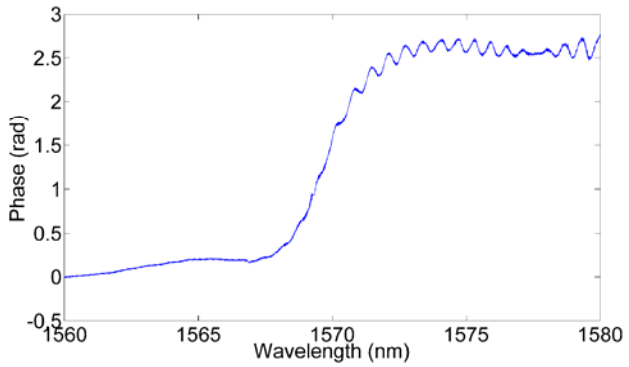

Figure 5.32 Scanned step height with no disturbance

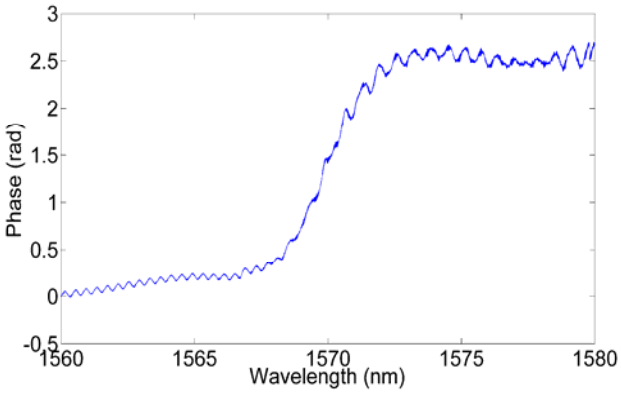

Figure 5.33 Scanned step height with 750nm peak to peak induced disturbance

The peak to peak uncertainty induced by the oscillation is clearly seen on the lower (lefthand) part of the step. It is approximately 0.1 rad which equates to 12 nm at a measurement wavelength of 1560 nm. The oscillation seen on the upper (righthand) appears to be part of the surface texture as it appears without the induced oscillation.

5.6.7 Discussion

5.6.8 Reference Interferometer Disturbance Rejection

This result suggests that the closed loop control system worked as anticpated by the theory presented in section 5.4.3, and it was feasible to reduce the effect of external vibrations using a PZT. The performance is actually slightly better than that derived by the theory though the discrepancy is well within reasonable limits considering some of the assumptions made about unknown parameters used in the control loop. The theory in section 5.4.4 suggested a 3 dB crossover frequency of 681 Hz compared with the experimental result of 800 Hz. This is possibly due to a too conservative estimate of slew rate which was taken for a movement over a full fringe (775 nm).

5.6.9 Measurement Interferometer Disturbance Rejection

With respect to figure 5.25, the unstabilised disturbances seen in both reference and measurement interferometers are of a similar magnitude. However upon activation of the control loop, the stability of the reference interferometer is substantially better than that of the measurement interferometer by a factor of approximately 20. Clearly this is a somewhat worrying result as it appears there must be some lack of commonality between the two paths.

It is clear that the measurement interferometer is much less stabilised than the reference interferometer which is of major concern. The reference interferometer shows 0.3 nm peak to peak disturbance while the measurement exhibits 5.5 nm. Intuitively it would seem unlikely that this instability could be caused by the non-common path section of the optical probe being as the travel is almost exclusively in air and thus the only cause would be air density variation.

5.6.10 Absolute Displacement Accuracy

Figure 5.26 from this experiment seems to further confirm that the reference interferometer is not stabilising low frequency drift in the measurement interferometer. The 50 nm steps appear to drift with a standard deviation of 4.1 nm averaged over all measurements. This confirms that the MFI is able to determine absolute displacements to a certain degree of accuracy but there is still a problem with drifting.

The second set of results shown in figure 5.27 and figure 5.28 for the repeated measurement also shows some variation. The effect of aligning each measurement by removing the DC component improves repeatability, so higher frequency variation would seem to be less of a problem. This could be explained by the fact that naturally occurring vibrations tend to diminish with frequency however.

5.6.11 First Step Height

This measurement confirmed that it was possible for the MFI to discern a step feature of approximately 310 nm with an uncertainty of 30 nm. However there are severe oscillations apparent on the measurement in figure 5.30. It is likely that these are a result of a Fabry-Perot etalon set up between the front and back faces of the glass slide. Because of the lack of tight focus on the beam, the depth of field is also large, thus the beam reflects from both the front and back faces of the slide. Index matching gel was smeared onto the back of the slide to try and reduce the back reflection from the rear air-glass interface and disperse it. This reduced the amplitude of the effect by about 75%, which confirms the origin. The non-optimised beam optics will compound this problem, a more tightly focused beam spot will have a reduced depth of field will be reduced thus reducing this problem.

Figure 5.30 also shows the presense of distortion in the steps which are clearly quite pronounced. This could be attributed to a slight mis-focus of the objective lens on the diffraction point at the grating. This yields a diverging (or converging) beam incident on the sample causing a change in optical path length over the span of the surface. The result is a slight arch (or dip) across the phase map. This can be cleared up by more careful attention to the collimating lens position. It is also possible that it is due to a longer period modulation caused by another etalon created somewhere in the system.

5.6.12 Second Step Height

The value of the step height as determined by the MFI was approximately 0.28 μm. The main aspect of the experiment was to determine if a measurement could be made in the face of a purposefully induced vibration of the measurand surface. In figure 5.33 the residual disturbance is clearly present especially on the lower (left) side of the step. The peak observed variation between the stabilised and un-stabilised measurements was approximately 33.7 nm, corresponding to a 13.4 dB reduction of induced disturbance in the final measurement result. Although it is not possible to show the effect of the full fringe modulation it should be clear that it would have completely obliterated the measurement data. In this sense the experiment is a success, although some further improvement in the effectiveness of the disturbance rejection is certainly desirable.

5.7 Conclusion

The experimental results show some evidence that the technique of multiplexing twin fibre interferometers can feasibly be used in a surface measurement application. It was seen that 50 nm displacements where discernable with an uncertainty of 4.1 nm rms. The disturbance rejection of the control loop did dramatically reduce the effects of large induced vibration on the measurand and enabled a measurement to be taken were previously this would have been impossible. Table 5.3 summarises the outcome of the experiments and compares the realised performance with the original specification outlined in section 5.1.

Parameter	Original Specification	Instrument Performance
Measurement Time	< 60 s	8 s
Vertical Uncertainty	< 0.5 nm RM (3 nm pk-pk)	11 nm pk-pk
Vertical Range	> 0.5 μm	0.775 μm
Lateral Range	Diffraction Limited	~3 mm
Lateral Resolution	Diffraction Limited	Untested

5.3 Comparison of instrument performance against specification

It appears that the only area where an improvement needs to be made is the uncertainty. The results of the experiments show there is operating point drift in the measurement interferometer, which appears to be a low frequency phenomenon and occurs even when the disturbance rejection is enabled. This is contributing to the magnitude of the measurement uncertainity. Higher frequency disturbance appears to be better attenuated which is at odds with the control theory analysis given in section 5.4.4.

Secondly, it appears there are some issues with the step height samples being used. The first sample was deemed non ideal due to its transparent nature and the creation of an etalon between its front and back faces of the glass substrate.

The main concern is the presence of low frequency drifting which is contrary to what is anticipated for the closed loop vibration compensation. Further investigation is required to determine the source of this drift.

Finally, the performance of the PZT based disturbance rejection system is somewhat limited in its upper frequency due to the dynamic limitations of the PZT actuator used. It would be of great benefit to increase the performance by improving the frequency response of the actuator in some way. This would allow more effective compensation of higher frequency disturbance.

6 Noise in Fibre Interferometers

6.1 Introduction

Noise in any form of instrumentation is of upmost importance because it defines the baseline for performance, both in terms of repeatability and resolution. The simple fact is that any noise, regardless of where it originates within an instrument, impinges directly upon the measurement result if it falls within the measurement bandwidth. The combination of all the noise sources defines the lower limit of repeatability for any instrument. To attain the necessary repeatability, the major noise sources must be identified and then methods must be implemented to reduce their magnitudes until the desired performance is obtained. Of course this is often much easier said than done.

This chapters aims to develop a comprehensive study of the myriad noise sources that affect a multiplexed fibre interferometer; this includes those common in all electro-optical instruments as well as some specific to phase-shifting fibre interferometers.

Each of the predominant noise sources will be described, and a theoretical treatment of the mechanisms involved will be given. In turn, the theory will be used to try and quantify the effect of each noise source on the final instrument, yielding a transfer function for the system as a whole. A theoretical baseline will be derived for the best case performance of the instrument in terms of both sensitivity and repeatability and this will be compared to the experimental results obtained.

Finally, in light of a theoretical study of noise sources, the strategies used in reducing the effect of the noise on the final instrument are described in detail.

A brief examination of noise theory is given in Appendix C.1. This provides background for the analyses carried out in this chapter.

6.2 Noise Categories

With such a large range of possible sources of noise in a fibre interferometer, it makes sense to try and group them in some form of organised fashion. Noise sources can be grouped in several ways; the mechanism of effect, severity, origin or point of

entry in an instrument for instance. Here a two tier approach will be taken; the sources first being split by origin and then by mechanism.

From the point of view of origin, noise sources may fall into two fundamental categories; external noise and intrinsic noise.

6.2.1 External Noise

These noise sources are derived from the environment surrounding the instrument. They act upon the instrument in such a way that unwanted signals are produced at the output of the instrument. Important examples of external noise in the context of fibre interferometry are temperature fluctuation and mechanical vibration.

6.2.2 Intrinsic Noise

This originates from within component parts that make up the instrument itself. Such examples are relative intensity noise (RIN) in laser sources, shot noise at detectors and thermal noise generated by electronic components.

With these two categories in mind we can begin to separate the major noise sources likely to occur in a fibre interferometric system and analyse how each conspires to reduce the accuracy of a measurement taken with an instrument. The noise mechanisms fall into 3 basis categories.

6.2.3 Electronic Noise

This describes all noise sources emanating from electronic components in the instrument. Such sources include Johnson noise in resistors, shot noise from detectors and amplifier noise. These noise sources are generally fairly straightforward to analyse and are generally quantifiable. Quantisation noise created by analogue to the analogue to digital conversion is generally lumped into this category even though it is not strictly a physical effect.

6.2.4 Optical Noise

This area of noise falls into two categories; those that are easily quantifiable (laser RIN noise, source phase noise) and those which are produced due to external noise sources such as etaloning and polarisation state evolution. The severity of latter

category cannot feasibly be determined by theoretical analysis as it is dependent on external influence. We may however examine the mechanisms and attempt to define their effects theoretically. Empirical work on real instruments can then provide an idea of the magnitude of these sources.

6.2.5 Mechanical Noise

Much of this area is crosses over within the external noise sources section, as the effects of vibration and temperature are the sources. However we must also consider how the structures of an instrument can lead to resonant behaviour thus effectively amplifying any environmental effects. The effect of temperature induced expansion can also have an effect on measurement instrumentation. In addition, some of these effects are fibre specific.

6.2.6 Summary

All the noise sources types covered in the above section are examined in detail in Appendix C.2. Here the various specific types of noise, their origins and likely magnitudes are analysed. There likely effect upon the operation of the instrument are considered. One particular noise source however is reserved for detailed discussion in this chapter, that resulting from polarisation evolution. This is because it is at the heart of the instability found in the instrument in chapter 5.

6.3 Polarisation Instability

Polarisation instability in optical fibre is a major problem for interferometric applications as it causes instability in the intensity output for any given phase which means that the intensity locking method attempted in the instrument in chapter 5 shows some low frequency drift at the output. State of polarisation (SOP) evolution in individual fibre arms results also results in the reduction of fringe visibility at the output causing signal fading and lessening SNR.

This section outlines the causes of SOP evolution in optical fibres and describes the effects on interferometry. Contemplation of various avenues for mitigating these effects is also presented.

6.3.1 Modelling SOP Evolution in Optical Fibre using Elliptical Retarders

A further optical component shall now be considered, the elliptical retarder, so called because its eigenvectors are both elliptical SOPs. Such a component can be viewed as the combination a linear retarder followed by a rotator (see section 3.5.3). Such a device is of great importance to the study of fibre interferometers because it may be used to describe the overall SOP evolution of light travelling down an optical fibre. Any length of optical fibre may be viewed as a single elliptical retarder for this purpose.

Examination of an all-fibre Mach-Zehnder fibre interferometer provides a suitable base for discussing how SOP evolution in optical fibre occurs and how this affects fringe visibility.

For an optical fibre with a perfectly cylindrical core, the two polarisation states are degenerate and thus the SOP remains constant. However, for real optical fibres, strains induced in the fibre core by bending, vibration, temperature change as well as manufacturing irregularities result in birefringence in the fibre. This in course results in a change in the SOP of the input light over the length of the fibre. This SOP change is impossible to predict as environmental factors constantly alter internal stresses in the fibre core and thus the birefringence. The overall stress induced birefringence over a length of optical fibre may be modelled by an elliptical retarder of an orientation, R with a phase rotation of magnitude, Ω. So for a given length of fibre the total overall (lumped) birefringence may be represented by a single elliptical retarder (Simon & Ulrich 1977). We note at this point that the operator $R(\Omega)$ is a Mueller matrix operator, which transforms a Stokes vector to describe the changed SOP.

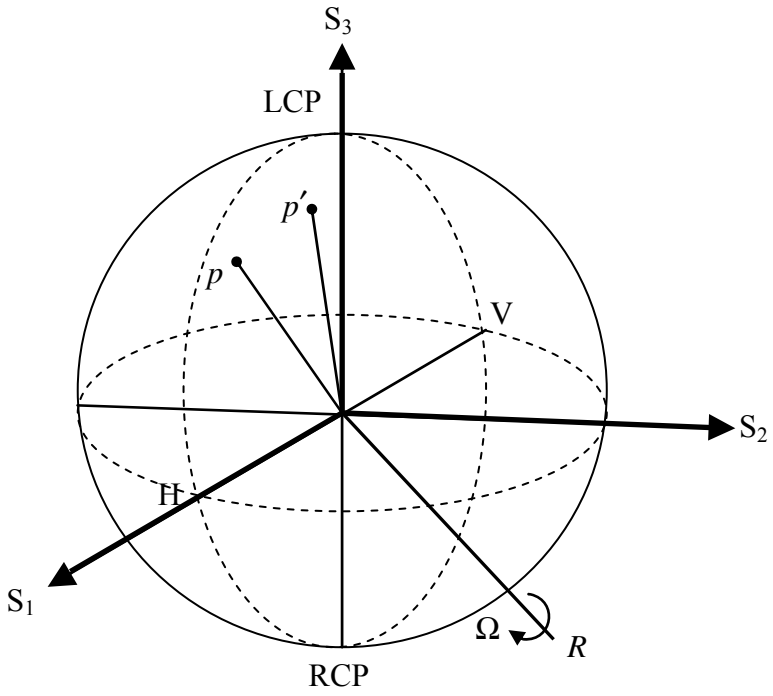

Figure 6.1 Poincaré sphere representation on an elliptical retarder and its effect on an SOP, p

6.3.2 Fringe Visibility Dependence on SOP Evolution

The output fringe visibility of the interferometer output is dependent in the relative SOP of the light in each arm upon recombination. This relationship is governed by,

$$V = \cos\eta \tag{6.1}$$

Where V is the visibility (between 0 and 1) and 2η is the angle of the great circle subtended by the two output SOP vectors, C_r and C_m when they are plotted on the Poincaré sphere. This is shown in figure 6.2.

The position of each vector on the Poincaré sphere is dependent on the birefringence experienced through their respective interferometer arms, $R_r(\Omega_r)$ and $R_m(\Omega_m)$. So, as these birefringences vary with environmental perturbation, so do the vectors C_r and C_m, and thus the visibility.

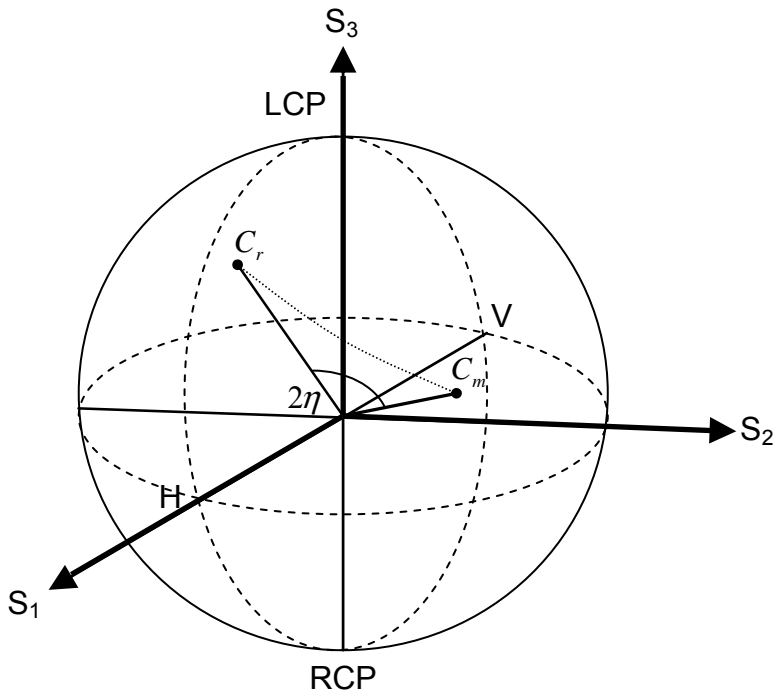

Figure 6.2 Poincaré sphere representation of the SOPs in an interferometers arms

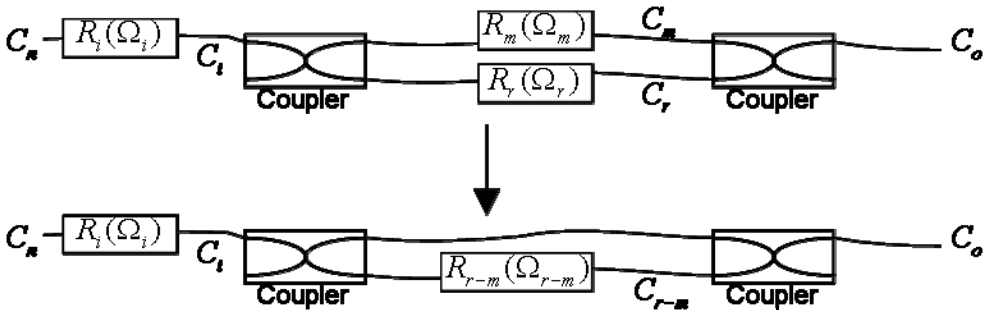

Figure 6.3 Lumping two birefringences into one differential birefringence

It has been shown that the two birefringences can be lumped together as a single differential birefringence $R_{r-m}(\Omega_{r-m})$, the model is shown in figure 6.3. In the interferometric setup described in chapter 5, the interferometer arms are not contained in fibre, they are in free space so that, $R_{r-m}(\Omega_{r-m})$ must remain fixed to a good approximation. However in the case of the all-fibre interferometer discussed in chapter 7, $R_{r-m}(\Omega_{r-m})$ will also be random and time varying. We should then consider the most general case where both the input SOPs and the differential birefringences vary.

The visibility variance for an interferometer with a time varying differential birefringence, $R_{r-m}(\Omega_{r-m})$ can be shown using circular geometry to be,

$$V = \cos\eta = \sqrt{1-\sin^2\theta\cdot\sin^2(\Omega_{r-m}/2)} \tag{6.2}$$

Where θ is now the angle subtended by the great circle joining the input SOP vector, C_i and the differential birefringence, $R_{r-m}(\Omega_{r-m})$. The relationship is shown on figure 6.4.

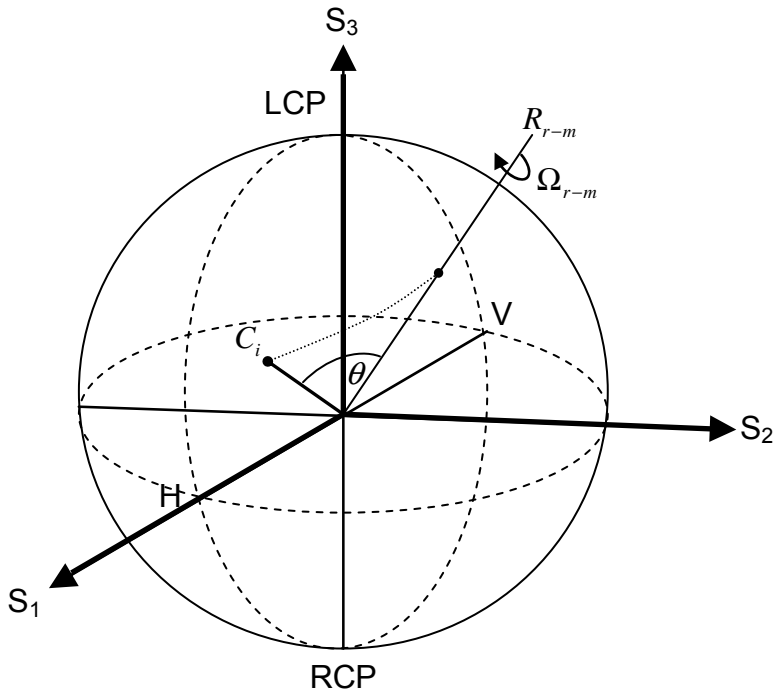

Figure 6.4 Poincaré sphere representation of the input SOP and a differential birefringence

It is immediately apparent from (6.2) that as long as $|\Omega_{r-m}| \neq \pi$ (modulo 2π) the visibility, $V > 0$. The maximum visibility, $V_{\max} = 1$ occur when the input light vector C_i makes an angle of 0 or π, that is it is aligned with the eigenvectors of $R_{r-m}(\Omega_{r-m})$. The minimum visibility, $V_{\min} = \cos(\pi/2)$ and occurs when C_i is orthogonal to the eigenvectors of $R_{r-m}(\Omega_{r-m})$ that is, θ is $\frac{\pi}{2}$ or $\frac{3\pi}{2}$.

It may also be shown that the sensitivity of the visibility to input SOP fluctuation is at a minimum as C_i is aligned with the eigenvectors of $R_{r-m}(\Omega_{r-m})$. This is important

as it represents two eigenmodes at which the visibility is at a maximum yet the sensitivity to disturbance is at a minimum. When C_i approaches orthogonality with the eigenvectors of $R_{r-m}(\Omega_{r-m})$ visibility sensitivity is increased (Kersey et al. 1990). The results suggest that by controlling the input SOP it should be possible keep the visibility stable and at a maximum. However, in the case of the all-fibre interferometer in chapter 7 the eigenvectors of $R_{r-m}(\Omega_{r-m})$ are constantly changing and as such it would be necessary to control the individual SOPs of the input and the two interferometer arms.

6.3.3 Practical Observations of Polarisation Effects

A experiment was conducted in order to observe the effect of SOP evolution in optical fibre on the output of a fibre interferometer. The reference arm path length was modulated at several kHz using the PZT mounted mirror. The modulation was of such a magnitude that oscillated the output over a full fringe. In this way it was possible to determine the interferometer visibility. The output of fibre interferometer was sampled over a 10 second period while at the same time the input fibre lead was physically manipulated. The output of the fibre interferometer is shown in

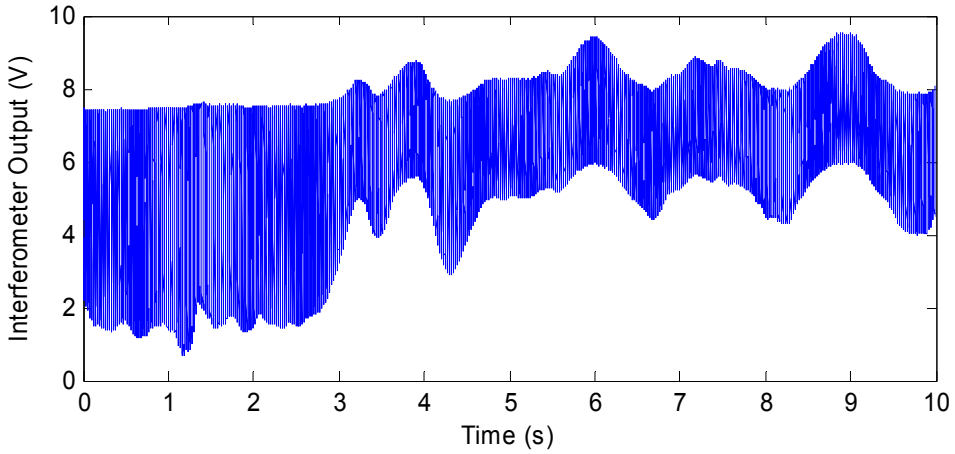

Figure 6.5 Fringe visibility variance due to SOP evolution

The output clearly shows both visibility and magnitude variation as the fibre is manipulated. The effect is amplified over what might be reasonably expected from normal interferometer operation, but it is apparent that this presents a serious problem for the use of intensity feedback quantity for closed loop stabilisation.

6.3.4 Overcoming Polarisation Effects in Optical Fibre Interferometers

The preceding results suggest that in order to increase the performance of a given fibre interferometer one must ensure that the sensitivity to environmental is disturbance is reduced as much as possible and that the visibility is maximised, resulting in a reduced sensitivity to any perturbation. Several methods have been researched and they are briefly mentioned in the following section.

The Lefèvre Polarisation Controller

The simplest method of controlling polarisation in optical fibres is to use the so called Lefèvre polarisation controller. This method uses the fact that a coiled fibre exerts a bend induced birefringence due to the elasto-optic properties of silica. The radius, R required to produce the required birefringence can be calculated by,

$$R = 2\pi a r^2 \frac{N}{\lambda / m} \qquad , \qquad m > 0 \tag{6.3}$$

Where a is a coefficient describing the ratio of the refractive index difference between the induced fast and slow axes, $a \approx 0.133$ for silica fibres. N is the number of turns of the coil over a radius of r. λ is the wavelength of the incident light and m is set to apply the required path difference between the fast and slow axes. Thus setting $m = 2$ we obtain a half wave plate, setting $m = 4$ provides a quarter wave plate.

By creating three fibre coils, equating to a quarter wave plate (QWP), half wave plate (HWP) and another quarter wave plate can create a polarisation controller that can take any input SOP and convert to any output SOP. The method is entirely analogous to the equivalent type of controller in classical optics. The first QWP is rotated so that the input SOP is converted to LP. The HWP is then used to rotate the LP light to the desired angle, where the rotated angle if twice that of the physical coil angle.

The system has limitations as it is not readily controllable using an automated method and is quite bulky. Nevertheless it is cheap and is of use for initially acquiring a certain SOP from an optical fibre. For systems where visibility is slowly varying, it is sometimes enough to adjust the SOP to gain maximum visibility and it will remain stable enough for a time.

Fibre Squeezer Method

Squeezing an optical fibre induces birefringence in the deformed length because of the elasto-optic effect, as in the previous method. By setting up several squeezing actuators along a fibre at differing azimuths one can induce birefringence in order to control the SOP of light in the fibre. Although originally the squeezing actuators were electromagnetic devices, commercial versions have tended to use piezoelectric methods which provide a faster response time. In its simplest form, the system uses two squeezers one orientated so that its force is applied at an azimuth of 45° and the other at 0° along a length of fibre. A small amount of the output light is tapped off using a beamsplitter of some type and two orthogonal polarisation states are separated; this could be done with a Wollaston prism for example. The intensities of the two orthogonal polarisation states are monitored using photodetectors, providing the error signals used to control the squeezers. These intensities map as distances along the x and y axes respectively on the Poincaré sphere.

Clearly there control voltage limits on the fibre squeezers as well as a physical limit of force that may be applied to a fibre before damage is incurred. This means that the SOP evolution cannot be continuously tracked with two squeezer systems, there will be discontinuities as the squeezers are reset.

Continuous tracking has been made possibly however by the use of three and four squeezer systems and there are several variations on this theme in the literature (Heidrich et al. 1998). Benefits of the fibre squeezer method are the very low levels of insertion loss and back reflection as the devices are all-fibre.

The $LiNbO_3$ Polarisation Controller

The Pockels effect which is strongly present in lithium niobate ($LiNbO_3$) waveguides can also be harnessed to produce a very fast tracking polarisation controller, unaffected by mechanical time constants. Generally a $LiNbO_3$ polarisation controller is formulated on an analogous scheme as the QWP-HWP-QWP method as used by the Lefèvre manual polarisation controller earlier. It is possible to create a compact, integrated optic device whereby a voltage applied across electrodes situated on either side of the waveguide channel can create the same affect on an input SOP as a waveplate. The length of the channel over which the effect occurs determines the

induced phase shift to produce either a QWP or a HWP. 3 pairs of electrodes of the required length may be placed along the waveguide channel to provide the QWP-HWP-QWP electric fields.

It has been shown that by holding the two outer QWPs with their fast axes orientated in a crossed position (by applying suitable offsetting voltage), then endless (i.e. no resetting required) polarisation control attained with a relatively simple control algorithm. Only two factors require control; that is the azimuth of the two crossed QWPs and that of the HWP. The system basically produces an elliptical retarder of phase rotation, $\Omega = \pi$ which may take any orientation desired (Heismann 1994).

The $LiNbO_3$ polarisation controller generally has response times of $< 1\,\mu s$ and requires a less complicated control algorithm than its mechanical counterpart making it much faster in operation and able to track SOP changes due to harsh mechanical manipulation. Its main disadvantage is the relatively high insertion loss associated with it, 2-3 dB compared to around 0.05 dB for an all-fibre based squeezer based method.

Polarisation Scrambling

Polarisation scrambling has been shown to be effective in reducing the SOP variation in interferometers as a result of input fibre manipulation. Here, the SOP of the light is changed at very high frequency (100's of kHz) and appears depolarized for longer time constants. Scrambling may be done in a variety of ways using integrated optics similar to the polarisation controller discussed in the previous section. All fibre methods based on fibre squeezers are also commercially available and feature very low insertion loss. The method can reduce input fibre induced polarisation disturbance by 35 dB at the cost of slightly reduced visibility at the output. However the effect of SOP evolution in the arms (the migration of $R_{r-m}(\Omega_{r-m})$ over the Poincaré sphere) still remains unattenuated. Thus the use of a polarisation scrambler only provides a complete solution if the arms of the interferometer can be fixed and isolated from disturbance (Kersey et al. 1990).

Faraday Rotator Mirrors

This technique involves using a 45° Faraday rotator in front of the mirror at the end of an interferometer arm to rotate the polarisation state of the reflected beam at 90° to

the input state. This in effect causes the polarisation state to 'unwind' on its return journey. With a Faraday rotator mirror in each arm, it is possible to maintain a constant visibility of close to unity regardless of the changing SOP in the fibre arms. This technique suffers from the imperfections in couplers used, specifically slight birefringence and non-exact coupling ratios. Furthermore, it is impossible to place a Faraday Rotator Mirror in the measurement arm of the interferometer since the measurand is the reflector (Ferreira et al. 1995).

High Birefringence Fibre

The final common method for reducing visibility dependence on the polarisation scrambler is to use high-birefringence (also known as polarisation maintaining fibre). Such fibre has an elliptical core resulting from induced stress at manufacture. This stress is induced by rods of differing material inserted in the cladding layer. Various rod constructions are available, e.g. bowtie, panda etc. but they all essentially perform the same function; to create a core with an elliptical cross-section. The core is seen exhibit very high birefringence on account of its elliptical shape. It has two axes, which have different propagation velocities, these being called the fast and slow axes. The separation of the two polarisation modes prevents them cross-coupling and the polarisation of the light throughout the fibre is maintained as long as the input SOP is precisely aligned with one of the fibre axes. The performance of polarisation maintaining fibre is measured on the extinction ratio, ER between the fast and slow axes.

$$ER = 10\log\left(\frac{P_{\max}}{P_{\min}}\right) \tag{6.4}$$

Where $P_{\max}$ and $P_{\min}$ are the maximum and minimum intensities respectively obtained from a rotated linear polariser at the output of a length of polarisation maintaining fibre. Assuming careful alignment of the fibre core with the input SOP, extinction ratios of up to 35 dB may be obtained from polarisation maintaining fibre, however 20 dB is a more practical value (Hobbs 2000, ch. 8).

It is also possible to obtain all the components required for the interferometer, specifically couplers, circulators in a polarisation maintaining form also. These components are in general much more expensive than there equivalent single mode

types and the requirement for the exact alignment of the polarisation state could be problematic is the measurand surface causes the alteration of the polarisation state in anyway.

Rapid Phase Shifting

The physical mechanisms for SOP evolution in single mode fibre are similar to those of environmental effects. Unlike environmental effects, there magnitude or rate does not scale with fibre length. Hence it is found SOP variation generally occurs at low frequencies. With that in mind it is feasible to consider whether it may be possible to execute the phase shifts at a fast enough rate that the intensity error induced because of the SOP evolution can be neglected. Indeed, with a fast enough phase shift it would also be possible to minimise the effects of any environmental disturbance leading to the possibility of open loop phase shifting. Of course such a technique would only be feasible if a fast enough phase shifting actuator were available. Chapter 7 considered the operation of an MFI with an electro-optic modulator as a very fast frequency response in which a rapid phase shifting method is applied.

6.4 Discussion

As can be seen by the sections covered in this chapter and appendix C, the number of noise sources that impinge upon a fibre interferometers performance are numerous and varied in both their origins and magnitudes. The list of noise sources contained within this chapter is by no means exhaustive, but from the point of view of instrument design, only those sources likely to be of such a magnitude to limit accuracy are in need of consideration.

It is worthwhile to recap the analysed noise sources and group them together along with their anticipated severity. This has been done in table 6.1.

Noise Type	Magnitude	Units	Type
RIN	76.1	SNR(dB)	1
Source Phase Noise	168.1	SNR(dB)	1
Intrinsic Fibre Phase Noise	23.48	μrad rms	2
Amplifier	109	SNR(dB)	3
Quantisation	62	SNR(dB)	3

Table 6.1 Summary of noise sources and their magnitudes

As has been shown in appendix C.4, the results between different noise types are not directly comparable as the severity of the effect differs for each noise type. In order to determine the effect of the worst case noise sources a simulation of the phase shifting algorithm was performed in which all noise types where applied. The worst case noise values for each noise type were taken from the table and used in the simulation. Once again a visibility value of 0.1 was used and full scale digitisation assumed.

This simulation combines those results obtained in Appendices C.2, C.3 and C.4 in order arrive at a total anticipated noise figure for a final measurement. Figure 6.6 and figure 6.7 show the simulation results and noise distribution respectively.

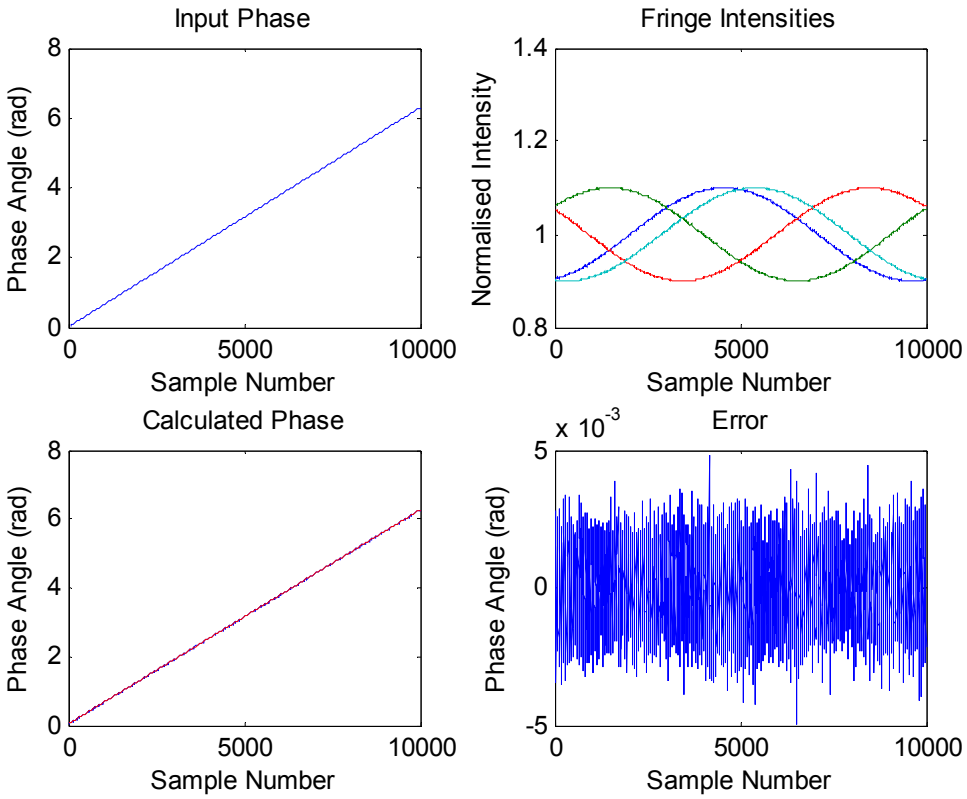

Figure 6.6 Estimated worst case noise on MFI from quantifiable noise sources

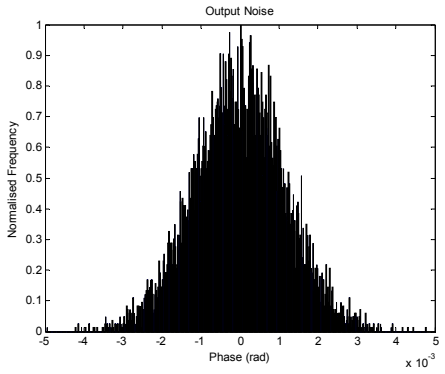

Figure 6.7 Output noise histogram

From the Gaussian distribution calculated rms value for the error is 0.006 rad. It is thus possible to consider that the peak to peak noise will be approximately 0.036 rad. This equates to a peak to peak error in the calculated height of 4.48 nm.

Bearing in mind that these are the theoretical minima and other unquantifiable effects such as etaloning and SOP evolution are not included in this analysis meaning that in reality this figure is most likely too generous. A rule of thumb is that the noise level

should be at the very most an order of magnitude lower than the required measurement resolution. However from table 6.1 it is seen that the quantisation noise is the limiting factor. Just increasing the resolution of the ADC converter to 16 bits would raise they SNR to above that contributed by RIN. The NI PCI-6221 DAQ card used in the first instrument for instance has an approximate SNR of 89 dB. This would suggest a noise level of 0.0012 rad rms or 0.8637 nm peak to peak with the device now being RIN noise limited.

One extremely important factor in the noise performance is the visibility of the output fringes. Table 6.2 shows the peak to peak noise in nm for a range of different visibilities for the RIN noise limited scenario discussed in the preceding paragraph.

Visibility	Noise (nm pk-pk)
0.1	0.8951
0.2	0.4778
0.5	0.1841
0.9	0.1087

Table 6.2 Effect of fringe visibility on output noise

It can be seen from table 6.2 that increasing the visibility causes an equivalent reduction in output noise. It is therefore vital that the visibility is kept to a maximum at all times. During the experimental work it was found that a working visibility of over 0.5 was easily maintainable.

6.5 Conclusion

The major sources of noise occurring in optical interferometers have been identified, and where possible quantified. Simulation was used to analyse the effects of the various noise types for a phase shifting interferometer. The Carré phase shifting algorithm was shown to slightly reduce the effects of type 2 and 3 noise. Type 1 noise such as laser source RIN however was found to be amplified.

The results suggests that the inherent limitation in the sensitivity of the instrument to make sub-nanometre measurement is currently RIN in the laser sources assuming all other instabilities such as etalon effects, polarisation instability and environmental

disturbance can be reduced to a low enough level is the RIN noise. The figures arrived at were purposefully conservative, all being worst case scenarios. For an average fringe visibility of 0.5, a peak to peak noise figure of 0.184 nm was derived. In order to reduce this any further it would be necessary to use RIN reducing techniques. This is however more than an order of magnitude less given for peak to peak repeatability of 3 nm given in the original specification in section 5.1. In conclusion there is no theoretical reason why the pecification cannot be reached provided that the instability caused by the SOP evolution is overcome.

The noise analysis in this chapter derives the minimum requirements for the interferometer in order for it to meet the specification. The results explain the limitations of the instrument described in chapter 5, which were determined to be mainly due to polarisation instability. The same results will be taken forward and used to explain the limitations concerning the instrument in chapter 7 which will be seen to be mainly due to the ADC used.

7 Rapid Phase Shifting Interferometer

7.1 Introduction

The MFI described in chapter 5 was shown to have potential for surface profiling using wavelength scanning and optical fibre. It suffered from several disadvantages however. The active stabilisation scheme appeared to be somewhat ineffective at low frequencies. The measurement interferometer exhibited a low frequency drift of 5.5 nm peak to peak which translated into a measurement repeatability of approximately 11 nm. This was shown in section 6.3 to be due to SOP evolution in the fibre which causes fringe visibility variation. This means that there is not a stable intensity to phase relationship and as such the stabilisation method is flawed at the low frequencies over which SOP evolution occurs.

Clearly a more stable feedback parameter is necessary if the interferometer is to be stabilised effectively enough for carrying out surface metrology. The ideal situation would be to use the phase of the interferometer as the feedback quantity since this is what we are trying to stabilise. This requires the use of phase shifting algorithms to calculate it and in order to carry this out for use in a real time control loop it would require an extremely fast phase shifting actuator.

The original specification as described in chapter 5 is shown below to recap.

Performance Target	Value
Measurement Time	< 60 s
Vertical Uncertainty	<0.5 nm rms
Vertical Range	> 0.5 µm
Lateral Resolution	Diffraction Limited
Lateral Resolution	Diffraction Limited

Table 7.1 Instrument specification

7.2 Rapid Phase Shifting Method

7.2.1 Overview

As mentioned in section 6.3 the fringe visibility and intensity variation arising from SOP evolution and polarisation dependent components in the interferometer arms is a relatively low frequency effect, with most of the energy being below 1 kHz. The novel idea introduced here is to perform the phase shifting extremely quickly in order to determine the phase before any significant movement of the operating point has occurred due to environmental disturbance or SOP evolution. This would in effect present a stable snapshot of the current phase of the interferometer. If the phase shifting could be carried out at sufficient speed it would be possible to use the phase as the feedback quantity by which to stabilise the interferometer. Figure 7.1 illustrates the concept of a rapid phase shifting method.

A mechanical shifted mirror mounted on a PZT is far too slow to contemplate using such a method. In addition the problems of non-linearities and hysteresis mean that the attainable open loop accuracy might well be problematic for stable measurement. What is required is a fast phase shifter that can supply open loop accuracy at very high speeds. This possibility lies in the form of an EOPM (electro-optic phase modulator).

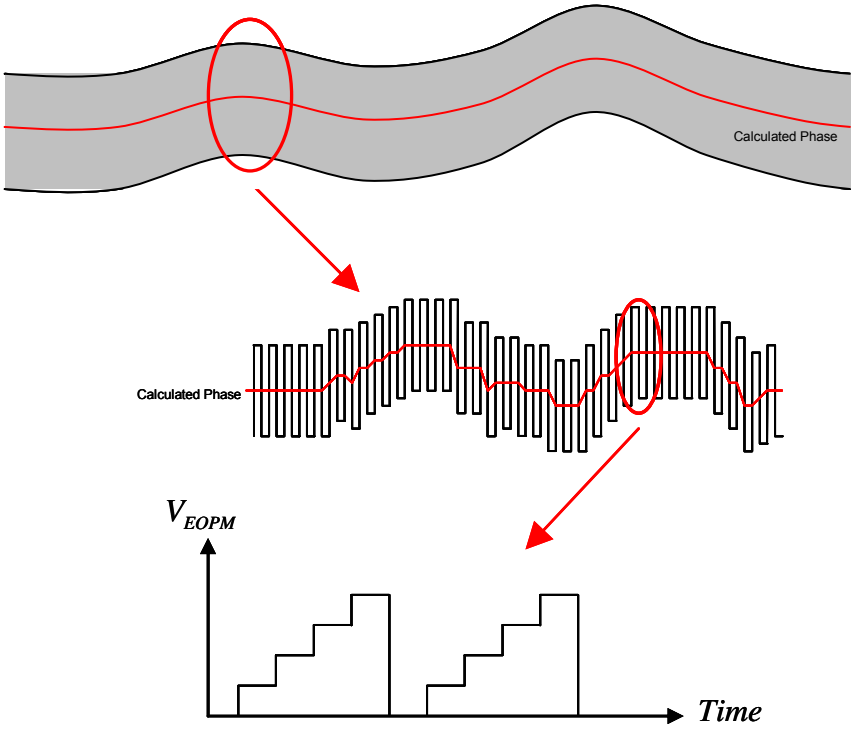

Figure 7.1 The rapid phase shifting concept

7.2.2 Electro-Optic Phase Modulator (EOPM)

An electro-optic modulator (EOPM) is capable of providing very rapid variation in its refractive index when a strong electric field is applied across it. By placing an EOPM in the arm of an interferometer it can be used to vary alter the phase in that arm as the refractive index change in the crystal alters the optical path length. This has the same effect as the PZT mounted mirror in the first scheme. However, there are no moving parts involved and access times are much quicker. The variation of optical path length by changing the refractive index over part of the geometric path results change in the overall optical path.

There are two types of electro-optical effect; the Kerr effect and the Pockels effect. The Kerr effect is a quadratic electro-optic effect in which the index change is proportional to the square of the applied electric-field. The Pockels effect is a linear electro-optic effect and in generally is much stronger than the Kerr effect. For this reason it is much more commonly harnessed for the production of electrooptic modulators. A Pockels cell acts as a variable wave plate and as such if placed between crossed polarisers can be used as an intensity modulator. The other application is as a phase modulator.

Lithium Niobate ($LiNbO_3$) is a common crystalline material for Pockels cells as it exhibits a strong effect and is transparent for wavelengths from 0.4 – 4.5 μm. The electro-optic coefficient is found to be non zero only along certain crystal axes and as such the orientation of the optical axis and the applied electric field through the modulator is critical to its operation. Lithium niobate is naturally birefringent in the absence of an applied electric field and its index ellipsoid is given by

$$\frac{x^2}{n_o^2}+\frac{y^2}{n_o^2}+\frac{z^2}{n_e^2}=1 \qquad (7.1)$$

where n_o and n_e are the ordinary and extraordinary indices. If the optical axis is aligned with the crystal z axis then any linear polarisation state is maintained. The electro-optic coefficients in lithium niobate vary with orientation with the crystal axes. In general it is preferable to align the direction of the applied electric fields with the direction of the strongest coefficients in order to maximise the efficiency of the device. The figure of merit for an electro-optic modulator is the half-wave voltage,

$V_\pi L$ product which is the voltage required to alter the phase by π radians multiplied by the length of the device (Saleh & Teich 1991, ch. 12).

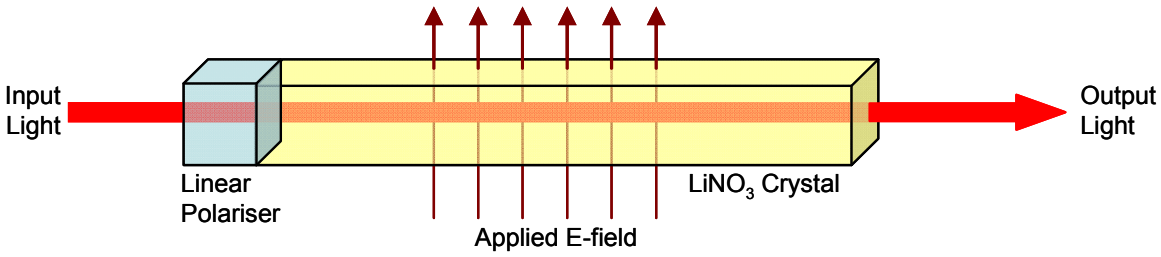

Figure 7.2 Operating principle of an electro-optic phase modulator

7.2.3 Bulk Electro-optic Phase Modulators

Traditional bulk optic EOMs are expensive to drive as they have large apertures and thus large crystal thickness requiring very large voltage to be applied in order to set up the required electric field. This is true of both transverse and longitudinal modulators, although transverse modulators generally have a much lower $V_\pi L$ product at the expense of polarisation dependent operation (New Focus 2009).

Typical values of V_π for bulk optic EOMs are in the range of 300V at operating wavelengths around 1500nm. Thus with a driver operating with a ±400V range, and bearing in mind that any phase shift introduced in the arms of a Michelson interferometer is effectively doubled, a total phase tracking range of roughly 5.2π radians (4.16 μm actual displacement) is possible with commercially available equipment. However, the electronic drivers are complex and expensive. Speeds are also limited due a combination of very high slew rates, the voltages required and the capacitive load the EOPM presents. A few such interferometric systems have been developed already by Sandoz et al. (1999) as well as Zhao & Burge (2001).

7.2.4 Integrated Optics EOMs

Communications technology provides a cheaper and much improved solution that may be integrated into a fibre optic interferometer to provide the same stabilisation feature. Integrated optic phase modulators perform the same function as there bulk counterparts, but due to the long length of the waveguide compared to its narrow

width, values of V_π can be as low as 3V. They also present a small capacitive load, typically a few picofarads, which means that the driving electronics can be relatively simple for modulation speeds of a several MHz, although cutting edge design has seen operation at a frequency of 100 GHz (Saleh & Teich). Generally the upper frequency limit is defined by the capacitance of the modulator and the length of the active waveguide structure. The reason for the latter is that the transition time of the light wave must be short enough that the refractive is approximately constant during its time in the waveguide.

The optical fibre based design of the MFI makes the use of an integrated-optic EOPM an attractive proposition and suggests a good potential for implementing a fast phase shifting technique for real time phase retrieval.

Figure 7.2 shows the structure of a typical EOPM. In order to make use of the maximum electro-optic coefficient, it is normal for the crystal to be placed in the so called x-cut orientation. This means the optical axis aligned with the y axis of the crystal while the electric field is applied along the z axis. This results in the following equations for degenerate polarisations states along the z and x axes.

$$n_z = n_e - \frac{n_e^3}{2} r_{33} E_z \tag{7.2}$$

$$n_x = n_o - \frac{n_o^3}{2} r_{13} E_z \tag{7.3}$$

The polarisation along the z and x crystal axes represents the TE and TM polarisation states in the waveguide respectively. The electro-optic coefficients values are $r_{33} = 30.9 \times 10^{-12}$ and $r_{13} = 9.6 \times 10^{-12}$ m/V . As such it is quite clear from 7.1 and 7.2 that the magnitude of the index change is different for the TE and TM polarisations. The result is that a varying birefringence is created since the phase of the TE and TM are altered unequally. Therefore in order for the EOPM work at its most efficient and without altering the SOP of the light it is critical that the input light is aligned to the TE axis. One approach to this is to install a linear polariser with a suitably aligned active axis in front of the active waveguide element of the EOPM. This provides a simple approach for use in single mode fibre coupling where the polarisation state is unknown and varies with time. The disadvantage is the loss of some light power in

the arm of the interferometer containing the EOPM and the addition of added intensity dependence on the SOP.

An EOSpace Inc. phase modulator was acquired for the experimental work presented in this chapter. Its specification suggests a return loss of >50 dB and an insertion loss of <10dB combined with a $V_\pi < 4$ V . The maximum operating voltage range is ±30 V which yields a total equivalent operating range of approximately 15 μm. It has a capacitance of 80 pF.

7.2.5 Rapid Phase Shifting Method

In order to perform phase shifting with the EOPM all that is required is to apply a staircase voltage waveform of sufficient accuracy. The output intensity of the interferometer is then sampled after suitable settling time has been allowed. The settling time requirement is due to the interaction of the driving electronics and the intrinsic capacitance of the EOPM. It should not be confused with mechanical settling time as might be experienced with the stepwise shifting of a PZT.

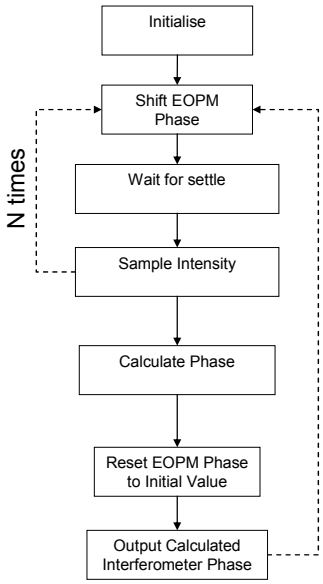

Figure 7.3 Flow of events during rapid phase shifting

In order to define stabilise the interferometer it is necessary to servo the phase in opposition to the change induced by environmental factors. This is easily done during the phase stepping process by simply altering an offset voltage on the output. This is

independent of the phase stepping and is simply added to the output. It may be thought of as adjusting the DC offset of the phase stepping waveform.

In order to use the modulator effectively as an open loop phase shifter, it is necessary to characterise exactly the response of the modulator to an input voltage. In order to do this the EOPM was placed in the arm of an all fibre Mach-Zehnder Interferometer and modulated with a triangular waveform with a frequency of 20 kHz. The amplitude of the modulating wave form was such that it created just over a full fringe phase shift. The fast modulation frequency ensures the results are not distorted by any low frequency environmental disturbance.

Figure 7.4 shows the output of the interferometer (red trace) and the modulating voltage waveform (black trace). The sinusoidal intensity response to the linearly ramped phase input is quite apparent. The operating wavelength was 1550 nm.

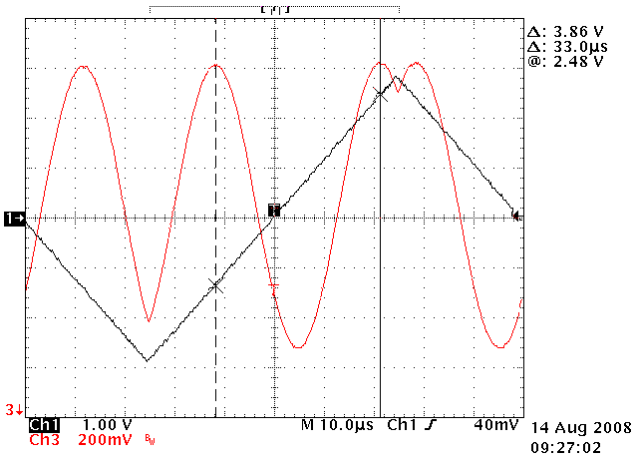

Figure 7.4 Calibration of V_π for an EOPM

From figure 7.4 it is clear that the modulation voltage required to produce one full fringe is 3.86 volts. Bearing in mind that a Michelson interferometer apparatus, which the EOPM will ultimately be used in, has double the phase shift of a Mach-Zehnder the conversion gain is,

$$K_{EOM} = \frac{4\pi}{3.86} = \frac{\pi}{0.965} \text{ rad/V} \qquad (7.4)$$

This equates to a voltage step of 0.483 V to create a 90.0° phase shift.

7.3 Experimental Setup

7.3.1 Apparatus

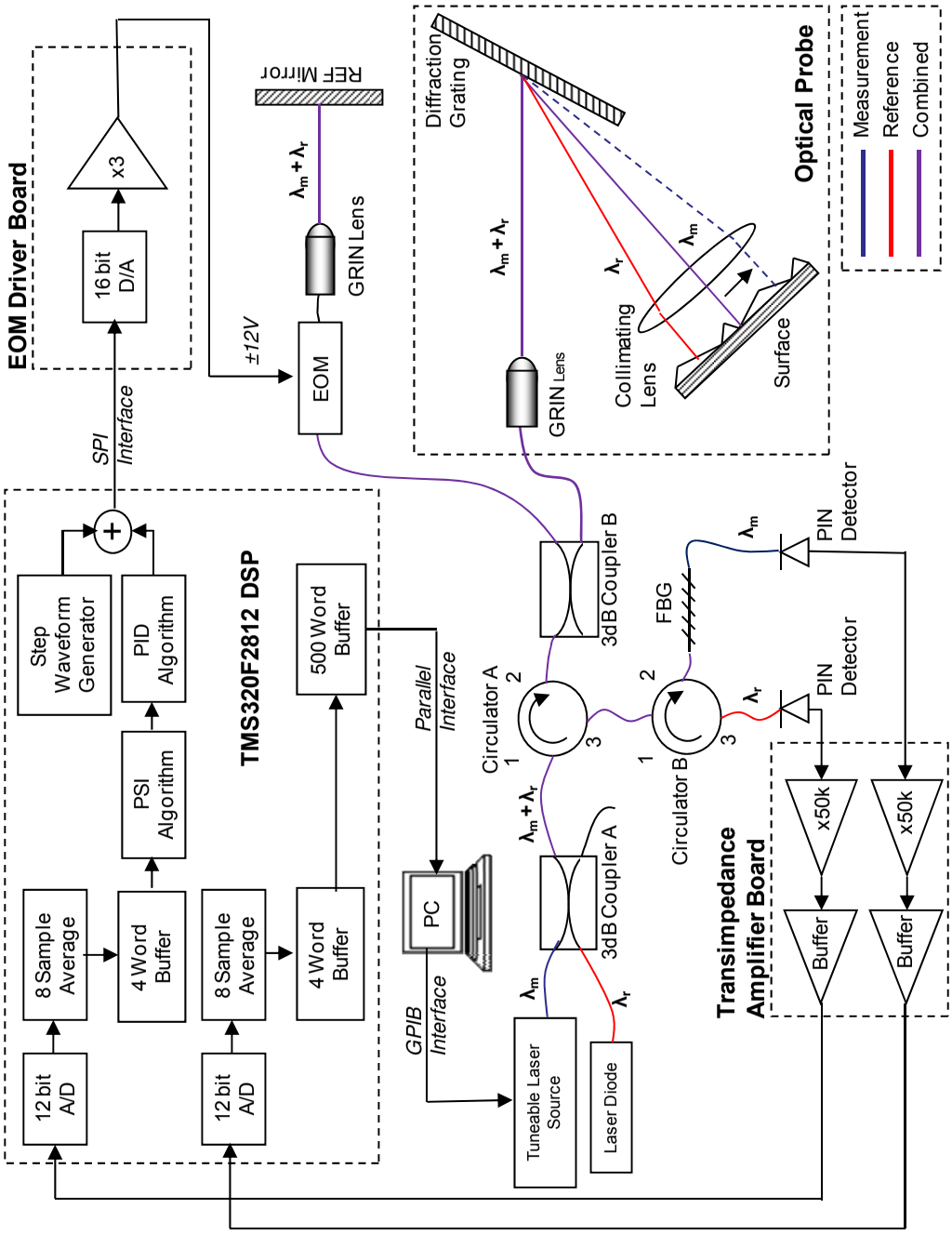

Figure 7.5 Experimental Setup

Many of the features of the experimental setup in this chapter are identical to those contained in the instrument described in the chapter 5. As such the reader is referred to section 5.3 for detail on those features which are common to both instruments.

The experimental setup investigated in this chapter is shown in figure 7.5. A laser diode and the tuneable laser (Hewlett Packard 6181F) illuminate the reference and measurement interferometers respectively. This tuneable laser source replaced the Ando AQ4320D that was used in the setup in chapter 5, the reason being an irreparable malfunction.

The laser diode operates at a wavelength of 1550nm and the TLS is operated between 1555 nm and 1575 nm. Both sources are multiplexed into the same fibre by a 3dB coupler, which is followed by a circulator to provide isolation. A second coupler then splits the light into two fibres, which form the arms of a Michelson interferometer.

The polarisation state of the input light is adjusted using a Lefevre type polarization controller (see section 6.3.4). The polarisation controller is somewhat limited in that it cannot maximise the polarisation state of both light sources at the same time, a separate controllers at the output of each source would be required for that. It does however allow a rough adjustment to gain good fringe visibility in order to maximise SNR. Once this coarse adjustment is made it maintains a good degree of stability for several minutes.

7.3.2 Optical Probe

A key difference in this scheme when compared to the setup in chapter 5 is in the design of the optical probe. The main difference is the lack of a reference mirror; in fact the zero order is not utilised at all. The first order beam is diffracted as before, and the sweep angle altered by wavelength tuning as described in section 5.4.2. The analysis for the scanned profile length is similar but with differing parameters due to a different objective lens.

The objective lens use in this setup is the Thorlabs LSM-03 object telecentric scanning lens. It is specifically designed for optical coherence tomography (OCT) applications where by a light beam is scanned very quickly over the lens aperture whereby it is focussed upon the objective surface. This is a very similar action to the one carried out in this instrument and as such provides performance advantages for this system in terms of spot size when compared to the basic achromatic doublet as used in chapter 5.

The effective focal local of the LSM-03 lens is 35.98 mm, and with a 4 mm collimated gaussian beam at the aperture it will provide a focussed 25 μm spot size with a 580 μm depth of field. The maximum scanning range is limited by the field of view of 9.4 mm.

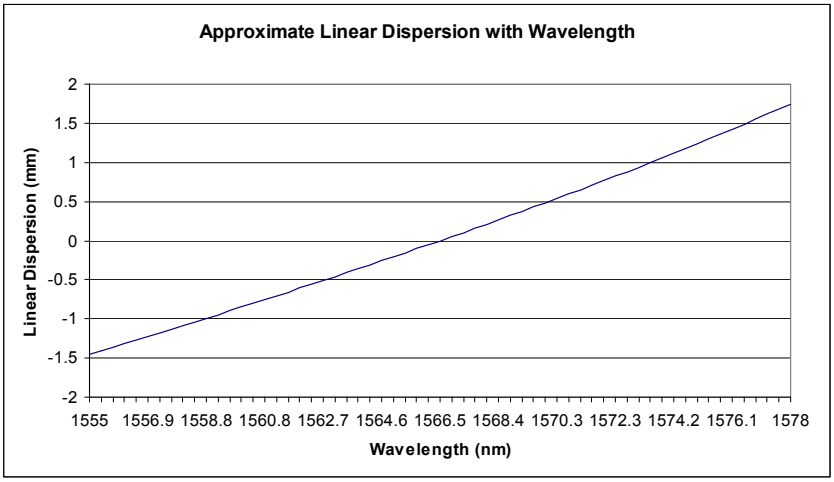

Figure 7.6 Optical probe scanning profile

A numerical analysis similar to that carried out in section 5.4.2 was carried out with the grating incidence, $\alpha = 26°$. It can be seen that the scan range is approximately 3.2 mm. The wavelength scanning range is slightly reduced from that used in section 5.4.2 because of the slightly reduced wavelength scanning range of the HP8168F tuneable laser; the output intensity was found to drop off rapidly above 1578 nm.

It is likely that the current configuration the produced spot size is not optimal as the collimated $1/e^2$ beam width supplied by the collimating GRIN lens is only 0.85 mm rather than the specified 4mm. Further beam expansion optics would be required between the GRIN lens and the grating.

Overall the probe created for this apparatus is much smaller than that of the instrument in chapter 5 due to the fact there is no reference arm contained within the bulk optic element. The probe head form factor is reduced from 70 x 100 mm to approximately 70 x 30 mm.

7.3.3 Reference Arm

The reference arm of the interferometer is now formed in fibre by the second coupler output. It contains the EOPM which is used to stabilise the interferometer and perform phase shifting. The integrated optic EOPM comes fibre pigtailed so connection to the optical circuit is a simple matter.

Because there is EOPM has a relatively limited range (≈15 μm) it is necessary to pass the light through a GRIN lens so it may be incident on an external reference mirror. This is less efficient than directly silvering the fibre end but allows the mounting of the mirror on a translation stage. This method means the interferometer is easily balanced manually, until it lies in the EOPM operating range. This type of adjustment would be necessary if the objective lens was to be changed to one of a different magnification for instance; the path length in the measurement arm would then change substantially. If fully automated operation was deemed to be necessary, the translation stage could be easily be motorised.

7.3.4 Electronic Hardware

One of the largest differences between the instrument described in chapter 5 and this one is in added electronic hardware needed to implement the rapid phase shifting technique. This section gives an overview of the electronic elements of the apparatus and explains their function and inter-relationship.

A functional representation of the hardware is given in figure 7.7.

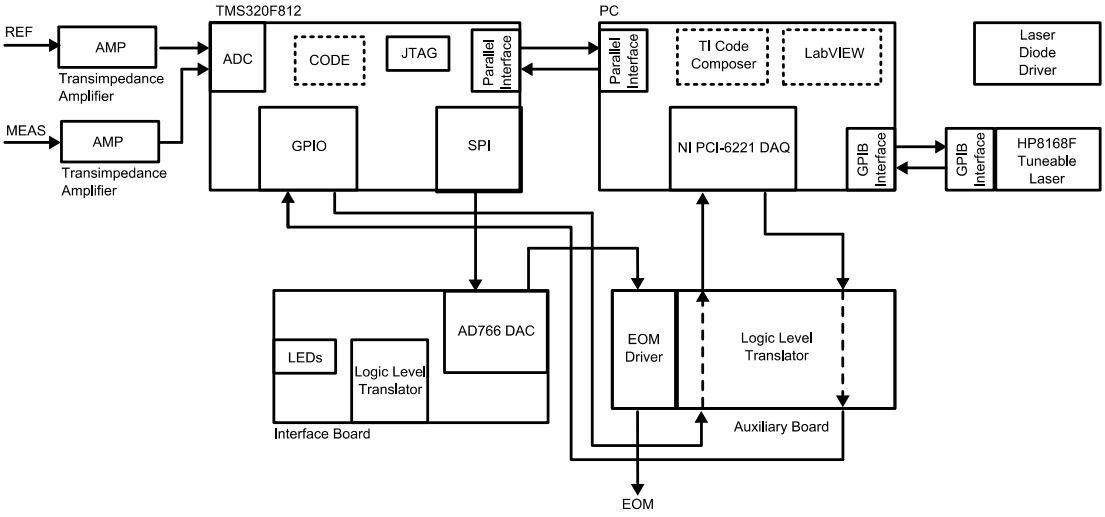

Figure 7.7 Functional representation

The diagram is divided in physical terms with each of the large boxes representing a different physical printed circuit board (PCB). The PCBs contain a number of sub-circuits which are represented inside the main boxes. The full circuit diagrams for each of the sub-circuits are contained in appendix B. The arrows on the diagram indicate the direction of dataflow. Software is represented by the dashed boxes. A full diagram, included pinouts relating to the subcircuit diagrams in Appendix B.1 to B.3 may be found in Appendix B.4

Transimpedance Amplifier

The fast phase shifting requires a transimpedance amplifier with fast frequency response since this translates directly to rise times. With this in mind the THS4062 opamps were used since they provide a very high GBW and fast response. A full noise analysis is carried in appendix A.2. There are two transimpedance amplifiers, for the reference and measurement interferometer outputs respectively. They are two stage amplifiers which allows for high speed and gain adjustment in order to condition the signal for full scale analogue to digital conversion. The outputs from both transimpedance amplifiers are fed to the ADC on board the TMS320F2812 PCB.

Auxiliary Board

The auxiliary board contains several logic level translators to isolate the sensitive 3.3 V CMOS inputs of the DSP and convert from the TTL levels used by the PCI-6221 DAQ card. It also provides for the reverse conversion for the DSP outputs as necessary.

The EOPM driver provides a gain of 3 to amplify the output of the DAC (±3 V) into a larger value in order to provide for a larger range of operation. The THS4062 opamp also provides a high frequency response to ensure the system bandwidth is not limited here.

The response of the EOPM driver and the transimpedance amplifier during phase stepping is shown in figure 7.8.

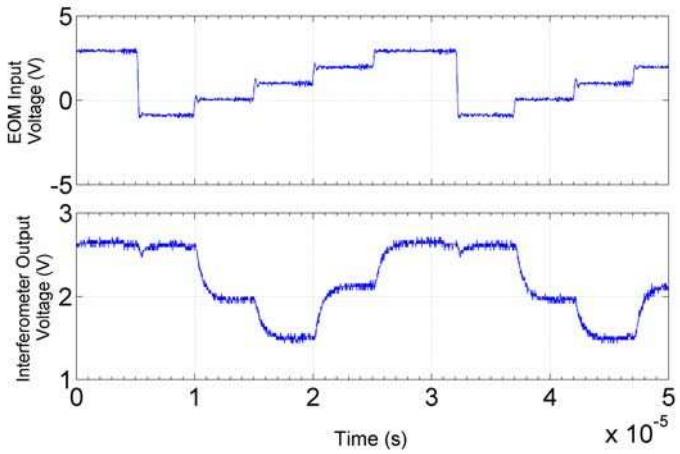

Figure 7.8 Response of MFI to phase shifting

It is quite clear that the EOPM voltage has a much faster rise time than the response of the transimpedance amplifier. The transimpedance response is seen to be critically damped in order to ensure a fast settling time for sampling. This was done by adjusting the feedback capacitance of the amplifier (see appendix A.1). Figure 7.9 shows more clearly the voltage across the EOPM (red trace) from an input (green trace). The 34 ns rise times equates to an approximate bandwidth of 10 MHz assuming a first order approximation for the response.

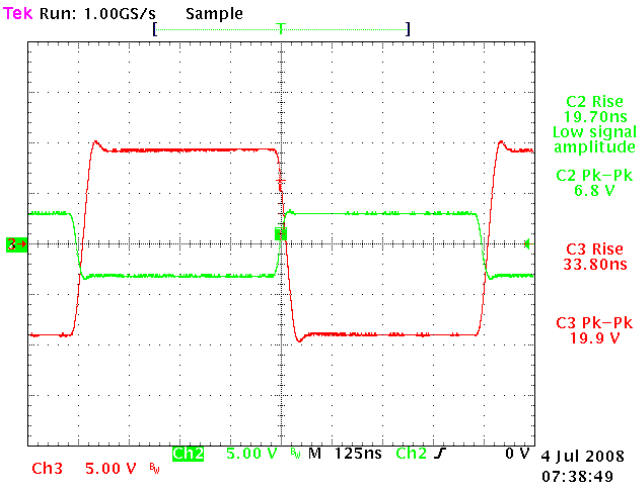

Figure 7.9 Response of EOPM voltage to an input square wave

TMS320F2812 Digital Signal Processor

In order to provide real time phase calculation for the interferometer at a speed fast enough be used in a servo control loop a digital signal processor (DSP) is very

suitable. It benefits from being deterministic in operation, something that is difficult to obtain on a PC loaded with a modern day operating system. The TMS320F2812 is a fairly cheap processor which still provides 32 bit fixed point processing at 150 MIPS as well as 18 k (16 bit words) of onboard mixed use memory (programs or data). In addition it hosts a number of onboard peripherals, the most relevant to this application being the ADC, serial peripheral interface (SPI) and the configurable general purpose inputs/outputs (GPIO).

The DSP is connected to a PC by a parallel interface and built in JTAG module. This allows the downloading of program code and the upload of stored data from the DSP and provides in-circuit software debugging. Texas Instruments Code Composer software provides an integrated development environment (IDE) with includes a C/C++ compiler and debugger. In addition a set of functions is provided for carrying floating point arithmetic and trigonometric functions on the fixed point architecture.

The ADC is has 12 bit resolution and features a multiplexed input so up to 16 inputs may be sampled, though overall sample rate is shared between them. The input signal range is 0-3.3 V and as such the transimpedance signals must be conditioned correctly. Maximum sample rate is 12.5 MSPS. The ADC is used in simultaneous sample mode where two inputs are sampled simultaneously; A0 and B0 which are connected to the reference and measurement interferometer outputs respectively.

The SPI is a 4 wire bi-directional synchronous serial interface, the clock being provided by the DSP. For this application it is used in a uni-directional mode (3 wire) to supply 16 bit values to the DAC which provides the analogue voltage signal to the EOPM. The maximum bit rate of the SPI is 12.5 Mb/s which means the maximum update rate is approximately 735 kHz (16 + 1 bits/sample). This equates to a 1.36 µs delay between DAC updates.

The GPIO interface provides configurable digital input and output. Two ports are set up to provide a simple means of synchronising with the Labview code running on the PC for the task of changing the laser wavelength. In addition to this some outputs are provided for flagging/debugging and timing analysis.

Interface Board

The interface board provides three functions. It has logic level translators to convert the 3.3 V CMOS outputs from the DSP to power LEDs for signalling. It also has 3 TTL to 3.3 V CMOS converters to allow for protected digital signalling to the GPIO inputs on the DSP.

The most important function of the interface is the AD766JN DAC which provides the analogue output for driving the EOPM. It is connected to the DSP by a 3 wire uni-directional SPI and accepts data in 16 bit words at a rate of up to 12.5 Mb/s. The AD766JN DAC has a 16 bit resolution and a worse case settling time of 1.5 μs after a data value change. Combined with the 1.76 μs delay caused by the transfer time of the SPI the overall delay time is 2.86 μs; this means a real world maximum update rate 350 kHz.

PC

The PC performs several functions and runs two software applications, Labview and Code Composer. The Labview software liaises with the PCI-6221 DAQ card and the GPIB interface. The Labview code performs the post-processing duties on retrieved data from the DSP after a measurement has taken place. It also controls the HP8168F tuneable laser via the GPIB interface. The Code Composer software is dormant during the measurement cycle, its only function is to upload that measurement data from the DSP for post-process once the measurement is finished.

Laser Diode Driver

The laser diode driver is based around a specialised laser diode driving IC. It provides a quiet constant current source, and uses feedback from the monitor photodiode integrated in the laser diode to provide feedback for intensity control. There is a modulation input provided which may be used to modulate the injection current at frequencies a few kHz by the simple application of voltage waveform. This is a useful function which aids optical path length balancing prior to measurement.

7.3.5 Software

DSP Code Overview

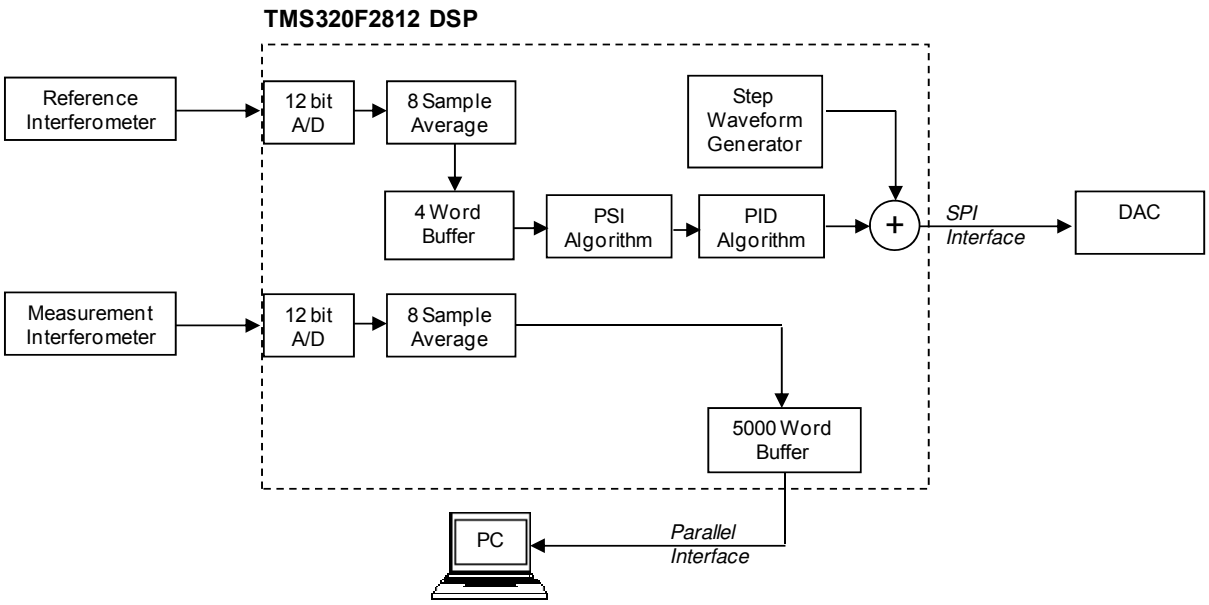

Figure 7.10 DSP code function diagram

Figure 7.10 shows the functions of the DSP code in terms of task modules. First the intensity data from both the reference and measurement interferometer are sampled 8 eight times in 80 ns intervals. The sample values are then averaged in an attempt to lower noise slightly. The reason for the choice 8 values is that this is the maximum buffer size on the ADC module and division by eight is quickly achieved in binary processing by right shifting the register value by 3 bits.

The 8 averaged sample value is then stored in a buffer and the SPI outputs the next phase shift value. After a delay of 2.86 μs in order to allow the DAC to update and settle the sampling process is repeated.

The phase shift sampling is carried out 4 or 5 times depending whether the Carré or Schwider/Hariharan algorithms, respectively, are selected for calculating the phase. The step voltage values are supplied by the step waveform generator which is a simple circular buffer containing the required voltage value.

The PSI algorithm themselves are coded using the supplied IQmath C functions that allow for emulation of floating point arithmetic and trigonometric functions with maximum efficiency. This important because the phase calculation is the most significant single delay in the servo loop. Figure 7.11 shows the voltage applied to

the EOPM during the phase shifting process, the total time for phase calculation using the Schwider-Hariharan is approximately 27 µs.

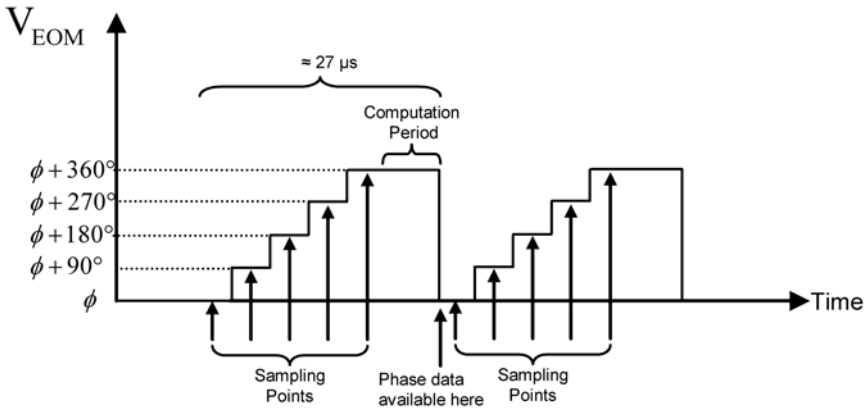

Figure 7.11 Diagram of Schwider-Hariharan phase shifting method

The Carré algorithm only requires 4 phase shifts which should save 2.86 µs over the Schwider-Hariharan but in reality the square root in the numerator removes this advantage. Evaluation of this take 63 clock cycles (5.04 µs) and in addition the conditions testing for the arctangent quadrant determination is more complex (see section 5.5.3). The relatively simple Schwider-Hariharan, when evaluated at a 90° phase shift, works out to be substantially faster.

After the phase is calculated it is used to update the PI control algorithm. Because of the digitisation of the phase signal it makes good sense to use a discrete control algorithm on the DSP, since it is easily configurable and convenient. It imparts a minimal delay due to its simple nature, being only effectively a recursive 3 tap filter. The output from the control algorithm is added to the step voltage value

Samples captured from the measured interferometer synchronously with those from the reference interferometer. However, in order to maximise the loop rate, the phase is not evaluated and the raw intensity values are simply stored in memory. Add the end of the measurement cycle the intensity data is uploaded to the PC via the parallel interface after which the phase is evaluated using Labview code.

Labview Code Overview

In comparison to the Labview code for the MFI in chapter 5 the requirements in this instrument are relatively little. This is in the main because the majority of the actions are performed on the DSP.

The Labview code simply communicates with the HP8168F laser during the measurement cycle, via the GPIB interface, and commands it to shift wavelength as necessary. It also post-processes the upload measurement intensity data from the DSP to provide the final profile data. A full run down of the functions is given in appendix F.

7.3.6 General Points

The wavelength de-multiplexing method remains the same as the MFI described in chapter 5. The main difference in the optical setup is that this is now an all-fibre interferometer in the sense that the interference of the returning waves in each of the interferometer arms now takes place at the coupler. This is an importance difference compared to the instrument in chapter 5 which was essentially a bulk optic interferometer where the arms were in free space. The all-fibre nature of the apparatus described here is such that it is substantially less stable and much more sensitive to vibration and temperature change. Clearly this places more of a challenge for the servo control loop.

Onboard memory limitations mean that the buffers for storing the calculated reference phase values and the raw measurement intensity data are limited to 1000 and 5000 (16 bit words) respectively. The larger allocation for the measurement data it is necessary because of it is unprocessed until the end of the measurement cycle.

The algorithm used to calculate the phase feedback signal may be selected as the Carré algorithm (4 phase shifts) or the Schwider-Hariharan (5 phase shifts).

7.3.7 Balancing the Optical Paths

In order to balance the optical paths a simple procedure is carried out in which the wavelength of the laser diode is modulated. This is done by altering the injection current by applying a voltage waveform to the *mod in* input on the laser diode driver (see appendix B.3). The DSP code is run and it proceeds to lock the interferometer stable. The modulation of the injection current causes a shift in intensity and in

addition a small variation in wavelength. This is due mainly to the associated temperature change in the cavity due to changing injection current modulation. For an unbalanced interferometer, any wavelength modulation will result in a modulation of the output phase. As such this modulation is servoed against by the closed loop control.

By monitoring the measurement interferometer output waveform, which looks similar to that shown in figure 7.8, it is possible to see the servoing of the control loop as a shift in the positions of the observed steps. The rapid phase shifting techniques overcomes any problems with the change in fringe intensity that results in by modulating the laser diode intensity as long as the level does not drop too low.

By modulating the laser diode slowly at 0.5 Hz and observing the output of the measurement interferometer the reference mirror is translated on a micrometer stage until the stepped intensity waveform is completely stable. At this point the optical paths of the interferometer are balanced and the measurement may proceed.

7.3.8 The Measurement Cycle

A full transcript of the DSP and Labview code is given in appendices D and E2, however it is worth describing the operation in terms of event flow in order to maintain clarity.

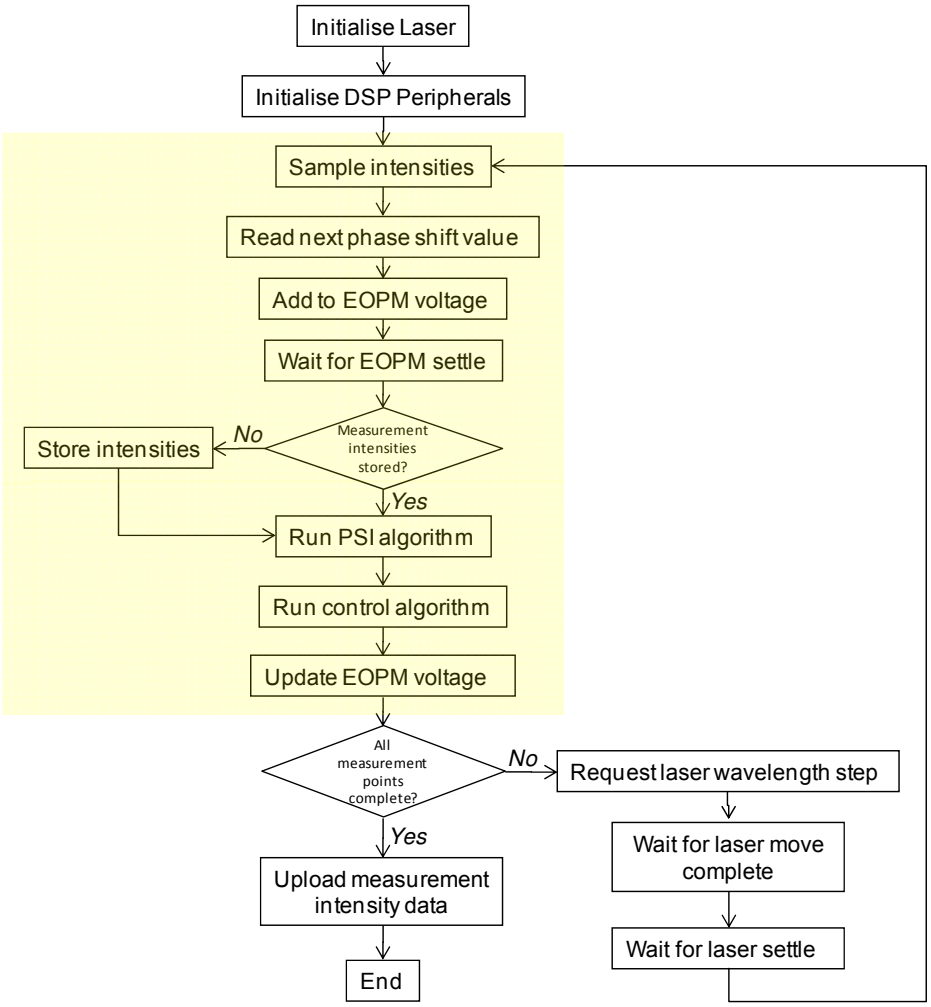

Figure 7.12 Event flow during measurement cycle

First the tunable laser is initialised and the wavelength is set at 1555 nm to place the measurement point at the start of the profile. During this time the DSP code is downloaded on the DSP and started up. This runs several routines for setting up the onboard peripherals with the required parameters for correct operation. Ones these have been set up the DSP runs in phase shifting mode.

It is important to note that the phase shifting, evaluation and control algorithms run continuously during the whole of the measurement cycle, regardless of what position in the event flow the rest of the code is. This is achieved by using the hardware interrupt and an associated interrupt service routine (ISR) which automatically runs at specified intervals regardless of the current position in the overall program. The interrupt utilised is the ADC conversion complete interrupt; this is called every time a conversion is complete. In this way the code automatically jumps into the routine

every time the intensity has been sampled and deals with the sample accordingly. The ADC conversion complete ISR is shown on the event flow diagram as a yellow square. By using an interrupt driven control loop in this way, the timings are deterministic, with a total control delay of 27µs.

There is only one occasion when the DSP needs to communicate with the Labview code and that is to request for the laser wavelength to be shifted to the next point on the profile. The actual step values are help in an array in Labview and are user configurable. To do this the DSP logic pin PWM11 high which is detected by DAQ card on pin 0.0. The Labview code then issues a command, via the GPIB interface, to set the laser to the next wavelength step and waits for a service request (SRQ) from the laser which signifies the wavelength shift has completed. The DAQ card pin 0.1 is then set to logic high to inform the DSP code that the laser shift has completed; this is picked up by DSP pin PWM10 (see figure 7.7). The DSP then pulls PWM11 low to acknowledge and the interface returns to an original state. Figure 7.13 shows a timing diagram describing this procedure.

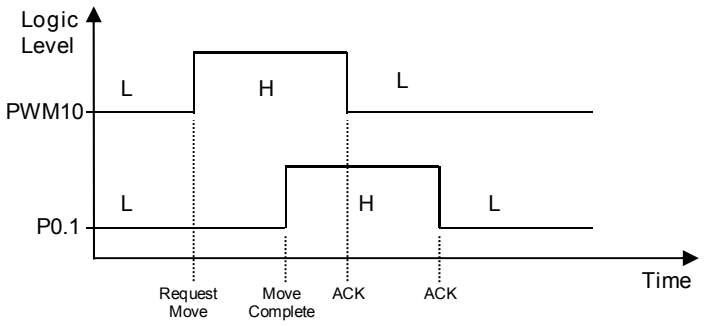

Figure 7.13 Laser move request timing diagram

There are various parameters that may be altered in the code for such things as algorithm selection, control loop gains, phase stepping values and various delay times. However, the full code listing and explanation of the parameters is given appendix E.

7.3.9 Rapid Phase Shifting Operation

Figure 7.14 shows an oscilloscope trace of the rapid phase shifting method using the Carré. The right hand side figure is simply a zoomed in version of the left hand side. The black trace shows the interferometer output while the green trace shoes the voltage applied to the EOPM. The red trace is a timing flag; the trace is high whenever the DSP is calculating phase

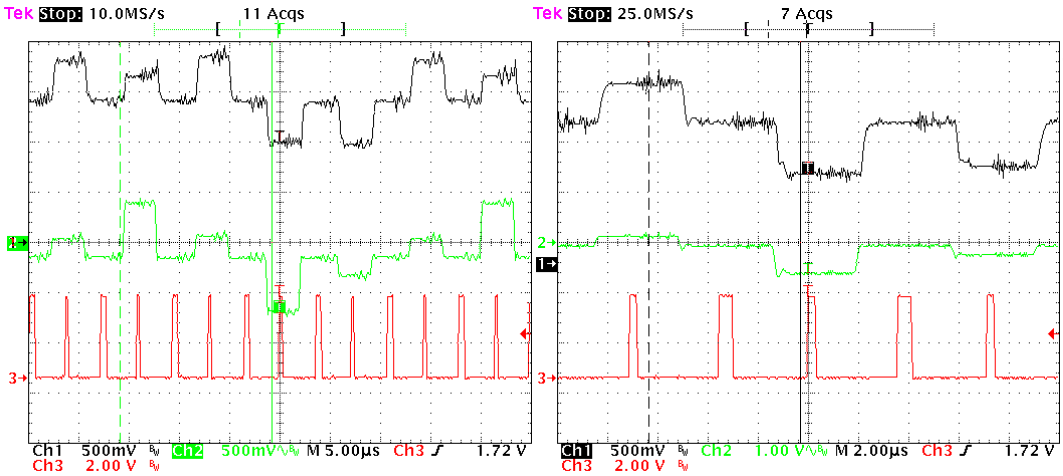

Figure 7.14 Oscilloscope trace showing rapid phase shifting with Carré algorithm

Figure 7.15 again shows an oscilloscope trace of the rapid phase shifting method, this time using the Schwider-Hariharan algorithm. This time the red trace shows the interferometer output while the black trace shoes the voltage applied to the EOPM, while the green trace is the timing flag.

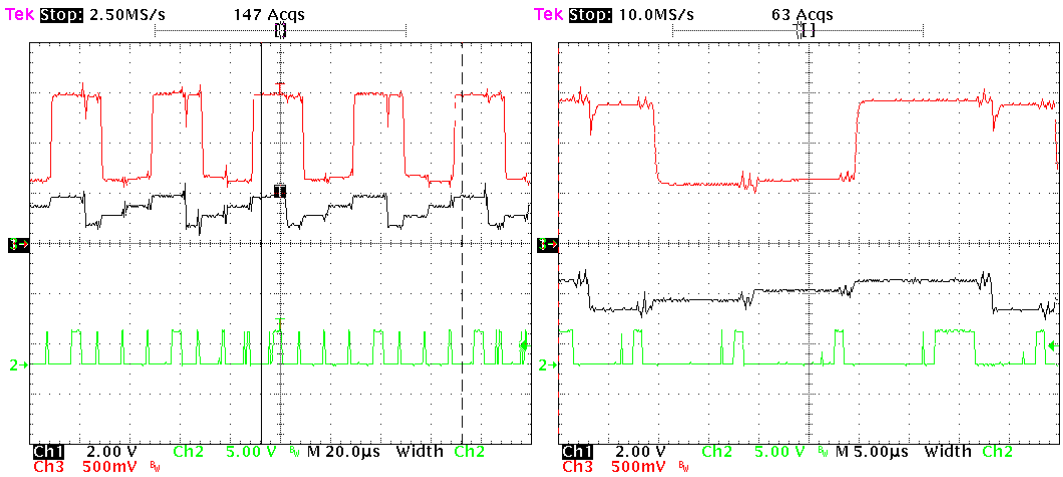

Figure 7.15 Oscilloscope trace showing rapid phase shifting with the Schwider-Hariharan algorithm

The small transients seen on the EOPM voltage and interferometer output occur during the write cycle for the DAC, there is some crosstalk or feed forward occurring. It does not effect the accuracy of the phase shifting however because the sampling does not occur until 1.5 μs after the DAC write has finished. This delay is to allow the DAC to settle to within its specification. The extended time required at the end of each 5 step phase shift sequence in order to execute the phase shifting algorithm is quite clear.

7.4 Control Loop Analysis

7.4.1 Introduction

The control loop analysis given in section 5.4.4 anticipated how the stabilised reference interferometer would respond to the any induced disturbance. In this section a similar analysis is carried out for the fast phase shifting method. There are three important distinctions between this method and the one convered in chapter 5. The control loop is now digitally implemented, the dynamic of the phase modulator are substantially different to that of the PZT and finally, the feedback parameter is now calculated phase.

As such it is to be expected that the control loop behaviour may be substantially different.

7.4.2 Block Diagram

In order to implement a suitable control loop one must first consider the representation of the all the elements in the control loop. Figure 7.16 shows the representation of an intensity feedback control loop. $U(s)$ being the target intensity and $Y(s)$ the actual interferometer output intensity. G_{EOM}, G_{IF} and G_{PIN} represent the transfer functions of the EOPM, interferometer and the detector, while $C(s)$ is some controller that we shall use to stabilise the system.

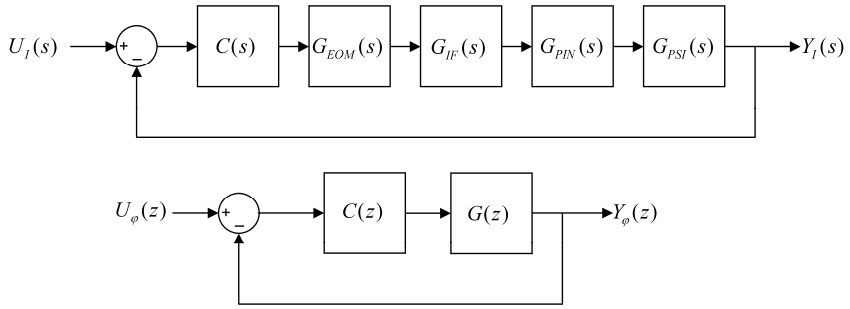

Figure 7.16 Representation of control loop

To simplify the analysis and convert to a phase based approach it is possible to make some simplifications. First consider the effect of the phase shifting algorithm in a control loop; it is not necessary to be concerned with the details of its workings from the point of view of analyzing its effect on the control loop, it may be considered as a 'black box' which takes an input phase demand and delivers an output phase.

The action of the PSI algorithm is not continuous however, but discrete, providing a phase output value every 27 μs after the code has run. As such, it is better consider the loop as a z-domain representation having a sampling interval of 27 μs. The z-domain is the discrete time equivalent of the s-domain representation and shares many of its properties (Leigh 1985, ch. 2).

The upper half of figure 7.16 shows the full control loop in terms of s-domain transfer functions. The lower half shows the simplified version in terms of z-domain transfer functions.

7.4.3 z-domain Analysis

The z-domain transfer functions for a proportional-integral (PI) controller, $C(z)$ and the phase shifting algorithm, $G(z)$ are

$$G(z) = z^{-1} \tag{7.5}$$

$$C(z) = K_p\left[1 + \frac{Tz}{K_i(z-1)}\right] \tag{7.6}$$

T is the sampling interval and K_p and K_i are the controller gain and integration time respectively. The forward loop transfer function is then simply;

$$C(z)\cdot G(z) = K_c \frac{\left(T/K_i + 1\right)z - 1}{z^2 - z} \tag{7.7}$$

From section 5.4.3, the sensitivity transfer function is then

$$S_G^D = \frac{G(z)}{1 + C(z)G(z)G(z)} \tag{7.8}$$

where the disturbance $D(z)$ enters at the point in the loop between $C(z)$ and $G(z)$ on figure 7.16 The process for the discretisation of a continuous time PI controller is given in appendix A.3.

7.4.4 Numerical Simulation

At this point numerical simulation was used to derive suitable values for K_P and K_i in order to supply a stable closed loop and reasonable performance. This was done in much the same manner as for the instrument in chapter 5. The script used may be found in appendix D.5.

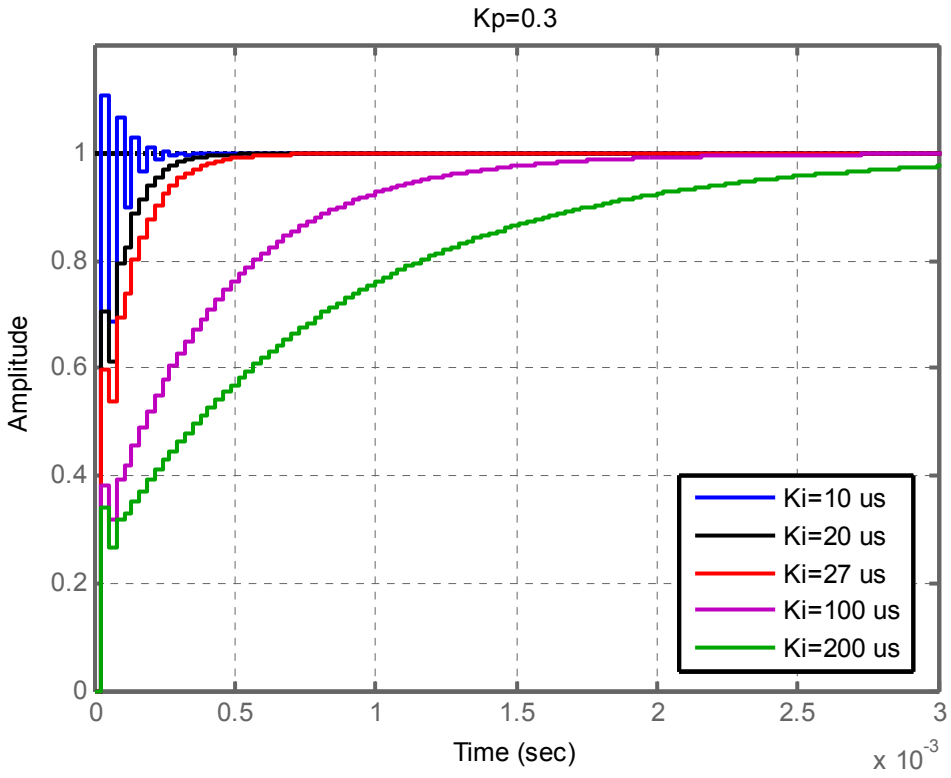

Figure 7.17 Simulated closed loop step response

Figure 7.17 shows the step response for various values of integration period (the reciprocal of integration gain). The proportional gain was held steady at 0.3 throughout the simulation and the discrete nature of the output is quite clear.

Increasing the integration gain results in a faster response, up until a certain point after which closed loop instability occurs. A critically damped response is apparent when the integration period is equal to the PSI algorithm delay.

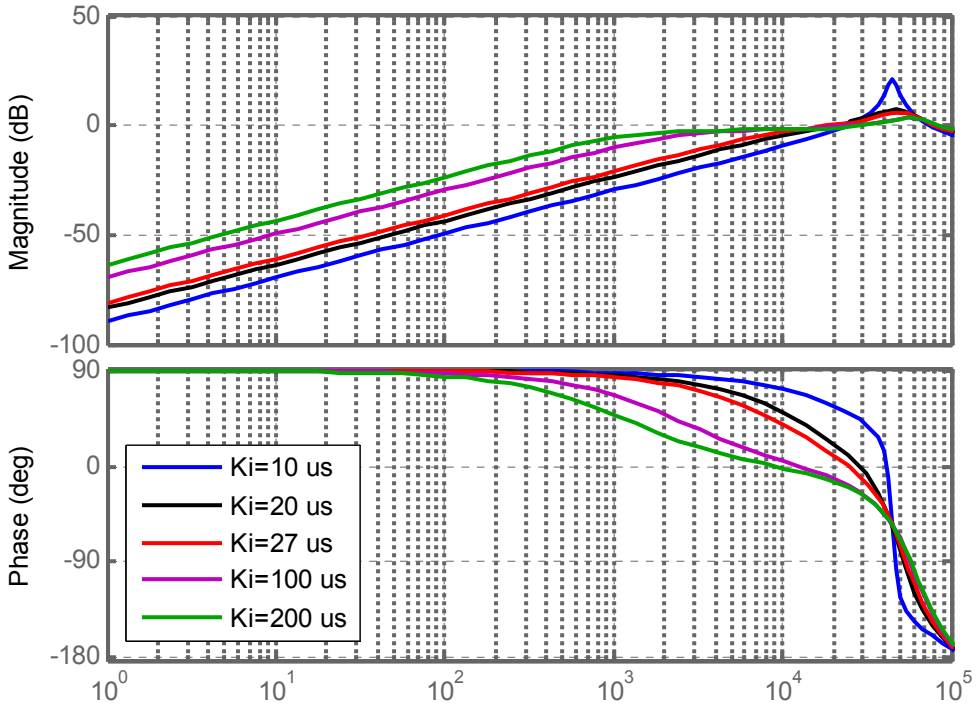

Figure 7.18 Bode plot of sensitivity function

Figure 7.18 shows a bode plot taken from the Matlab simulation. For $K_i = 20$ µs and $K_p = 0.3$ it suggests that the -3dB point for disturbance rejection will occur at approximately 1.6 kHz. As expected increasing the integration gain (reducing the integration period) will improve the disturbance rejection up to the point of closed loop instability.

It is clear that the main factor affecting the ability to upper frequency response of the stable closed loop is the sampling interval of the loop enforced by the algorithm execution time. The imposed sampling interval could be increased by a faster DSP

and by using a parallel loading DAC with a faster settling time, thus reducing the wait time between phase shifts.

7.5 Experimental Results

7.5.1 Introduction

A similar set of experiments were carried out on this instrument in order to assess its performance and compare it to the instrument in chapter 5. First, the stability of the reference interferometer is measured, with the control enabled and disabled. The effectiveness of the control loop is analysed with both the Carré and Schwider-Hariharan algorithms used to calculate the realtime phase data. The SOP drift is then measured to demonstrate the effect on long term stability. The stability of the reference interferometer is then studied in detail over a shorter period of 10 seconds. The measurement interferometer stability is also examined over the same period and also at several different wavelengths. Finally, a step height sample is measured with the MFI and also a Taylor Hobson CCI to provide a comparsion with a commercial instrument.

7.5.2 Stabilised Reference Interferometer

In order to test the effectiveness of the phase feedback method for stabilising the interferometer a variety of experiments were devised. First, the interferometer was set free running with the stabilization control loop switched off, and the reference interferometer output was monitored during this time. The control loop was then enabled and once again the reference interferometer output was monitored. The duration of monitoring was 2 seconds and the data sampling rate was 100 Hz; the results are shown in figure 7.19. The results have been converted from phase to nanometres of optical path change.

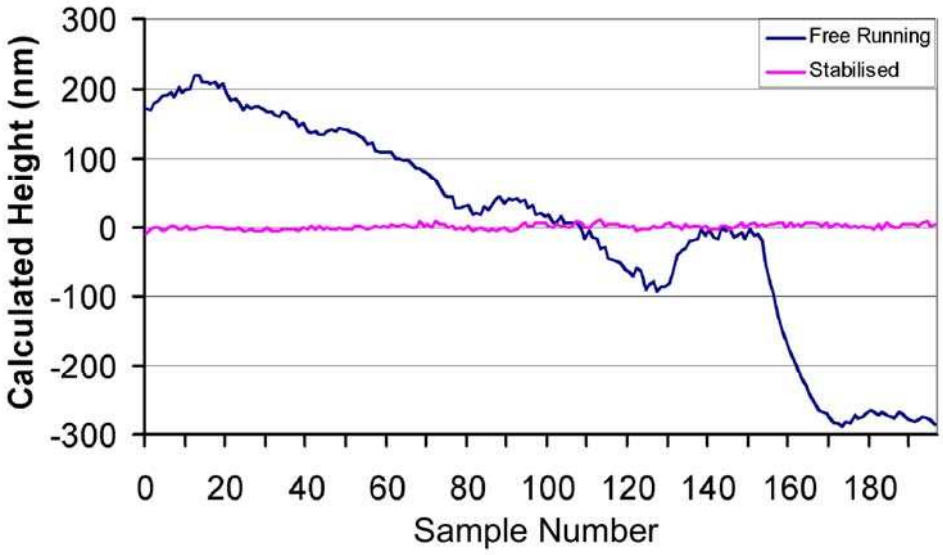

Figure 7.19 Drift seen in the stabilised/free running fibre interferometer

It is obvious that the drift when the interferometer is free running is severe and would certainly impinge substantially on any real measurement attempted. The reference interferometer output appears to be much improved when locked with the control loop.

7.5.3 Short Term Reference Interferometer Stability

Figure 7.20, figure 7.21 and figure 7.22 show the reference interferometer calculated phase output buffer. They represent the unlocked interferometer, a locked interferometer using the Carré algorithm, and a locked interferometer using the Schwider-Hariharan algorithm respectively. The sample rate was the maximum rate for phase calculation at 37 kHz which equates to a 27 ms period for the 1000 phase values recorded. The output phase values from the buffer are in radians.

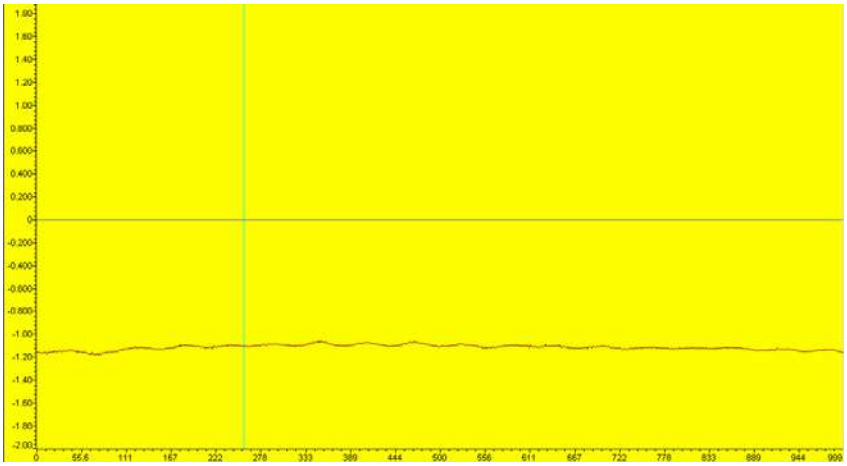

Figure 7.20 Unstabilised reference interferometer with using the laser diode source[1]

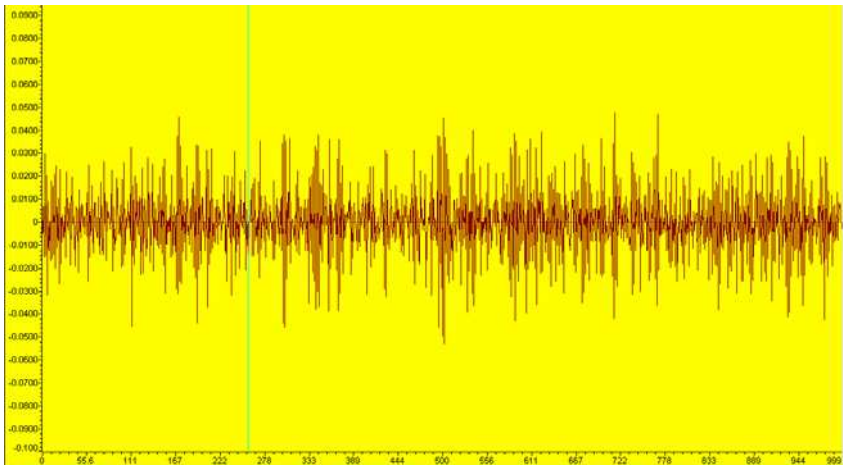

Figure 7.21 Stabilised output using Carré algorithm[1]

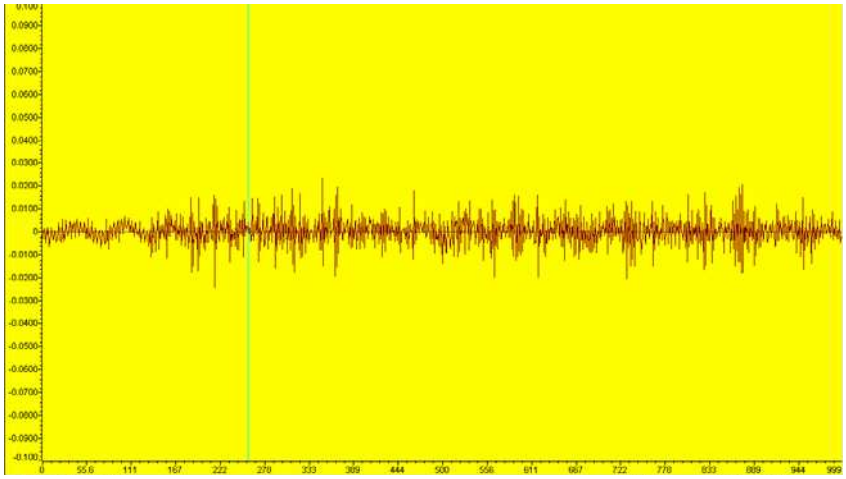

Figure 7.22 Stabilised output using Schwider-Hariharan[1]

It should be noted that the scale in figure 7.20 is 20 times larger than that of figures figure 7.21 and figure 7.22. Besides the obvious improvement in the stability over that of the unlocked interferometer, it is also noticeable that there is significant reduction in the noise present using the Schwider-Hariharan compared with the Carré algorithm.

7.5.4 SOP Variation in the Stabilised Measurement Interferometer

Figure 7.23 shows raw captured intensity data from the measurement interferometer with the active stabilisation switched on. The data were sampled at 100 Hz for an 8 second period. These are the raw intensity data that are post processed in Labview in order to produce the measurement phase. Each coloured line represents an intensity

[1] The y-axis in figure 7.20-23 represents calculated phase. Note the difference in scales between figures 7.20 and 7.21 compared with 7.22. The x-axis shows the sample number.

set from a different phase shifted position. It is clear that although the interferometer is locked, the intensities are varying due to SOP variation in the fibre. The drift seen in figure 7.23 shows clearly why intensity feedback is not very effective for stabilising fibre interferometers.

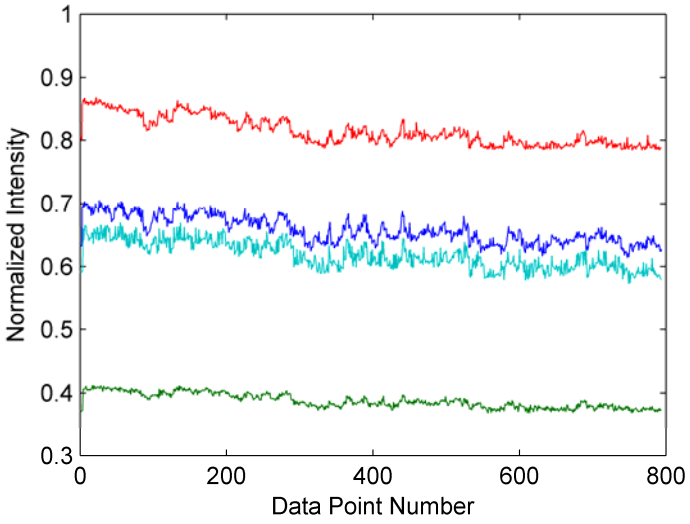

Figure 7.23 Drift of captured intensity values due to SOP variation

7.5.5 Reference Interferometer Stability Histogram

In order to ascertain the behaviour of the reference interferometer and to develop an expectation of performance a detailed look at the statistics of the recorded positions was made. 1000 consecutive reading of the calculated reference interferometer phase where taken with the active stabilisation turned on. The results are shown in figure 7.24 in histogram format. The sample rate was 100 Hz thus the observation period was 10 seconds.

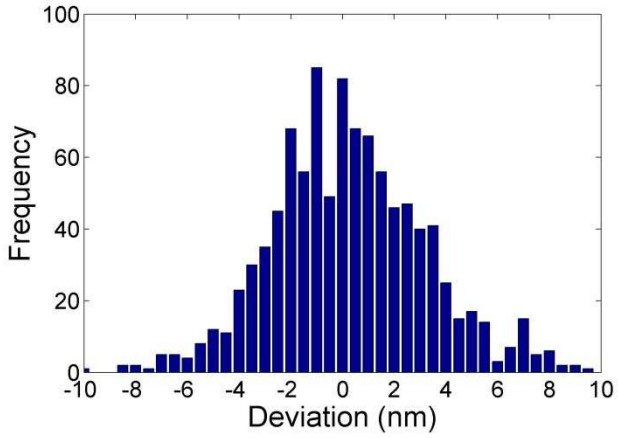

Figure 7.24 Histogram of stabilized interferometer values

As might be expected there is an approximately normal distribution of values with a standard deviation of 2.98 nm. It may be expressed from this result that approximately ±9 nm range of stability has been achieved over 3 standard deviations from the mean.

7.5.6 Stabilised Measurement Interferometer

While the preceding results show that the control loop effectively stabilises the reference interferometer it is more important to concern ourselves with the stability of the measurement interferometer. It is here that any variance of this phase that will map directly onto the measurement result.

900 readings (imposed by DSP memory constraints) of the measurement interferometer were taken at a particular wavelength with the interferometer locked. In essence, the experiment made multiple measurements of the same point on the measurand surface. The procedure was repeated at several wavelengths to see if there was any variation over the effectiveness of the stabilisation over the whole scan range. The sample rate was 100 Hz, thus the experiment covered an observation period of 9 seconds.

Measurements were taken at 1560, 1565, 1570, and 1575 nm and the resulting spread of surface height values at each operating wavelength are shown in histogram format in figure 7.25.

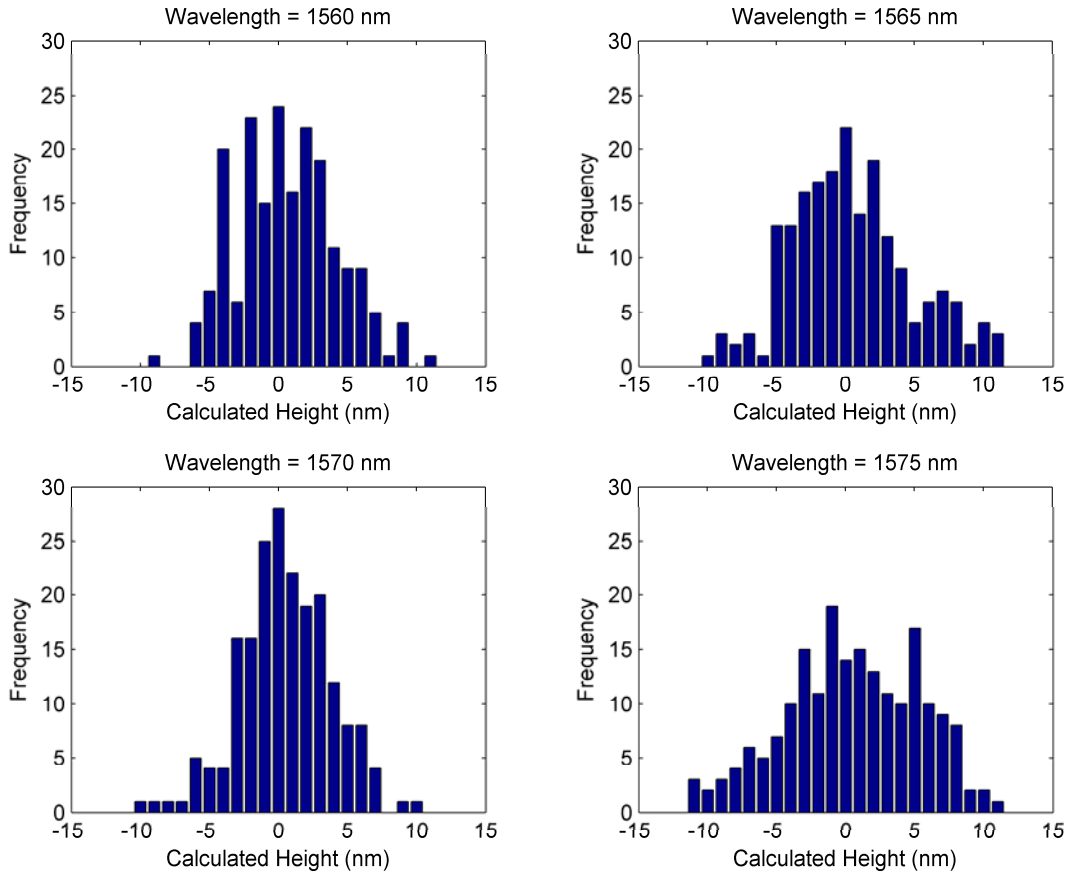

Figure 7.25 Histograms of stabilised measurement interferometer at various tunable laser wavelengths

7.5.7 Step Height Measurement

The next stage of the analysis was to determine the abolsute accuracy of the instrument within the bounds of its noise performance. In order to do this it is necessary to perform a measurement of a known artefact; the same step height as was used in section 5.6.6. In this experiment a different section (chrome coated) was used however.

Figure 7.26 shows an areal representation the step height sample as captured using a commercial scanning white light interferometer (Taylor Hobson CCI). The sample was cold chrome coated to ensure equivalent optical properties for both the CCI and our instrument especially with regard to phase change on reflection, thus ensuring the results are directly comparable. A photograph of the sample is shown in figure 5.29.

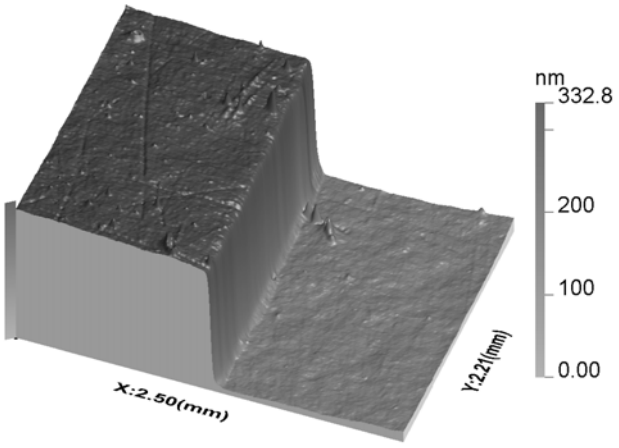

Figure 7.26 Step height sample measured using Taylor Hobson CCI

Analysis of the step height shown in figure 7.26 suggests a step of 287 nm is present. The angle of incidence on the diffraction grating in the MFI was setup to yield approximately 2.5 mm of lateral scanning as the wavelength range was tuned from 1555 to 1575 nm. This ensured that the profile length was comparable to that produced by the Taylor Hobson CCI which had a 3.68 mm^2 field of view with the lens used; the CCI results were cropped to match up the profile lengths.

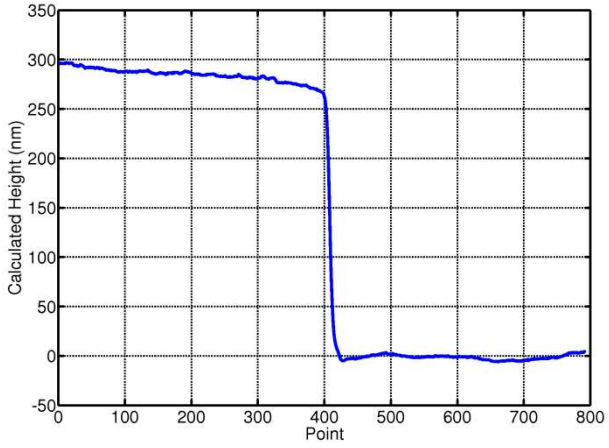

Figure 7.27 Step sample profile as determined experimentally using a Taylor Hobson CCI

The total measurement time was about 120 seconds, this being due to tunable laser used having a stepwise scan and requiring a long settling time of 0.5 seconds for a stable intensity to be obtained after each step. Each data point was averaged 4 times and figure 7.28 shows the acquired data using the MFI.

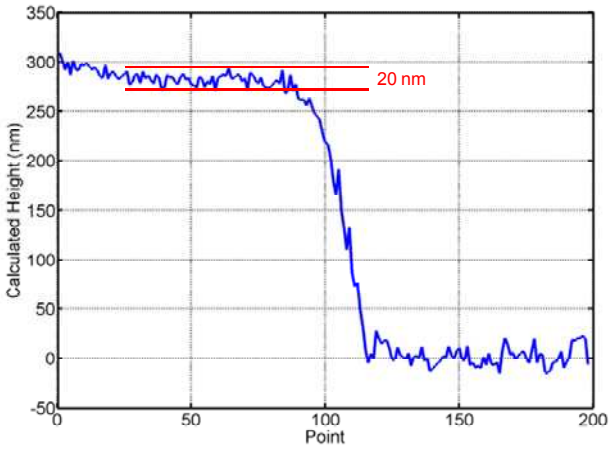

Figure 7.28 Step Height as measured using the fibre interferometer

A peak to peak uncertainity of approximately 20 nm is clearly present on the measurement result.

7.6 Discussion

7.6.1 Stabilised Reference Interferometer

The results for the unstabilised interferometer in section 7.5.1 are clearly quite severe and the qualitative improvement with the active stabilisation is enabled is stark. This is a good indication that the control loop is acting correctly.

Figure 7.19 suggests that the environmental drift is much worse than that experienced by the instrument in chapter 5. The laboratory conditions were identical in both situations, but figure 5.22 in chapter 5 shows much less drift on that instrument. This was anticipated as the fibre arms are virtually all fibre and as such would be expected to exhibit substantial optical path length change with environmental perturbation. There is also another polarising element in the reference arm, the linear polariser in the EOPM, which cause intensity variation in that arm. This is in addition to the polarisation dependency of the diffraction grating already present in the measurement arm.

7.6.2 Short Term Reference Interferometer Stability

The difference in the stability results between using the Schwider-Hariharan and the Carré algorithms is of some interest. The results are substantially better with the

Schwider-Hariharan which is apparently at odds with the slower loop rate it produces due to the 5 steps it uses which adds approximately 1.5 μs to the phase calculation period. This is somewhat offset by the longer execution time required by the Carré algorithm. This is in the main due to the square root in the numerator and the more complex arctangent unwrapping routine; as such similar performance might expected. One explanation could be due to the fact that the numerator in the Carré algorithm can become imaginary due to noise. This results in a zero being evaluated by the DSP and would then feed into the control algorithm with a resulting transient being applied to the EOPM.

7.6.3 SOP Variation in the Stabilised Measurement Interferometer

The results show very clearly the problem that SOP variation causes in the fringe visibility and certainly explains why there was low frequency drift present with the intensity based feedback used in chapter 5. Figure 7.23 clearly show large drift of the raw intensity values captured, even though the system is phase feedback stabilisation is active. The fact that all four intensity values drift in a similar fashion, that is the all are diminishing simultaneously in figure 7.23, suggests that it is an intensity variation in one or both of the interferometer arms due to a polarising element.

7.6.4 Reference Interferometer Stability Histogram

The control loop analysis performed in section 7.4 suggests that the vibration compensating performance should be improved over the PZT based method in chapter 5 which showed a 3 dB frequency of 1.6 kHz for the sensitivity function. In reality the peak to peak drift was found to be about ±10 nm when compared to roughly ±5 nm seen in chapter 5. In section 6.4 it was shown that the likely best case peak to peak noise was likely to be 4.4 nm due to the current ADC used. Bearing in mind that the noise analysis only considered those sources that were quantifiable, i.e. not of environmental origin, to land within a factor of two of the theoretical value seems reasonable. Because the limiting case of quantisation this must be attributed to the hugely increased disturbance imparted on the interferometer because of its all fibre nature.

7.6.5 Stabilised Measurement Interferometer

The values no longer form an obvious normal distribution but it would appear that the stability remains within 10 nm for over the full profile scan range. The resulting values are, as expected, somewhat worse than those for the reference interferometer. This is possibly in part due to the different optical paths taken from the point of diffraction to the surface. Perhaps surprisingly the results do not seem to degrade as the wavelength goes up and the measurement point moves away from the reference.

7.6.6 Step Height Measurement

Figure 7.27 and figure 7.28 show that the step height acquired with the MFI correlates well with the step height determined by the commercial instrument. The mean step height was approximately 283 nm for the MFI and 287 nm for the CCI, although the imperfect nature of the step height adds some uncertainty. Certainly the results are reasonable and lie within the uncertainty due to noise present on the MFI result.

Part of the inconsistency in profile could be due to some uncertainty in the exact positioning of the two profiles taken with each instrument. The step edge is seen to be much sharper due on the CCI results due to the higher NA lens used, resulting in greater lateral resolution. In addition the larger (non-optimised) spot size of the MFI setup effectively low pass filters this edge. The potential scan range of course is much longer though (9.4 mm) with the current lens used.

7.6.7 General Points

The measurement time is quite slow at 120 seconds however this is due to a limitation of the HP8168F laser (see section 4.6.6). The instability after a wavelength shift was not apparent with the previous Ando AQ4320D tuneable laser. Without the additional settling time for the laser the wavelength shifting would take only several ms yielding a much shorter measurement period. This could be further improved by using the continuous scanning tuneable laser.

With regards to the issues of noise and speed it may be anticipated that the instrument would benefit from the use of a 16 bit ADC to reduce the quantisation noise. In addition, the current DSP used is a low end model and much faster models are available on the market. A faster DSP would increase the loop rate and thus the

effectiveness of the stabilisation by making algorithm calculation faster. This would only be effective however if the DAC used to drive the EOPM was also changed. Currently it is a serial loading DAC (via the SPI) and as such is quite slow to update; this combined with its settling time means the phase stepping rate is mainly limited by this. A faster, parallel loading DAC would see an improvement in phase stepping. This would not only reduce the phase shift durations, which would enhance the insensitivity to SOP variation, but also increase the loop rate.

7.7 Conclusion

A rapid phase shifting method was implemented using an integrated optic electro-optic phase modulator (EOPM) as the actuator. This was operated in an open loop mode to provide fast phase stepping which in conjunction with a digital signal processor provided real time phase evaluation using a phase stepping algorithm. This calculated phase information was used as the feedback quantity for closed loop control in which the offset of the phase stepping waveform was adjusted to compensate for environmental disturbance.

The calculated phase data from the reference interferometer were stored in the DSP along with the associated raw phase shifted intensity values from the measurement interferometer. The values from the measurement interferometer were then uploaded at the PC at end of the measurement cycle and post processed in Labview to derive the surface height profile.

Several experiments were carried out to derive the effectiveness of the new phase retrieval and control method. Measurements were made of the reference interferometer stability as well as the measurement interferometer around several points on the profile. The results suggested peak to peak noise of ±10 nm for the measurement interferometer.

A step height measurement was also taken of a cold chrome coated step height sample. This result was seen to tally well with those taken from a Taylor Hobson CCI white light interferometer when the inherent differences in lateral resolution are taken into account. The MFI measured a step height of 283 nm, while the Taylor Hobson CCI produced a result of 287 nm. This confirms the operation of the MFI against a

commercial equivalent falls within the bounds of 20 nm peak to peak uncertainity present

The results of the experiments are summarised in table 7.2.

Parameter	Original Specification	Instrument Performance
Measurement Time	< 60 s	120 s
Vertical Uncertainty	< 0.5 nm RM (3 nm pk-pk)	20 nm pk-pk
Vertical Range	> 0.5 µm	0.775 µm
Lateral Range	Diffraction Limited	~3.2 mm
Lateral Resolution	Diffraction Limited	Untested

7.2 Experimental Results

Clearly the measurement time is much longer than the original specification, but this is due to the slow nature of the HP8168F tuneable laser.

It is anticipated that the stability of the MFI will be much improved by an increase of phase stepping speed and reduction of quantisation noise. The phase stepping speed may be increased by using a faster parallel loading DAC and faster DSP. The reduction in quantisation noise could be obtained by using a higher resolution ADC than that currently used onboard the DSP. This is easily achievable in engineering terms by implementing higher specification commercial integrated circuits.

The probe size resulting from this design is seen to be substantially more compact than that of chapter 5 as the reference arm of the interferometers is contained within the optical fibre.

As with chapter 5, the lateral range and resolution have not been assessed for diffraction limited performance as this will only be achievable by custom optical probe design and manufacture. As such it is outside the scope of this thesis.

8 Discussion and Conclusions

8.1 Introduction

The aim of this chapter is to summarise and consider the results from the investigations made in chapters 5, 6 and 7. At the end of each of chapter there has already given a comprehensive and detailed discussion of the results obtained. Here the aim is to tie that together, compare the results and draw an overall conclusion.

The two practical instruments investigated are both multiplexed fibre interferometers which use wavelength scanning to realise the measurement of a surface profile using an optical stylus technique. There were two major differences between the instruments investigated in chapters 5 and 7. First, the control method used to stabilise the sensitive fibre interferometer against the effects of acoustic and temperature change in the environment. Secondly, the physical structure (and size) of the optical probe used to carry out the wavelength scanning. The instrument in chapter 7 has a substantially smaller footprint due to the removal of the reference arm from the optical probe. These results will be fully quantified in the following sections

8.2 Summary of Investigations

8.2.1 First Multiplexed Fibre Interferometer

In chapter 5 an interferometer was investigated in which separate reference and measurement interferometers were wavelength multiplexed into the same length of optical fibre. This allowed for the use of a reference interferometer to actively control the interferometer in the face of optical path length variation due to environmental effects. The active stabilisation was realised using an analogue PI controller to actuate a piezoelectric translator (PZT) mounted mirror in the reference arm. This active stabilisation also allowed for highly accurate closed loop implementation of phase shifting interferometry to deduce the phase due to surface height. In this way the usual non-linearities associated with PZT operation were minimised.

The instrument also developed the idea of an optical stylus that was realised using wavelength scanning and an optical probe consisting of a reflective grating and

objective lens. Using this method the structure of a step height was successfully resolved.

One major issue discovered with the stability of the instrument was that although relatively high frequencies were being successfully compensated by the control loop, there was still some low frequency drift apparent. This was determined to be due to low frequency drift associated with state of polarisation (SOP) evolution in single mode fibre. Although the instrument was essentially a free space interferometer, the input SOP was time varying and the diffraction grating showed some polarisation dependence.

8.2.2 Second Multiplexed Fibre Interferometer with Rapid Phase Shifting.

Chapter 7 describes a second instrument designed to overcome the effects of SOP variation in single mode fibres by using a rapid phase shifting (RPS) method. The aim was to rapidly acquire the raw intensity data using phase shifting within a period of microseconds. In this way an accurate phase result can be calculated with negligible effect from any low frequency drift associated with SOP variation.

The RPS was implemented using a digital signal processor (DSP) and an electro-optic phase modulator (EOPM) to provide the fast open loop phase shifting needed. Active stabilisation was then implemented digitally using calculated phase as the feedback element as opposed to intensity. The method was shown to successfully stabilise the interferometer although the stability appeared to be somewhat worse than that experienced in the first instrument.

A step height sample was once again measured using this method and was found to be in good agreement with a result from a Taylor Hobson CCI. The step heights obtained were within the uncertainty imposed by the residual noise present on the MFI. Confirmation of the optical stylus method for the measurement of step heights was thus obtained.

8.2.3 Noise Sources and Magnitudes

In chapter 6 the various sources of noise effecting fibre interferometers were considered in depth. Their likely worst-case magnitudes were calculated with consideration to their power spectral densities and listed in order of severity.

Currently it would appear that the rapid phase shifting (RPS) method is limited by a combination of the analogue to digital converter (ADC) resolution and the signal conditioning which is needed to make use of the full ADC range.

Importantly, the theoretical evaluation of the major noise sources suggests that there are no fundamental noise sources present that would prevent sub-nanometric resolutions being attained. The theoretical calculations in section 6.4 derived an anticipated peak to peak uncertainty of 0.184 assuming a working fringe visibility of 0.5 nm.

8.3 Discussion Points

8.3.1 Instrument Comparison

Table xxx presents a side by side comparison of the two instrument types studied in this thesis, along with the original specification as laid out in section 5.1

Parameter	Original Specification	Chapter 5 Instrument	Chapter 7 Instrument
Measurement Time	< 60 s	8 s	120 s
Vertical Uncertainty	< 0.5 nm RM (3 nm pk-pk)	11 nm pk-pk	20 nm pk-pk
Vertical Range	> 0.5 µm	0.775 µm	0.775 µm
Lateral Range	Diffraction Limited	~3 mm	~3.2 mm
Lateral Resolution	Diffraction Limited	Untested	Untested
Probe Form Factor	Not Specified	70 x 100 mm	70 x 30 mm

Table 8.1 Comparison of instrument performance

It is clear from the table that while the form factor of the optical probe has been substantially reduced in the chapter 7 instrument, the measurement time and vertical uncertainty performance is somewhat worse. Furthermore neither instrument meets the original specification in terms of vertical uncertainty.

8.3.2 Discrepancy between Stability Results

One obvious concern is that the peak to peak stability measured in the reference interferometer in chapter 7 is worse than that seen in the instrument in chapter 5.

There would be an expectation of an improvement if the RPS method had overcome the problem of low frequency drift. There are several feasible explanations for this and it is likely that a combination have conspired to produce the result.

The instrument in chapter 7 is inherently much more unstable than that of chapter 5 due to its all-fibre configuration. It is also substantially more sensitive to SOP variation due to the added polariser integrated to the EOPM. This gives a more difficult challenge for any control loop from the outset. Nonetheless, the theoretical evaluation given in section 7.4 suggests that the evaluation rate of the RPS should be enough to compensate successfully above the frequencies managed by the PZT method in chapter 5. In addition the SOP variation issue should be solved by the RPS method.

The noise evaluation in chapter 6 suggests that the problem may lie in the ADC front end. Table 6.1 shows the calculated SNR due to quantisation noise for the 12 bit ADC used. This in itself accounts for 4.8 nm peak to peak deviation. Of course the noise value derived assumes the signal fully covers the conversion range and anything less will degrade the noise performance further.

Further evidence for the argument that the instability is down to quantisation noise is given by examination of the reference interferometer stability in figure 7.24. Here it can be seen that although that the reference interferometer outputs form a normal distribution. This is not indicative of random low frequency drift affecting the control accuracy of the control loop. The normal distribution is clearly centred on the control setpoint.

8.3.3 Relative Probe Sizes

One important point to be made for the instrument in chapter 7 is the relative compact size of the optical probe. This is due to the fact that the reference arm is no longer present in the probe itself, but is formed remotely through an optical fibre which may be ‘folded’ away from the on-line mounted optical probe. This opens up the way for substantial miniaturisation of the probe with a more optimised custom design. Both the diffraction grating and the objective lens could be made substantially smaller than they currently are. The instrument in chapter 5 has its reference arm as part of the optical probe, as it uses the zero order (reflected) beam

from the diffraction grating. This as substantial foot print to the any optical probe using such a design. This importance of being able to miniaturise probe size should not be underestimated as small probe size is a key factor in any on-line application.

8.3.4 Measurement Period

One of the important attributes outlined in chapter 2 for an on-line probe is that the measurement should be fast in order to limit downtime in the manufacturing process. The measurement cycle for the instrument in chapter 5 was around 5 seconds which is acceptable. However in chapter 7 the measurement period is substantially longer at 120 seconds. The important point to note is that this is not inherent in the measurement method, but is due to a limitation in the HP8168F tuneable laser. When the laser turns on there is a substantial transient in the intensity output and as such after each wavelength shift it is necessary to allow the laser to settle. This takes in the region of 1.5 seconds; the time required to acquire the data for a measurement is only about 25 μs. Thus with a faster laser source, with continuous tuning (like the original Ando AQ4320D) sub-second measurements are feasible.

8.3.5 Stability and Noise Performance

The investigations carried out in chapter 5 with regard to noise rejection appeared to be quite promising and suggested that a separate measurement interferometer works well at rejecting disturbance from surface vibration. The measurement interferometer stability for both the instruments in chapters 5 and 7 was shown to be somewhat worse than the reference interferometer stability.

Even though the optical probe design is similar in the case of both instruments, the difference in stability for the instrument in chapter 5 is larger than in chapter 7. This can be attributed to the lack of SOP resistant compensation provided by the intensity feedback used in the control loop. Any reference variation caused by visibility variation (as opposed to path length change) will result in an error signal being imparted upon the measurement interferometer.

In chapter 7 the stability difference between the reference and measurement interferometers is found to be much smaller. While this is promising and indicative of

the benefits of using the RPS method for improving stability, there is still some degradation.

It is considered that there could be several reasons for the stability reduction in the measurement interferometer. One obvious possibility is that the optical paths are only common up until the dispersion takes place at the grating. After this they follow slightly different paths, separated in air.

Another likely contributor is the fibre Bragg gratings (FBGs) used to de-multiplex the reference and measurement wavelengths. Here it was found that the units used only provided 25 dB of isolation between the reference and measurement wavelengths. As such it is possible that during wavelength scanning some of the varying measurement interferometer power could feasibly leak into the reference interferometer output. Any error caused by such a power leakage would results in noise being imparted onto the optical path compensation loop. Even without the wavelength scanning it is possible that fringe visibility variation due to SOP change in the measurement interferometer could produce a similar effect.

One solution would be to improve the isolation of the reference wavelength using a different method for de-multiplexing the two wavelengths; possible using a grating or narrowband thin film filter.

8.4 Conclusion

Two interferometry based instruments were investigated with a view to producing a device with a compact probe that is robust against environmental effects. The aim was to deliver non-contact profiling measurement at the nano-scale with the potential for on-line application.

Both instruments investigated were based upon the concept of combining wavelength scanning and a dispersive element to create an optical stylus that could be swept along a surface profile. By sweeping the stylus height information can then be determined using phase shifting interferometry.

Both instruments investigated required the stabilising of the optical path lengths in the interferometer arms before any surface measurement took place. This was done by multiplexing in a separate reference wavelength to track the path length change. It

was then possible to servo the path length using closed loop control and a suitable actuator.

The first instrument, investigated in chapter 5 was used to successfully resolve a step height and was shown to be able to substantially reduce an induced disturbance to the measurand within a frequency range limited by the PZT actuator. However, the system was seen to be susceptible to low frequency drift due to polarisation state evolution in the fibre.

A second instrument, described in chapter 7, aimed to solve the low frequency drift problem by employing a rapid phase shifting method to allow real-time phase evaluation of the reference interferometer. The rate at which the phase was calculated allowed it to be used directly as the feedback element in the control loop. This resulted in a more environmentally stable interferometer even in the face of SOP variation. The absolute stability was seen however to be limited by the resolution of the analogue to digital conversion process.

The all-fibre design of the second instrument also allowed for an optical probe that could be substantially reduced in size with a more optimal custom design. This feature, due to the fact that the all-fibre reference arm can be remote from the measurement arm, is vital if a small optical probe for online mounting is to be fashioned.

The outcome of the investigations described in this thesis is to prove the feasibility of an optical fibre based approach to non-contact probing for surface metrology using an optical stylus technique. Clearly there are improvements that must be made from an engineering standpoint; the analogue to digital conversion process needs improving, and a faster digital signal processing unit should improve performance in terms of environmental robustness. In addition an optimised optical probe, corrected for aberration and suitable calibrated is required.

In chapter 6 it was determined that there should be no theoretical limitation, due to fundamental physical effects, to achieving sub-nanometre resolutions with the stabilised fibre interferometer.

The novel work contained within this thesis is comprised of:

- Development and demonstration of a rapid phase shifting technique using an integrated optic electro-optic modulator to obtain real-time phase information from a fibre interferometer which is insensitive to polarisation state evolution.
- Development and demonstration of active vibration compensation using real-time calculated phase feedback to stabilise the all-fibre interferometer path length by the use of a separate reference wavelength.
- Demonstration of a stabilised multiplexed fibre interferometer to resolve a step height of several hundred nanometres using a compact, remote mountable fibre probe.

The work contained in chapter 5 of this thesis has been published in Applied Optics (Martin et al. 2008). The instrument is also covered by an international patent (Jiang et al. 2007c).

The work carried out on the instrument in chapter 7 published in Optics Letters (Martin & Jiang, 2009)

In addition the work lead to the award of 'The Vice-Chancellor's Prize of Postgraduate Researcher of the Year 2009'. The work is also covered by an international patent. A full publications list is given in the 'Publications and Awards' section at the rear of this thesis.

9 Further Work

The work contained in this thesis suggests the feasibility of an optical fibre based approach to surface profiling at the nanoscale. However there are several areas that require further development and investigation in order to make the fibre interferometer a viable tool for nano-scale surface measurement.

The excessive noise still present in the system must be reduced further. As was shown in chapter 6 it is highly likely that this could probably be done by simply improving the ADC electronics to improve the effective resolution of the closed loop control. The theoretical treatment of potential noise sources within the fibre interferometer suggests that there are no other noise sources of comparable magnitude, however this needs to be confirmed experimentally.

In general the system requires work in optimising the signal processing in terms of speed and noise reduction. Because of the relative low-level of technology used for the real-time phase calculation there is plenty of scope for reducing execution time and increasing the control loop rate. This will increase the closed loop frequency response and will increase robustness against external vibration. It may well also improve the noise performance at a lower level.

The other main limitation is that of the HP8168F tuneable laser used as the measurement interferometer source. The major limitation is the speed at which it is able to tune wavelength. The stepwise nature of the wavelength tuning is not only slow, but it became apparent in operation that a large period of settling time is required between steps in order for the laser amplitude to stabilise. One solution to this problem is quite clear, a more suitably specified tunable laser could be sourced.

Another potentially more interesting route would be to utilise a miniaturised integrated-optic tuneable laser. This device is being developed at the University of Huddersfield in conjunction with the Centre for Integrated Photonics (EPSRC Grant EPE03733X1). Such a device has two major benefits over commercially available tuneable laser devices. First, the small form factor of the device could aid integration of the source into any fibre interferometer for on-machine mounting. Secondly, the device design utilises passive mounting of the various component parts wherever

possible. When coupled with mass producible technologies such as vapour deposition and etching which are used to produce the integrated waveguides, the costs of such a device are envisaged to be substantially lower than current commercial tuneable lasers. This is particularly attractive as the tuneable laser is by far the most costly component of the fibre interferometer system.

A more detailed analysis of the optical probe needs to be performed. This work would lead to a more optimal design in terms of lateral resolution and overall probe size. In addition the effects of potential lens aberrations need to be fully understood in terms their effect on lateral resolution on optical path variation over the field of view. It is anticipated that the latter could, to a large degree, be accounted for using a suitable calibration procedure.

The system needs to be applied to a larger variety of artefacts to deduce performance limits in terms of such surface parameters as slope angle and reflectivity. This will determine the capabilities for the measurement of more complex structures.

Considering the concept of an alternative light source in place of a tunable laser also presents an interesting avenue for further work. The replacement of the relatively expensive tuneable laser with a broadband light source such as a super luminescent light emitting diode (SLED) would also be hugely beneficial in reducing the costs of the overall measurement system. One possible idea for such a system is shown in figure 9.1.

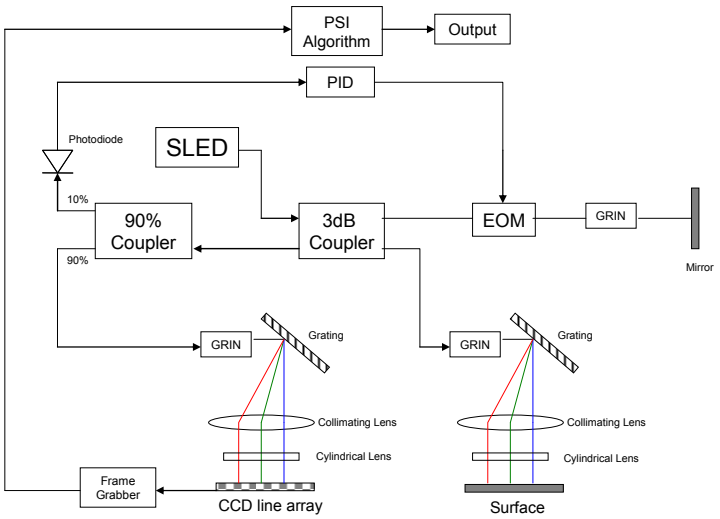

Figure 9.1 Proposed idea for SLED based fibre interferometer.

Here the whole profile is illuminated simultaneously with a broadband light source. A CCD line array and grating is used as a spectrometer and the phase shifting is performed by an EOPM. Such a setup would likely require a change in fibre components suitable for an operating wavelength range suitable for the use of CCD detectors in order to be financially viable. SLEDs operating at wavelengths as short as 650 nm are commercially available at the time of writing.

Such a system would be beneficial not only in terms of cost but also in terms of speed because the whole profile is captured simultaneously. It is feasible to have profile capture rates up to 10 kHz if fast CCD line arrays are used with a powerful enough SLED source. The reduction of the operating wavelength would reduce the range obtainable in operation, a 830 nm SLED would provide a unambiguous vertical range of 415 nm. This would be coupled with a increase in vertical and lateral resolution however making such a method potentially suited for some nano-scale measurement applications.

Publications and Awards

Refereed Journal Papers

Martin, H. and Jiang, X. (2009) Rapid phase-shifting fibre interferometer with optical stylus. Opt. Lett. 35(5), pp. 655-657.

Martin, H., Wang, K. and Jiang, X. (2008) Vibration compensating beam scanning interferometer for surface measurement. Appl. Opt. 47, 888-893.

Martin, H., Wang, K. and Jiang, X. (2008) Actively stabilized optical fibre interferometry technique for online/in-process surface measurement. Rev. Sci. Instrum. 79, 023109.

Refereed Conference Papers

Martin, H. and Jiang, X. Stabilising fibre interferometers for online surface measurement. Polymer Process Engineering International Conference, Bradford, UK, October 2009.

Wang, K., Jiang, X. and Martin, H. Advances of optical fibre interferometer for on-line surface measurement. The 11th International Conference on Metrology and Properties of Engineering Surfaces (Met & Props 2007), 17th-20th July 2007, University of Huddersfield, Huddersfield, UK

Wang, K., Jiang, X., Martin, H. and Blunt, L. Light-beam scanning interferometry for on-line ultra precision surface measurement. 7th international conference of the European Society for Precision Engineering and Nanotechnology, Bremen, Germany, May 2007

International Patents

Jiang, X., Wang, K., Martin, H. and Yang, S. (2007), (WO/2007/144654) Surface Characteristic Determining Apparatus.

Non-refereed Conference Papers

Martin, H and Jiang, X. (2008) Stabilising Fibre Interferometers. University of Huddersfield Researchers' Conference. Huddersfield, UK

Martin, H and Jiang, X. (2007) Vibration Compensating Beam Scanning Interferometer for Surface Measurement. University of Huddersfield Researchers' Conference . Huddersfield, UK

Martin, H and Jiang, X. (2006) A self-stabilising multiplexed fibre interferometer for on-line surface measurement. University of Huddersfield Researchers' Conference, Huddersfield, UK.

Awards

Vice-Chancellor's Prize of Postgraduate Researcher of the Year 2009

References

Abbott, E. and Firestone, F. 1933. Specifying surface quality: a method based on accurate measurement and comparison. Mechanical Engineering. 55, pp. 569-572.

Ando Electric Co., Ltd., 1999. Ando AQ4320 Series User Manual. Japan.

Annovazzi-Lodi, V., Donati, S. and Merlo, S. 1996. Thermodynamic phase noise in fibre interferometers. Optical and Quantum Electronics. 28, pp. 43-49.

Bass, M. and Stryland, E., 2001. Fibre optics handbook: fibre, devices, and systems for optical communications. 2nd ed. New York: McGraw-Hill.

Bauza, M., Woody, S., Smith, S. and Hocken, R. 2006. Development of a rapid profilometer with an application to roundness gauging. Precision Engineering. 30, pp. 406-413.

Blunt, L. and Jiang, X. 2003. Numerical Parameters for Characterisation of Topography. In L. Blunt and X. Jiang eds. Advanced Techniques for Assessment Surface Topography. London: Kogan Page Science. Ch. 3.

Bucholtz, F., 1991. Fibre Optic Magnetic Sensors. In E. Udd ed. Fibre Optic Sensors: an Introduction for Engineers and Scientists. New York: John Wiley & Sons. Ch. 12.

Buck, J.A., 2004. *Fundamentals of Optical Fibers*. 2nd ed. New Jersey: John Wiley & Sons

Buckingham, M. 1983. Noise in Electronic Devices and Systems. Chichester, UK: Ellis Horwood Limited.

Burr Brown. 1996. BUF634 Datasheet. Available at http://www.ti.com/lit/gpn/buf634 [Accessed 1st July 2009].

Carré, P., 1966. Installation et utilisation du comparateur photoelectrique et interferentiel du Bureau International des Poids et Mesures. Metrologia 2(1), pp. 13-23.

Charlette, P. and Hunter, I., 1996. Robust phase-unwrapping method for phase images with high noise content. Appl. Opt. 35(19), pp. 3506-3513.

Cheng, Y. and Wyant, J., 1985a. Two-wavelength phase shifting interferometry. Applied Optics, 23(24), pp. 4539-4543.

Cheng, Y. and Wyant, J., 1985b. Multiple-wavelength phase-shifting interferometry. Applied Optics, 24(6), pp. 804-807.

Cheng, Y. and Wyant, J., 1985c. Phase shifter calibration in phase-shifting interferometry. Appl.Opt. 24(18), pp. 3049-3052.

Chomycz, B., 2000. Fibre Optic Installer's Field Manual. New York: McGraw-Hill.

Cliche, J. and Têtu, M. 2005. Effect of Laser Linewidth Reduction Systems on Coherence Length and Interferometer Noise. Digest of the LEOS Summer Topical Meetings. San Diego, 25-27 July 2005, IEEE.

Cole, J., Danver, B. and Bucaro, J., 1982. Synthetic-Heterodyne Interferometric Demodulation. IEEE J. of Quantum Electronics, 18(4), pp.694-697.

Collett, E., 2003. *Polarized Light In Fibre Optics.* USA: SPIE Press

Conroy, M. 2009. Advances in thick and thin film analysis using interferometry. Wear 266, pp. 502-506.

Creath, K., 1988. Phase-Measurement Interferometry Techniques. In E. Wolf ed. Progress in Optics. XXVI. Amsterdam: Elsevier Science Publishers. Ch. 5.

Culshaw, B. and Giles, I., 1982. Frequency Modulated Heterodyne Optical Fibre Sagnac Interferometer. IEEE, J. of Quantum Electronics, 18(4), pp.690-693.

Dandridge, A. and Tveten, A. 1981. Phase noise of single mode diode lasers in interferometer systems.

Dandridge, A. and Tveten, A., 1982. Phase compensation in interferometric fibre-optic sensors. Opt. Lett. 7(6), pp.279-281.

Dandridge, A., and Goldberg, L., 1982. Current-induced frequency modulation in diode lasers. Electronics Letters. 18(7), pp. 302-304.

Dandridge, A., Tveten, A., Miles, R. and Giallorenzi, T. 1980. Laser noise in fibre-optic interferometer systems. Appl. Phys. Lett. 37(6), pp. 526-528.

Depuy, M. 1967. High-precision optical profilometer for the study of micro-geometrical surface defects. Proc Instn Mech Engrs. 182(3K), pp. 255-259.

Dhanasekar, B., Mohan, N., Bhaduri, B. and Ramamoorthy, B. 2008. Evaluation of surface roughness based monochromatic speckle correlation using image processing. Precision Engineering. 32, pp. 196-206.

Dorf, R. and Bishop, R. 1998. Modern Control Systems. 8th ed. Menlo Park, CA: Addison Wesley Longman.

Dresel, T., Hausler, G., and Venzke, H., 1992. Three-dimensional sensing of rough surfaces by coherence radar. Appl. Opt., 31(7), pp. 919-3925.

Dutton, H.J.R., 1998. *Understanding Optical Communications*. New Jersey: Prentice Hall.

E.C. Contract No SMT4-CT98-22561. 1998. The Development of a Basis for Three

Dimensional Surface Roughness Standards.

Elmore, W. and Heald, M. 1985. *Physics of Waves.* New York: Dover Publications.

Engelberg, S. 2007. Random Signals and Noise a Mathematical Introduction. Boca Raton, FL: Taylor & Francis Group.

Ferreira, L., Santos, J. and Farahi, F. 1995. Polarization-induced noise in a fibre-optic Michelson interferometer with Faraday rotator mirror elements. Applied Optics. 34(28), pp. 6399-6402.

Fish, P. 1993. Electronic Noise and Low Noise Design. London: The Macmillan Press.

Fritsch, K. and Adamovsky, G., 1981. Simple circuit for feedback stabilisation of a single mode optical fibre interferometer. Rev. Sci. Instrum. 52(7), pp.996-1000.

Gao, G., Aoki, J., Ju, B. and Kiyono, S. 2007. Surface profile measurement of a sinusoidal grid using an atomic force microscope on a diamond turning machine. Precision Engineering. 31, pp. 304-309.

Gasulla, I. and Campany, J., 2008. 1 Tb/s·km Multimode fibre link combining WDM transmission and low-linewidth lasers. *App. Opt.*, 16(11), pp.8033–8038

Gerrard, A. and Burch, J.M., 1994. *Introduction to Matrix Methods in Optics*, London: John Wiley & Sons.

Glenn, W. 1989. Noise in Interferometric Optical Systems: An Optical Nyquist Theorem. IEEE J. of Quantum Electronics. 25(6), pp. 1218-1224.

Goldstein, D., 2003. *Polarized Light*. 2nd ed. New York: Marcel Dekker.

Hariharan, P., 1992. The Basics of Interferometry. London: Academic Press Ltd.

Hariharan, P., Oreb, B. and Eiju, T., 1987. Digital phase-shifting interferometry: a simple error-compensating phase calculation, Appl. Opt., 26(13), pp. 2504-2506

Heidrich, H., Hoffman, D. and Noé, R. 1998. Endless Polarisation Control Systems for Coherent Optics. J. Lightwave Technology 6(7), pp. 1199-1208.

Heismann, F. 1994. Analysis of a Reset-Free Polarization Controller for Fast Automatic Polarization Stabilization in Fibre-Optic Transmission Systems. J. Lightwave Technology 12(4), pp. 690-699.

Herraez, M., Gdeisat, M., Burton, D. and Lalor, M., 2002. Robust, fast and effective two-dimensional automatic phase unwrapping algorithm based on image decomposition. Appl. Opt. 31(35), pp. 7445-7455.

Hewlett Packard, 1998. HP 8168 Series User Manual. Available at http://cp.literature.agilent.com/litweb/pdf/08168-91031.pdf [Accessed 2 June 2009].

Hicks, T. and Atherton, P. 1997. The Nanopositioning Book. Bracknell, UK: Queensgate Instrument Ltd.

Ho, H., Lo, K., Fong, W. and Wu, C., 2000. Passive phase demodulation and laser-noise compensation scheme for fibre interferometers. Electronics Letters, 36(16), pp. 1362-1651.

Hobbs, P. 1997. Ultrasensitive laser measurements without tears. Applied Optics. 36(4), pp. 903-920.

Hobbs, P.C.D., 2000. Building Electro-Optical Systems. Making It All Work. New York: John Wiley & Sons.

Horowitz, P. and Hill, W., 1994. The Art of Electronics. 2nd ed. Cambridge: Cambridge University Press.

Huang, P. and Zhang, S., 2006. Fast three-step phase-shifting alogorithm. Appl. Opt. 45(21), pp. 5086-5091.

IEEE 488.1. (2003). Standard For Higher Performance Protocol for the Standard Digital Interface for Programmable Instrumentation. IEEE.

IEEE 488.2. (1992). Standard Codes, Formats, Protocols, and Common Commands For Use With IEEE-488.1. IEEE.

Ishii, Y., Chen, J. and Murata, K. 1987. Digital phase-measuring interferometry with a tuneable laser diode. Opt. Lett., 12(4), pp. 233-235

Jackson, D., Kersey, A., Corke, M. and Jones, J., 1982. Pseudoheterodyne detection scheme for optical interferometers. Electronics Letters. 18(25), pp. 1081-1083

Jackson, D., Priest, R., Dandridge, A. and Tveten, A., 1980. Elimination of drift in a single-mode optical fibre interferometer using a piezoelectrically stretched coiled fibre. Appl. Opt. 19(17), pp.2926-2929.

Jenkins, F.A. and White, H.E., 1976. *Fundamentals of Optics*. 4th ed. New York: McGraw-Hill.

Jiang, X. and Blunt, L. 2004. Third generation wavelet for the extraction of morphological features from micro and nano scalar surfaces. Wear 257, pp. 1235-1240.

Jiang, X., Scott, P., Whitehouse, D. and Blunt, L. 2007a. Paradigm shifts in surface metrology. Part I. Historical philosophy. Proceedings of the Royal Society A. 463, pp. 2049-2070.

Jiang, X., Scott, P., Whitehouse, D. and Blunt, L. 2007b. Paradigm shifts in surface metrology. Part II. The current shift. Proceedings of the Royal Society A. 463, pp. 2071-2099.

Jiang, X., Wang, K., Martin, H. and Yang, S. 2007c. Surface characteristic determining apparatus. WO2007144654.

Johnson, M. (1981). Poincaré representation of birefringent networks. Appl. Opt. 20(12), pp. 2075-2080.

Johnson, M. 2003. Photodetection and Measurement.Blacklick, OH, USA: McGraw-Hill Professional Publishing.

Johnson, M., 1981. Poincaré representation of birefringent networks. Appl. Opt., 20(12), pp.2075-2080.

Kaminow, I and Li, T. 2002. Optical Fibre Telecommunication IVA Components. London: Academic Press.

Kaminow, I. 1981. Polarization in Optical Fibers. Journal of Quantum Electronics. 17(1), pp. 15-22.

Kashyap, R. and Nayar, B., 1983. An All Single-Mode Fibre Michelson Interferometer Sensor. IEEE J. of Lightwave Technology, 1(4), pp.619-624.

Kemao, Q., Fangjun, S., and Xiaoping, W. 2000. Determination of the best phase step of the Carré algorithm in phase shifting interferometry. Meas. Sci. Technol. 11, pp. 1220–1223.

Kersey, A., Marrone, M. and Dandridge, A. 1990. Analysis of Input-Polarization-Induced Phase Noise in Interferometric Fibre-optic Sensors and Its Reduction using Polarization Scrambling. J. Lightwave Technology 8(6), pp. 838-845.

Kiong, T., Quing-Guo, W. and Chieh, H. Advances in PID Control. London: Springer-Verlag.

Koo, K., Tveten, and Dandridge, A., 1982. Passive stabilization scheme for fibre interferometers using (3x3) fibre directional couplers. Appl. Phys. Lett. 41(7), pp.616-618.

Kråkenes, K. and Bløtekjær. 1995. Comparison of Fibre-Optic Sagnac and Mach-Zehnder Interferometers with Respect to Thermal Processes in the Fibre. J. of Lightwave Technology. 13(4), pp. 682-686.

Lehmann, P., Patzelt, S. and Schöne, A. 1997. Surface roughness measurement by means of polychromatic speckle elongation. Applied Optics. 36(10), pp. 2188-2197.

Leigh, J. 1985 *Applied Digital Control*. 2nd ed. Hemel Hempstead, UK: Prentice-Hall Ltd.

Lin, D., Jiang, X., Fang, X., Zhang, L., Zhang, W. and Bennion, I., 2004. High stability multiplexed fibre interferometer and its application on absolute displacement measurement and on-line surface metrology. Optics Express, 12(23), pp. 5729- 5734.

Lynn, P. and Fuerst, W. 2000. *Introductory Digital Signal Processing with Computer Applications.* Chichester, UK: John Wiley & Sons Ltd

Martin, H. and Jiang, X. (2009) Rapid phase-shifting fibre interferometer with optical stylus. Opt. Lett. 35(5), pp. 655-657.

Martin, H, Wang, K and Jiang, X. (2008) Vibration compensating beam scanning interferometer for surface measurement. Appl. Opt. 47(7), pp. 888-893.

Mazzeo, A., Stein, A., Trumper, D. and Hocken, R. 2009. Atomic force microscope for accurate dimensional metrology. Precision Engineering. 33, pp. 135-149.

Medicus, K., Chaney, M., Brodziak, J. and Davies, A., 2007. Interferometric measurement of phase change on reflection. Appl. Opt. 46(11), pp. 2027-2035.

Mitchell, G., 1991. Intensity Based and Fabry-Perot Interferometer Sensors. In E. Udd ed. Fibre Optic Sensors: an Introduction for Engineers and Scientists. New York: John Wiley & Sons. Ch. 12.

Molesini, G. and Quercioli, F. 1986. Pseudocolor effects of longitudinal chromatic aberration. Journal of Optics (Paris). 17(6), pp. 279-282.

Moshlei, B. 1986. Analysis of Optical Phase Noise in Fibre-optic Systems Employing a Laser Source with Arbitrary Coherence Time. Journal of Lightwave Technology 4(9), pp. 1334-1351.

Moshlei, B. 1986. Noise Power Spectra of Optical Two-Beam Interferometers Induced by the Laser Phase Noise. J. of Lightwave Technology. 4(11), pp. 1704-1709.

Muller, E., Reichert, W., Ruck, C. and Steiner, R., 1993. External Cavity Laser Design and Wavelength Calibration. HP Journal, 4(1), pp.20-27. Available at http://www.hpl.hp.com/hpjournal/pdfs/IssuePDFs/1993-02.pdf [Accessed 2 June 2009].

Muralikrishnan, B., Stone, J. and Stoup, J. (2006) Fibre deflection probe for small hole metrology. Precision Engineering 30, pp. 154-164.

Musha, T., Kamimura, J. and Nakazawa, M., 1982. Optical phase fluctuations thermally induced in a single-mode fibre. Appl. Opt., 21(4), pp. 694-698.

National Instruments. 2007. NI 622x Specifications. Available at http://www.ni.com/pdf/manuals/371290g.pdf [Accessed 1st July 2009].

New Focus. 2009. *New Focus Application Note 2.* http://www.newfocus.com/products/documents/literature/apnote2.pdf; Date accessed 9/9/2009.

Newson, T., Farahi, F., Jones, J. and Jackson, D. 1989. Reduction of semiconductor laser diode phase and amplitude noise in fibre optic sensors. Applied Optics. 28(19), pp. 4210-4215.

NG, T. 1996. The one-step phase-shifting technique for wave-front interferometry. J. of Modern Optics, 43(10), pp. 2129-2138.

Noda, J., Okamoto, K. and Sasaki, Y. 1986. Polariazation-Maintaining Fibres and Their Applications. Journal of Lightwave Technology. Vol LT-4 (8), pp. 1071-1088.

Nussbaum, A. and Phillips, R.A., 1976. *Contemporary Optics For Scientists And Engineers.* New Jersey: Prentice-Hall

Okoshi, T. 1985. Polarisation-State Control Schemes for Heterodyne or Homodyne Optical Fibre Communications. J. Lightwave Technology 3(6), pp. 1232-1237.

Palmer, C. 2005. *Diffraction Grating Handbook.* 6th ed., Newport Corporation. Available at http://gratings.newport.com/information/handbook/cover.asp [Accessed 11 June 2009].

Pampaloni, F. and Enderlein, J., 2004. Gaussian, Hermite-Gaussian, and Laguerre-Gaussian beams: A primer. *prepress*, arXiv:physics/0410021.

Petermann, K. and Weidal, E. 1981. Semiconductor Laser Noise in an Interferometer System. J. of Quantum Electronics. 17(7), pp. 1251-1256.

Physik Instrumente 2005. Designing with PiezoElectric Transducers: Nanopositioning Fundamentals. Available at http://www.physikinstrumente.com/en/pdf_extra/PI_designing_with%20piezo_actuators_tutorial_2005c.pdf [Accessed 1st July 2009].

Physik Instrumente. 2008. E-661 Piezo Controller with Parallel Interface. Available at http://www.physikinstrumente.com/en/pdf/E661_Datasheet.pdf [Accessed 1st July 2009].

Physik Instrumente. 2009a. P-810 · P-830 Piezo Actuators. Available at http://www.physikinstrumente.com/en/pdf/P810_Datasheet.pdf [Accessed 1st July 2009].

Physik Instrumente. 2009b. P-721 PIFOC Piezo Flexure Objective Scanner. Available at http://www.physikinstrumente.com/en/pdf/P721_Datasheet.pdf [Accessed 1st July 2009].

Pickelmann, L. 2003. Piezomechanics: An Introduction. Available at http://www.piezomechanik.com/f/core/frontend/http/http.php?dl=47-file-1 [Accessed 1st July 2009].

Polhemus, C., 1973. Two-Wavelength Interferometry. Applied Optics, 12(9), pp. 2071-2074.

Qian, K., Fangjun, S. and Xiaoping, W. 2000. Determination of the best phase step of the Carré algorithm in phase shifting interferometry. Meas. Sci. Technol. 11, pp. 1220-1223.

Rashleigh, S. 1983. Origins and Control of Polarisation Effects in Single-Mode Fibers. Journal of Lightwave Technology. LT-1(2), pp. 312-331.

Rhee, H., Vorburger, T., Lee, J. and Fu, J. 2005. Discrepancies between roughness measurements obtained with phase-shifting and white-light interferometry. Applied Optics. 44(28), pp. 5919-5927.

Saleh, B.E.A and Teich, M.C., 1991. *Fundamentals of Photonics*. New York: John Wiley & Sons.

Salehi, M. and Cabon, B. 2004. Theoretical and Experimental Analysis of Influence of Phase-to-Intensity Noise Conversion in Interferometric Systems. J of Lightwave Technology. 22(6), pp. 1510-1518.

Sandoz, P., Calatroni, J. and Tribillon G. 1999. Potential of a wavelength sampling approach for profilometry by phase shifting interferometry. Journal of Modern Optics 46(2), 327-339.

Sarma, A., 1977. New experimental methods for determining the parameters of elliptical retarders. J. Phys. D.:Appl. Phys. 10, pp. 2019-2030.

Sarma, A., 1977. New experimental methods for determining the parameters of elliptical retarders. *J. Phys. D.:Appl. Phys.* 10, pp.2019-2030.

Schwider, J., Burow, R., Elssner, K., Grzanna, J., Spolaczyk, R. and Merkel, K., 1983. Digital wave-front measuring interferometry: some systematic error sources. Appl. Opt., 22(21), pp. 3421-3432.

Scott, P. 2003. Novel Areal Characterisation Techniques. In L. Blunt and X. Jiang eds. Advanced Techniques for Assessment Surface Topography. London: Kogan Page Science. Ch. 3.

Scott, P. 2009. Feature Parameters. Wear 266, pp. 548-511.

Sheem, S., Giallorenzi, T. and Koo, K., 1982. Optical techniques to solve the signal fading problem in fibre interferometers. Appl. Opt. 21(4), pp.689-693.

Simon, A. and Ulrich, R. 1977. Evolution of polarisation along a single-mode fibre. App. Phys. Lett. 31(8), pp. 517-520.

Song, J. and Vorburger, V. 1991. Stylus Profiling at high resolution and low force. Applied Optics, 20(1), pp. 42-50.

Spillman, W., 1991. Multimode Polarization Sensors. In E. Udd ed. Fibre Optic Sensors: an Introduction for Engineers and Scientists. New York: John Wiley & Sons. Ch. 12.

Sprague, R. 1972. Surface Roughness Measurement Using White Light Speckle. Applied Optics. 11(12), pp. 2811-2816.

Stotlar, S. 2000. Visible Detectors. In R. Waynant and M. Ediger eds. Electro-Optics Handbook. New York: McGraw-Hill. Ch. 16.

Stout, K., Sullivan, P. and Dong, W. 1994a. Comprehensive study of parameters for characterising three-dimensional surface topography III: Parameters for characterising amplitude and some functional properties. Wear, 178, pp. 29-43.

Stout, K., Sullivan, P. and Dong, W. 1994b. Comprehensive study of parameters for characterising three-dimensional surface topography IV: Parameters for characterising special and hybrid properties. Wear, 178, pp. 45-60.

Surrel, Y. 1997. Additive Noise effect in digital phase detection. Applied Optics. 36(1), pp. 271-276.

Taguchi, A., Miyoshi, T., Takaya, Y. and Takahashi, S. 2003. Optical 3D profilometer for in-process measurement of microsurface based on phase retrieval technique. Precision Engineering. 28, pp. 152-163.

Taylor Hobson, 2009a. Talysurf CCI Lite Marketing Brochure. Available at http://taylorhobsonmedia.sitedesign.net/uploads/images/talysurf-cci-lite.pdf [Accessed 2 June 2009].

Vacharanukul, K. and Mekid, S. 2005. In-process dimensional inspection sensors. Measurement. 38, pp. 204-218.

VanWiggerden, G. and Roy, R. 1999. Transmission of linearly polarized light through a single-mode fibre with random fluctuations of birefringence. Appled Optics. 38(18), pp. 3888-3892.

Veeco, 2009 Wyko NT9800 Marketing Brochure. Available at http://www.veeco.com/pdfs/datasheets/DS542%20NT%209800%20Final_282.pdf [Accessed 2 June 2009].

Visioli, A. 2006. Practical PID Control. London: Springer-Verlag.

Vorburger, T. and Teague, E. 1981. Optical techniques for on-line measurement of surface topography. Precision Engineering 3(22), pp. 61-83.

Wanser, K. 1992. Fundamental phase noise limit in optical fibres due to temperature fluctuations. Electronics Letters. 28(1), pp. 53-54.

Weckenmann, A., Peggs, G. and Hoffmann, J. 2006. Probing systems for dimensional micro- and nano-metrology. Meas. Sci. Technol. 17, pp. 504-509.

Whitehouse, D. 1982 The parameter rash is there a cure. Wear 83, 75–78.

Whitehouse, D. 1994. Handbook of Surface Metrology. London: Institute of Physics Publishing.

Whitehouse, D. 1997. Surface Metrology. Meas. Sci. Technol. 8, pp. 955-967.

Whitehouse, D. 2002. Surfaces and their Measurement. London: Hermes Penton Science.

Wingerden, J., Frankena, H. and Smorenburg, C. 1991. Linear approximation for measurement errors in phase shifting interferometry. Applied Optics. 30(19), pp. 2718-2729.

Wuhan Telecommunications. PDDM981 Datasheet. Wuhan Telcommunications Devices Co. Wuhan, China.

Wyant, J. and Creath, K., 1992. Advances in Interferometric Optical Profiling. Int. J. Mach. Tools Manufact., 32(1/2), pp. 5-10.

Wyant, J., 1974. White Light Extended Source Shearing Interferometer. Appl. Opt., 13(1), pp. 200-202.

Wyant, J., Koliopoulos, C., Bhushan, B. and George, O., 1984. An Optical Profilometer for Surface Characterization of Magnetic Media. ASLE Transactions, 27(2), pp. 101-113.

Yu, F. and Yang, X., 1997. Introduction to Optical Engineering. Cambridge: Cambridge University Press.

Zhang, J. and Cai, Lilong. 1997. Profilometry using an optical stylus with interferometric readout. Meas. Sci. Technol. 8, pp. 546-549.

Zhao, C. and Burge, J. 2001. Vibration compensated interferometer for surface metrology", App. Opt. 40, 6215.

Appendices

A Transimpedance Amplifiers

A.1 Derivation of Transimpedance Amplifier Response

Transimpedance amplifiers are effectively current to voltage converters and as such as much used in for the amplification of photodiodes. The ideal model of a photodiode consists of a current source in parallel with a junction capacitance, C_j and shunt resistance R_{sh} as shown in Figure A.1. The junction capacitance is the capacitance of the semiconductor junction and as such scales with active junction area. This may however be mitigated to some degree by applying a reverse bias to the photodiode in operation.

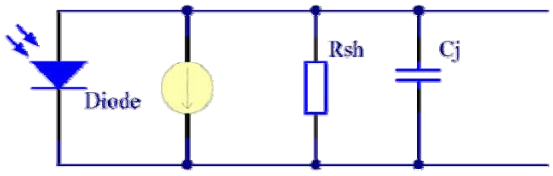

Figure A.1 Photodiode equivalent circuit diagram

A simple load resistor is an effective current to voltage converter, but for small currents the shunting of the required high value load resistor with the parasitic photodiode capacitance results a high pass filter which severely limits bandwidth. In addition, the output impedance of this circuit varies severely over the bandwidth of interest which can cause problems for subsequent amplification stages.

A far better solution to the problem of photodiode amplification is to use a transimpedance amplifier which provides a virtual earth into which the photocurrent may flow. This effectively negates the bandwidth limiting effect of the parasitic capacitance. An efficient and practical way of designing a transimpedance amplifier is by using an op amp.

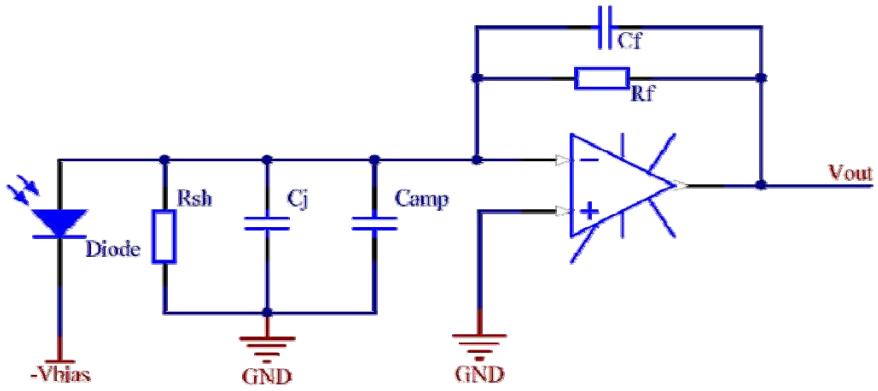

Figure A.2 Transimpedance amplifier circuit diagram

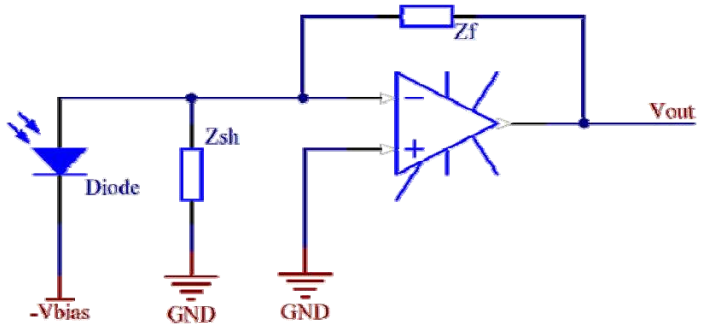

Figure A.3 Transimpedance amplifier represented with complex impedances

Figure A.2 shows one transimpedance amplifier design using an unspecified op amp while figure a.3 shows a simplified representation using complex impedances. z_f is the feedback impedance which consists of the parallel combination of a feedback resistance, used to set the overall gain of the amplifier and a feedback capacitance which determines the gain roll off. Z_{sh} is the parallel combination of the a capacitance $C_d = C_j + C_{amp}$ which comprises of the op amp input capacitance and the photodiode junction capacitance as well as the shunt resistance R_{sh}. Equation (A1.0) shows the s-domain (complex frequency domain) representation circuit in terms of a control loop and provides a useful way of analysing the circuit. A_{ol} is the open loop gain response of the ideal op amp under consideration.

In terms of voltages, forward loop transfer function is simply A_{ol}. In this case the closed loop transfer function (CLTF) is then

$$G(s) = \frac{A_{ol}(s)}{1 + \beta(s) A_{ol}(s)} \tag{A1.0}$$

where β is the feedback fraction. In terms of voltages this can be represented by the output of the voltage divider produced between z_{sh} and z_f. The feedback fraction is then is then simply

$$\beta(s) = \frac{z_{sh}(s)}{z_{sh}(s) + z_f(s)} = \frac{1}{1 + {}^{z_f(s)}\!/_{z_{sh}(s)}} \tag{A1.1}$$

(A1.1) is the derivation of the closed loop transfer function in terms of voltage gain, but of course the input of the system is from a current source, iph. In order to obtain the response of the circuit to a photocurrent, a transfer function for the input impedance of the circuit must be derived. Inspection of Figure A.3 reveals that the impedance seen by the current source is the parallel combination of z_{sh} and z_f which is

$$G'(s) = \frac{z_{sh}(s) \cdot z_f(s)}{z_{sh}(s) + z_f(s)} = \frac{z_f(s)}{1 + {}^{z_f(s)}\!/_{z_{sh}(s)}} \tag{A1.2}$$

The overall transfer function describing the voltage response from a circuit for an input current function is then

$$G(s)G'(s) = \frac{A_{ol}(s)}{1 + \beta(s) A_{ol}(s)} \cdot \frac{z_f(s)}{1 + {}^{z_f(s)}\!/_{z_{sh}(s)}} = \frac{A_{ol}(s) z_f(s)}{1 + A_{ol}(s) + {}^{z_f(s)}\!/_{z_{sh}(s)}} \tag{A1.3}$$

(A1.3) in this form is not particularly intuitive but we may use Matlab to plot the response of such a system if we first consider the complex impedances, z_{sh} and z_f which are simply the parallel combination of their respective capacitor and resistor,

$$z_f(s) = \frac{R_f \cdot {}^{1}\!/_{sC_f}}{R_f + {}^{1}\!/_{sC_f}} = \frac{R_f}{1 + sC_f R_f} \tag{A1.4}$$

$$z_{sh}(s) = \frac{R_{sh} \cdot {}^{1}\!/_{sC_d}}{R_{sh} + {}^{1}\!/_{sC_d}} = \frac{R_{sh}}{1 + sC_d R_{sh}} \tag{A1.5}$$

The response may be calculated then if the values of $R_{sh}, R_f, C_{amp}, C_j$ and the open loop gain response of the opamp in question, A_{ol}. From a design point of view everything but R_f and C_f are so it is these values that must be decided upon to elicit the required response. Of course the changing of an op amp to a faster model will of course alter the response dramatically. Generally the figure of merit used for an op amp is the gain-bandwidth product (GBW) which is the unity gain crossover frequency of the open loop response, A_{ol}.

It should be pointed out that the photocurrent flow in the circuit in the diagram is in fact from the diode anode to cathode and is thus flowing out of the summing junction. As a result the response is actually inverted

In the Matlab script used in this analysis, A_{ol} is modelled as a simple first order lag response which is calculated to approximate the response given on the opamp datasheet. Figure A.4 shows the various response curves calculated for a LF356 set up as a transimpedance amplifier.

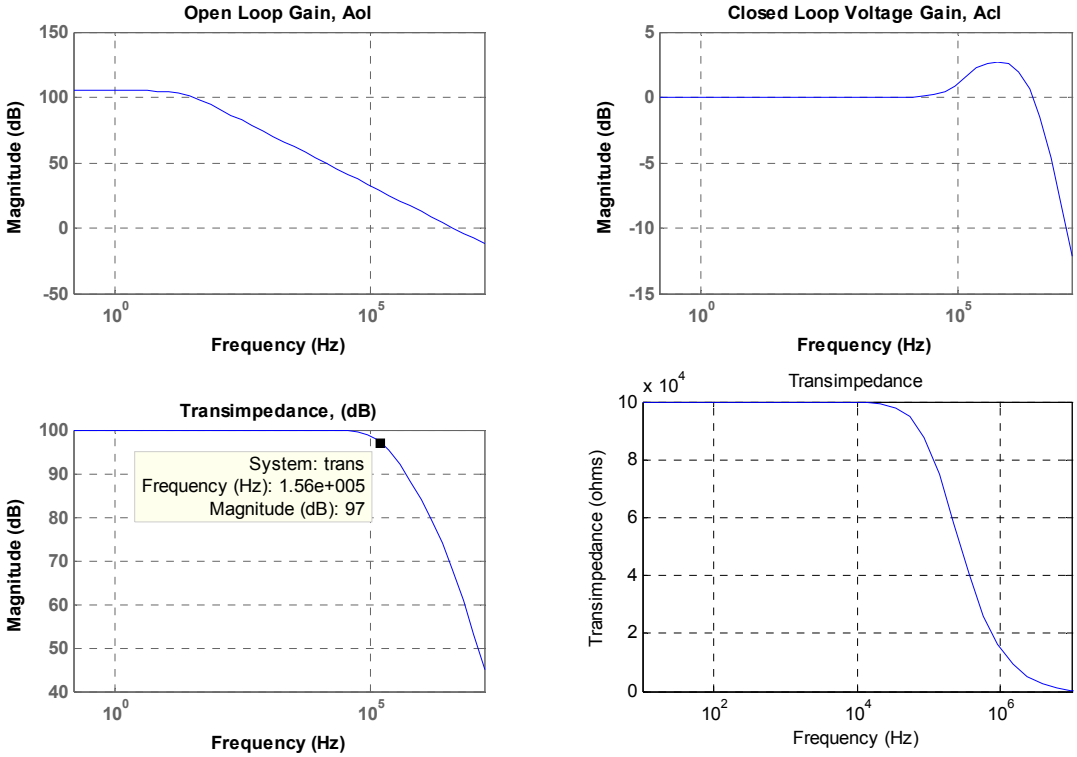

Figure A.4 LF356 transimpedance response

The 3 dB point is seen to be placed at 1.56 kHz when the value of C_f was adjusted for the maximum frequency response without gain peaking. The values of the various parameters are given in Table A.1.

Parameter	Value
R_{sh}	5 GΩ
R_f	100 k
C_{amp}	3 pF
C_j	1 pF

Table A.1 Parameter values for non-peaking response

A.2 Noise Analysis of a Transimpedance Amplifier

The noise contribution of the detection circuitry is of great importance in any electro-optical instrumentation. The aim in the design is that the performance here should be shot noise limited so that the detection circuitry has do deleterious effect on the measurement, that is it should provide a clear 'window' for viewing the interferometer output. This section will consider first the LF356 based transimpedance amplifier used in the instrument in chapter 5 and then compare its performance with a circuit using a THS4062 based amplifier used in chapter 7.

First it useful to consider a general noise model for a transimpedance amplifier as shown in Figure A.5.

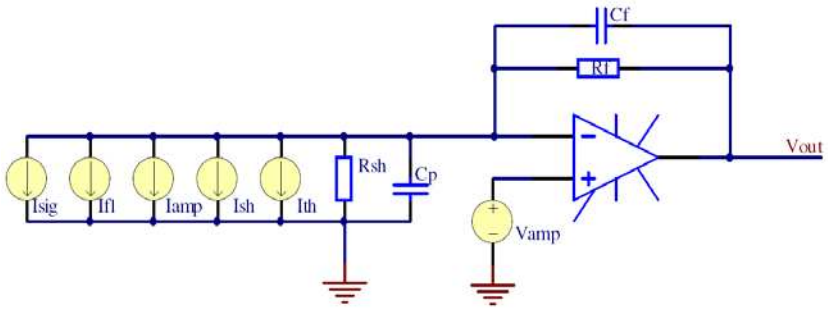

Figure A.5 Transimpedance amplifier noise model

The majority of the noise sources are modelled as equivalent current sources (referred to input) and as such are amplified by the closed loop transimpedance just as the photocurrent is. $I_{sig}, I_{fl}, I_{amp}, I_{sh}$ and I_{th} are the signal photocurrent, flicker noise contribution, amplifier current noise, shot noise and thermal noise. In addition there is an amplifier voltage noise whose amplification is governed by the closed loop voltage gain. All the noise sources have a Gaussian pdf and as such there statistics are relatively easy to determine.

The procedure for analysis is to derive the power spectral density (PSD) for each noise contribution. The current noise contributions then modified by the transimpedance response of the amplifier circuit attain the output PSD due to current noise. This operation may be conveniently carried out in the s domain as a multiplication the transimpedance response derived in appendix A.1,

$$S_I(s) = G(s)G'(s)\left[I_{sig} + I_{amp} + I_{shot} + I_{th}\right] \tag{A2.0}$$

Conversion from the s domain (complex frequency) to the frequency domain is then necessary. This is done easily by considering that $s = j\omega$ so that an alternative phasor representation may be written,

$$S_I(s) = S_I(j\omega) = \left|S_I(j\omega)\right| e^{j\phi(j\omega)} = \left|S_I(\omega)\right| \angle\phi(\omega) \tag{A2.1}$$

As we are only interested gain information it is possible to simply discard the phase information.

The mean square noise voltage measured at the output due to current noise is then,

$$e_i^2 = \int_{2\pi f_1}^{2\pi f_2} S_I(\omega)\, d\omega \tag{A2.2}$$

where f_1 and f_2 form the measurement bandwidth limits in hertz, which are taken in this analysis to be $0.1 \le f \le 1\times10^9$ since the measurement cycle lasts less than ten seconds and 1 GHz is far above the low pass filtering of later circuit stages. In this sense it represents a worse case range.

The approach for voltage noise sources is similar except it is amplified by closed loop voltage gain of the transimpedance amplifier circuit used. Since there is only one

voltage noise source present, V_{amp} the mean squared voltage noise at the output is simply,

$$e_v^2 = \int_{\omega_1}^{\omega_2} S_I(\omega)\, d\omega \tag{A2.3}$$

Flicker noise must also be considered but by its nature it is only relevant in the first 4 decades of operation after which it becomes much less than other noise sources such as thermal or amplifier noise. The mean square flicker noise may be approximated by

$$e_{fl}^2 = K_f \ln(f_2 / f_1) \tag{A2.4}$$

where K_f is the PSD at 1 Hz. For 4 decades of operation, that is between 0.1 Hz and 1 kHz the mean square voltage noise is

$$e_{fl}^2 = 9.210 K_f \tag{A2.5}$$

The flicker noise associated with the op amp is a voltage and is thus amplified by the closed loop voltage gain. However at the low frequencies considered that gain is simply one. Hence the flicker noise contribution is generally negligible.

The total rms noise voltage as seen at the output due to all noise sources within a transimpedance amplifier is from (6.15) written as,

$$e_{tot} = \sqrt{e_v^2 + e_i^2 + e_{fl}^2} \tag{A2.6}$$

A worked analysis of the LF356 based circuit used in chapter 5 is now presented. This is then followed by simulation results for both a LF356 and THS4062 (as used in chapter 7) based circuit.

Shot Noise

There shot noise contributions associated with both the dark current, i_{dk} flowing through the photodiode and the photocurrent, i_{ph} . The total shot noise spectral density is

$$S_{sh}(f) = \sqrt{2e\left(i_{ph} + i_{dk}\right)} \tag{A2.7}$$

where $i_{dk} = V_{bias} / R_{sh}$ and is set by the amount of reverse bias applied to the photodiode. $e = 1.602 \times 10^{-19}$ and is the charge on an electron in coulombs. It can be seen that there is a trade off between increasing speed by increasing the reverse bias voltage and the addition of dark current shot noise to the output. There is no frequency dependence since shot noise is white noise and is thus constant across the bandwidth.

Evaluating A2.7 for $V_{bias} = -5$ V and $R_{sh} = 5$ GΩ taken from the circuit design and assuming $i_{ph} = 40\ \mu$A, as taken from experimental observation of the instrument in practice,

$$S_{sh}(f) = 2e\left(40 \times 10^{-6} + 1 \times 10^{-9}\right) = 12.82 \times 10^{-24}\ \text{A}^2 / \text{Hz}$$

Thermal Noise

Each resistance in the transimpedance circuit produces a thermal noise current contribution. The thermal noise associated with the feedback resistor, R_f may be placed equivalently in the same orientation as that associated with the photodiode shunt resistance R_{sh}. The combined thermal current noise spectral density of the two resistors is then

$$S_{th}(f) = 4k_B T\left(\frac{1}{R_f} + \frac{1}{R_{sh}}\right) \qquad \text{(A2.8)}$$

where k_B is Boltzmann's constant (1.38×10^{-23} JK^{-1}) and $T = 300$ K is the operating temperature in Kelvin. For $R_{sh} = 5$ GΩ and a typical value of $R_f = 50$ kΩ the spectral density is then

$$S_{th}(f) = 4k_B T\left(\frac{1}{50 \times 10^3} + \frac{1}{5 \times 10^9}\right) = 1.656 \times 10^{-25}\ \text{A}^2 / \text{Hz} \qquad \text{(A2.9)}$$

These first set of noise sources are all constant for a given input light intensity while the following are dependent upon the specific opamp IC used. The LF356 (or dual version, LF355) is considered in this next section, while later results will also show the analysis for a circuit based upon the THS4062 used in chapter 7.

Amplifier Current Noise

This information may be gleaned from the opamp datasheet and is considered to be constant across all frequencies. For the LF356 it is found that

$$S_{iamp}(f) = 1\times10^{-28}\ \mathrm{A}^2/\mathrm{Hz}. \tag{A2.10}$$

Amplifier Voltage Noise

This is given in the datasheet as

$$S_{iamp}(f) = 2.25\times10^{-16}\ \mathrm{V}^2/\mathrm{Hz} \tag{A2.11}$$

Flicker Noise

This can be approximately modelled as a set noise contribution and added on at the end of the analysis. The mean squared voltage noise contribution over 4 decades using a datasheet value $K_p = 12.1\times10^{-15}$ is,

$$e_{fl}^2 = 1.114\times10^{-13}\ \mathrm{V}^2 \tag{A2.12}$$

This is seen to be insignificant compared to the other noise source contributions from the simulation and as such is conveniently ignored.

Figure A.6 shows the results of the noise simulation for both a LF356 based op amp as well as a THS4062 op amp. Figure A.7 also show the bandwidths of these circuits in order make a performance comparison. In each simulation the value of the feedback capacitor was adjusted for a minimal amount of gain peaking and thus maximum frequency response. This will yield worst case values for noise as it is always possible to damp the response further.

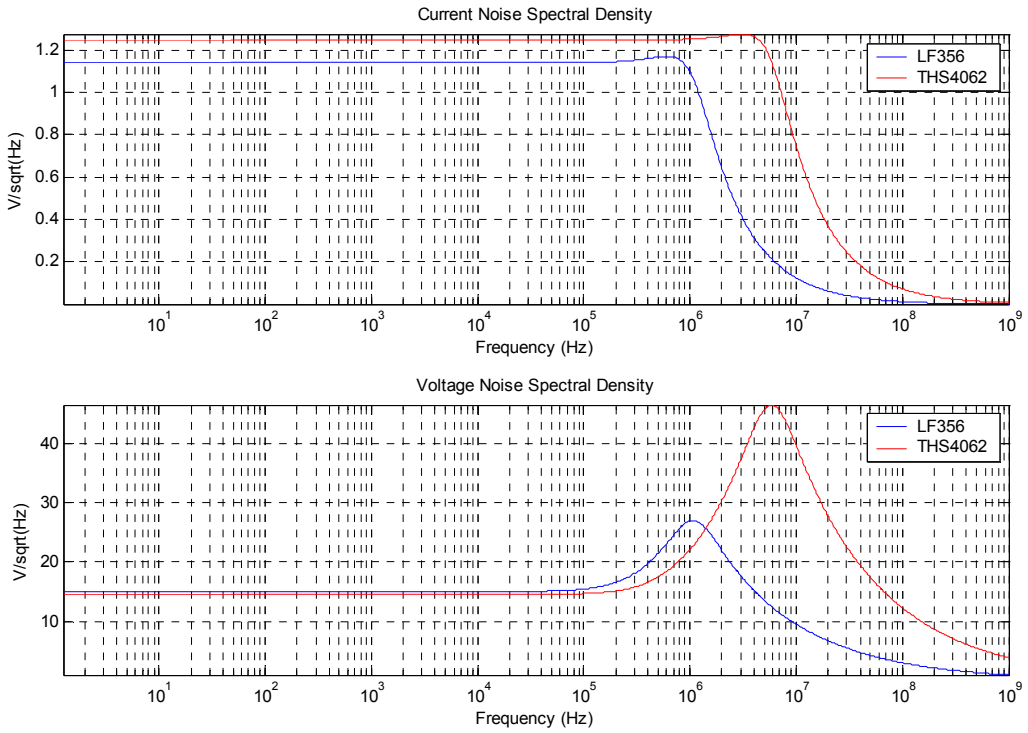

Figure A.6 Voltage and current noise simulation of LF356 and THS4062 transimpedance amplifiers

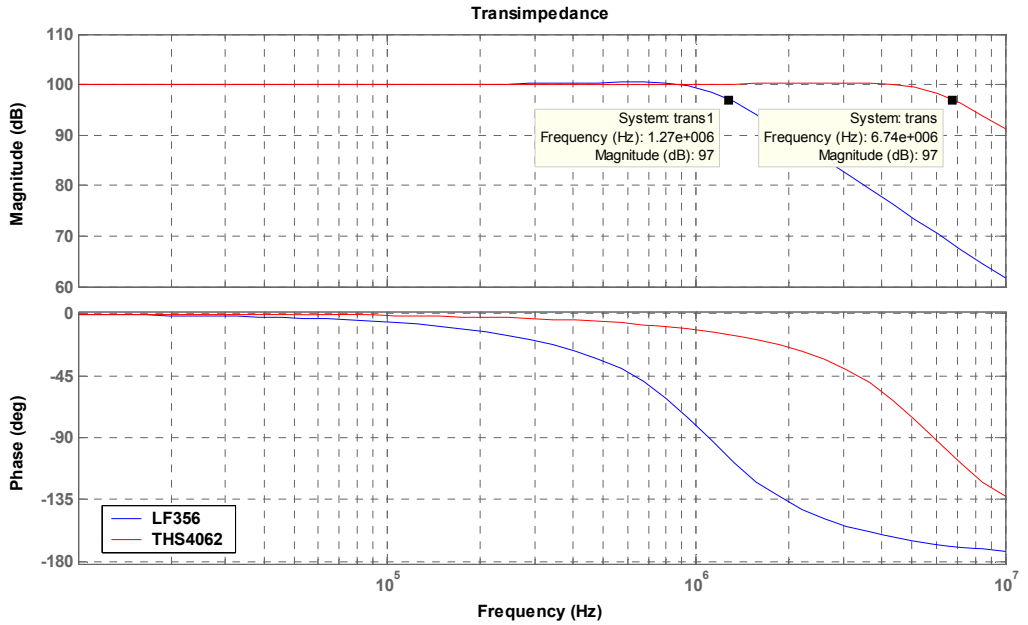

Figure A.7 Frequency response for LF356 and THS4062 transimpedance amplifiers

The mean square values of the noise contributions and the overall rms noise were calculated using the Matlab script and are shown in Table A.2.

	LF356	THS4062
Mean-sq. Noise from current sources (μV)	1.694	4.268
Mean-sq. RMS Noise from voltage source (μV)	82.00	291.7
RMS Noise (μV)	9.15	17.20
SNR (dB)	121.6	109.0

Table A.2 Simulated transimpedance amplifier noise magnitudes

The worst case example of SNR occurs with the THS4062 based transimpedance amplifier, the trade off being for the increased frequency response. Neither amplifier design is shot noise limited since the amplifier voltage noise in Table A.2 is substantially higher than the any other noise contribution. However, as is shown in chapter 6, the overall noise figures are so low that they do not limit the overall instrument performance in any meaningful way.

A.3 Discretisation of an Analogue PI Controller

The discrete model is formed by taking the s-domain format and converting it using z-transforms to produce a discrete time version.

For the plant, $G_p(s)$ in series with a zero-order-hold, $G_p(s)$ to model the effect of sampling:

$$G_o(s)G_p(s) = K_p \cdot \frac{(1-e^{-sT})}{s} \cdot \left(\frac{1}{(1+s\tau_p)} \right) \tag{A3.0}$$

Where T is the sampling interval, τ_p the process time constant and K_p, the process gain. After simplification, and using standard transform tables, the overall discrete time z-domain function is;

$$G(z) = K_p \left(\frac{1-e^{-T/\tau_p}}{z-e^{-T/\tau_p}} \right) \tag{A3.1}$$

A series PI controller takes the form:

$$G_c(z) = K_c \frac{z+A}{z-1} \tag{A3.2}$$

Where $A = \left(\frac{T}{\tau_i} - 1 \right)$ and τ_i is the integrator time constant. K_c is the controller gain.

It can be shown that such a controller may be implemented by the following recursive formula;

$$y_n = y_{n+1} + K_c \left[k_0 e_n - e_{n+1} \right] \tag{A3.3}$$

Where y_n is the controller output and e_n is the error value.

$$k_0 = \left(1 + \frac{T}{\tau_i} \right) \tag{A3.4}$$

The formula above was coded for the DSP hardware and was shown to execute in approximately 500ns. While this is very good (yielding a sample rate of 2 Mhz), the actual sample rate is limited by the digital to analogue converter (DAC).

B Electronic Hardware

B.1 Introduction

This section outlines the design of the various electronic hardware used throughout this work.

B.2 Proportional-Integral Control Circuit

Description of Operation

National Semiconductor LF356 and LF355 (dual version) op amps are used to provide most functions in the circuit. In addition a circuit switching interface is provided using the MAX313CPE analogue switch IC which allows elements of the circuit to be switched in and out from a remote PC hosting a DAQ card with digital outputs.

A summary of circuit subsections follows and is given logically by individual IC function. All analysis is considered for ideal op amp behaviour to simplify the description.

IC1

Input unity gain buffer with adjustable attenuation using VR4. The input signal is obtained from a transimpedance amplifier connected to the reference interferometer output.

IC2B

Unity gain subtractor which subtracts the input voltage from the setpoint input to generate the error signal.

$$V_{error} = V_{set} - V_{pd} \tag{B.0}$$

IC5A

This is a simple unity gain inverter which inverts the error signal. In this manner it can be seen that non-inverted and inverted error signals are available at ports A2 and A1 respectively. This is used to provide the setpoint switching required as either signal may be directed to port B by a suitable selection logic at DAQ1(TOGGLE)

and DAQ2(TOGGLE). It should be noted that the logic must always take opposing values at those inputs.

IC3A

Integration stage which integrates the error signal thus getting rid of steady state error.

$$V_{I1} = -VR2 \cdot C10 \int V_{error} dt \tag{B.1}$$

The values given provide a range of integration gain, $10 < K_i < \infty$ (Hz).

IC3B

Proportional part of the PI controller it is a simple inverting amplification stage.

$$V_P = -V_{error} \frac{VR3}{R12} \tag{B.2}$$

This supplies a range of proportional gain, $0 < K_p < 4.8$

IC5B

Provides an inverting unity gain summation stage to add the P and I components together.

$$V_{PI} = -\left(V_{I2} + V_P\right) \tag{B.3}$$

Output from the stage is directed to port C which may be switched on and off by the appropriate logic voltage applied to port DAQ4(S/P ENA). This allow the control loop to be effectively switched off which is necessary when modulating the PZT in order to determine fringe visibility.

IC4A

This stage provides a secondary input for applying a signal directly to the PZT. This provides simple method of modulating the PZT for the purposes of determining fringe visibility. A triangular wave signal is applied to the offset input when the control loop is disabled in order to perform this function. VR6 provides gain adjustment.

IC4B

This stage simply sums the outputs from the PI controller stages and the offset input stage. In normal operation only one input is actually present at any one time.

IC6

This is a unity voltage gain stage which has a BUF634T current amplifier inside its feedback loop. This effectively provides a current boosting which raises the 40 mA compliance of the LF356 op amps to 250 mA to ensure the PZT is not slew rate limited because of the driving electronics.

MAX313CPE

This IC provides analogue switching for the various reasons outlined in the preceding sections. It takes inputs from the DAQ in the form of TTL compatible voltage levels.

PI Controller Circuit Diagram

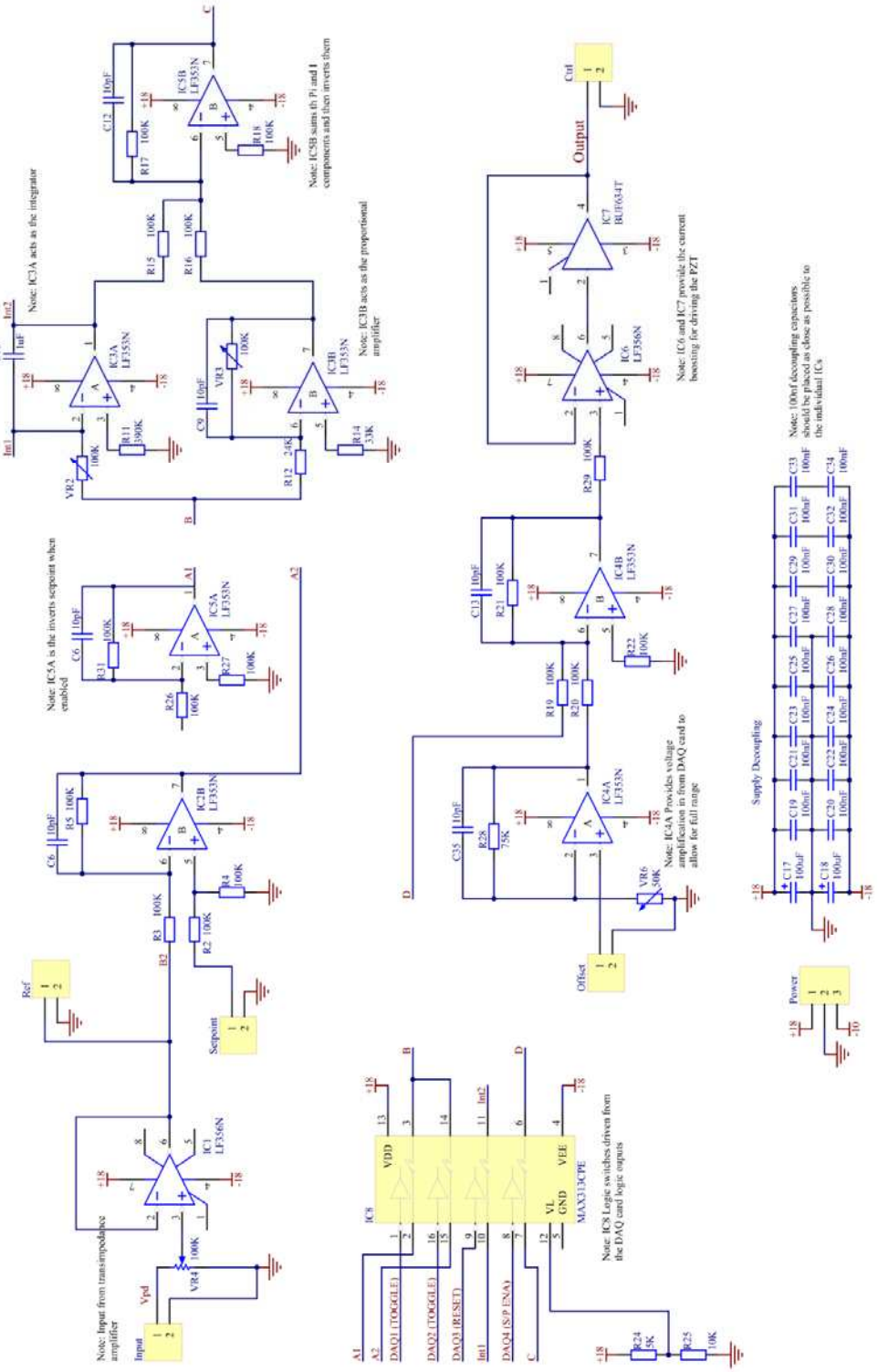

Figure B.1 PI Controller Circuit Diagram

B.3 Other Circuitry

Transimpedance Amplifier Circuit Diagrams

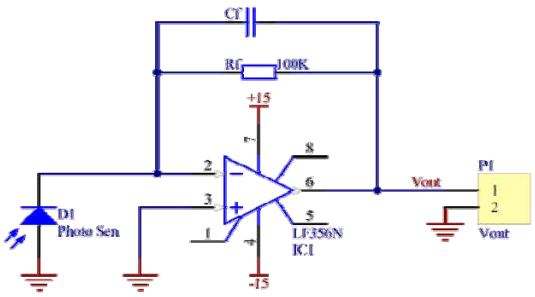

Figure B.2 LF356 based transimpedance amplifier circuit

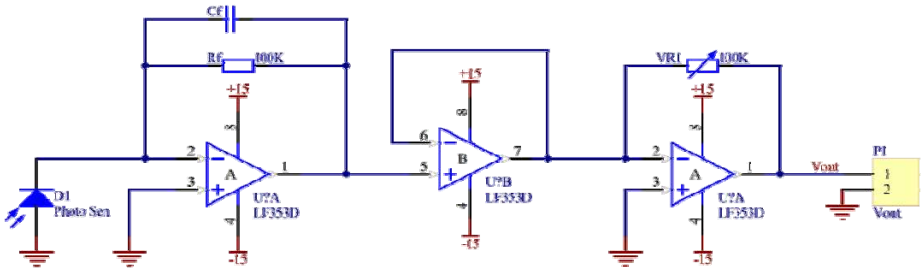

Figure B.3 THS4062 based transimpedance amplifier circuit

Interface Board Circuit Diagram

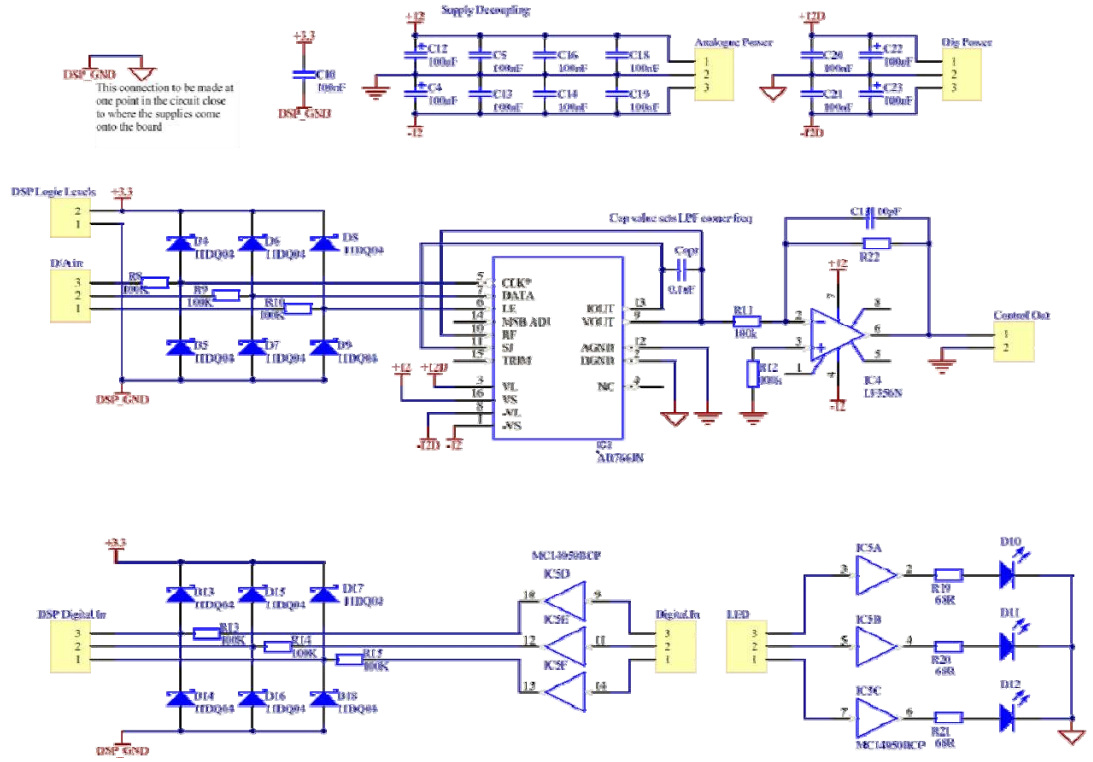

Figure B.4 Interface Board Circuit Diagram

Laser Diode Driver

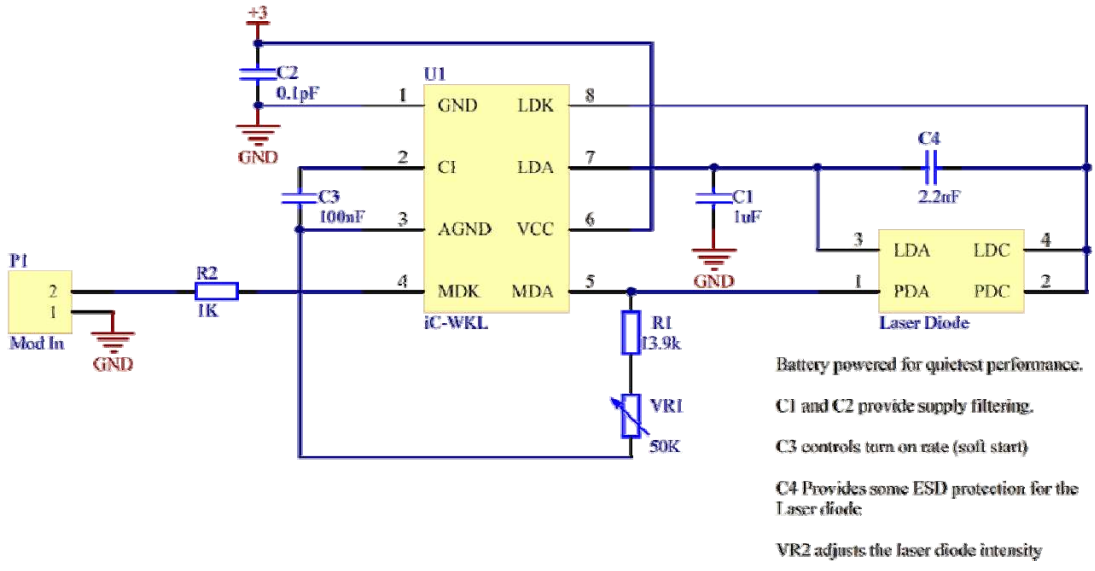

Figure B.5 Laser Diode Driver

EOPM Driver and Logic Level Translator Diagram

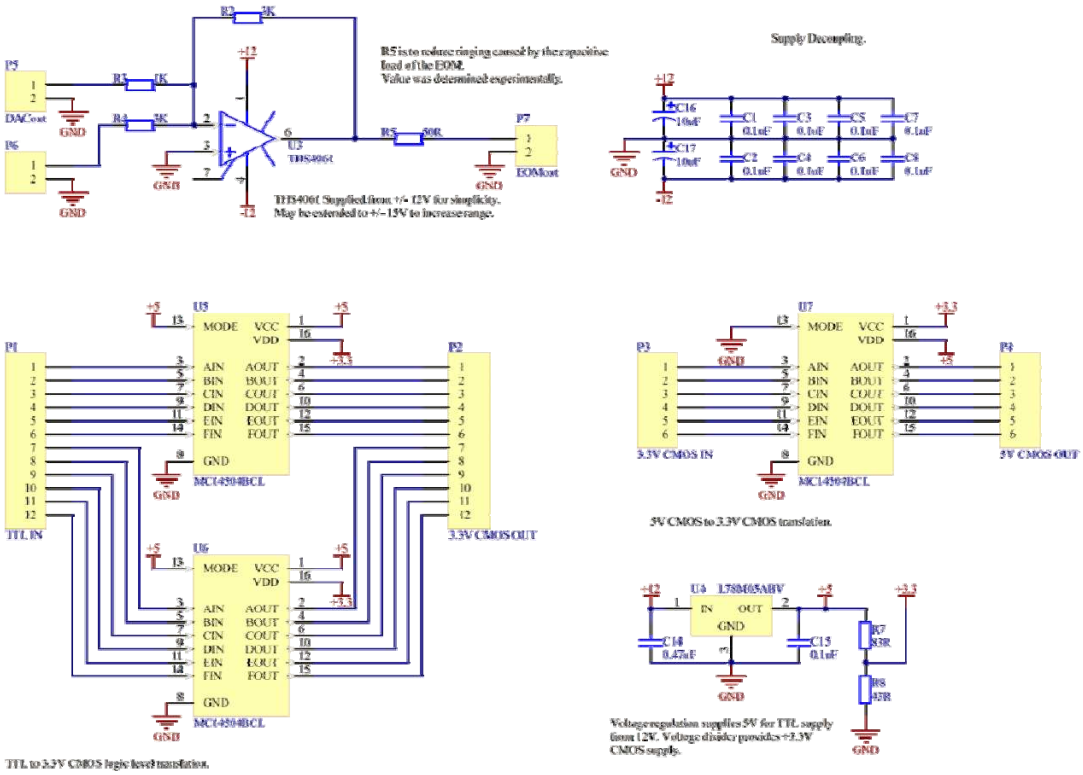

Figure B.6 Driver and Logic Level Translator Circuit Diagrams

B.4 Rapid Phase Shifting Functional Overview

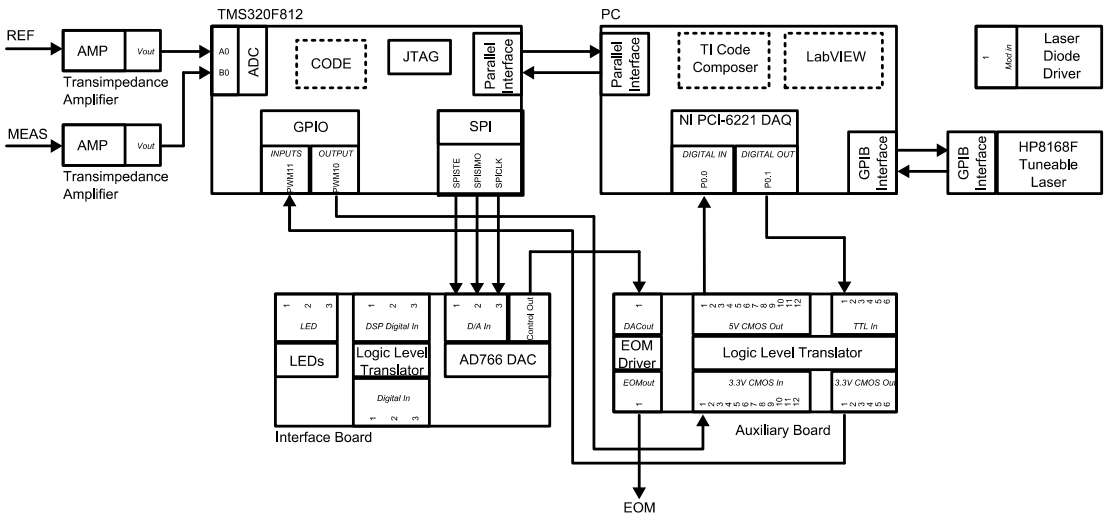

Input and output for the circuits are shown as pin numbers (or names where applicable) at the perimeters of the main boxes. The italicised names correlate to the header designations on the circuit diagrams in appendix B1-3. The arrows on the

diagram indicate the direction of dataflow. Software is represented by the dashed boxes.

C Noise Theory

C.1 Definition of Noise

Noise may be defined simply as any unwanted signal in a system. This definition is where the simplicity ends unfortunately since the sources of noise affecting an electro-optic instrument are wide ranging in there type and severity. Noise may be characterised as a random signal and produced from a stochastic process.

Defining noise mathematically relies upon the use of probability theory and random variables and it is useful to consider some of the basic terminology. The probability of some random variable X assuming some discrete value $X_i\,(i=1,2,3...)$ occurs n_i times in a total number of N results,

$$P(X_i)=\lim_{N\to\infty}\frac{n_i}{N} \tag{C.1}$$

For the case of a continuous random variable, the probability that X is in some range, ΔX centred about X_i is then,

$$P_\Delta(X_i)=P\left(X_i-\Delta X/2<X\le X_i+\Delta X/2\right)=\lim_{N\to\infty}\frac{n_i}{N} \tag{C.2}$$

where n_i is now the total number of outcomes in the range $X_i-\Delta X/2$ to $X_i+\Delta X/2$ for a total number of N results. It is more useful however to consider the limit $\Delta X\to 0$ by which one derives the continuous probability density function (PDF),

$$p(X)=\lim_{\Delta X\to 0}\frac{P_\Delta(X_i)}{\Delta X} \tag{C.3}$$

It is now possible to say that the probability of X falling in the range $X_1\to X_2$ is

$$P\left(X_1<X\le X_2\right)=\int_{X_1}^{X_2}p(X)\,dX \tag{C.4}$$

where by definition

$$\int_{-\infty}^{\infty}p(X)\,dX=1 \tag{C.5}$$

From the PDF it is also possible to derive the mean value of the random process which is given as

$$\bar{X} = \int_{-\infty}^{\infty} Xp(X)\,dX \tag{C.6}$$

and the mean square value (variance),

$$\sigma_X^2 = \int_{-\infty}^{\infty} \left(X - \bar{X}\right)^2 p(X)\,dX \tag{C.7}$$

The standard deviation, or root-mean-square (rms) value, is then given by

$$\sigma_X = \left[\int_{-\infty}^{\infty} \left(X - \bar{X}\right)^2 p(X)\,dX\right]^{1/2} \tag{C.8}$$

A common PDF seen in noise sources is given by the a Gaussian function

$$p(X) = \frac{1}{\sigma_X\sqrt{2\pi}} \exp\left(\frac{X - \bar{X}}{2\sigma_X^2}\right) \tag{C.9}$$

where $\bar{X}$ is the mean and σ_X^2 is the standard deviation. The central limit theorem states for a large number of independent identically distributed (IID) random variables, their sum will converge to a Gaussian PDF. As such a Gaussian PDF is often seen in the study of the random processes describing many common noise sources in electronics and optics.

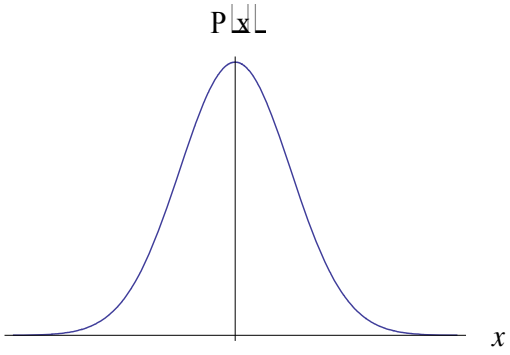

C.1 A Gaussian PDF

Specific properties of the Gaussian PDF are that the probability of a random variable being within in $2\sigma_X$ of the mean is 0.9554. The probability that the outcome will be

within $3\sigma_X$ either side of the mean is 0.9973. This leads directly to the useful rule of thumb derived for noise exhibiting a Gaussian PDF; the peak to peak noise value will be 6 times the rms noise value.

For the study of noise one is generally concerned with not just a single number but with a random function in time. The production of a random function in time is termed a stochastic process. A wide sense stationary random process is one in which the mean and autocorrelation function are independent of time. It is then possible to say that the mean or expected value of X at a time t for a random process normally given by

$$\bar{X}(t) = \varepsilon\left[X(t)\right] = \int_{-\infty}^{\infty} Xp(X;t)dX \tag{C.10}$$

may be simplified to

$$\bar{X} = \varepsilon\left[X\right] = \int_{-\infty}^{\infty} Xp(X)dX \tag{C.11}$$

while the expected value of the mean square of x is

$$\bar{X}^2 = \varepsilon\left[X^2\right] = \int_{-\infty}^{\infty} X^2 p(X)dX \tag{C.12}$$

If the process is also ergodic then the complete statistics for that random process may be derived by time averaging. All the noise signals to be considered in this chapter are wide sense stationary and ergodic and as such the time dependence of all statistical properties is removed.

The autocorrelation for an ergodic stationary random process is given by

$$R_{XX}(\tau) = \varepsilon\left[\left(X(t)-\bar{X}\right)\left(X(t+\tau)-\bar{X}\right)\right] = \left\langle\left(X(t)-\bar{X}\right)\left(X(t+\tau)-\bar{X}\right)\right\rangle \tag{C.13}$$

where the expected value is derived from time averaging over a long period. When the time shift $\tau = 0$ the peak of the autocorrelation is found.

$$R_{XX}(0) = \left[X(t)-\bar{X}\right]^2 \tag{C.14}$$

For zero mean processes it is clear from **Error! Reference source not found.** that the peak of the autocorrelation is equal to the variance. In general it is possible to

deduce any Gaussian PDF as long as you know the mean and the autocorrelation of the random process.

The auto-correlation of a signal is seen to be related to its power-spectral density (PSD) by the Wiener-Khinchin theorem. This is an analogous relationship to that of linewidth and coherence time for an optical wave as discussed in section 3.4.6.

$$S(\omega) = \frac{1}{2} S'(\omega) = \Im\{R(\tau)\} \tag{C.15}$$

where $S(\omega)$ and $S'(\omega)$ are the bilateral and unilateral PSDs respectively.

Because a linear system driven by a signal with a Gaussian PDF will have an output signal with a Gaussian PDF it is possible to determine the nature of the output if the frequency response of the system in known. In fact all statistical properties of interest e.g. mean, rms may all be derived.

The general practice when dealing with noise sources having a Gaussian PDF is to use the rms values. This is due to the fact that uncorrelated noise sources are added using root-sum-square addition such that,

$$e_{\text{total}} = \sqrt{\sum_{1}^{k} e_k^2} \tag{C.16}$$

where e_k is the rms value of the k^{th} uncorrelated noise source.

Because of this the summation it is this found that in any system there are generally a reduced set of noise sources whose rms values contribute to a much larger portion of the overall rms noise value. Hence any noise reduction strategy will tend to pinpoint these first and attempt to reduce or eliminate them. After this process the effect of more minor sources then starts to become significant. In general, the contribution of a noise source whose rms is less than a third of the highest rms value in a set of uncorrelated noise sources is negligible.

Signal to noise ratio is often an important quantity for the analysis of noise as it yields a generalised parameter for comparison. It is defined as

$$SNR = \frac{P_{sig}}{\varepsilon\left[X^2\right]} \tag{C.17}$$

where P_{sig} is the signal power and $\varepsilon\left[X^2\right]$ is the expected value of the variance of the noise signal. Generally SNR is written as a decibel value and in terms voltages for electrical usage,

$$SNR(dB) = 20\log\left(\frac{V_{sig}}{e_n}\right) \tag{C.18}$$

where V_{sig} is the signal voltage and e_n is the rms noise voltage.

Noise sources magnitudes often also have a frequency dependence, either inherent in the process or due to filtering at detection. Even though white noise sources theoretically have a flat band noise power spectral density (PSD) that extends to an infinite frequency, the reality is that it will be filtered by the various components of the instrument. An example of this is the flat band thermal noise of a resistor in an electronic op amp circuit. Such a noise source is often modelled as a voltage source for analysis purposes and in order to derive the correct rms values for the total noise at the circuits output we must integrate under the power spectral density. In theory the PSD extends to infinity, thus so must the rms noise power. To calculate realistic noise values one must consider the bandwidth in which the op amp circuit operates and truncate the PSD accordingly. Well thought out filtering strategies are vital throughout an instrument, regardless of the domain under consideration be that optical, electrical or mechanical.

C.2 Electronic Noise Types

This section outlines relevant electronic noise sources and quantifies there likely magnitudes where possible.

Shot Noise

Shot noise is a fundamental noise source that is related to the fact that an electric current is made up of discrete charge carriers. Shot noise is the statistically uncertainty surrounding the measurement of any electric current. ‘Full’ shot noise occurs only in certain situations, where the charge carriers act independently of each other. One relevant case is in the flow of charge carriers across a junction where the movement occurs through the process of diffusion. This is significant in the

photocurrents produced by photodiodes, especially when coupled with the fact that the generated currents are often very small.

The full shot noise exhibited by a photocurrent generated by a photodiode may be shown to have a root normalised power spectral density of;

$$i_n = \sqrt{2qI_p} \tag{C.19}$$

where q is the charge on the charge carrier (in this case an electron), I_p the mean photocurrent generated. The noise forms a Gaussian distribution for any appreciable quantity of photoelectron creating events and as can seen from **Error! Reference source not found.** it is constant for all frequencies; as such it is white noise.

Charge carriers flowing through metallic conductors do not exhibit independent behaviour, the result of which is that they show much less than full shot noise.

The term 'shot noise limited' is often used to describe an instrument were all other noise sources have been reduced to below this fundamental level; in this sense the instrument is performing optimally.

Thermal (Johnson) Noise

Johnson noise results from the random agitation of electrons in a conductor and is always present, depending only on the temperature and resistance of the conductor. This noise is white noise for all practical frequencies of operation and Gaussian in distribution. In circuit theory, the noise may be modelled by a noise source in series with a perfect, noiseless resistor. The spectral density is a useful interpretation for the purposes of analysing transimpedance amplifiers;

$$S_{th}(f) = \frac{4k_bT}{R} \tag{C.20}$$

where T is the temperature, R the resistance and k_b Boltzmann's constant. Good circuit design can generally ensure that the Johnson noise contribution to the output of a detection circuit remains below that of shot noise in applications where bandwidth and amplification requirements not overly challenging.

1/f, Flicker or Excess Noise

1/f noise is any noise type that has equal power per frequency decade, it may also be called pink noise, flicker noise or excess noise. 1/f noise occurs in many situations such as the base current of transistors and in the resistance of a resistor. It also occurs in a wide ranging array of other situations completely unconnected with electronics. The sources of 1/f noise are as varied as the situations in which it is found, sometimes a specific mechanism may be determined for a given case. From the point of view of building optical instrumentation one is concerned with its contribution in long term and baseband type measurements. Excess noise is of importance only over the frequency range where it is higher than the thermal or shot noise contributions. Any circuit will lowpass filter flicker noise by virtue of the fact it will be turned off at some interval. Excess noise has a Gaussian pdf and a normalised spectral density of

$$S_{fl}(f) = \frac{K_f}{f^{\alpha}} \tag{C.21}$$

where K_f is value of the spectral density at 1 Hz and α depends on the application and can vary in value between 0.8-1.4, but is generally approximated to unity for practical purposes. The mean square noise voltage over a frequency range $f_1 \le f \le f_2$ is then

$$e_{fl} = \int_{f_1}^{f_2} \left(K_f / f \right) df = K_f \ln\left(f_2 / f_1 \right) \tag{C.22}$$

Burst (Popcorn) Noise

Occurring in semiconductors, its origins are not completely understood. It appears to be linked to impurities in the semiconductor material and causes random step changes in voltage or current levels. It is random and unpredictable making it very difficult to design contingencies for its occurrence. The reduction of popcorn noise in semiconductor devices is done by screening the finished products; thus the purchase of quality screened semiconductor devices is the best way of mitigating the effects of popcorn noise.

Amplifier Noise

Amplifier noise lumps voltage and current noise and is a catch all term used to provide a general idea of the noise to be expected when using commercial electronic ICs. Information is generally to be found on the datasheet, and is often given in the graphical form of a power spectral density plot. Such noise sources are generally referred to input, that is the data given is for a current/voltage noise source applied to the input terminals of an amplifier. The circuit design which determines the frequency response of the amplifier will affect how this noise is amplified at the output.

Quantisation Noise

The reality of most optical instrumentation is that the analogue signals obtained will at some point be sampled and digitised in order that they may be processed, stored and displayed by computer. The act of digitising signals adds results in the addition of quantisation noise to a signal. There are two essential types of quantisation, rounding and truncation.

Rounding generally occurs in the analogue to digital conversion, the analogue signal being rounded to the nearest discrete level on conversion. This leads to a maximum possible error of $\pm \frac{1}{2}\,\mathrm{LSB}$ (least significant bit).

Truncation can occur during floating point computation, especially when a multiplication takes place and the LSBs of the result must be truncated in order to be stored in a register. The maximum possible error through truncation is 1 LSB.

The range of analogue voltages present between the LSB of the analogue-to-digital converter (ADC) is critical in determining the scale of quantisation noise present. The quantisation band q represents the range covered by 1 LSB and is given by

$$q = \frac{\Delta V}{2^N} \tag{C.23}$$

where ΔV is the voltage range covered by the ADC and N is the number of bits used in the digitisation process. Clearly the input signal must be conditioned so that its peak to peak range equal to the full scale voltage range of the ADC or the effective value of q will be smaller.

The two areas of optical instrumentation where the injection of quantisation noise will affect operation are in the final accuracy of data captured, and in the action of any discrete time control loops that may be implemented.

Due to the quantisation process and in the absence of the other noise sources, the maximum resolution of the instrument is given by the measurand change that will instil a variation of $q/2$ in the analogue signal.

In a control loop it is possible that quantisation noise could produce non-optimal performance and even lead to instability. However in well designed robust control systems the noise will be well within the maximum parameter variation boundaries.

The use of a digital-to-analogue converter (DAC) in control loops to produce the actuating signal also creates additional quantisation noise if the resolution of that DAC is less than the numerical resolution used for the preceding computation. This will result in a maximum resolution for servo control which if too large may cause settling problems and unstable operation.

The effects of quantisation are much more complicated than the relatively simple process itself might suggest. It is unusual to fully analyse all the effects throughout a control system as often the effects are negligible. There are danger areas where quantisation noise can be serious such as when it precedes a large gain.

Consider an analogue signal that is to be digitised, its value can be anywhere between $\pm q/2$ once digitised will be and the error between the continuous and digitised signal can be considered as a noise source. The error probability distribution can be considered to be constant within the band formed by q which is practically justifiable, although only strictly correct for non-deterministic signals. The expected value of the error, $E(e)$ is seen to be zero in the case of rounded digitising processes (such as those in an ADC). The variance is then,

$$\text{var}(e) = E\left(e^2\right) - \left[E(e)\right]^2 = \frac{1}{q}\int e^2 de = \frac{1}{q}\frac{e^3}{3}\Bigg|_{-q/2}^{+q/2} = \frac{q^2}{12} \qquad \text{(C.24)}$$

Generally other distortions and noise processes will conspire to reduce the SNR of an ADC below the ideal level.

The DAQ card using the instrument in chapter 5 has an ADC resolution of 16 bits. However the onboard ADC on the DSP card used in the instrument in chapter 7 has only 12 bit resolution hence this value will be used for worst case analysis. The datasheet SNR for the onboard ADC is 62 dB for full scale operation.

The obvious way of reducing these effects is to increase the resolution of the ADCs and DACs used in the system, possibly at the expense of sampling rate and added complexity. Within the bounds of a given resolution it is essential to use appropriate signal conditioning prior to the digitisation to ensure the full range of an ADC utilised. Good coding of algorithms will ensure that finite word length errors will be of little consequence to the overall operation.

C.3 Optical Noise Types

This section outlines relevant electronic noise sources and attempts to quantify their likely magnitudes where possible.

Relative Intensity Noise (RIN)

RIN is the fluctuation in laser output relative to its mean output and is a catch all term for the contributions of various processes. RIN is generally defined as the noise over and above the shot noise level that forms the ultimate noise floor. As suggested by its name, RIN is measured relative to the actual output power from the source. Some early experimental measurements of RIN occurring in semiconductor lasers, with application to interferometry, were made by Dandridge at al. (1980).

The power spectral density (PSD) for semiconductor lasers is generally found to be at its highest up to several tens of megahertz and the falls toward the shot noise level at higher frequencies. A resonant peak in the RIN PSD may well be observed due to relaxation oscillations in the laser cavity. RIN specifications are usually given in dBc which is the power fluctuation, ΔP relative to the carrier power P_c.

$$RIN(dB) = 10\log\left(\frac{\Delta P}{P_c}\right) \tag{C.25}$$

The RIN specification for the Ando AQ4320 is given as -145 dBc/Hz which as no information is given on the PSD shape is assumed to be flatband. The rms RIN over a 7.85 MHz bandwidth is then,

$$P_{rms} = \sqrt{10^{-145/10} \times 7.85 \times 10^{6}} = 1.575 \times 10^{-4} \cdot P_c \qquad \text{(C.26)}$$

The 7.85 MHz bandwidth value is chosen as it is the brick-wall equivalent bandwidth for a single pole filter response for a 5 MHz cut frequency, as exhibited by the fastest transimpedance amplifier used in this thesis. As such this provides a worst case figure and equates to an optical SNR of

$$SNR_0(dB) = 10\log\left(\frac{1}{1.575 \times 10^{-4}}\right) = 38.03 \text{ dB} \qquad \text{(C.27)}$$

It should be noted that SNR is a power ratio but the square law nature of the PIN detector converts optical power into amplitude (voltage). As such, the equivalent electrical SNR value is,

$$SNR_e = \left(SNR_0\right)^2 \qquad \text{(C.28)}$$

which means one simply doubles the optical SNR quantity in decibels to arrive at an electrical SNR of 76.1 dB for the RIN noise contribution.

The distributed Bragg reflector laser diode (see section 4.6.6) used as the reference source can be expected to perform as well as the external cavity based Ando AQ4320 tuneable laser in terms of RIN assuming it is driven by a stable low noise current source.

Source Phase Noise

Phase noise is the random variation of phase in the output of laser source. One effect is to cause a broadening of the linewidth of a laser source and thus a corresponding reduction in the coherence length of the source. In interferometric applications, phase noise is converted directly into fringe intensity variation over time, reducing its definition and thus the resolution of the instrument. This is usually modelled as the reduction of the SNR, the effect of which is added to the RIN derived in section **Error! Reference source not found.**.

Petermann and Weidel (1981) derived the spectral density functions for intensity noise at the output of an interferometer due to phase noise for the specific case of in-quadrature operation. Early experimental measurements on a range of laser diode were made by Dandridge and Tveten (1981). Moslehi (1986) extended the theoretical analysis of the phase noise of a single mode laser diode operating at any bias point. Salehi and Cabon (2004) then further considered the effects of dispersion on the results for long fibre lengths (tens of kilometres). Cliche and Têtu (2005) considered the effects of linewidth reduction systems on the phase noise.

Since the length of fibre being considered in the instruments in this thesis is relatively short, the effects of dispersion may be neglected. Also as the maximum sensitivity to phase noise occurs at the quadrature operating point, it is reasonable to use definition for the PSD of intensity noise occurring due to phase noise. An approximation, given by Moslehi (1986), for the bilateral spectral density is valid in the coherent regime in which the instruments operate,

$$S_{ph}(f) \approx \frac{I_0^2}{2}\frac{|T|^2}{\tau_c}\operatorname{sinc}^2(fT) \tag{C.29}$$

where $|T|$ is the differential time delay between the interferometer arms, τ_c is the coherence time and I_0 is the input power.

Taking the PSD profile of the laser output to be Lorentzian, and knowing the FWHM to be 1 MHz (Ando AQ430D), it is possible to determine the coherence time using the definition given in section 3.4.6 as

$$\tau_c = \frac{1}{1\times10^6\pi} = 318.3 \text{ ns} \tag{C.30}$$

Given that the interferometers are only being considered over one full fringe we can consider the largest differential time delay as being at the full extent of the range, which in the case of 1550 nm operating wavelength is 775 nm. The equivalent time delay is,

$$T = \frac{nl}{c} = 2.583 \text{ fs} \tag{C.31}$$

bearing in mind that the added imbalance takes place in free space. Over the frequency range at which either instrument operates the maximum frequency is $f = 7.85$ MHz . Over this range it is found that $\mathrm{sinc}^2(fT) \approx 1$ and **Error! Reference source not found.** becomes,

$$S_I(f) \approx \frac{I_0^2}{2}\frac{|T|^2}{\tau_c} \tag{C.32}$$

Since the power spectral density is approximately constant over the bandwidth, the normalised rms value of the amplitude noise is then simply given by,

$$S_{ph}(f) \approx \sqrt{\frac{|T|^2 \Delta f}{\tau_c}} = 2.566\times10^{-8} \tag{C.33}$$

where $\Delta f = 7.85$ MHz is the full bandwidth of operation. This gives an electrical SNR of 168.1 dB at the detector.

Although the effect of linewidth broadening may result in fringe definition being reduced, the associated reduction in coherence length can actually be beneficial from the point of view of fibre interferometers resulting as it does in reduced etalon fringes by eliminating some of the coherent mixing.

Etalon Fringes

An etalon is an optical resonator (or cavity) formed from planar reflectors. Etalons see wide use as high finesse filters (such as the Fabry-Pérot interferometer) where the reflectors are partially silvered mirrors separated in air. However an etalon may just as well be formed from a solid piece of transparent material; the Fresnel reflection caused by the discontinuity of the refractive index at the material – air boundary of the facets results in the formation of an etalon.

Etalons formed between any two surfaces in an optical system can cause major headaches in instrument utilising coherent light, especially when dealing with fibre optics. In general, the reduction of etalons is done by using suitable coatings on surfaces to reduce reflections and the deliberate misalignment of surfaces (canting) to ensure the reflections end up somewhere harmless.

Each etalon acts as an interferometer and has the effect of causing FM-AM conversion of the light due to the interference of light with delayed copies of itself. In the case of fibre optics, each connection between fibres/integrated optic components results in the creation of multiple etalons. Furthermore, the spatial coherence is extremely high in single mode fibres due to the exact alignment and the Gaussian wavefront of the single guided mode. There is no 'washing out' (averaging) of the fringes over the wavefront; thus the interference produces a fringe with almost full contrast. This means that even relatively low levels of back reflected light from etalons can cause severe problems with generated intensity noise (Hobbs p243).

Any source phase noise is converted to amplitude noise by each etalon in the system, the magnitude of the noise being dependent upon the etalon length and the strength of the reflections. Reducing the linewidth of the source does not necessary help matters because the associated increase in coherence length can result in more etalons being setup.

The longer the coherence length of the light source, the more etalons that can mix coherently, further compounding the problem. In this case, a broader linewidth source may be beneficial for reducing this effect, at the expense of added phase noise.

Reducing etalon fringes in fibre requires the reducing the back reflection occurring at any interfaces within the optical circuit. Any point in the circuit has a refractive index differential can form an etalon. Fibre connectors, used to facilitate the coupling of lengths of fibre together are often the worse candidates. In addition, any fibre linked integrated-optic device will suffer from back reflection at the fibre-waveguide interface.

Return loss (or reflection loss) is that loss in power of a transmitted signal due to reflection at an interface. In optical terms return loss describes the amount of power reflected back from a refractive index discontinuity. The return loss, L_R in decibels is simply the ratio of the input power, P_i to the reflected power, P_r;

$$L_R(dB) = 10\log\left(\frac{P_i}{P_r}\right) \qquad \text{(C.24)}$$

One example of return loss commonly experienced in a fibre optic circuit is that caused by the Fresnel loss between the interface of a bare fibre end, cleaved normally to its axis, and air. The reflectivity, $\Re$ is the fraction of power reflected back (return loss in this case) and is dependent on the two refractive indexes forming the interface, n_0 and n_1;

$$\Re = \left(\frac{n_0 - n_1}{n_0 + n_1} \right)^2 \tag{C.25}$$

If **Error! Reference source not found.** is evaluated for a fibre to air interface where, $n_0 = 1.48$ is the index of the fibre core and $n_0 = 1$ approximates the index of air. The reflectivity, $\Re$ is then seen to be 0.0375 (≈ 4%) producing a return loss of 14.3 dB, an extremely large and problematic value.

Minimising the return loss associated with bare fibre ends is done by ensuring the end is placed in a quantity of a suitable index matched gel. This acts as a beam dump, ensuring the efficient coupling of the beam from the fibre and dispersing it harmlessly. We must consider also the importance of index match between the gel and the fibre core; a mismatch of 0.01 in their refractive indexes will result in a return loss of 24.7 dB.

Another common place for etalon creation to occur between connectors used to couple fibre sections together. The standard FC/PC polished connectors that are commonly used in laboratories for the quick and easy coupling of single mode fibres will have at best a return loss of 40 dB and this is subject to increase as the connector wears through several mating cycles. This is decreased to 50 dB for the more highly polished FC/UPC version and is seen to be much improved to 60 dB for the angled FC/APC connector. The end of the FC/APC version of the connector is polished at an angle of 8° thus ensuring that most of the Fresnel reflected light is directed back into the fibre at above the acceptance angle and thus passes harmlessly into the cladding rather than being guided. In addition to the use of high quality connectors, it is possible to reduce return loss significantly, even with FC/PC connectors by applying a suitable index matching gel to the mating faces before connecting. This is often not suitable for field use, or where regular re-connection is anticipated; in a clean optical

laboratory, and with diligent cleaning between mating cycles it is an effective method of reducing return loss.

A better way to reduce the potential for etalon creation in an optical fibre circuit is not to use couplers at all were possible but to use a fusion splicer to join fibre lengths wherever possible. Clearly this limits flexibility somewhat, but towards the final stages of development of an instrument, may well prove critical.

In addition, the use of all-fibre devices should also be investigated. One example of such a device is an all-fibre coupler. These devices are created twisting fibre together and fusing of them. The result is to produce the same effect as an integrated optic coupler, but because the light never leaves the fibre, return loss is generally seen to be lower.

There are times that integrated-optic components must be used, for example an electro-optic phase modulator (EOPM) is unavailable as an all-fibre entity. In the case of the EOPM used in the instrument developed in this thesis (EOSpace low V_{pi}) the total return loss is 50 dB. This includes the return loss from the fibre connectors as well as the fibre-to-device interface itself.

In summary, etaloning is a serious problem in any high coherence optical instrument but is particularly serious when dealing with optical fibres as the alignment if fixed. It is also not feasible to give a theoretical analysis of etaloning in an instrument and in general the solution must be reduce any back reflection at interfaces as much as possible by paying attention to all index interfaces and coatings.

Intrinsic Fibre Phase Noise

In any optical medium the refractive index undergoes several statistical fluctuations due to thermodynamic processes. They are more pronounced in optical systems that have their optical paths contained in a solid material. The solid waveguide coupled with generally long path lengths mean that fibre optic systems are particularly susceptible to this noise type. The mechanisms involved in generating thermodynamic phase noise are related to the larger scale difference in path length change we see during external perturbation due to temperature drift and vibration but generally it is treated separately due to the smaller scale mechanics involved.

The intrinsic fibre phase noise is results from the statistical fluctuation of density and temperature which results in a variation of index. The two mechanisms have differing magnitudes and frequency dependence, hence they are treated separately and then summated to give an overall result.

The original derivation was given by Glenn (1989) for the case of a fibre with infinite cladding. This was then considered further by Wanser (1992) who extended the definition of the thermodynamic element to include a finite cladding diameter. This analysis results in lower noise values at frequencies below 200 Hz. These results were then experimentally verified by Wanser (1993). Kråkenes and Bløtekjær (1995) considered the effects of phase noise on Mach-Zehnder and Sagnac interferometers. Annovazzi-Lodi et al. (1996) extended the comparisons further to include the Fabry Perot interferometer and ring resonator.

In general at low frequencies it is found that the thermodynamic fluctuation is of much greater magnitude than the density fluctuation. It is now possible to consider the two cases separately.

Density Fluctuation

Glenn (1989) derives spectral density of the contribution due to density fluctuation as

$$\left\langle \phi(\omega)^2 \right\rangle_\rho = -k_b T \frac{1}{V}\left(\frac{\partial V}{\partial T}\right)_\rho \frac{4.75}{\upsilon\lambda^2} q \int_{-q}^{q} \frac{\sin^2 x}{x^2} dx \qquad \text{(C.26)}$$

which is valid for the special case when $\frac{\omega a}{\upsilon} \ll 1$. k_b is Boltzmann's constant, T is the temperature, λ the operating wavelength and $\frac{1}{V}\left(\frac{\partial V}{\partial T}\right)_\rho$ is the compressibility of silica. υ is the acoustic velocity in silica and $q = \frac{\omega l}{2\upsilon}$ where l the total length of fibre being considered and a is the core radius.

The special case is valid when $w \ll 190$ MHz and is thus valid for this analysis considering that the highest cut frequency of the transimpedance amplifiers used is 5 Mhz.

The integral in **Error! Reference source not found.** can be approximated for all practical purposes by πq which leads to the simplification

$$S_{\Delta\rho}(\omega) = -k_b T \frac{1}{V}\left(\frac{\partial V}{\partial T}\right)_\rho \frac{4.75\omega l}{2\pi\upsilon^2\lambda^2} \tag{C.27}$$

The mean square value of the phase noise is then simply the integral of **Error! Reference source not found.** which from DC to $f_{\max}$ in hertz is

$$\left\langle \phi^2 \right\rangle_\rho = -k_b T \frac{1}{V}\left(\frac{\partial V}{\partial T}\right)_\rho \frac{4.75 l}{2\pi^2\upsilon^2\lambda^2} f_{\max}^2 \tag{C.28}$$

Thermal Fluctuation

Wanser (1992) gives the power spectral density of the noise due to thermal processes in the fibre as

$$\mathrm{S}_{\Delta\phi}(\omega) = \frac{k_b T^2 l}{2\kappa\lambda^2}\left(\frac{dn}{dT} + n\alpha_L\right)^2 \ln\left\{\frac{\left[\left(2/w_0\right)^2 + \left(\omega n/c\right)^2\right]^2 + \left(\omega/D\right)^2}{\left[\left(2.405/a_f\right)^2 + \left(\omega n/c\right)^2\right]^2 + \left(\omega/D\right)^2}\right\} \tag{C.29}$$

where κ is the thermal conductivity of the fibre, D the thermal diffusivity and α is the linear thermal coefficient of expansion. dn/dT signifies the change in index with temperature of the fibre while ω_0 and a_f are the mode field radius and outer radius of the cladding. All other parameters are as defined for **Error! Reference source not found.**.

A zero frequency case is also given to correct for the effect of finite cladding diameter for the low frequencies,

$$\mathrm{S}_{\Delta\phi}(0) = \frac{k_b T^2 l}{2\kappa\lambda^2}\left(\frac{dn}{dT} + n\alpha_L\right)^2 \ln\left(\frac{2a_f}{2.405 w_0}\right) \tag{C.30}$$

The result of this is a reduction in the noise magnitude for low frequencies but over the 5 MHz bandwidth operated on by the instruments in this theory this slight improvement below is insignificant and therefore neglected.

A typical set of values for a single mode fibre operating at room temperature and at a wavelength of 1550 nm is shown in Table C.1**Error! Reference source not found.**.

Property	Notation	Value
Temperature	T	300 K
Temperature coefficient of index	$\frac{dn}{dT}$	13.5×10^{-5} K^{-1}
Compressibility	$\frac{1}{V}\left(\frac{dV}{dP}\right)_T$	$-1/3.6\times10^{10}$ Pa^{-1}
Acoustic velocity	υ	5962 ms^{-1}
Thermal conductivity	κ	$1.37\ W(m\cdot K)^{-1}$
Linear expansion coefficient	α_L	0.41×10^{-6} K^{-1}
Thermal diffusivity	D	0.82×10^{-6} m^2s^{-1}
Outer cladding diameter	a_f	125 μm
Operating wavelength	λ	1550 nm
Index	n	1.468
Mode field radius	w_0	10 μm

Table C.1 Parameter values for Silica

Matlab was used to plot the spectral density functions for the density and phase contributions and the result is seen in figure C.2**Error! Reference source not found.**. It is quite apparent that the temperature fluctuation contribution is much more important at low frequencies. However there is a cross over point at around 700 kHz after which it is seen that density fluctuation is the main contributor to the overall noise.

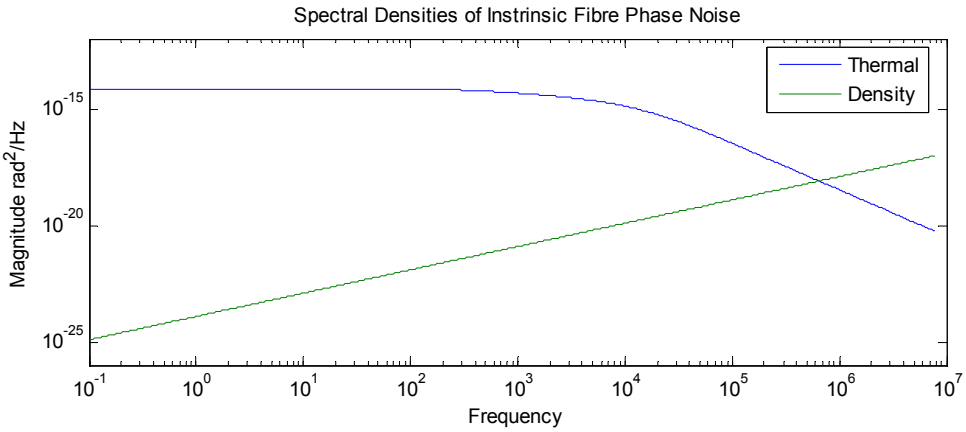

C.2 Spectral Densities of intrinsic fibre phase noise contributions

Matlab was used to calculate the mean square noise values for both the density and phase fluctuation contributions over a 5 MHz bandwidth from DC. They are respectively,

$$\phi_\rho^2 = 15.36 \text{ µrad} \tag{C.31}$$

$$\phi_\rho^2 = 17.76 \text{ µrad} \tag{C.32}$$

where the fibre length is 20 m. For a Michelson interferometer this equates to a total fibre length of 10 m since a double pass of each arm is made. The total rms contribution is then seen to be

$$\phi_{rms} = \sqrt{\phi_\rho^2 + \phi_T^2} = 23.48 \text{ µrad} \tag{C.33}$$

which in terms of measured height at an operating wavelength of 1550 nm is

$$\phi_{nm} = \frac{\lambda \phi_{rms}}{4\pi} = 2.896 \text{ pm} \tag{C.34}$$

Thermodynamic phase noise can be a serious and limiting noise source in fibre interferometric sensors. It generally presents the noise floor for any significant combination of fibre length and detected power. In the case of the instruments described in this thesis it effects are not particularly debilitating because of the short length of fibre under consideration.

C.4 Computationally Induced Noise

Although the various noise sources present in optical fibre interferometers have been considered individually, it also remains to consider their effect on any signal processing performed on the recorded intensity data. From the point of view of phase shifting interferometry specifically, the main concern is how noise propagates through the phase shifting algorithms that are used to derive the interferometer phase from the raw intensity outputs.

A wide selection of phase shifting algorithms have been developed starting with the Carré algorithm in 1966. Phase shifting algorithms all work in a similar fashion, by solving a set of simultaneous equations provided by a multiple set of intensity measurements taken from an interferometer at various phases (see section 4.7.8). Their sensitivity to varying noise sources within a system is variable however and this is one of the reasons for the multitude of different algorithms; they have different strengths when it comes to the reduction of differing noise types (Creath 1998).

Typical variations in phase shifting algorithms are the number of shifts performed, with the general trend being the reductions of error caused by noise in the raw data decreasing as the shift number increases. Clearly with an increased number of phase shifts, there is a performance hit due to increased acquisition and computation time. In general, the lengthening of the acquisition period can result in increased inaccuracies due to drift creeping into the measurement.

Wingerden et al. (1991) defined three noise types that can act upon a PSI algorithm and went on to estimate their effects on numerous algorithms by using linear approximation techniques. The three noise types defined were systematic, random with sinusoidal dependence and random with no correlation to initial phase. They are named as type 1, 2 and 3 noise respectively.

The noise types may be usefully represented by error terms in the interferometer equation

$$I = \left\{ \left(I_0 + \varepsilon_1(t) \right) \left[1 + V \cos\left(\phi + \varepsilon_2(t) \right) \right] \right\} \varepsilon_3(t) \qquad \text{(C.35)}$$

where $\varepsilon_N(t)$ is a noise source of type N.

From **Error! Reference source not found.** it is clear where the source of each noise type originates. Type 1 results from intensity variation (RIN) in the light source and

any etalon effects. Type 2 is phase noise which results from environmental disturbance and intrinsic fibre phase noise. Type 3 is noise introduced after the interference has taken place and is mainly the result of electronic noise introduced by the detection front end.

A numerical simulation can provide a good indication of the behaviours of phase shifting algorithms. Matlab simulations for each of the three noise types were carried out and the scripts may be found in appendix C. The simulations add a random noise having a Gaussian distribution and then monitor the resulting error induced in the calculated output phase. The optimal Carré phase shift of $\alpha = 55°$ with regard to random noise elimination is used throughout the simulations. The simulation was carried out with a linearly increasing phase difference between 0 and 2π to see whether the noise output varies on the input phase. The simulation runs over 10000 samples for any given input range, thus it is possible to be confident of the results due to the large amount of trials.

Type 1 Noise Simulation

Figure C.3**Error! Reference source not found.** shows the consequences of type 1 noise upon the Carré algorithm. There are several components which are clockwise from the top left; the input phase value, the input intensities for each phase shift (after phase noise addition), calculated phase and error in the calculated output. The input intensities at each phase shift are represented by a seperate colour.

A relatively large amount of noise was introduced to make the effects of the noise clear. The input noise was white noise having a Gaussian distribution, the signal to noise ratio is 40 dB and the fringe visibility is 0.9. The issue of wraparounds is quite evident at the extremes of the unambiguous phase range.

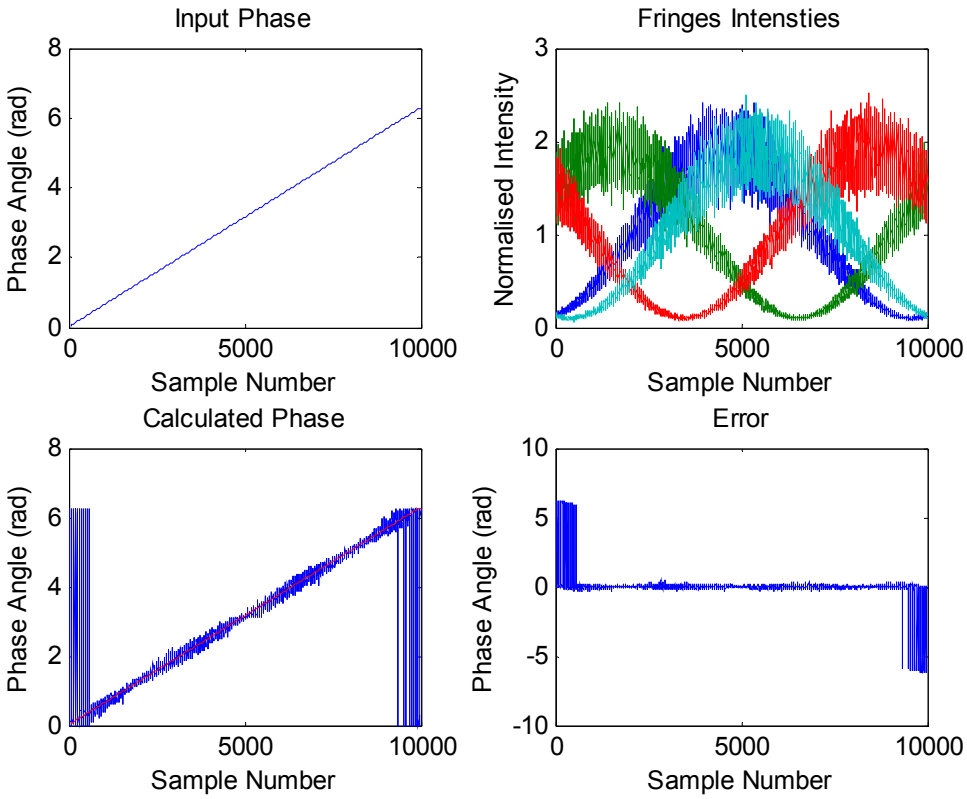

C.3 Effect of type 1 noise showing induced wraparounds

The gross errors that occur around the 0 and 2π boundaries are due to phase wrapping distortions. This is clearly and major issue if phase unwrapping techniques are being used to make measurements larger than one full fringe, but is really is a specific difficulty in those circumstances. What is of more interest in this apparatus is the noise propagation for smaller optical path changes. For this reason is makes sense to reduce the phase angle range over which the simulation operates while keeping in mind the severity of the effect just seen. In **Error! Reference source not found.** the same analysis is performed but with the input phase angle range between $0.1\pi \le \phi \le 1.9\pi$, the wraparound errors are now excluded. The results are shown in figure C.4.

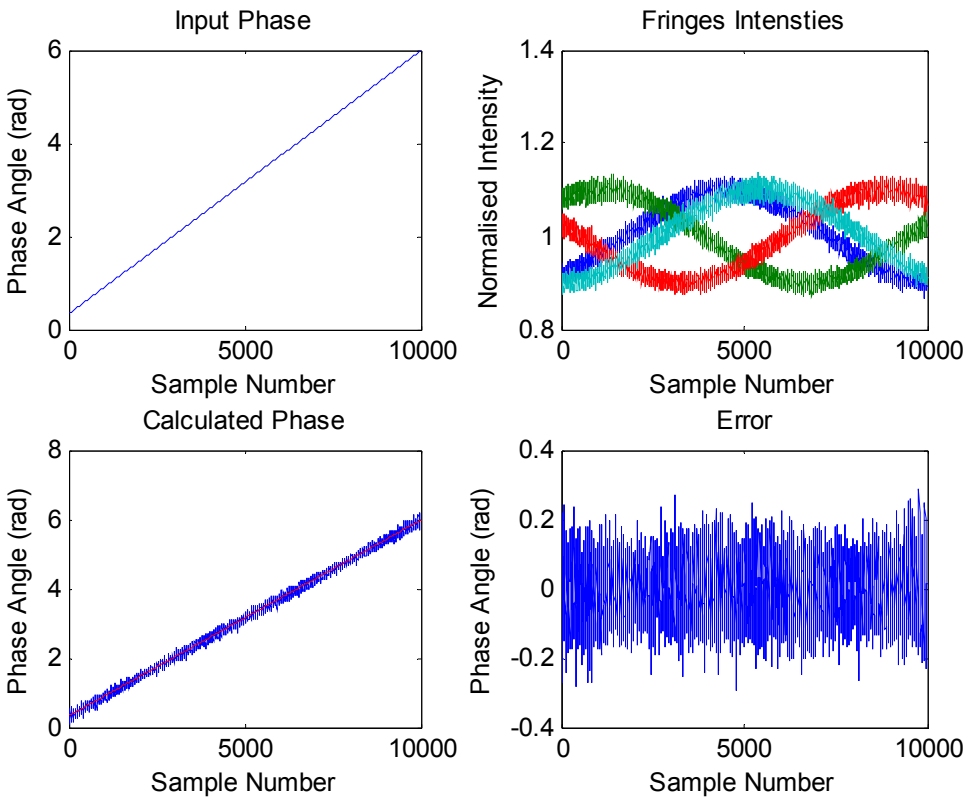

C.4 Effect of type 1 noise

The average SNR for the error signal was calculated and found to be 22.6 dB. This means that a loss of 17.4 dB is incurred by using the phase shifting algorithm at a visibility of 0.1. As might be expected, the noise performance degrades with a reduction of visibility.

Figure C.5**Error! Reference source not found.** shows histogram profiles for the input noise sources and the output noise to give an idea of the pdfs.

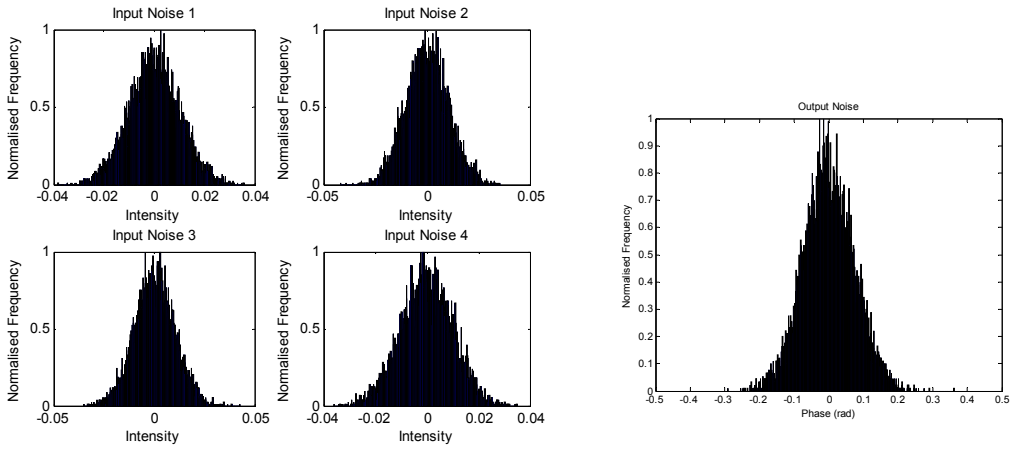

C.5 Histograms of type 1 input and output noise

Error! Reference source not found. Figure C.6 shows the case with a larger visibility of 0.9 but a noisier input intensity of 25 dB. Some other artefacts are now somewhat clearer. It would appear that the output error has a dependency upon the input phase value where maximum noise sensitivity appears at input phase values of 0, 110°, 220°.

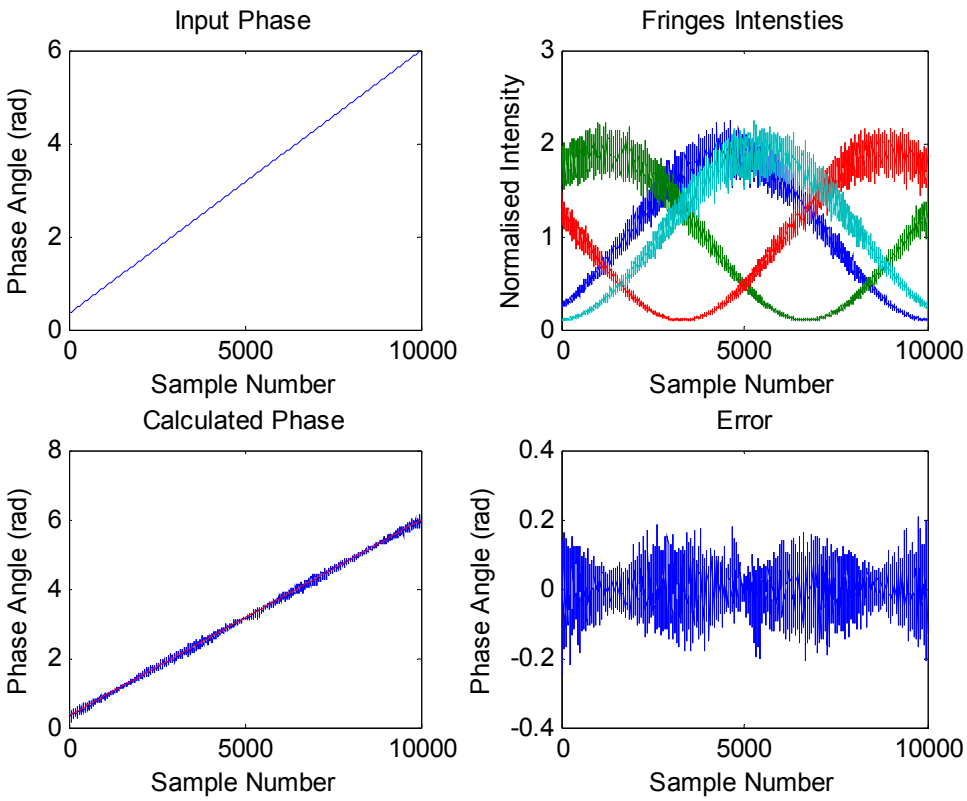

C.6 Glitch induced by type 1 noise

Also apparent is a glitch between in the region of input phase of 180°. The reason for this occurrence is due to the fact that the numerator in the Carré algorithm shown in (5.25) can become imaginary in the presence of input intensity noise. Computation of this yields a zero in the output of the algorithm when the results of which are clearly seen in the region around 180°. This can be considered a major weakness in the Carré algorithm for use in PSI situations with noisy intensity sources.

Type 2 Noise Simulation

This noise type arises from phase variation because of environmental effects and intrinsic fibre phase noise. Also any noise present in the EOPM driving signal will also be apparent as this type of phase noise.

Figure C.7**Error! Reference source not found.** shows the results of the first simulation for a constant rms phase noise of 0.1 rad. This would equate to 12.3 nm rms deviation optical path length or approximately 74 nm peak to peak. To use an

SNR value in this case is somewhat nonsensical because of the variation of the base input phase value.

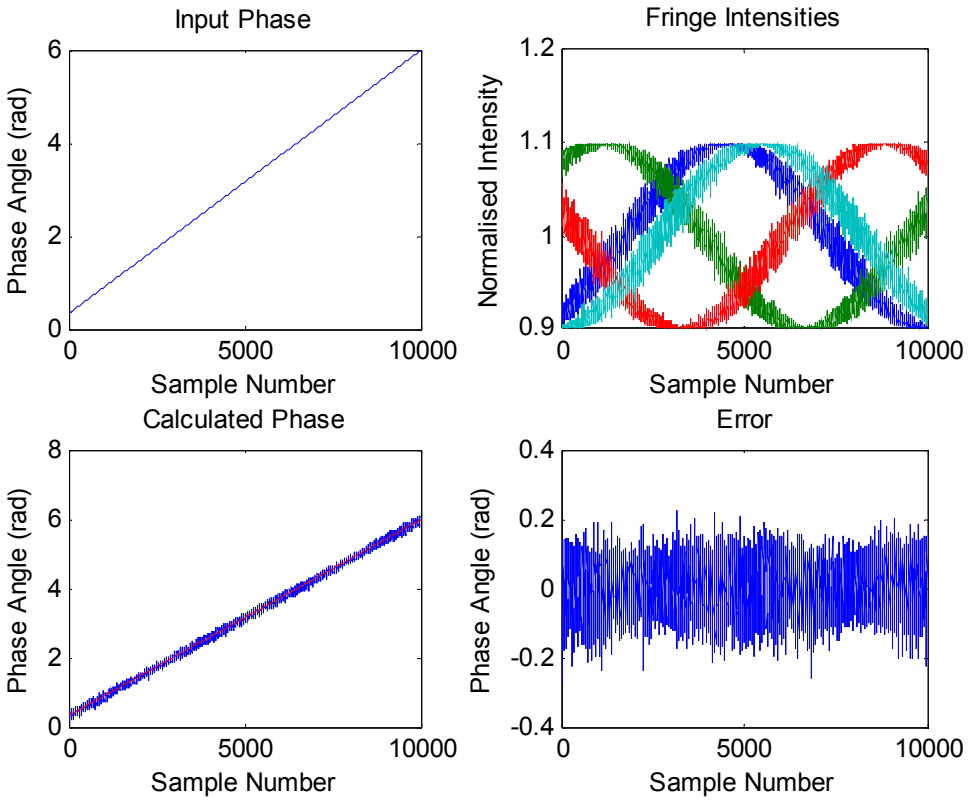

C.7 Effect of type 2 noise

The mean of the rms figures for the input noise was calculated by the script as 0.1000 rad while the output phase noise was 0.0637 rad. This amounts to a reduction of phase noise by approximately 36% for a phase shift of 55°. There is no obvious dependency on the input phase value so we can anticipate that regardless of the input phase value, the Carré algorithm has an averaging effect and slightly attenuates any random phase noise present during phase shifting. In addition it is found that there is no dependence of the noise performance due to fringe visibility.

Type 3 Noise Simulation

The last area of interest is that of noise applied after the interference has taken place. This may mainly be attributed to the electronic noise occurring when the output light intensity is converted to a voltage and quantisation noise added when digitising the

signal. **Error! Reference source not found.** Figure C.8 shows the results of the analysis for a fringe visibility of 0.1 and an input SNR of 40 dB.

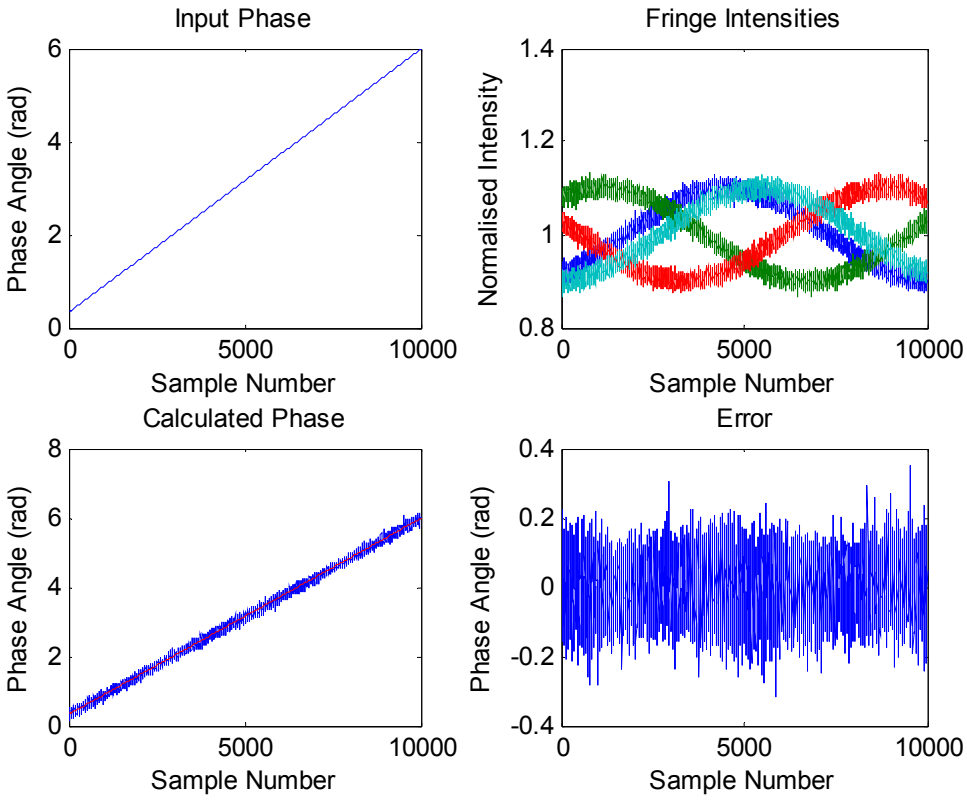

C.8 Effect of type 3 noise

The SNR of the error signal was seen to be 22.5 dB thus a reduction in error signal SNR of 17.5 dB occurs in the algorithm. This value does vary with visibility however experimental work shows that a fringe visibility of 0.1 is a reasonable worst case scenario.

It should be mentioned that the simulation for type 3 noise is not strictly accurate. It assumes that the input noise is independent of the input intensity. For shot noise **Error! Reference source not found.** shows that this is clearly not true. It is however true for all the other electronic noise sources in the detection front end and, these sources override the shot noise contribution for the instruments discussed in this thesis.

Noise Dependence on Phase Shift Angle

Qian et al. (2000) determined that for general purpose use 55° provides the best phase shifting angle, unless there is a particular systematic error in the system that requires minimisation. In such a special case it may be useful to select a different phase shifting angle.

In the MFI the wavelength scanning means the phase shifted angle is not static across the scanned profile. If the phase shift is set to 55° at the reference interferometer wavelength of 1550 nm, the measurement interferometer phase shift will be $53.78° \leq \alpha \leq 54.82$ for a scan range of 1555 – 1585 nm. In this case it is necessary to find whether the noise performance of the algorithm degrades away from the idea phase shift value.

In order to do this the simulations for type 2 noise and type 3 noise were for varying phase shift angles where $0° < \alpha < 180°$. The ratio of the output to input noise, or noise gain, was then plotted against the phase step value. The results are shown in figure C.9.

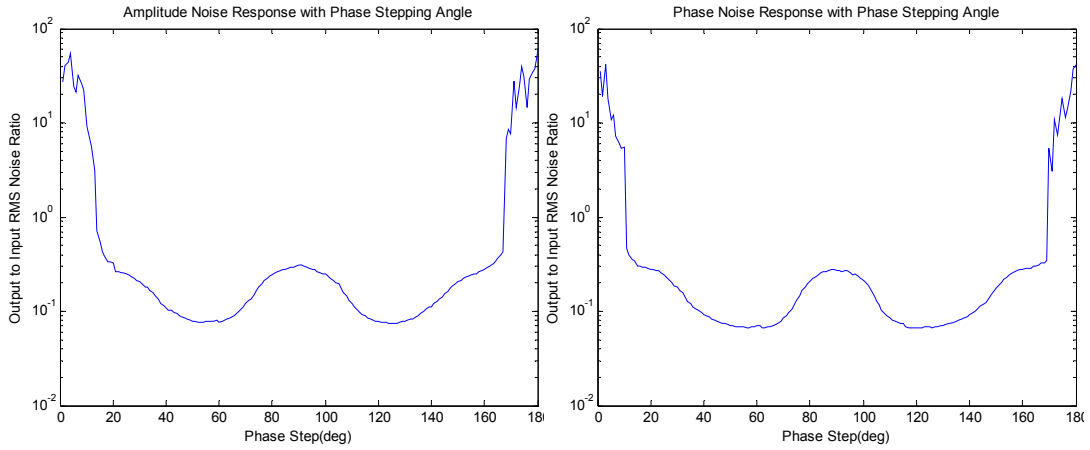

C.9 Effect of phase angle on type 2 and 3 noise

It can be seen that for both type 2 and type 3 noise there is little variation in noise gain between phase stepping angles of 55° and 53° so it is possible to be confident in operating the algorithm within these limits.

In summary it is possible to say that without we can reasonably expect the action of PSI algorithms to be insignificant in noise terms under normal operation and away from the boundaries of the unambiguous range. With phase unwrapping techniques it is possible to reduce the problems that can occur when a wraparound is enforced.

D Matlab Scripts

D.1 Matlab Script for LF356 Transimpedance Analysis

```
% This script describes the response of a LF356 transimpedance amplifier.
% Component Values go here
Rd = 5e9          % Diode shunt resistance
Cd = 1e-12         % Diode parasitic capacitance
Cin =3e-12        % Opamp input capacitance
Rf = 50e3        % Feedback resistance
Cf = 10e-12       % Feedback capacitance
Cp = Cd + Cin      % Total parasitic capacitance
% Aol is approximated by a 1st order LPF with a break frequency of 28Hz and 20dB/decade roll off.
Aol = 1.77828e5 * tf([1] , [(1/(45*pi)) 1]) ;        % Open loop voltage gain LF356 (105 dB, GBW 4 Mhz)
% Calculate the shunt complex impedance at the input due to diode
% characteristics and parasitic capacitances.
Zsh = tf( [Rd] , [(Cp*Rd) 1]);
% Calculate feedback complex impedance for the transimpedance amplifier. This
% provides the response roll off
Zf = tf( [Rf] , [(Cf*Rf) 1]);
% Here we calculate the feedback fraction, beta and the resulting CL
% voltage gain and transimpedance
beta = 1 / (1 + (Zf / Zsh));                 % Feedback Fraction, Beta
Acl = Aol / (1 + (beta * Aol));               % Closed Loop Gain
trans = (Aol * Zf ) / (1 + Aol + (Zf / Zsh));   % Transimpedance
%%%%%%%%%%%%%%%%%%%%%%%%%%%%%%%%%%%%%%%%%%%%%%%%%%%%%%%%%%
% Determine transimpedance values in numeric terms
[MAGtrans,PHtrans,Wtrans]=bode(trans,{1,1e8});
MAGtrans = MAGtrans(:);
PHtrans = MAGtrans(:);
Ftrans = Wtrans./ (2*pi)
% Graphical Routines go here
figure(1)
step(trans);                         % Plot Step Response
figure(2)
subplot(2,2,1);                       % Plot Op Amp Open Loop Gain
bode(Aol,{1,1e8})
title('Open Loop Gain, Aol')
xlabel('Frequency (Hz)')
ylabel('Voltage Gain (dB)')
%axis([10 1e7 0 130])
subplot(2,2,2);                       % Plot Closed Loop Voltage Gain
bode(Acl,{1 1e8})
title('Closed Loop Voltage Gain, Acl')
xlabel('Frequency (Hz)')
ylabel('Voltage Gain (dB)')
%axis([10 1e7 0.1 10])
subplot(2,2,3);                       % Plot Transimpedance (dB)
bode(trans,{1,1e8})
title('Transimpedance, (dB)')
xlabel('Frequency (Hz)')
ylabel('Current Gain (dB)')
%axis([10 1e7 0 130])
subplot(2,2,4);                       % Plot Transimpedance (ohms)
semilogx (Ftrans,MAGtrans);
title('Transimpedance')
xlabel('Frequency (Hz)')
ylabel('Current Gain (Iph/V)')
axis([10 1e7 0 Rf])
```

D.2 Matlab Script for THS4062 Transimpedance Analysis

```
% This script describes the response of a THS4062 transimpedance amplifier.
% Component Values go here
Rd = 5e9          % Diode shunt resistance
Cd = 1e-12         % Diode parasitic capacitance
Cin =3e-12        % Opamp input capacitance
Rf = 100e3        % Feedback resistance
Cf = 10e-12       % Feedback capacitance
Cp = Cd + Cin      % Total parasitic capacitance
% Aol is approximated by a 1st order LPF with a break frequency of 28Hz and 20dB/decade roll off.
Aol = 1.77828e5 * tf([1] , [(1/(45*pi)) 1]) ;        % Open loop voltage gain LF356 (105 dB, GBW 4 Mhz)
% Calculate the shunt complex impedance at the input due to diode
% characteristics and parasitic capacitances.
Zsh = tf( [Rd] , [(Cp*Rd) 1]);
% Calculate feedback complex impedance for the transimpedance amplifier. This
% provides the response roll off
Zf = tf( [Rf] , [(Cf*Rf) 1]);
% Here we calculate the feedback fraction, beta and the resulting CL
% voltage gain and transimpedance
beta = 1 / (1 + (Zf / Zsh));                  % Feedback Fraction, Beta
Acl = Aol / (1 + (beta * Aol));               % Closed Loop Gain
trans = (Aol * Zf ) / (1 + Aol + (Zf / Zsh));   % Transimpedance
%%%%%%%%%%%%%%%%%%%%%%%%%%%%%%%%%%%%%%%%%%%%%%%%%%%%%%%%%
% Determine transimpedance values in numeric terms
[MAGtrans,PHtrans,Wtrans]=bode(trans,{1,1e8});
MAGtrans = MAGtrans(:);
PHtrans = MAGtrans(:);
Ftrans = Wtrans./ (2*pi);
% Graphical Routines go here
figure(1)
step(trans);                        % Plot Step Response
figure(2)
subplot(2,2,1);                      % Plot Op Amp Open Loop Gain
bodemag(Aol,{1,1e8})
title('Open Loop Gain, Aol')
%xlabel('Frequency (Hz)')
%ylabel('Voltage Gain (dB)')
%axis([10 1e7 0 130])
subplot(2,2,2);                      % Plot Closed Loop Voltage Gain
bodemag(Acl,{1 1e8})
title('Closed Loop Voltage Gain, Acl')
%xlabel('Frequency (Hz)')
%ylabel('Voltage Gain (dB)')
%axis([10 1e7 0.1 10])
subplot(2,2,3);                      % Plot Transimpedance (dB)
bodemag(trans,{1,1e8})
title('Transimpedance, (dB)')
%xlabel('Frequency (Hz)')
%ylabel('Current Gain (dB)')
%axis([10 1e7 0 130])
subplot(2,2,4);                      % Plot Transimpedance (ohms)
semilogx (Ftrans,MAGtrans);
title('Transimpedance')
xlabel('Frequency (Hz)')
ylabel('Transimpedance (ohms)')
axis([10 1e7 0 Rf])
grid on;
%[MAG,PHASE] = BODE(Aol,(4e6)*(2*pi));
%MAG = 20*log10(MAG)
```

D.3 Matlab Script for Disturbance Rejection Analysis

```
% Script to simulate the behaviour of the closed loop disturbance
% rejection method employed on the MFI.
% Haydn Martin 1/4/2008
clear all;
% PI Parallel Controller Definition
Kp = [0 0.001 0.01 0.1 1]         % Prop Gain Matrix
Ki = [1e3 2e3 3e3 4e3 5.75e3]       % Integrator Gain Matrix
%Ki = 5.75e3                     % Integrator Gain
% Setup up SISO transfer function matrix with varying Kp and Ki values
for n=1:5,
   for j=1:5,
   %Gc(1,1,j,n) = Kp(j) + tf(Ki(n) , [1 0]);    % Integrator Transfer Function
   Gc(1,1,j,n) = tf([Kp(j) Ki(n)] , [1 0]);    % Integrator Transfer Function
   end
end
% Modelling of PZT response
k = 18.67e6                    % Stiffness (N/m)
m = 1e-3                      % Mass (kg)
Fres = 22e3                     % Unloaded piezo resonance (Hz)
m0 = k/((2*pi*Fres)^2)         % Calculate unloaded mass
meff = m + m0              % Effective mass includes PZT unloaded mass + load mass
Wn = sqrt(k/meff)          % Calculate resonant frequency (rad) from stiffness and mass
Q = 5                    % Quality factor. Decreases with increased damping
Fn = Wn/(2*pi)                        % Resonant frequency (Hz)
%Q=[1 2 5 10 20]
%for n=1:5,
%Gpzt(1,1,1,n) = tf(Wn^2, [1 (Wn./Q(n)) Wn^2]);        % PZT Response Model
%end
Gpzt = tf(Wn^2, [1 (Wn/Q) Wn^2]);
%%%%%%%%%%%%%%%%%%%%%%%%%%%%%%%%%%%%%%%%%%%%%%%%%%%%%%%%%%%%%%%%%%%%%%%%%
%
% Conversion Gains of the Photodiode frontend and the interferometer
Kpd = 150e3
Kif = 1/50e3
%%%%%%%%%%%%%%%%%%%%%%%%%%%%%%%%%%%%%%%%%%%%%%%%%%%%%%%%%%%%%%%%%%%%%%%%%
%
Gs = Gc*Gpzt*Kif*Kpd;  % Calculate openloop transfer function
CLTF = feedback(Gs,1);      % Calculate closed loop transfer function
sens = Kif*Kpd/(1 + (Kif*Kpd*Gc*Gpzt));  % Disturbance sensitivity function
%ltiview(pzt,PI,closed)
% STUDY OF INTEGRATION GAIN VARIATION
% Tests for stability are CL Step Response, Open Loop Bode and Open Loop Nichols
Psel = 4;        % Select Kp array number for graphing
figure(1)
step(CLTF(:,:,Psel,1),'b',CLTF(:,:,Psel,2),'k',CLTF(:,:,Psel,3),'r',CLTF(:,:,Psel,4),'m',CLTF(:,:,Psel,5),'g')
grid on;
legend('Ki=1 kHz','Ki=2 kHz','Ki=3 kHz','Ki=4 kHz','Ki=5.75 kHz');
title('Kp=0.1')
axis([0 7e-3 0 1.2])
figure(2)
bode(Gs(:,:,Psel,1),'b',Gs(:,:,Psel,2),'k',Gs(:,:,Psel,3),'r',Gs(:,:,Psel,4),'m',Gs(:,:,Psel,5),'g',{1,10e5})
grid on
legend('Ki=1 kHz','Ki=2 kHz','Ki=3 kHz','Ki=4 kHz','Ki=5.75 kHz');
title('Kp=0.1')
axis auto
figure(3)
nichols(Gs(:,:,Psel,1),'b',Gs(:,:,Psel,2),'k',Gs(:,:,Psel,3),'r',Gs(:,:,Psel,4),'m',Gs(:,:,Psel,5),'g',{1,10e5})
axis tight;
legend('Ki=1 kHz','Ki=2 kHz','Ki=3 kHz','Ki=4 kHz','Ki=5.75 kHz');
title('Kp=0.1')
axis auto
% Peformance Study is Sensitivity Bode
figure(4)
bode(sens(:,:,Psel,1),'b',sens(:,:,Psel,2),'k',sens(:,:,Psel,3),'r',sens(:,:,Psel,4),'m',sens(:,:,Psel,5),'g',{1,10e5})
grid on
legend('Ki=1 kHz','Ki=2 kHz','Ki=3 kHz','Ki=4 kHz','Ki=5.75 kHz');
title('Kp=0.1')
axis auto
% STUDY OF PROPORTIONAL GAIN VARIATION
Isel = 3;        % Select Ki array number for graphing
```

```
figure(5)
step(CLTF(:,:,1,Isel),'b',CLTF(:,:,2,Isel),'k',CLTF(:,:,3,Isel),'r',CLTF(:,:,4,Isel),'m',CLTF(:,:,5,Isel),'g');
axis tight;
grid on
legend('Kp=0','Kp=0.001','Kp=0.01','Kp=0.1','Kp=1');
title('Kp=3 kHz')
axis auto
figure(6)
bode(Gs(:,:,1,Isel),'b',Gs(:,:,2,Isel),'k',Gs(:,:,3,Isel),'r',Gs(:,:,4,Isel),'m',Gs(:,:,5,Isel),'g',{1,10e5});
axis tight;
grid on
title('Kp=3 kHz')
legend('Kp=0','Kp=0.001','Kp=0.01','Kp=0.1','Kp=1');
axis auto
figure(7)
nichols(Gs(:,:,1,Isel),'b',Gs(:,:,2,Isel),'k',Gs(:,:,3,Isel),'r',Gs(:,:,4,Isel),'m',Gs(:,:,5,Isel),'g',{1,10e5});
title('Kp=3 kHz')
legend('Kp=0','Kp=0.001','Kp=0.01','Kp=0.1','Kp=1');
axis auto
figure(7)
nichols(sens(:,:,1,Isel),'b',sens(:,:,2,Isel),'k',sens(:,:,3,Isel),'r',sens(:,:,4,Isel),'m',sens(:,:,5,Isel),'g',{1,10e5});
title('Kp=3 kHz')
legend('Kp=0','Kp=0.001','Kp=0.01','Kp=0.1','Kp=1');
axis auto
% Peformance Study is Sensitivity Bode
figure(8)
bode(sens(:,:,1,Isel),'b',sens(:,:,2,Isel),'k',sens(:,:,3,Isel),'r',sens(:,:,4,Isel),'m',sens(:,:,5,Isel),'g',{1,10e5});
grid on
title('Kp=3 kHz')
legend('Kp=0','Kp=0.001','Kp=0.01','Kp=0.1','Kp=1');
axis auto
figure(9)
step(Gpzt);
grid on
```

D.4 Matlab Script for Transimpedance Amplifier Noise

```
% This script describes the response of a transimpedance amplifier.
clear all;
% Universal Constants/Settings
kB = 1.3806503e-23;  % Boltzmann constant, m2 kg s-2 K-1
T = 300;             % Operating temperature, K
elec = 1.60217646e-19;  % Charge on an electron, Coulombs
i_ph = 40e-6;        % DC Photocurrent produced
Vbias = 5;
Rf = 100e3;          % Feedback resistance
Rd = 5e9;            % Diode shunt resistance
Cd = 1e-12;          % Diode parasitic capacitance
f = logspace(0.1,9,1000);       % Setup frequency array for integration
frad = f*2*pi;
% LF356 Component Values go here
Cin =3e-12;          % Opamp input capacitance
Cf = 1.3e-12;        % Feedback capacitance
% Aol is approximated by a 1st order LPF with a break frequency of 28Hz and 20dB/decade roll off.
Aol = 1.77828e5 * tf([1] , [(1/(45*pi)) 1]) ;        % Open loop voltage gain LF356 (105 dB, GBW 4 Mhz)
% Calculate the shunt complex impedance at the input due to diode
% characteristics and parasitic capacitances.
Cp = Cd + Cin;       % Total parasitic capacitance
Zsh = tf( [Rd] , [(Cp*Rd) 1]);
% Calculate feedback complex impedance for the transimpedance amplifier. This
% provides the response roll off
Zf = tf( [Rf] , [(Cf*Rf) 1]);
% Here we calculate the feedback fraction, beta and the resulting CL
% voltage gain and transimpedance
beta = 1 / (1 + (Zf / Zsh));                 % Feedback Fraction, Beta
Acl = Aol / (1 + (beta * Aol));               % Closed Loop Gain
trans = (Aol * Zf ) / (1 + Aol + (Zf / Zsh));   % Transimpedance
trans1=trans;
%%%%%%%%%%%%%%%%%%%%%%%%%%%%%%%%%%%%%%%%%%%%%%%%%%%%%%%%%%%%%
% Define white noise sources
Vn_amp = (15e-9) ^ 2        % LF 356 amplifier voltage noise (white), V^2/Hz
In_shunt = (4*kB*T/Rd)    % Johnson current noise from shunt resistance, A^2/Hz
In_feed = (4*kB*T/Rf)    % Johnson current noise from feedback resistance, A^2/Hz
In_photo = 2 * elec * i_ph  % Shot noise associated with photo-current, A^2/Hz
In_dark = 2 * elec * (Vbias/Rd)  % Shot noise associated with dark current, A^2/Hz
In_amp = (0.01e-12) ^2           % Amplifer current noise, this is taken as flatband A^2/Hz)
In_total = In_shunt + In_dark + In_photo + In_feed + In_amp   % Total current spectral density, A^2/Hz
% Calculate Power Spectral Densities
In_PSD = trans * In_total;           % Current noise PSD V/root Hz
Vn_PSD = Acl * Vn_amp;                % Voltage Noise PSD V/root Hz
DC_output = i_ph * Rf;
% Integrate Power Spectral Densities to obtain RMS noise voltage
[Vn]= bode(Vn_PSD,frad);
Vn=squeeze(Vn);
rootVn=1e9*sqrt(Vn);
[In]= bode(In_PSD,frad);
In=squeeze(In);
rootIn=1e9*sqrt(In);
Vn_meansq = sqrt(trapz(f,Vn))
In_meansq = sqrt(trapz(f,In))
rms_total = sqrt(Vn_meansq + In_meansq)
SNR = 20*log(DC_output/rms_total)
% TDS4062 Specifications go here
Cin = 2e-12 ;        % Opamp input capacitance
Cf = 0.3e-12;        % Feedback capacitance
% Aol is approximated by a 1st order LPF with a break frequency of 28Hz and 20dB/decade roll off.
Aol = 15849 * tf([1] , [(1/(28274)) 1]) ;        % Open loop voltage gain LF356 (105 dB, GBW 4 Mhz)
% Calculate the shunt complex impedance at the input due to diode
% characteristics and parasitic capacitances.
Cp = Cd + Cin;       % Total parasitic capacitance
Zsh = tf( [Rd] , [(Cp*Rd) 1]);
% Calculate feedback complex impedance for the transimpedance amplifier. This
% provides the response roll off
Zf = tf( [Rf] , [(Cf*Rf) 1]);
% Here we calculate the feedback fraction, beta and the resulting CL
% voltage gain and transimpedance
beta = 1 / (1 + (Zf / Zsh));                 % Feedback Fraction, Beta
```

```
Acl = Aol / (1 + (beta * Aol));                % Closed Loop Gain
trans = (Aol * Zf ) / (1 + Aol + (Zf / Zsh));   % Transimpedance
% Define white noise sources
Vn_amp2 = (14.5e-9) ^ 2        % LF 356 amplifier voltage noise (white), V^2/Hz
In_shunt2 = (4*kB*T/Rd)    % Johnson current noise from shunt resistance, A^2/Hz
In_feed2 = (4*kB*T/Rf)    % Johnson current noise from feedback resistance, A^2/Hz
In_photo2 = 2 * elec * i_ph  % Shot noise associated with photo-current, A^2/Hz
In_dark2 = 2 * elec * (Vbias/Rd)  % Shot noise associated with dark current, A^2/Hz
In_amp2 = (1.6e-12) ^2            % Amplifer current noise, this is taken as flatband A^2/Hz)
In_total2 = In_shunt2 + In_dark2 + In_photo2 + In_feed2 + In_amp2   % Total current power spectral density, A^2/Hz
% Calculate Power Spectral Densities
In_PSD2 = trans * In_total2;             % Current noise PSD V^2/Hz
Vn_PSD2 = Acl * Vn_amp2;                 % Voltage Noise PSD V^2/Hz
DC_output = i_ph * Rf;
% Integrate Power Spectral Densities to obtain RMS noise voltage
[Vn2]= bode(Vn_PSD2,frad);
Vn2=squeeze(Vn2);
rootVn2=1e9*sqrt(Vn2);
[In2]= bode(In_PSD2,frad);
In2=squeeze(In2);
rootIn2=1e9*sqrt(In2);
Vn_meansq2 = sqrt(trapz(f,Vn2))
In_meansq2 = sqrt(trapz(f,In2))
% Calculate summed RMS noise at output
rms_total2 = sqrt(Vn_meansq2 + In_meansq2)
SNR2 = 20*log(DC_output/rms_total2)
% Graphical Routines go here
figure(1)
bode(trans1,'b',trans,'r',{2*pi*1e4,2*pi*1e7});
title('Transimpedance')
legend('LF356','THS4062');
grid on;
figure(2)
subplot(2,1,1)
semilogx(f,rootIn,'b',f,rootIn2,'r')
title('Current Noise Spectral Density')
ylabel('V/sqrt(Hz)')
xlabel('Frequency (Hz)')
grid on;
axis tight;
legend('LF356','THS4062');
subplot(2,1,2)
semilogx(f,rootVn,'b',f,rootVn2,'r')
title('Voltage Noise Spectral Density')
axis tight;
legend('LF356','THS4062');
ylabel('V/sqrt(Hz)')
xlabel('Frequency (Hz)')
grid on;
```

D.5 Matlab Script for Disturbance Rejection Analysis Rapid Phase Shifting Method

```
% Matlab Script for Control loop analysis of the Rapid Phase Shifting Method
% Haydn Martin 6/5/09
clear all;
% PI Parallel Controller Definition
Kp = [0.001 0.01 0.1 0.3 0.5]          % Prop Gain Matrix
Ki = [10e-6 20e-6 27e-6 100e-6 200e-6]  % Integrator Gain Matrix
                                % Integrator Gain
Ts = 27e-6                      % Sampling Interval
% Setup up SISO transfer function matrix with varying Kp and Ki values
for n=1:5,
   for j=1:5,
      Gc(1,1,j,n) = Kp(j) * (1 + tf([Ts 0],[Ki(n) -Ki(n)],Ts));    % Integrator Transfer Function
   end
end
%%%%%%%%%%%%%%%%%%%%%%%%%%%%%%%%%%%%%%%%%%%%%%%%%%%%%%%%%%%%%%%%%%%%%%%%%%%%%%%%%%
%
Gd = tf([1],[1 0],Ts);
Gs = Gc * Gd;
%%%%%%%%%%%%%%%%%%%%%%%%%%%%%%%%%%%%%%%%%%%%%%%%%%%%%%%%%%%%%%%%%%%%%%%%%%%%%%%%%%
%
CLTF = feedback(Gs,1);      % Calculate closed loop transfer function
sens = Gd/(1+ (Gc*Gd*Gd));  % Disturbance sensitivity function
% STUDY OF INTEGRATION GAIN VARIATION
% Tests for stability are CL Step Response, Open Loop Bode and Open Loop Nichols
Psel = 4;        % Select Kp array number for graphing
figure(1)
step(CLTF(:,:,Psel,1),'b',CLTF(:,:,Psel,2),'k',CLTF(:,:,Psel,3),'r',CLTF(:,:,Psel,4),'m',CLTF(:,:,Psel,5),'g')
grid on;
legend('Ki=10 us','Ki=20 us','Ki=27 us','Ki=100 us','Ki=200 us');
title('Kp=0.3')
axis([0 3e-3 0 1.2])
figure(2)
bode(Gs(:,:,Psel,1),'b',Gs(:,:,Psel,2),'k',Gs(:,:,Psel,3),'r',Gs(:,:,Psel,4),'m',Gs(:,:,Psel,5),'g',{1,10e5})
grid on
legend('Ki=1 kHz','Ki=2 kHz','Ki=3 kHz','Ki=4 kHz','Ki=5.75 kHz');
title('Kp=0.1')
axis auto
figure(3)
nichols(Gs(:,:,Psel,1),'b',Gs(:,:,Psel,2),'k',Gs(:,:,Psel,3),'r',Gs(:,:,Psel,4),'m',Gs(:,:,Psel,5),'g',{1,10e5})
axis tight;
legend('Ki=1 kHz','Ki=2 kHz','Ki=3 kHz','Ki=4 kHz','Ki=5.75 kHz');
title('Kp=0.1')
axis auto
% Peformance Study is Sensitivity Bode
figure(4)
bode(sens(:,:,Psel,1),'b',sens(:,:,Psel,2),'k',sens(:,:,Psel,3),'r',sens(:,:,Psel,4),'m',sens(:,:,Psel,5),'g',{1,10e5})
grid on
legend('Ki=10 us','Ki=20 us','Ki=27 us','Ki=100 us','Ki=200 us');
title('Kp=0.3')
axis auto
% STUDY OF PROPORTIONAL GAIN VARIATION
Isel = 3;        % Select Ki array number for graphing
figure(5)
step(CLTF(:,:,1,Isel),'b',CLTF(:,:,2,Isel),'k',CLTF(:,:,3,Isel),'r',CLTF(:,:,4,Isel),'m',CLTF(:,:,5,Isel),'g');
axis tight;
grid on
legend('Kp=0','Kp=0.001','Kp=0.01','Kp=0.1','Kp=1');
title('Kp=3 kHz')
axis auto
figure(6)
bode(Gs(:,:,1,Isel),'b',Gs(:,:,2,Isel),'k',Gs(:,:,3,Isel),'r',Gs(:,:,4,Isel),'m',Gs(:,:,5,Isel),'g',{1,10e5});
axis tight;
grid on
title('Kp=3 kHz')
legend('Kp=0','Kp=0.001','Kp=0.01','Kp=0.1','Kp=1');
axis auto
figure(7)
```

```
nichols(Gs(:,:,1,Isel),'b',Gs(:,:,2,Isel),'k',Gs(:,:,3,Isel),'r',Gs(:,:,4,Isel),'m',Gs(:,:,5,Isel),'g',{1,10e5});
title('Kp=3 kHz')
legend('Kp=0','Kp=0.001','Kp=0.01','Kp=0.1','Kp=1');
axis auto
figure(7)
nichols(sens(:,:,1,Isel),'b',sens(:,:,2,Isel),'k',sens(:,:,3,Isel),'r',sens(:,:,4,Isel),'m',sens(:,:,5,Isel),'g',{1,10e5});
title('Kp=3 kHz')
legend('Kp=0','Kp=0.001','Kp=0.01','Kp=0.1','Kp=1');
axis auto
% Peformance Study is Sensitivity Bode
figure(8)
bode(sens(:,:,1,Isel),'b',sens(:,:,2,Isel),'k',sens(:,:,3,Isel),'r',sens(:,:,4,Isel),'m',sens(:,:,5,Isel),'g',{1,10e5});
grid on
title('Kp=3 kHz')
legend('Kp=0','Kp=0.001','Kp=0.01','Kp=0.1','Kp=1');
axis auto
```

E TMS320F2812 DSP C Code

E.1 Introduction

This code listing gives all the generated code for the V2 MFI as described in chapter 7. Any functions or header files not listed are part of the supplied libraries from Texas Instruments. This includes specifically the *IQmathLib.h* header file which contain the function declarations for the IQmath floating point emulator used. Also some of the supplied initialisation routines for the DSP and its peripherals are used for the initial setup, with further parameter selection being done in this code listing.

- Overall the code listing is structured thus:
- Constant definitions
- Function declarations
- Variable initialisation
- DSP/peripheral initialisation
- Main loop
- Interrupt service routines (ISRs)
- General functions
- Peripheral setup functions

E.2 Code Description

The code is fully commented throughout but it is of benefit to discuss some of the user changeable functionality. Any parameter changes are accessed through the constant definitions so a brief description is given here.

SCHWIDER

If this constant is defined the Schwider algorithm is used to calculate the feedback phase. If commented out the Carré algorithm will be used instead.

INVERT

Inverts the output voltage signal to the DAC if defined. Useful only for some debugging purposes.

Fs

Defines the sample rate for the control loop. Note that this is the sample rate for the calculated phase feedback, not the individual phase shifts. It is used for calculating control loop parameters.

KC

Proportional gain term used in the control algorithm.

Ti

Integration time constant (reciprocal of integration gain) used in the control algorithm.

Defines the conversion gain for calculating the 16 bit value required to provide a 2π phase shift by the EOPM.

ULIM and LIM

DAC upper and lower limits, the control algorithm resets automatically if either of these limits is exceeded. Set for a 16 bit DAC.

DELAY

Sets the delay time for recording calculated phase data to the buffer. The value sets the number of times the phase is calculated before a value is committed to the buffer. Essentially the calculated phase is decimated before storage; a value of 40 provides an approximate phase buffer length of around 1sec (40 X 1000 values at 27 μs period).

WAIT

The intensity oscillation experienced using when the HP8168F tuneable laser is wavelength shifted means that an appropriate settling time needs to be allowed for before beginning intensity recording. This value controls a simple delay loop; a value of 1×10^7 provides approximately 1 second of delay.

SETTLE

This defines the delay from the initial beginning of the measurement cycle to the recording of intensity data. At the start up of the measurement cycle the action of the control loop causes a transient as it pulls the interferometer from its free running phase and into quadrature. The delay is necessary to ensure the intensity data is not recorded until the transient settles. It only effects the first measurement point taken.

POINTMAX

Defines the number of points to be taken during the measurement cycle.

AVERAGEMAX

Defines the number of intensity measurement sets to be taken on a single point. This is a noise reduction feature.

PBUFZ

Sets the buffer size for the calculated phase storage. Ultimately restricted by the DSP on board memory.

IBUFZ

Sets the buffer size for the measured intensity value storage. This should be 5 times the size of *PBUFZ* for Schwider algorithm use and 4 times for Carré type shifting.

CONTROL

If defined this enables the control loop. The control loop may be disabled by commenting out the definition.

E.3 D3 DSP Code Listing for Rapid Phase Shifting MFI

```
//###########################################################################
//
// FILE: fastPI.c V4.7
//
// Haydn Martin 07/4/2009
//
//
// CHANGES:
//
// Added dual step array for using both EOPM scales
//
//
// ASSUMPTIONS:
//
// This program requires the DSP281x V1.00 header files.
// As supplied, this project is configured for "boot to H0" operation.
//
// Make sure the CPU clock speed is properly defined in
// DSP281x_Examples.h before compiling this example.
//
// Connect signals to be converted to:
//
// REF = AD0
// MEAS= BD0
//
// DESCRIPTION:
//
// This example sets up the PLL in x10/2 mode, divides SYSCLKOUT
// by six to reach a 25Mhz HSPCLK (assuming a 30Mhz XCLKIN). The
// clock divider in the ADC is not used so that the ADC will see
// the 25Mhz on the HSPCLK. The EVA timer 1 clock period is set
// to yield a 284 kHz sample rate. Overflow interrupt is enabled
// and the EVA is setup to provide ADC SOC signal upon interrupt.
//
// A series format PI controller is implemented with IQmath and is
// executed during the ADC_ISR after sample conversion takes place.
// Parameters may be changed using the #defines.
//
// Phase stepping is performed, with the phase shift values being
// defined in the p_val array. The control loop operates throughout.
//
// SPI interface is implemented with 10 MHz bitrate, providing 16 bit
// update in 2us. Total time required for DAC update + settling is 3.5 us.
//
// Talkthru option is available to pass sampled inpt directly to the ADC
// (scaled) for debugging purposes.
//
//
//
//
#include "DSP281x_Device.h"  // DSP281x Headerfile Include File
#include "DSP281x_Examples.h"  // DSP281x Examples Include File
#include "float.h"

#define GLOBAL_Q 16  // Defines global Q-format for IQmath functions
#include "IQmathLib.h"  // For IQmath functions
#define PI 3.141592654

// ***************************************************************************
// User definable values
#define SCHWIDER  // Use SCHWIDER 5 step algorithm. Comment out to use Carré

#define INVERT  // Invert output to DAC
#define Fs 37.037e3  // Setup samplerate here
#define KC 0.3 // Gain//0.1
#define Ti 1/Fs // Integration time constant
//#define Ti 1e-5 // Integration time constant
#define PROP 2206.593  // EOPM -BLUE X3 Radian to radian scale factor
//#define PROP 3502.73 // EOPM -ORANGE X1 Radian to radian scale factor (reduced range)
```

```
//#define PROP 6600.73 // EOPM -ORANGE X1 Radian to radian scale factor (reduced range)
#define ULIM 32767 // DAC upper write limit
80 #define LLIM -32767 // DAC lower write limit
#define DELAY 40 // Delay value for phase buffer. 1 sec = 40
//#define WAIT 15000000 // Wait for TLS intensity to settle after move 1 sec = 1e7
85 //#define WAIT 10000000 // Wait for TLS intensity to settle after move
#define WAIT 100000 // Wait for TLS intensity to settle after move
#define SETTLE 300000 // Number of phase shift cycles to wait before recording intensity
#define POINTMAX 100 // Number of profile points taken
90
#define AVERAGEMAX 8 // Number of measurements taken for each point for averaging
#define PBUFSZ 1000 // Calculated phase buffer size
#define IBUFSZ 5000 // Calculated intensity buffer size
95
#define CONTROL // Enable Control loop
//*****************************************************************************
100 // Calculate the weighting coefficients for PI control
#define K0 KC * (1 + (1/(Fs * Ti))) // K0 applied to current error, e0
#define K1 -1 * KC // K1 applied to previous error, e1
105 #define RSHIFT SHIFT * (PI / 180) // Convert phase shift to rad
long GlobalQ = GLOBAL_Q; // Needed for IQmath gel based debugging
// Prototype statements for functions found within this file.
110
interrupt void adc_isr(void); // ADC conversion finished ISR
interrupt void cpu_timer0_isr(void); // CPU Timer0 ISR
interrupt void eva_t1_isr(void); // EVA timer1 overflow ISR
115 // Peripheral setup routines
void spi_fifo_init(void);
void adc_init(void);
void eva_t1_init(void);
120
// Other routines
_iq do_carre(_iq []);
_iq do_schwider(_iq []);
125 _iq do_cntrl (_iq);
void buffer_phase(_iq , Uint16);
void buffer_intensity(int16 []);
_iq get_intensityA(void);
int16 get_intensityB(void);
130 _iq chk_wrap(_iq);
_iq add_pshift(_iq);
_iq get_pshift(void);
void write_dac(_iq);
void move_laser(void);
135
_iq e0=0, e1=0, c_val=0; // PI control variables
// Define constants for arctan unwrapping in IQ format
// Ensure the IQ format is the same as used in the unwrap algorithm
140
_iq pi = _IQ(PI) , twopi = _IQ(2 * PI);
_iq halfpi = _IQ(PI/2), twothirdpi = _IQ(3 * PI/2);
// Phase shift values in rad and stored in global q.
145
#ifndef SCHWIDER // This sets up buffer for Carré algorithm shifting
#define SHIFT 55 // Set 55 deg phase shift for Carré
150 #define STEPS 4 // Set number of phase steps
_iq p_val[STEPS] = {_IQ(-3 * RSHIFT), _IQ(-1 * RSHIFT),_IQ(RSHIFT),_IQ(3 * RSHIFT)};
#endif //SCHWIDER
155
#ifdef SCHWIDER // This sets up for Schwider - Hariharan algorithm shifting
#define SHIFT 90 // Set 90 deg phase shift for Schwider 5 Step
160 #define STEPS 5 // Set number of phase steps
_iq p_val[STEPS] = {_IQ(-2 * RSHIFT), _IQ(-1 * RSHIFT),_IQ(0),_IQ(1 * RSHIFT),_IQ(2 * RSHIFT)};
#endif //SCHWIDER
165
_iq phase_step = 0; // Stores prefetched phase step values
_iq i_val_buf[STEPS] = {0}; // Buffer to store current ref intensity values
int16 m_val_buf[STEPS] = {0}; // Buffer to store current meas intensity values
170
float phase_buf[PBUFSZ]={0}; // Circular buffer to store calculated phase values
int16 intensity_buf[IBUFSZ]={0}; // Circular buffer to store intensity vales
175
Uint16 average = 0, points = 0; // Counter for averaging and points values
```

```
// Miscellaneous Vars
180 //_iq temp; // For general debug
Uint32 h=0; // Loop variable for zeroing buffers
main() {
185 Uint16 LoopCount=0; // Loop variable for main do nothing loop
InitSysCtrl();
EALLOW;  // Enable write to protected registers
190
// Set HSPCLK to SYSCLKOUT / 6 (25Mhz assuming 150Mhz SYSCLKOUT)
SysCtrlRegs.HISPCP.all = 0x3; // HSPCLK = SYSCLKOUT/6
195  // LOSPCP prescale register settings, set to give 150 Mhz (150/1)
SysCtrlRegs.LOSPCP.all = 0x0000; //LSPCLK = SYSCLKOUT/1
EDIS;  // Disable write to protected registers
200
// Step 2. Initialize GPIO:
// This example function is found in the DSP281x_Gpio.c file and
// illustrates how to set the GPIO to it's default state.
205  // InitGpio(); // Skipped for this example
GpioDataRegs.GPBCLEAR.all = 0x101E; // Clear all GPIOB outputs to initialise
EALLOW;  // Enable write to protected registers.
210
GpioMuxRegs.GPFMUX.all=0x000F; // Select GPIOs to be SPI pins
// Port F MUX - x000 0000 0000 1111
215  // Note here that masks are used so as only to write the bits we require
GpioMuxRegs.GPFMUX.all&=0xBFFF; // Selects T1PWM and T2PWM as I/O pins
// Port F MUX - x0xx xxxx xxxx xxxx
220 GpioMuxRegs.GPFDIR.all|=0x4000; // And set them all to outputs
// Port F DIR - x1xx xxxx 11xx xxxx
// The following sets PWM8:11 pins as output, for debugging purposes
225 GpioMuxRegs.GPBMUX.all&=0xEFE1; // Selects PWM8:11 and TCLKINB as I/O pins
// Port B MUX - xxx0 xxxx xxx0 000x
GpioMuxRegs.GPBDIR.all|=0x101E; // And set them all to outputs
// Port B DIR - xxx1 xxxx xxx1 111x
230
GpioMuxRegs.GPBDIR.bit.GPIOB4 = 0; // Set GPIOB/PWM11 to INPUT
GpioMuxRegs.GPBQUAL.bit.QUALPRD = 0x0F; // Set 32 x SYSCLKOUT debounce period on inputs
235 EDIS;
GpioDataRegs.GPBCLEAR.bit.GPIOB3 = 1; // Reset PWM10 to initialise
// Step 3. Clear all interrupts and initialize PIE vector table:
240  // Disable CPU interrupts. This ensures no false jumps when interrupt flags are SET
DINT;
// Initialize the PIE control registers to their default state.
245  // The default state is all PIE interrupts disabled and flags
// are cleared.
// This function is found in the DSP281x_PieCtrl.c file.
InitPieCtrl();
250
// Disable CPU interrupts and clear all CPU interrupt flags:
IER = 0x0000;
IFR = 0x0000;
255
// Initialize the PIE vector table with pointers to the shell Interrupt
// Service Routines (ISR).
// This will populate the entire table, even if the interrupt
// is not used in this example. This is useful for debug purposes.
260  // The shell ISR routines are found in DSP281x_DefaultIsr.c.
// This function is found in DSP281x_PieVect.c.
InitPieVectTable();
265  // Interrupts that are used in this example are re-mapped to
// ISR functions found within this file. Address for eaxh interrupt routine is loaded into the
// PIE vector table. The routine branches here when the interrupt origin has been determined.
EALLOW;  // This is needed to write to EALLOW protected register
270 PieVectTable.ADCINT = &adc_isr; // Enable PIE ADC complete interrupt
PieVectTable.TINT0 = &cpu_timer0_isr;// Enable PIE cpu timer0 interrupt.
PieVectTable.T1PINT = &eva_t1_isr; // Enable PIE eva timer 1 PERIOD interrupt.
EDIS;  // This is needed to disable write to EALLOW protected registe
275
// Step 4. Initialize all the Device Peripherals:
// This function is found in DSP281x_InitPeripherals.c
// InitPeripherals(); // Not required for this example
280  spi_fifo_init();  // Initialize the SPI only
InitAdc();  // Init the ADC to a known state. Always run this first
adc_init();  // Call our specific ADC setup routine
```

```
285  eva_t1_init();  // EVA setup routine to provide SOC for the ADC.
InitCpuTimers();  // Initialize the Cpu Timers
// Configure CPU-Timer 0 to interrupt every second:
290  // 150MHz CPU Freq, 1 second Period (in uSeconds)
// This is used to flash the led on the EzDSP board to show
// that the code is running and gives the main loop something to do.
ConfigCpuTimer(&CpuTimer0, 150, 1000000);
295
//while(!GpioDataRegs.GPBDAT.bit.GPIOB4) {} // Wait for laser ready i.e. PWM11 is high
// Step 6. Initialise intensity buffer to zero
300
while(h<lBUFSZ)
{
intensity_buf[h]=0;
305 h++;
}
310  // Step 7. User specific code, enable interrupts:
// Enable ADCINT in PIE
315 PieCtrlRegs.PIECRTL.bit.ENPIE = 1; // Enable the PIE block
PieCtrlRegs.PIEIER1.bit.INTx6 = 1; // Enable PIE Group 1, INT 6, for ADC complete int
PieCtrlRegs.PIEIER1.bit.INTx7 = 1; // Enable TINT0 in the PIE: Group 1 interrupt 7
320
PieCtrlRegs.PIEIER2.bit.INTx4 = 1; // Enable T1PINT EVA Timer1 Period Interrupt
IER |= M_INT1; // Enable CPU INT1 which is connected to TIMER0 and AtoD
IER |= M_INT2; // Enable CPU INT2 which is connected to T1PINT
325
EINT;  // Enable Global interrupt INTM
ERTM;  // Enable Global realtime interrupt DBGM
330
SpiaRegs.SPITXBUF = 0; // Write 0 to DAC
StartCpuTimer0();  // Start CPU timer to provde LED flash interrupts
335  // Wait forever for interrupt
for(;;)
{
LoopCount++;
340
if (average == AVERAGEMAX) // Test for complete averaging points taken
{
points++;
average = 0; // Reset counter and shift laser to the next p
345  move_laser();
}
350
if (points == (POINTMAX-1))
points = 1;
355 }
}
/*****************************************************************************/
360
// Interrupt Service Routines are contained within this section.
/* This ISR executes when an ADC conversion is complete. PI controller
365  calculates the next required value to send to the DAC
*/
interrupt  void adc_isr(void)
370 {
static Uint16 i=0;
static _iq calc_phase , dc_phase;
375 GpioDataRegs.GPBSET.all = 0x0002; // SET PWM8 pin (Connect to scope)
AdcRegs.ADCTRL2.bit.RST_SEQ1 = 1; // Reset Sequencer back to start (debug fix)
switch (i- (STEPS - 1)) {
380
case 0: // Final phase shift of sequence
i_val_buf[i] = get_intensityA(); // Get averaged intensity value
m_val_buf[i] = get_intensityB();
385 i = 0; // Reset shift counter
#ifndef SCHWIDER
calc_phase = do_carre(i_val_buf); // Perform Carre Algorithm
#endif
390
#ifdef SCHWIDER
calc_phase = do_schwider(i_val_buf);// Perform Schwider-Hariharan Algorithm
#endif
395
```

```
#ifdef CONTROL
dc_phase = do_cntrl(calc_phase); // Apply PI control
400
#endif  //CONTROL
//phasestep = add_pshift(dc_phase); // Add next phase step
405
write_dac(dc_phase + phase_step); // Write to DAC
410 buffer_phase(calc_phase , DELAY); // Write current phase to buffer
if (!GpioDataRegs.GPBDAT.bit.GPIOB3 && !GpioDataRegs.GPBDAT.bit.GPIOB4)
{
415 buffer_intensity(m_val_buf);
}
break;
default: // All other phase shifts
420
//phasestep = add_pshift(dc_phase); // Add next phase step
write_dac(dc_phase + phase_step); // Write to DAC
425 i_val_buf[i] = get_intensityA(); // Get averaged intensity value
m_val_buf[i] = get_intensityB(); // Get averaged intensity value
i++; // Increment shift counter
break;
430
}
// Here we provide for asymmetric timing of phase steps
// Step 4 is timed for longer to allow the do_carre() and
435  // do_cntrl() to execute.
// Extended period for Schwider is slightly shorter due to faster algorithm
#ifndef SCHWIDER
if (i == (STEPS -1)) EvaRegs.T1PR = 187; //Period = 7.5 us
440 else EvaRegs.T1PR = 125; // Period = 5us
#endif  //SCHWIDER
#ifdef SCHWIDER
if (i == (STEPS -1)) EvaRegs.T1PR = 170; // Period = 6.8 us
445 else EvaRegs.T1PR = 125; // Period = 5us
#endif  //SCHWIDER
// if (!GpioDataRegs.GPBDAT.bit.GPIOB3) // If Laser is ready i.e. PWM10 is low
450
// Reinitialize for next ADC sequence
AdcRegs.ADCST.bit.INT_SEQ1_CLR = 1; // Clear INT SEQ1 bit
PieCtrlRegs.PIEACK.all |= PIEACK_GROUP1; // Acknowledge interrupt to PIE
455
GpioDataRegs.GPBCLEAR.all = 0x0002; // Clear PWM8 pin (Connect to scope)
}
460  // This ISR simply flashes the LED on the EZDsp once per second
// Break points placed in this function allow the user to pull data
// from the DSP at 1Hz intervals
interrupt  void cpu_timer0_isr(void)
465 {
static Uint16 ledtoggle=0;
CpuTimer0.InterruptCount++;
470 ledtoggle ^= 1;
GpioDataRegs.GPFTOGGLE.all = 0x4000; //Toggle ? pin (Connected to LED on EzDsp)
// Acknowledge this interrupt to receive more interrupts from group 1
475 PieCtrlRegs.PIEACK.all = PIEACK_GROUP1; // Acknowledge Group 1 interrupts
}
/* EVA timer 1 ISR provides the SOC signal for the ADC. Various counter values
480  can be set to provide different sampling rates. PWM10 (P8-33 ezdsp) is
toggled at the start of the routine for debugging.
This ISR does nothing useful. So may be disabled for more efficient running.
485  NB: The EVA timer1 period interrupt does NOT need to be enabled to provide
the ADC SOC signal.
*/
490 interrupt  void eva_t1_isr(void)
{
GpioDataRegs.GPBSET.all = 0x0002; //SET PWM8 pin (Connect to scope)
495
// Note: To be safe, use a mask value to write to the entire
// EVAIFRA register. Writing to one bit will cause a read-modify-write
// operation that may have the result of writing 1's to clear
// bits other then those intended.
500
EvaRegs.EVAIFRA.all = 0x7FFF; // Clear T1PINT by writing here
phase_step = get_pshift(); // Prefetch next phase shift value to save time.
```

```
505
EvaRegs.EVAIMRA.bit.T1PINT = 1; // Enable more interrupts from this timer
// Acknowledge interrupt to receive more interrupts from PIE group 2
510
PieCtrlRegs.PIEACK.all = PIEACK_GROUP2;
GpioDataRegs.GPBCLEAR.all = 0x0002; //RESET PWM8 pin (Connect to scope)
}
515 /**********************************************************************************/
// General functions are contained within this section.
// PI control is carried out by this function
520
_iq do_cntrl(_iq phase)
{
static _iq k0 = _IQ(K0); // K0= KC * (1 + (Ts / Ti))
525 static _iq k1 = _IQ(K1); // K1 = -KC
e0 = phase ^ 0xFFFFFFFF; // Calculate error value and shift to
// the global Q-format.
c_val +=_IQmpy(k0,e0); // Previous output add weighted e0 value
530 c_val +=_IQmpy(k1,e1); // Previous output add weighted e1 value
e1 = e0; // Update error values
return(c_val);
535 }
// This function performs an IQMath based implementation of the Carre Algorithm
540 _iq do_carre(_iq i_val[])
{
static _iq9 num0,num1,num2,num3,num4; // Variables for 1st part of Carre
static _iq9 den, tmp, anum4, aden; // Variables for 2nd part of Carre
545
static _iq inter_phase; // Variables for 3rd part
static Uint32 den_sign;
550 // GpioDataRegs.GPBSET.all = 0x0002; //SET PWM8 pin (Connect to scope)
// Calculate Carre numerator
num0 = i_val[1] - i_val[2]; // This is used later for arctan unwrap
555
num1 = _IQ9mpyI32(num0,3);
num1 = num1 - i_val[0] - i_val[3];
560 num2 = i_val[0] + i_val[1] - i_val[2] - i_val[3];
num3 = _IQ9mpy(num1,num2);
anum4 = _IQ9abs(num3);
565
num4 = _IQ9sqrt(anum4);
// Calculate Carre denominator
570
den = i_val[1]+i_val[2]-i_val[0]-i_val[3];
aden = _IQ9abs(den);
575
// Do Arctangent function
tmp = _IQ9atan2(num4,aden);
580 inter_phase = tmp << (GLOBAL_Q-9); // Convert to GLOBALQ format
// This section carries out sign tests on numerator and denominator and unwraps
// the arctangent result correctly
585 if (num0==0) inter_phase = pi; // If numerator equal zero
else
{
den_sign = den & 0x80000000; // Get denominator sign
590
switch (num0 & 0x80000000){ // Test numerator sign bit
case (0): // numerator is +ve
if (den_sign) inter_phase = pi - inter_phase; // denominator is -ve?
else if (den == 0) inter_phase = halfpi; // denominator equals zero?
595 break; // Otherwise denominator is +ve, no action
default : // Numerator is -ve
if (den_sign) inter_phase += pi; // Denominator is -ve?
else if (den == 0) inter_phase = twothirdpi; // Denominator equal zero?
600 else inter_phase = twopi - inter_phase; // Denominator must be +ve
break ;
}
}
605 // GpioDataRegs.GPBCLEAR.all = 0x0002; //Toggle PWM8 pin (Connect to scope)
return(inter_phase-pi);
}
610 _iq do_schwider(_iq i_val[])
{
```

```
static _iq num, den;
static _iq inter_phase; // Variables for 3rd part
615
// GpioDataRegs.GPBSET.all = 0x0002; //SET PWM8 pin (Connect to scope)
620  // Calculate Schwider numerator
num = i_val[1] - i_val[3]; // This is used later for arctan unwrap
625 num = _IQmpyI32(num,2);
// Calculate Schwider denominator
630 den = _IQmpyI32(i_val[2],2);
den = den - i_val[4] - i_val[0];
// Do Arctangent function
635
inter_phase = _IQatan2(num,den);
// GpioDataRegs.GPBCLEAR.all = 0x0002; //Toggle PWM8 pin (Connect to scope)
640
return(inter_phase);
}
645  // This routine updates a circular buffer with calculated phase values
// The delay value essentially decimates the incoming phase values
void buffer_phase(_iq phase, Uint16 delay)
{
650 static Uint16 i=0 , j=0;
if (j>delay) // Store value if delay values
{   // have already passed
j=0;
655 phase_buf[i] = _IQtoF(phase); // Convert IQ to float for storage
i++;
if(i==PBUFSZ)
i=0;
}
660
j++;
return ;
}
665
// This routine updates a circular buffer with sampled intensity values
// The delay value essentially decimates the incoming phase values
670  void buffer_intensity (int16 x[])
{
static Uint16 i=0, j=0;
static Uint32 settle = SETTLE;
675 if (settle)
settle--;
else
{
while(j<STEPS) // Store value if delay values
680  {   // have already passed
intensity_buf[i+j] = x[j]; // Store current intensity value in buffer
j++;
i++;
685 if(i==IBUFSZ) i=0;
}
average++; // Increment points counter
j=0;
690 }
return ;
}
695
// This function retrieves 8 intensity values and then averages the
// result to provide one value.
700  _iq  get_intensityA (void)
{
static int32 intensity;
intensity = (AdcRegs.ADCRESULT0>>4) // Get sample values from ADC pin A0
705 + (AdcRegs.ADCRESULT2>>4)
+ (AdcRegs.ADCRESULT4>>4)
+ (AdcRegs.ADCRESULT6>>4)
+ (AdcRegs.ADCRESULT8>>4)
+ (AdcRegs.ADCRESULT10>>4)
710 + (AdcRegs.ADCRESULT12>>4)
+ (AdcRegs.ADCRESULT14>>4);
intensity = intensity >> 3; // Divide by 8
intensity -= 2048; // Convert to signed 16
```

```
715 intensity = intensity << 9; // Convert to IQ9 format
return (_iq)intensity;
}
int16  get_intensityB (void)
720 {
static int32 intensity;
intensity = (AdcRegs.ADCRESULT1>>4) // Get sample values from ADC pin B0
+ (AdcRegs.ADCRESULT3>>4)
725 + (AdcRegs.ADCRESULT5>>4)
+ (AdcRegs.ADCRESULT7>>4)
+ (AdcRegs.ADCRESULT9>>4)
+ (AdcRegs.ADCRESULT11>>4)
+ (AdcRegs.ADCRESULT13>>4)
730 + (AdcRegs.ADCRESULT15>>4);
intensity = intensity >> 3; // Divide by 8
intensity -= 2048; // Convert to signed 16
//intensity = intensity << 9; // Convert to IQ9 format
735 return intensity;
}
// This function adds the next phase shift value to the input
740
_iq add_pshift(_iq phase)
{
static Uint16 i=1;
745
phase += p_val[i]; // Add next phase shift value from the
// buffer
i++; // Step along buffer
750 if (i==STEPS) i=0; // Check for end of buffer and wrap
return(phase);
}
755
_iq  get_pshift (void)
{
static Uint16 i=1;
760
static _iq phase;
phase = p_val[i]; // Add next phase shift value from the
// buffer
765 i++; // Step along buffer
if (i==STEPS) i=0; // Check for end of buffer and wrap
return(phase);
770 }
// This function scales the value radians and outputs it to the DAC
// Limit testing is also performed to ensure written values stay
775  // within the 16bit range.
void write_dac (_iq phase)
{
static int16 dac_val;
780 static _iq prop = _IQ(PROP);
phase = _IQmpy(phase,prop); // Apply radian scaling
chk_wrap(phase); // Check limits
785
dac_val = phase >> GLOBAL_Q; // Convert to 16bit signed
#ifdef  INVERT  // Invert output if enabled
790 dac_val ^= 0xFFFF; // Invert Output
#endif  //INVERT
795 SpiaRegs.SPITXBUF = dac_val; // Send controller output to DAC
return;
}
800
// This function checks limits before DAC write occurs. The PI Controller
// is reset is this occurs.
_iq chk_wrap(_iq phase)
805 {
static _iq ulim = _IQ(ULIM);
static _iq llim = _IQ(LLIM);
if ((phase > ulim)|(phase < llim))
810 {
e0=0; // Reset all PI controller values
e1=0;
c_val=0;
}
```

```
815
return(phase);
}
void move_laser (void)
820 {
static Uint32 i=0;
GpioDataRegs.GPBSET.bit.GPIOB3 = 1; // Set PWM10 to command laser move
825 while(!GpioDataRegs.GPBDAT.bit.GPIOB4); // Wait for ACK
while(i<WAIT) i++;
i=0;
830 GpioDataRegs.GPBCLEAR.bit.GPIOB3 = 1; // Reset PWM10 to ensure measurement cycle begins
return ;
}
835 /*****************************************************************************/
// Peripheral initialisation routines are contained within this section.
840 /* SPI setup routine. Setup for 10MHz bus rate, TX only, master mode etc.
Essentially provides compatiable format for DAC.
NB: The latch enable (LE) signal to the AD766JN MUST be inverted by
logic otherwise there is a one sample delay on the DAC update.
845 */
void spi_fifo_init ()
{
850 // Initialize SPI FIFO registers
SpiaRegs.SPICCR.bit.SPISWRESET=0; // Reset SPI ready for register update
SpiaRegs.SPICCR.all=0x001F; // 16-bit character, Loopback mode disabled
855 SpiaRegs.SPICTL.all=0x0016; // Interrupt Disabled, Master/Slave XMIT enabled
SpiaRegs.SPISTS.all=0x0000; // Clear any overflow flags
// Select required baud rate here
860 SpiaRegs.SPIBRR=0x000C; // Baud rate = 12.5 MHz (150/12)
// SpiaRegs.SPIBRR=0x000E; // Baud rate = 10 MHz (150/15)
// SpiaRegs.SPIBRR=0x001D; // Baud rate = 500 KHz (15/30)
// SpiaRegs.SPIBRR=0x0077; // Baud rate = 125 KHz (15/120)
865
SpiaRegs.SPIFFTX.all=0x8000; // Disable FIFO's
// Disable FIFO state interrupts
870
SpiaRegs.SPIFFCT.all=0x00; // Set one CLK cycle delay between Words
// This is to enable the LE signal to be picked up by Ad766
SpiaRegs.SPIPRI.all=0x0010; // Correct emulation settings for eZdsp board
875
//SpiaRegs.SPICCR.bit.SPILBK = 0;
//SpiaRegs.SPIFFTX.bit.TXFFIENA = 0; // Disable FIFO interrupts
880 //SpiaRegs.SPIFFTX.bit.TXFIFO=1; // Enable FIFO Tx buffer
SpiaRegs.SPICCR.bit.SPISWRESET=1; // Re-Enable SPI
SpiaRegs.SPIFFTX.bit.TXFFINTCLR=1; // Clear FIFO INT flag
885
}
/* This routine initialises the ADC. SOC is provided by the EVA timer 1 period.
890 Maximum clock rate is passed to the ADC (25 MHz) to shorten the conversion
time and thus reduce control loop deadtime. Full conversion takes approx
300 ns.
*/
895 void adc_init (void)
{
AdcRegs.ADCMAXCONV.all = 0x0007; // Setup 8 double conversions on SEQ1
AdcRegs.ADCCHSELSEQ1.bit.CONV00 = 0x00; // Setup ADCINA/B0 as 1st SEQ1 conv.
900 AdcRegs.ADCCHSELSEQ1.bit.CONV01 = 0x00; // Setup ADCINA/B0 as 2nd SEQ1 conv.
AdcRegs.ADCCHSELSEQ1.bit.CONV02 = 0x00; // Setup ADCINA/B0 as 3rd SEQ1 conv.
AdcRegs.ADCCHSELSEQ1.bit.CONV03 = 0x00; // Setup ADCINA/B0 as 4th SEQ1 conv.
AdcRegs.ADCCHSELSEQ2.bit.CONV04 = 0x00; // Setup ADCINA/B0 as 5th SEQ1 conv.
AdcRegs.ADCCHSELSEQ2.bit.CONV05 = 0x00; // Setup ADCINA/B0 as 6th SEQ1 conv.
905 AdcRegs.ADCCHSELSEQ2.bit.CONV06 = 0x00; // Setup ADCINA/B0 as 7th SEQ1 conv.
AdcRegs.ADCCHSELSEQ2.bit.CONV07 = 0x00; // Setup ADCINA/B0 as 8th SEQ1 conv.
AdcRegs.ADCTRL3.bit.ADCCLKPS = 0x00; // NO HSPCLK clock prescaling
910 AdcRegs.ADCTRL1.bit.CPS = 0; // Disable divide by two prescaler
AdcRegs.ADCTRL1.bit.ACQ_PS = 0x1; // Set acquistion window width to one sample
AdcRegs.ADCTRL1.bit.CONT_RUN = 0; // Select Start/Stop mode
915 AdcRegs.ADCTRL1.bit.SEQ_OVRD = 0; // Select wraparound sequencing
AdcRegs.ADCTRL1.bit.SEQ_CASC =1; // Select cascaded operation
AdcRegs.ADCTRL2.bit.EVA_SOC_SEQ1 = 1; // Enable EVASOC to start SEQ1
AdcRegs.ADCTRL2.bit.INT_ENA_SEQ1 = 1; // Enable SEQ1 interrupt (every EOS)
920
AdcRegs.ADCTRL3.bit.SMODE_SEL = 1; // Enable Simultaneous sampling mode
```

```
}
/* This routine sets up the EVA to provide a SOC signal and interrupt whenever
925  the EVA Timer1 period is matched. Setting the period this sets the sample
rate.
*/
void eva_t1_init (void)
930 {
// Initialize EVA Timer 1:
// Setup Timer 1 Registers (EV A)
935 EvaRegs.GPTCONA.all = 0;
// Set the Period for the GP timer 1;
// Frequency = 25 MHz / EvaRegs.T1PR
940  //EvaRegs.T1PR = 0x04E2; // Period = 50us
//EvaRegs.T1PR = 0x0271; // Period = 25us
//EvaRegs.T1PR = 0x00FA; // Period = 10us
//EvaRegs.T1PR = 0x00E1; // Period = 9us
945 EvaRegs.T1PR = 0x007D; // Period = 5us
//EvaRegs.T1PR = 0x0064; // Period = 4us
//EvaRegs.T1PR = 0x0058; // Period = 3.52us
EvaRegs.T1CMPR = 0x0000; // Compare Reg initialise. Not used.
950
EvaRegs.EVAIMRA.all = 0x0000; // Disable all EVA INTS
EvaRegs.EVAIMRB.all = 0x0000;
EvaRegs.EVAIMRC.all = 0x0000;
955
EvbRegs.EVBIMRA.all = 0x0000; // Disable all EVB INTS
EvbRegs.EVBIMRB.all = 0x0000;
EvbRegs.EVBIMRC.all = 0x0000;
960 EvaRegs.EVAIFRA.all = 0x07FF; // Clear all INT flags to stop any unwanted jump
EvaRegs.T1CNT = 0x0000; // Clear the counter for EVA timer 1
965
EvaRegs.T1CON.all = 0x1040; // General Timer Setup. Upcount Mode
// HSPCLK source, no prescaling
// and enable.
970  // Easy access bits
EvaRegs.EVAIMRA.bit.T1PINT = 1; // Enable EVA t1 period int
EvaRegs.T1CON.bit.TPS = 0x0; // Set prescaler to HSPCLK/1 = 25Mhz
975
EvaRegs.GPTCONA.bit.T1TOADC = 2; // Send ADC SOC at period interrupt flag
EvaRegs.T1CON.bit.TECMPR = 0; // Disallow compare mode
EvaRegs.GPTCONA.bit.TCMPOE = 0; // Compare output disable
980  //EvaRegs.GPTCONA.bit.T1CMPOE = 1; // Compare output state. Not used
}
// END OF CODE
```

F LabView Code Listings

F.1 Introduction

This section gives a brief description of each routine in the code and it operation. The code listings are given fully in appendixF. The descriptions are in a roughly hierarchical order with the main routine first. The graphical nature of the code listing mean that code flow is generally from left to right and the descriptions will adhere to this.

Labview routines and subroutines are known as VIs and subVIs respectively, the VI standing for virtual instrument. This terminology will be used throughout this section. In addition the graphical nature of the code means that conditional statements are not easily represented. In the code listings the contents of various boxes, apparently disconnected to the main code, show the executed code for alternative conditions.

F.2 Labview Code

MFI V1 LabView Code Description

Carre10K_CL_BIGSTEP110.vi

This is the main VI for the phase measurement routine. The VI first initialises the laser and prepares it to sweep. It then outputs a voltage waveform from the NI PCI-6221 in order to assess the interferometer visibility. This is done by recording the output of the reference interferometer whilst modulating the phase. After a user command, the measurement sequence starts. The wavelength is scanned four times and the measurement interferometer output is recorded in addition to the Ando AQ4320 laser analogue voltage out. This is then used in a cross correlation routine to align the measurement data precisely. The Carré algorithm is then used to determine the surface height profile from the measurement intensities.

laser_full_config.vi

Initialise the various parameter such as power and wavelength of the Ando AQ4320D laser.

laser_sweep_config.vi

Sets up various wavelength sweep parameters on the AQ4320 laser.

laser_nm.vi

Sets the AQ4320D laser wavelength.

laser_sweep.vi

Command AQ4320D laser to perform wavelength sweep.

laser_wait_for_sweep.vi

Waits for laser to finish current wavelength sweep.

CarrePSI.vi

This VI applies the Carré algorithm to 4 an input array containing 4 raw intensity data streams. It also determines arctangent quadrant; the various conditions tests are shown in the numerous boxes in the listing. The VI outputs both an arctangent unwrapped phase and non-unwrapped, modulo $\pi/2$ phase.

REVERSE_PID.vi

Causes the PID controller to reverse by switching in an inverter into the control loop. This is used to move to phase shifts 3 and 4.

SP_ENABLE.vi

Enables the control loop by switching in the PI controller.

waveout.vi

Applies a sine wave to the PZT with the control loop off in order to detect the fringe visibility.

getvis.vi

Records the interferometer response to the sine wave applied by *waveout.vi* and then uses peak detection and averaging to determine the fringe visibility.

ramp_voltage.vi

Changes set point voltage. Uses voltage ramping to ensure a smooth transition.

generate_alpha_110.vi

generates the phase shift voltages required after the fringe visibility has been determined by *getvis.vi.*

RESET_PID_TIMED.vi

Resets the PI controller (by discharging the integrator capacitor).

carre10K_CL_BIGSTEP110.vi
D:\Desktop\carre10K_CL_BIGSTEP110.vi
Last modified on 07/05/2007 at 09:09
Printed on 07/08/2009 at 13:51

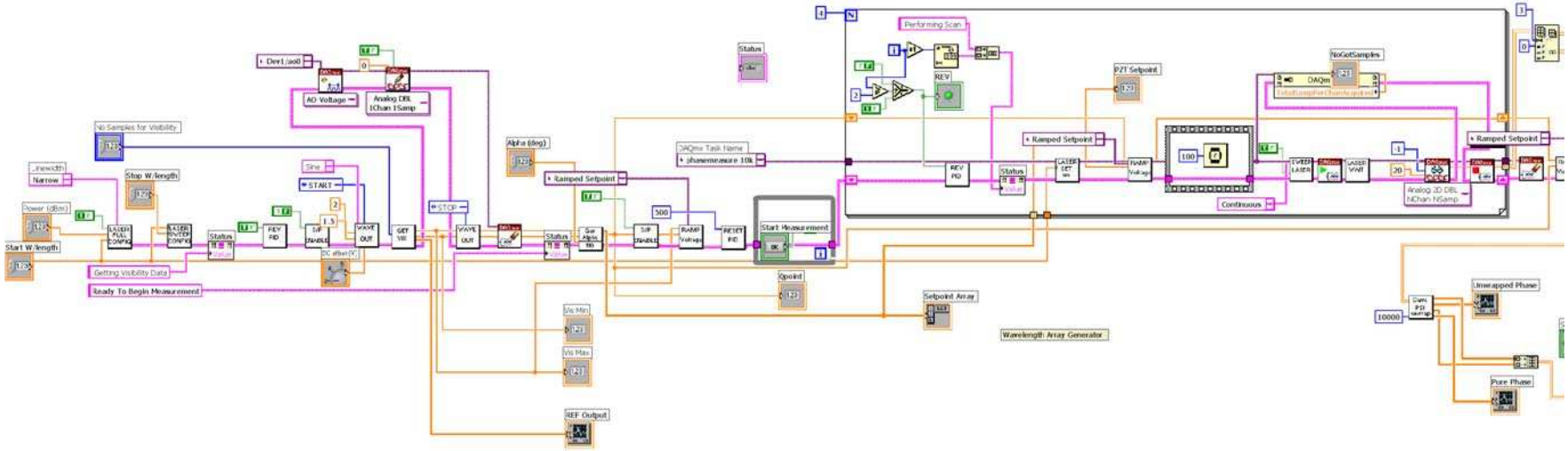

Get Phase CARRE

carre10K_CL_BIGSTEP110.vi
D:\Desktop\carre10K_CL_BIGSTEP110.vi
Last modified on 07/05/2007 at 09:09
Printed on 07/08/2009 at 13:51

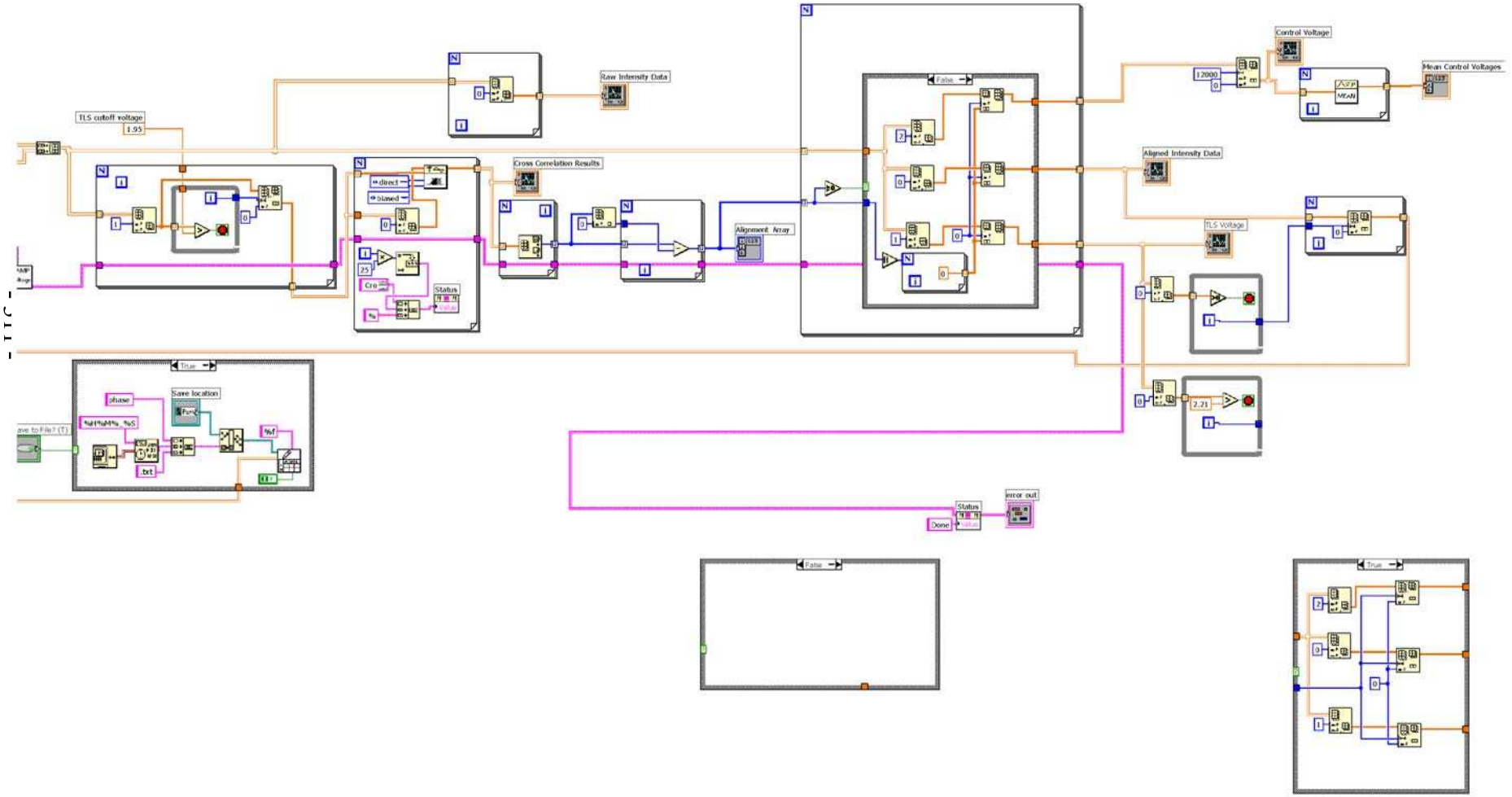

laser_full_config.vi
C:\Program Files\National Instruments\LabVIEW 8.0\user.lib\Laser\laser_full_config.vi
Last modified on 11/10/2006 at 11:36
Printed on 07/08/2009 at 13:52

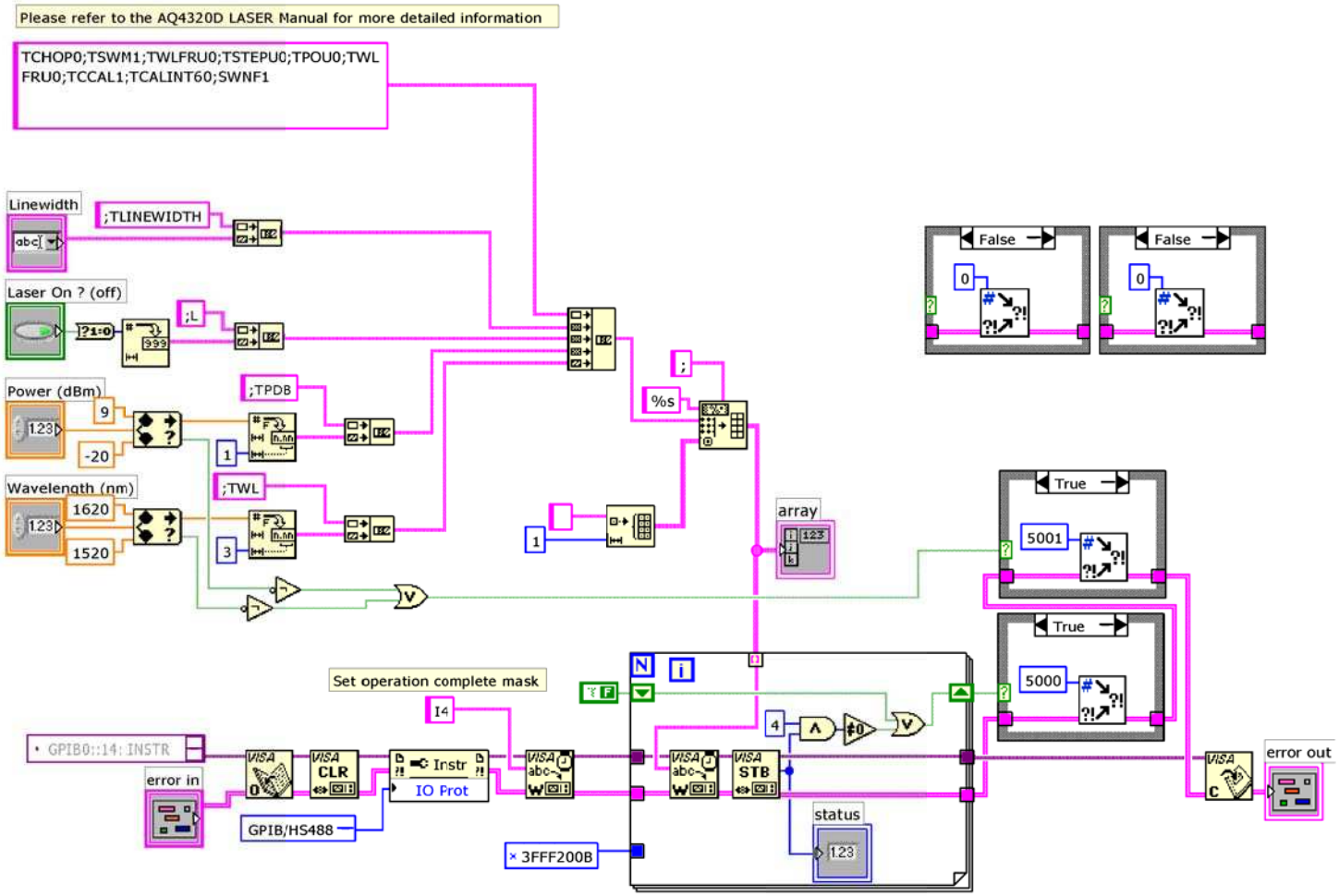

laser_nm.vi
C:\Program Files\National Instruments\LabVIEW 8.0\user.lib\Laser\laser_nm.vi
Last modified on 07/02/2006 at 10:47
Printed on 07/08/2009 at 13:52

Please refer to the AQ4320D LASER Manual for more detailed information

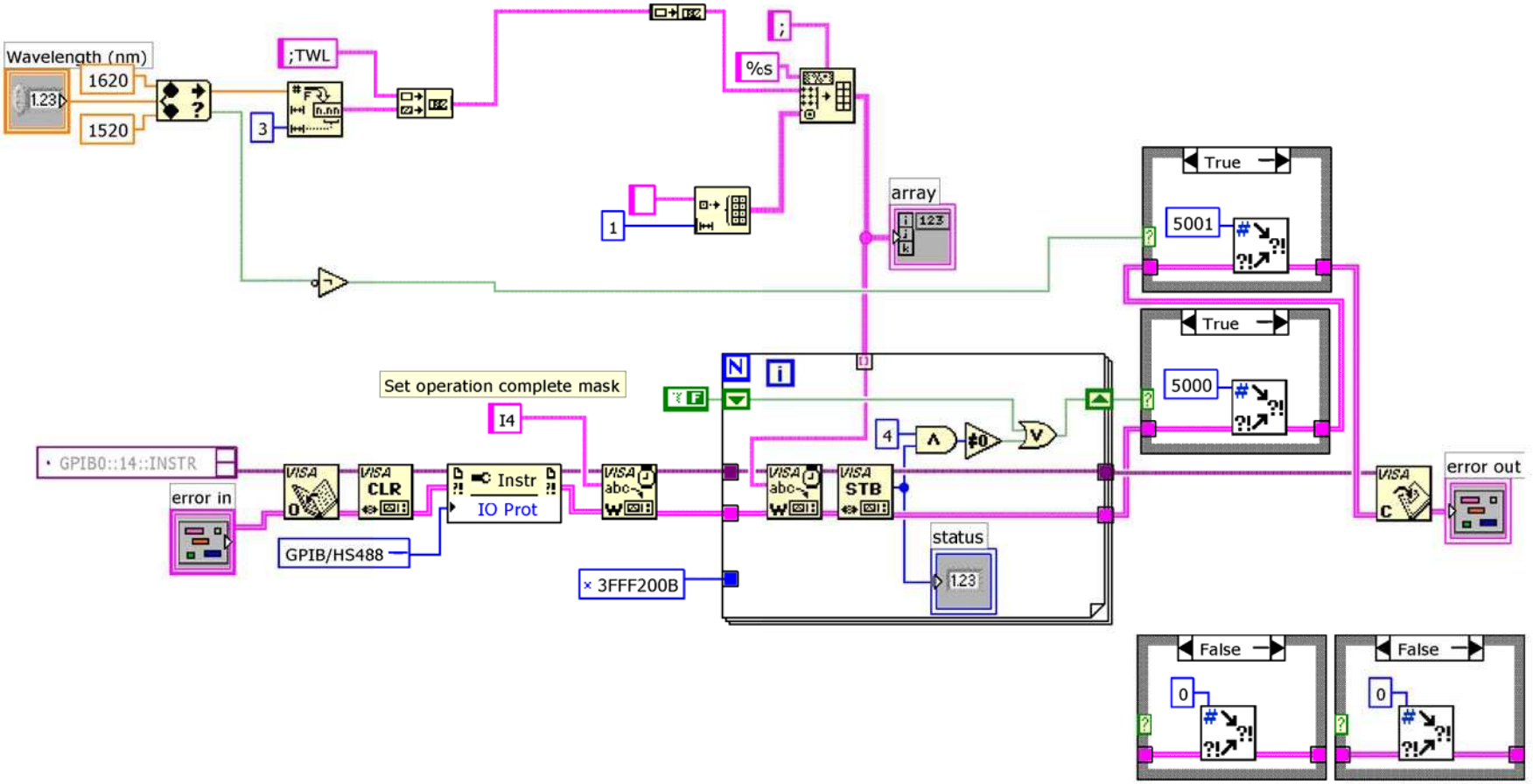

laser_sweep.vi
C:\Program Files\National Instruments\LabVIEW 8.0\user.lib\Laser\laser_sweep.vi
Last modified on 10/02/2006 at 15:40
Printed on 07/08/2009 at 13:52

laser_sweep.vi

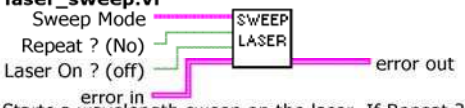

Starts a wavelength sweep on the laser. If Repeat ? value is FALSE then a single sweep is performed else a repeated sweep will be performed. Stepped or continuous wavelength sweeping is performed depending on the setting of 'Sweep Mode'.

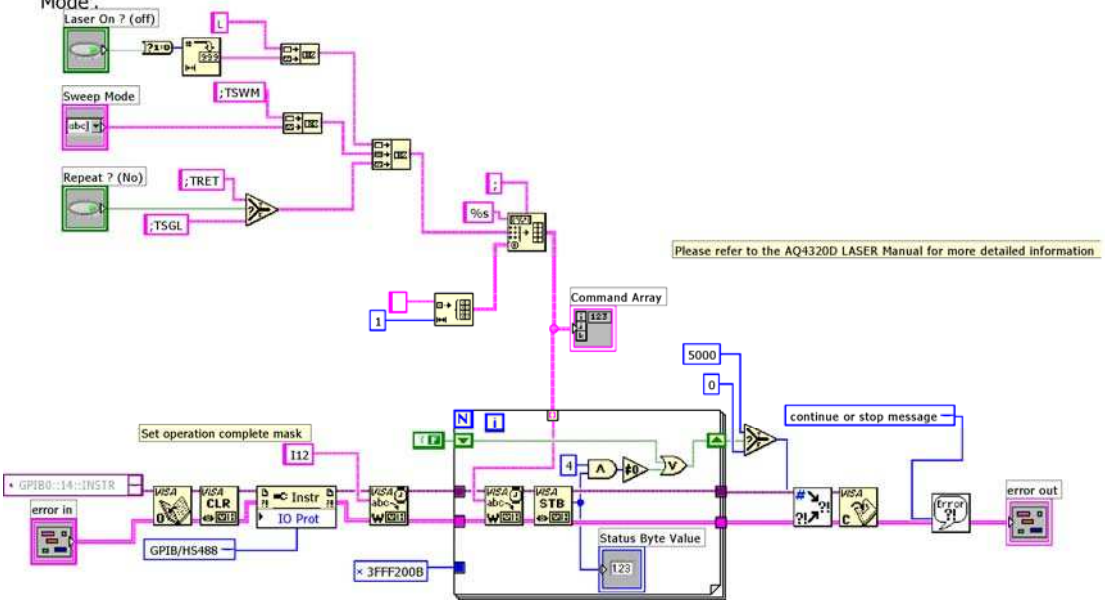

laser_wait_for_sweep.vi
C:\Program Files\National Instruments\LabVIEW 8.0\user.lib\Laser\laser_wait_for_sweep.vi
Last modified on 10/02/2006 at 14:49
Printed on 07/08/2009 at 13:52

laser_wait_for_sweep.vi

Waits for the Laser to complete the current sweep then exits. This VI will cause a pause in code while it waits for the current sweep to end.

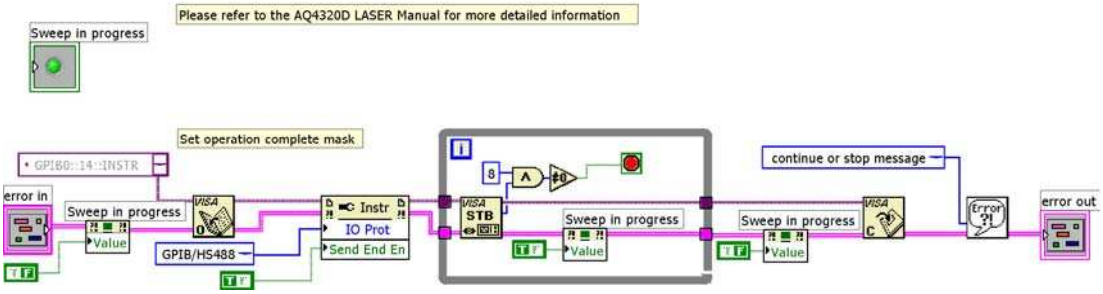

CarrePSI.vi
C:\Program Files\National Instruments\LabVIEW 8.0\user.lib\MEAS PSI\CarrePSI.vi
Last modified on 13/11/2006 at 14:51
Printed on 07/08/2009 at 13:52

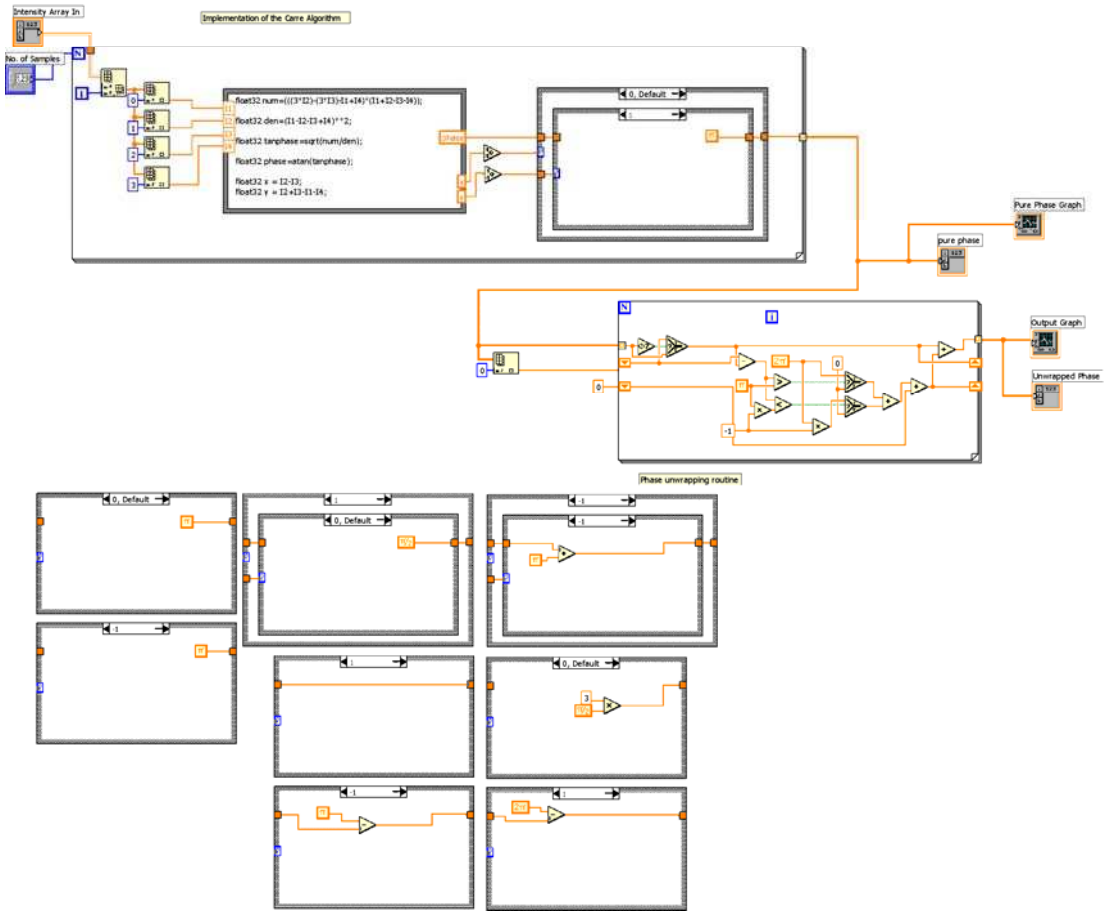

laser_sweep_config.vi
C:\Program Files\National Instruments\LabVIEW 8.0\user.lib\Laser\laser_sweep_config.vi
Last modified on 10/02/2006 at 15:40
Printed on 07/08/2009 at 13:52

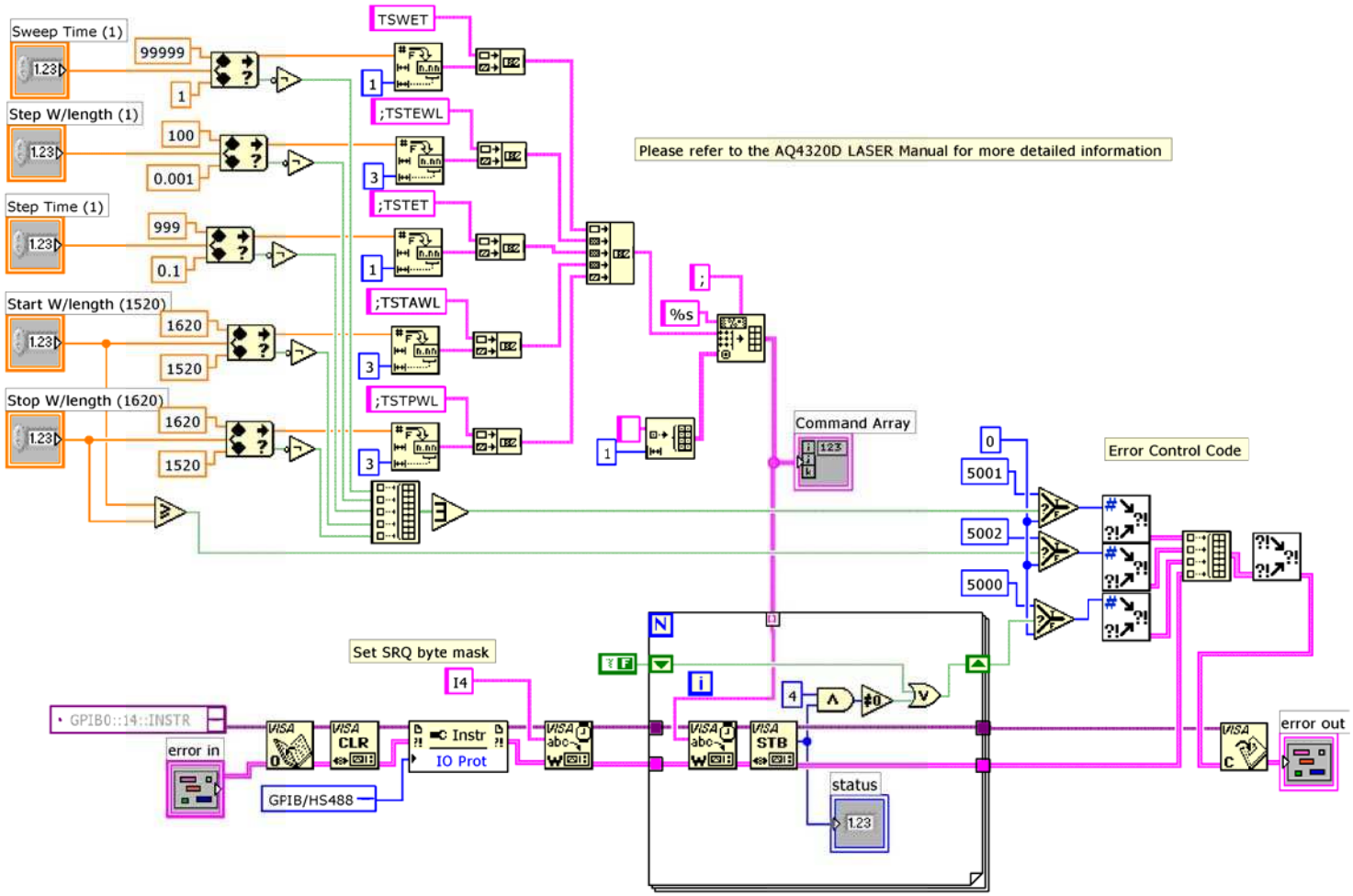

REVERSE_PID.vi
D:\Desktop\REVERSE_PID.vi
Last modified on 08/11/2006 at 13:23
Printed on 07/08/2009 at 13:52

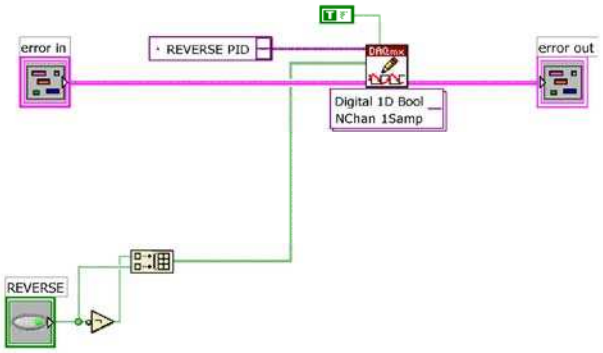

SP_ENABLE.vi
D:\Desktop\SP_ENABLE.vi
Last modified on 10/11/2006 at 15:20
Printed on 07/08/2009 at 13:52

SP_ENABLE.vi

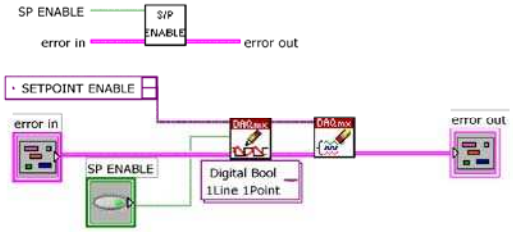

waveout.vi
D:\Desktop\waveout.vi
Last modified on 16/11/2006 at 16:02
Printed on 07/08/2009 at 13:52

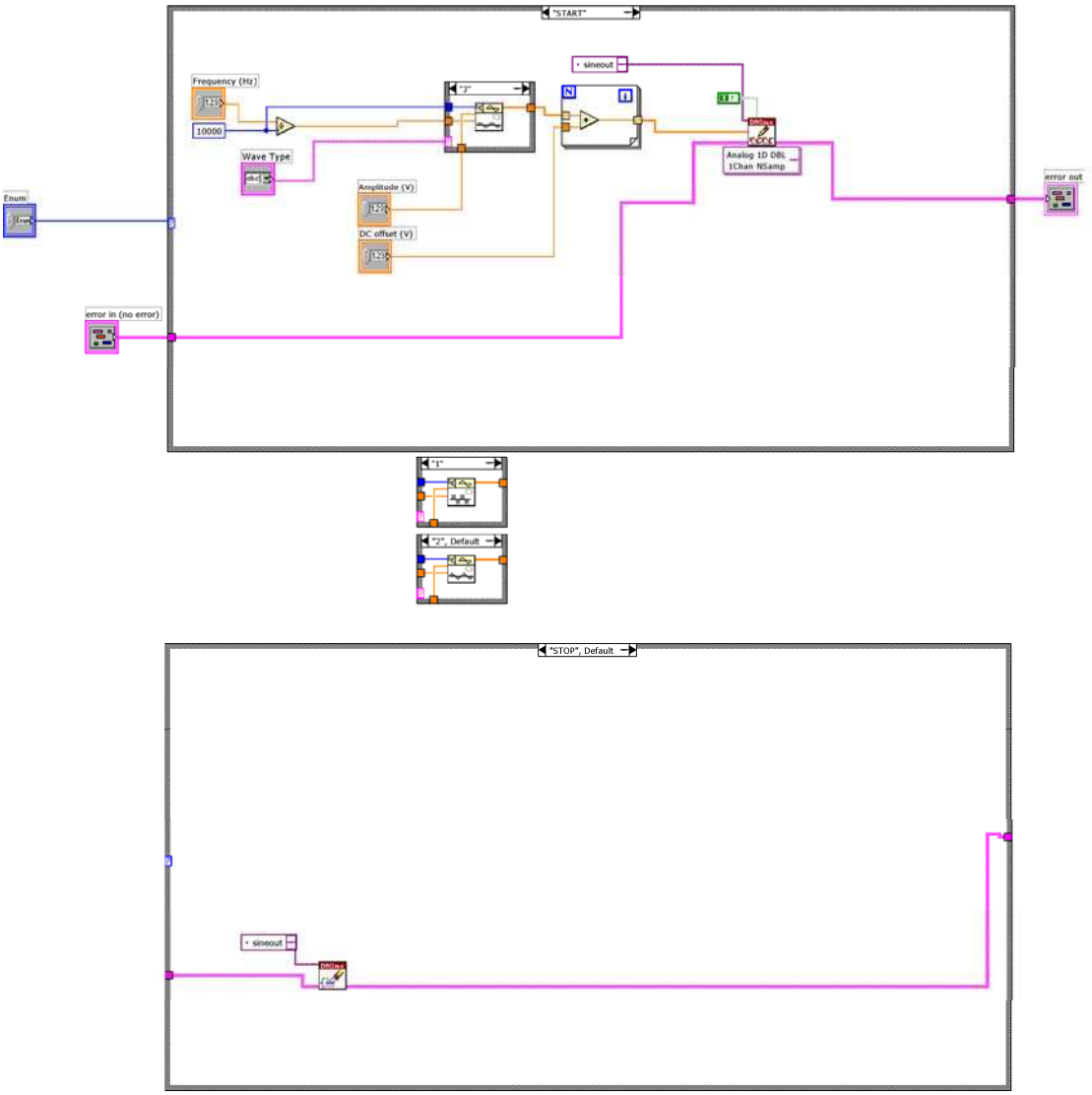

gettvis.vi
D:\Desktop\gettvis.vi
Last modified on 03/04/2007 at 15:30
Printed on 07/08/2009 at 13:52

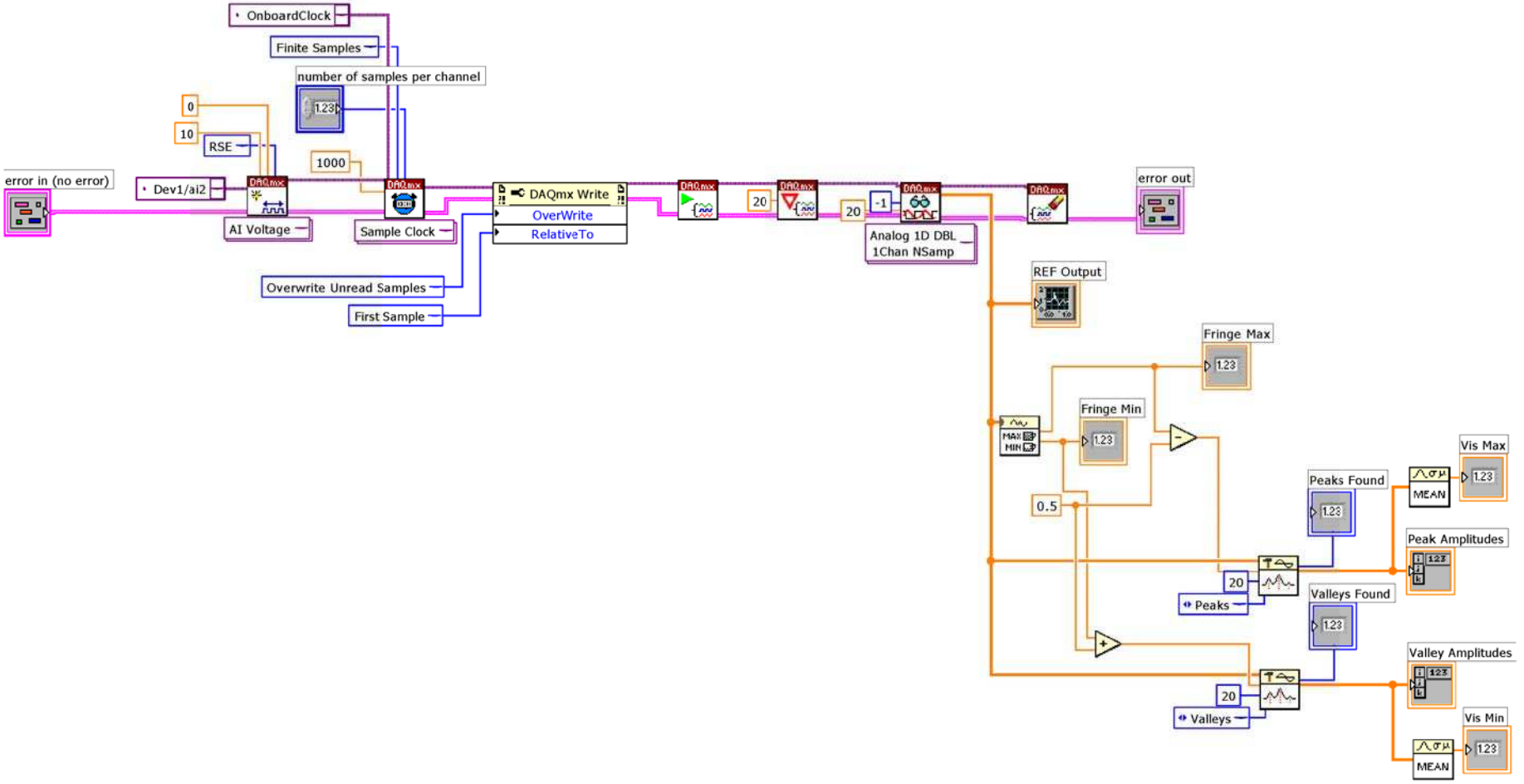

Page 2 RAMP Voltage

ramp_voltage.vi
D:\Desktop\ramp_voltage.vi
Last modified on 10/11/2006 at 15:36
Printed on 07/08/2009 at 13:52

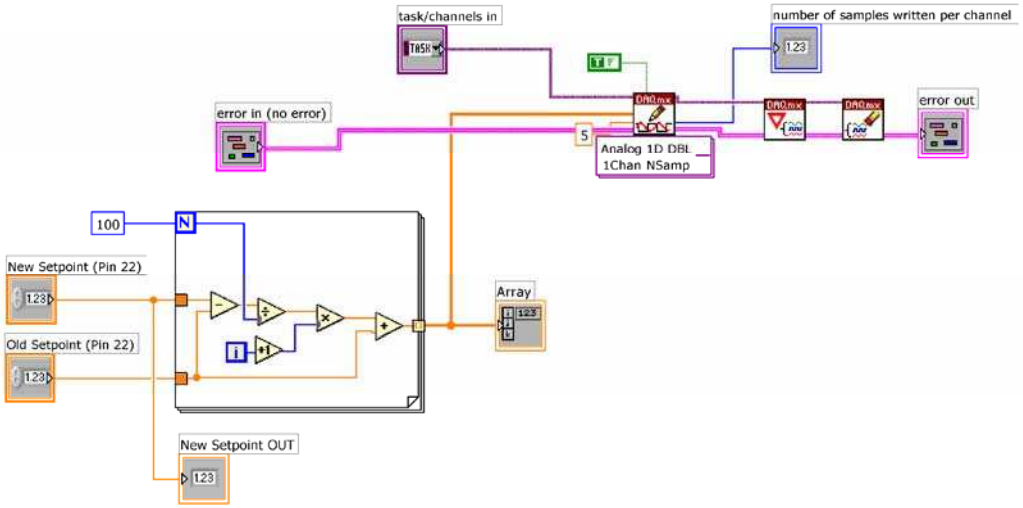

Page 2 RESET PID

RESET_PID_TIMED.vi
D:\Desktop\RESET_PID_TIMED.vi
Last modified on 13/11/2006 at 10:37
Printed on 07/08/2009 at 13:52

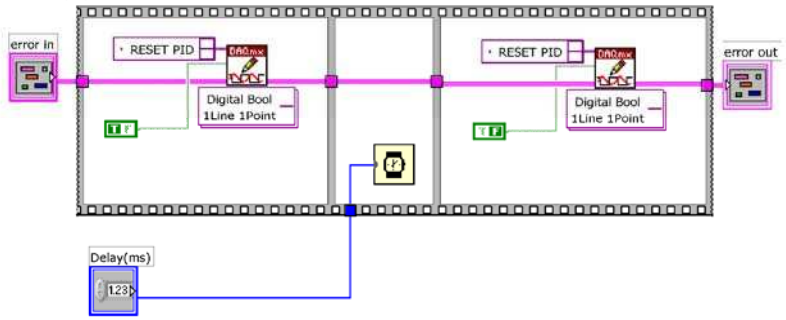

generate_alpha_110.vi
D:\Desktop\generate_alpha_110.vi
Last modified on 16/11/2006 at 15:09
Printed on 07/08/2009 at 13:52

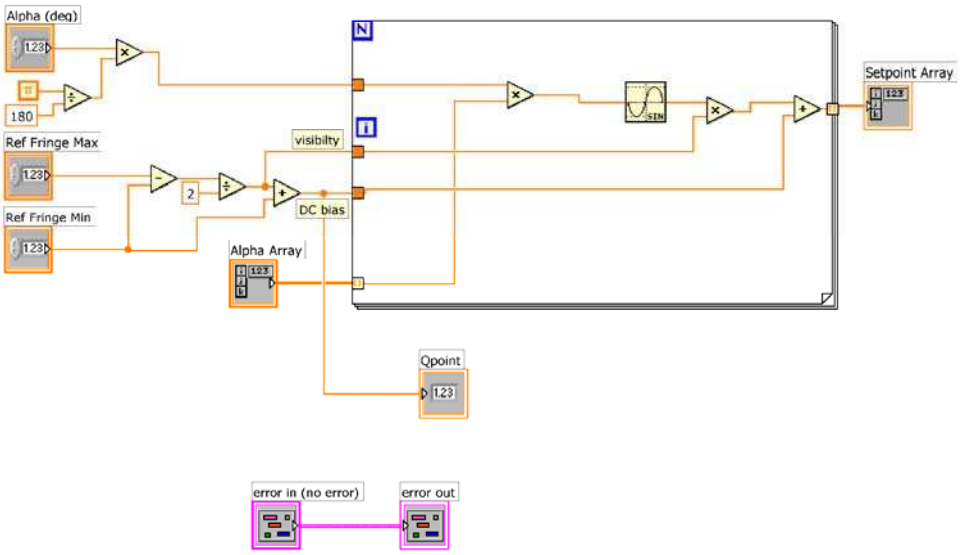

meas analysis.vi

This VI sets up the HP8168F tuneable laser using the GPIB interface and initialises it to the start wavelength position. On the front panel it is possible to select the power (in mW) for the scan, the start and stop wavelengths, and the number of points over which the scan will take place. Also a dummy move mode may be selected which allows for the laser wavelength to not physically wavelength. This bypasses some of the experienced oscillations when the laser power is toggled and used to some of the single point stability tests done in section 7.5. The VI waits here during the execution of *movelaser.vi* which interfaces with the DSP while the measurement cycle is carried out.

The VI then uploads the raw intensity data from the text file generated by the DSP code (*m.dat*) and divides it up into separate data streams, one for each phase shift (*I1* to *I5*). The intensity data is then processed using both the Schwider-Hariharan and Carré algorithms. The Carré algorithm is carried out by the subroutine, *CarrePSI.vi* and is passed the first 4 of the 5 data intensity streams. If phase data averaging was selected in the DSP code this is done in this VI after which the data is stored in the text file *meas.txt*.

CarrePSI.vi

See appendix F.2

movelaser.vi

This VI controls the shifting of the laser wavelength during the measurement cycle. It first initialises the HP8168F laser into a known state, then sets the chosen power and start wavelength. It also calculates an array of wavelength values based on the number of points and start/stop wavelengths selected. These are then passed to a loop which waits for a logic high on line *P0.0* on the NI PCI-6221 from the DSP. The laser is then moved using the *HP_nm.vi* subVI. When the move has successfully completed (several milliseconds) a logic high placed on *P0.1*. This is acknowledged by the DSP by pulling *P0.0* low after which the VI pulls *P0.1* low and the cycle repeats until all wavelengths in the scan have been selected. Figure 7.12 shows the

timing diagram for the sequence. If the dummy mode is selected, the laser is not actually moved but remains on one spot during at all times. However the event sequence on *P0.0* and *P0.1* is still followed to 'fool' the DSP into thinking a normal measurement cycle is going on.

HP_init.vi

This VI simply sets up various parameters of the HP8168F tuneable laser so they are in a known state, and set correctly for the required operation. An error check is also performed to ensure that the initialisation has executed correctly.

HP_nm.vi

This VI sets the wavelength of the HP8168F tuneable laser. It also performs an error check to ensure that execution has completed.

HP_mW.vi

This VI sets the output power of the HP8168F tuneable laser. It also performs an error check to ensure that execution has completed.

HP_on.vi

This VI switches the HP8168F tuneable laser on or off and performs and error check to ensure correct execution.

HP_errorchk.vi

This VI uses the provision made in the IEEE488.2 (GPIB) interface standard for error checking. This VI is called after a command is sent to the HP8168F tuneable laser. When the command has executed the HP8168F sends a service request (SRQ) over the GPIB interface. A status byte is then downloaded from the HP8168F and interrogated to see if the event status but (ESB) is set. If so, the event status register (ESR) contents are requested and examined to determine the error type. The VI is then halted and the error reported to the user via a dialog box.

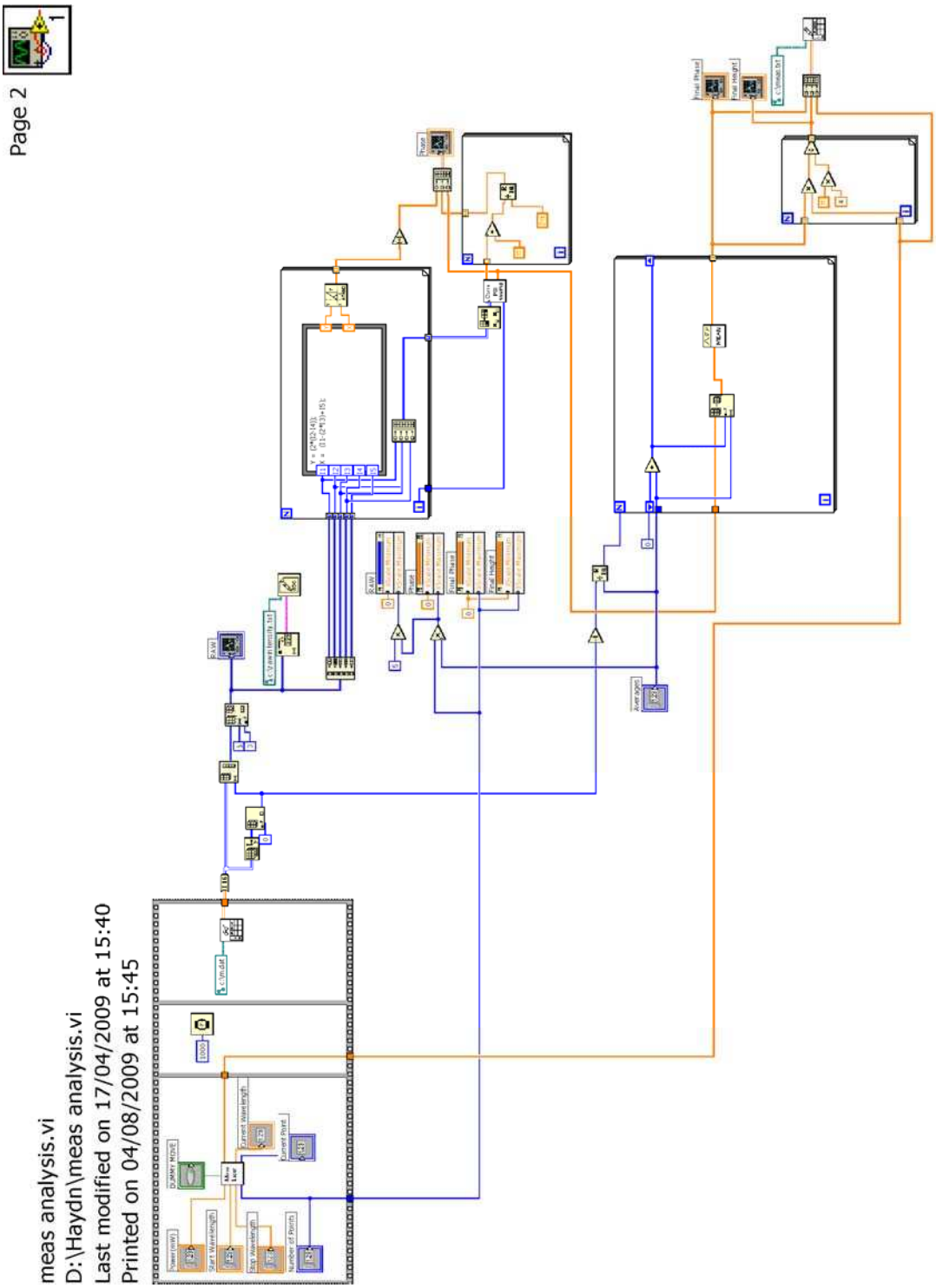
Page 2
meas analysis.vi
D:\Haydn\meas analysis.vi
Last modified on 17/04/2009 at 15:40
Printed on 04/08/2009 at 15:45

movelaser.vi
D:\Haydn\movelaser.vi
Last modified on 31/01/2009 at 20:45
Printed on 04/08/2009 at 15:45

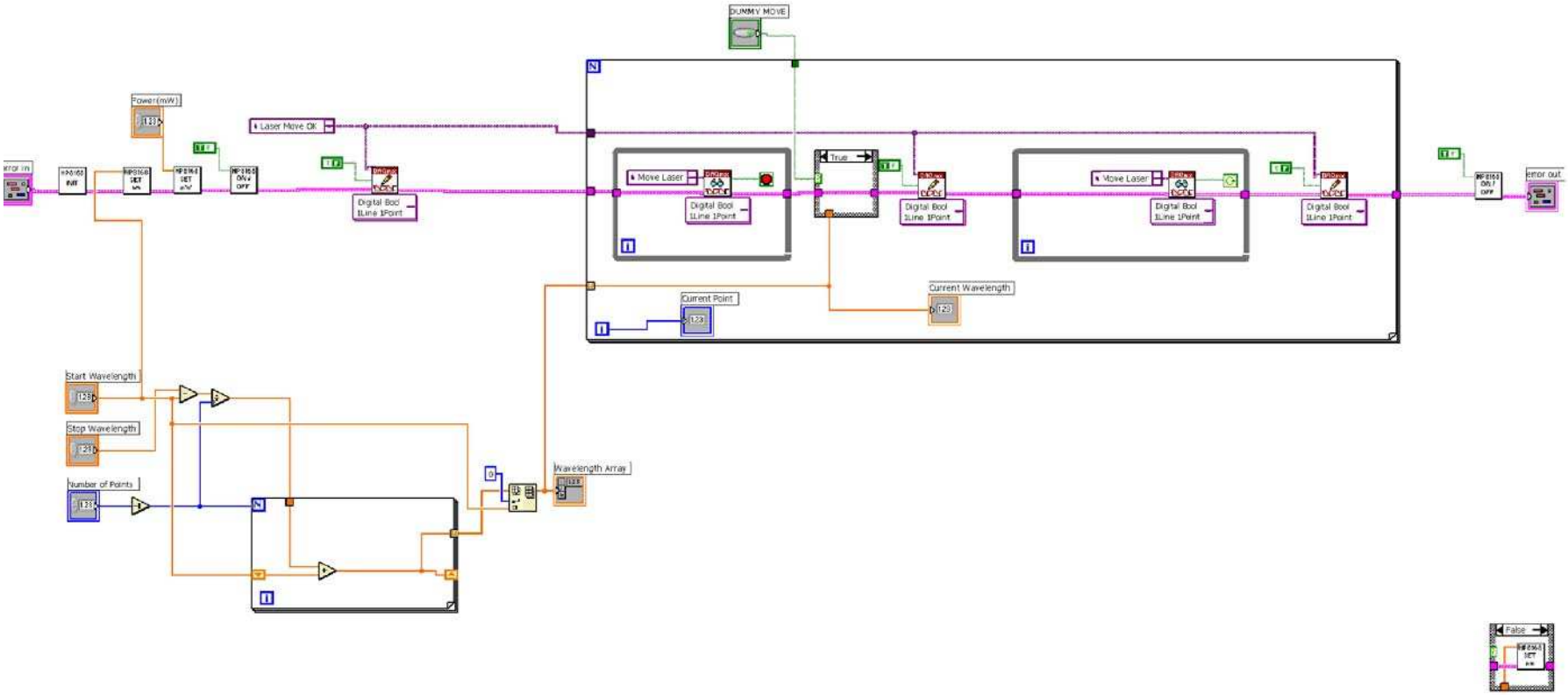

HP_init.vi
C:\Program Files\National Instruments\LabVIEW 8.0\user.lib\HP8168F\HP_init.vi
Last modified on 24/11/2008 at 10:56
Printed on 04/08/2009 at 15:45

HP_init.vi

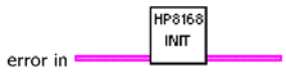

Performs full configuration of the laser. Run this VI before using any other laser VIs. Also sets wavelength, power and turn on state.

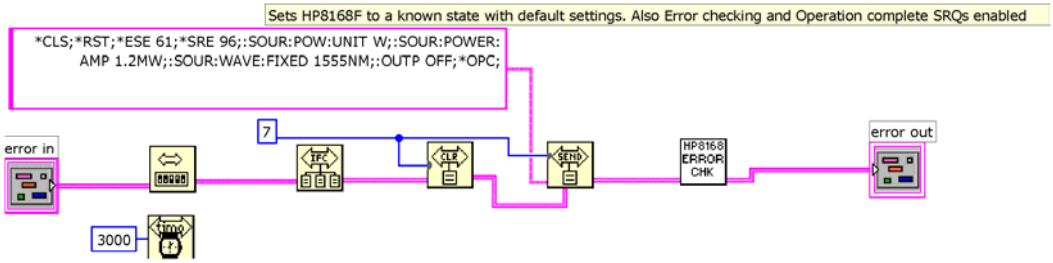

HP_errorchk.vi
C:\Program Files\National Instruments\LabVIEW 8.0\user.lib\HP8168F\HP_errorchk.vi
Last modified on 21/11/2008 at 14:35
Printed on 04/08/2009 at 15:45

HP_errorchk.vi

Sets power (in dBm) on laser.

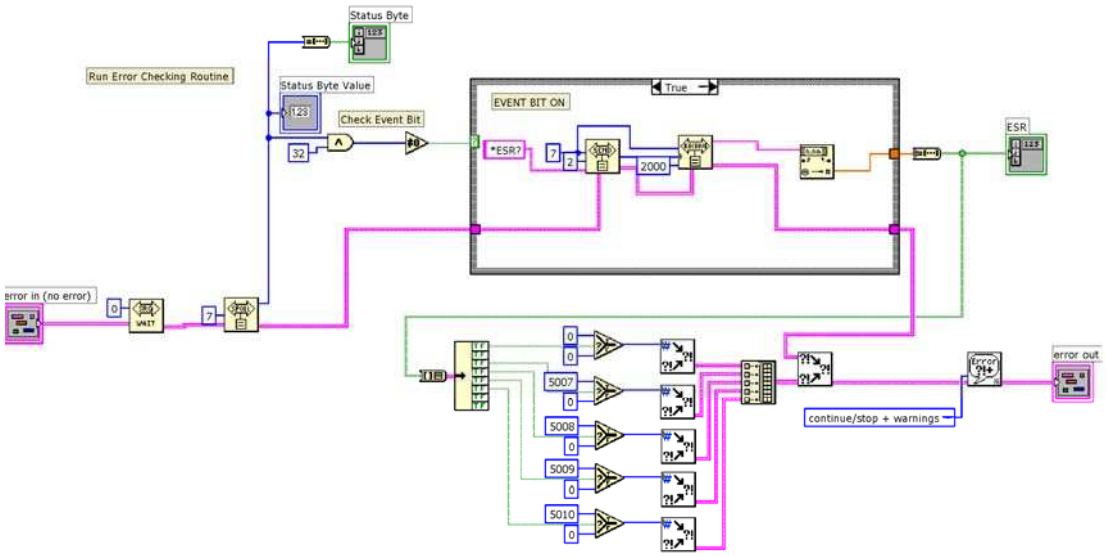

HP_errorchk.vi
C:\Program Files\National Instruments\LabVIEW 8.0\user.lib\HP8168F\HP_errorchk.vi
Last modified on 21/11/2008 at 14:35
Printed on 04/08/2009 at 15:45

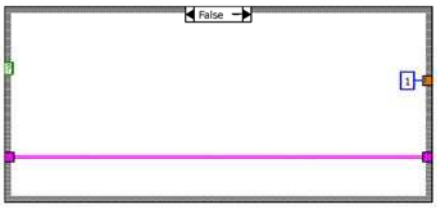

HP_nm.vi
C:\Program Files\National Instruments\LabVIEW 8.0\user.lib\HP8168F\HP_nm.vi
Last modified on 21/11/2008 at 14:21
Printed on 04/08/2009 at 15:45

HP_nm.vi

Sets lasers wavelength.

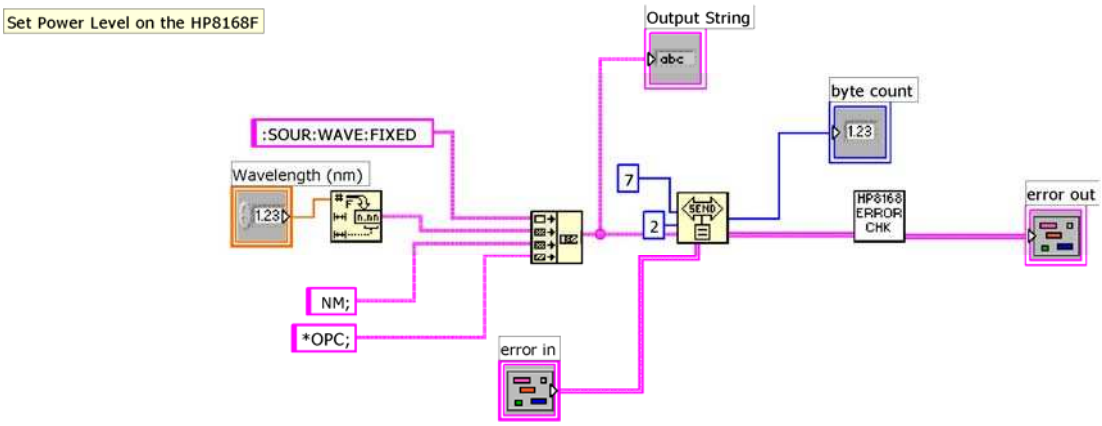

HP_mW.vi
C:\Program Files\National Instruments\LabVIEW 8.0\user.lib\HP8168F\HP_mW.vi
Last modified on 21/11/2008 at 13:34
Printed on 04/08/2009 at 15:45

HP_mW.vi

Sets power (in dBm) on laser.

Set Power Level on the HP8168F

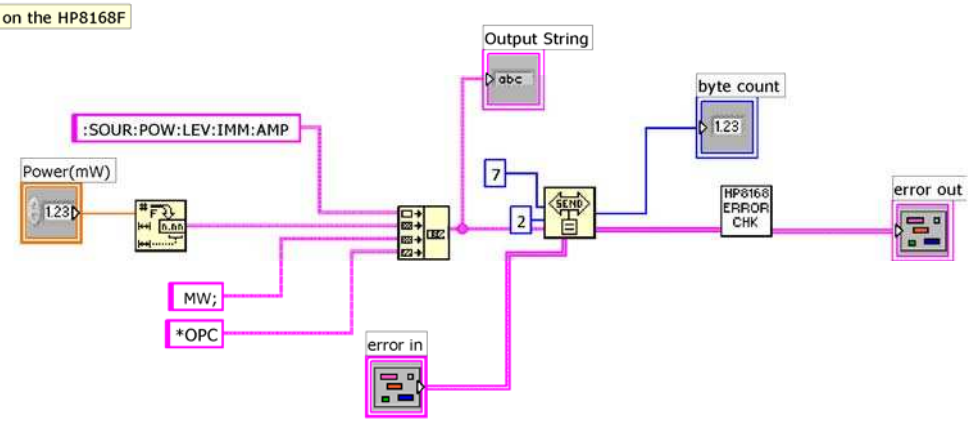

HP_on.vi
C:\Program Files\National Instruments\LabVIEW 8.0\user.lib\HP8168F\HP_on.vi
Last modified on 09/01/2008 at 16:24
Printed on 04/08/2009 at 15:45

HP_on.vi

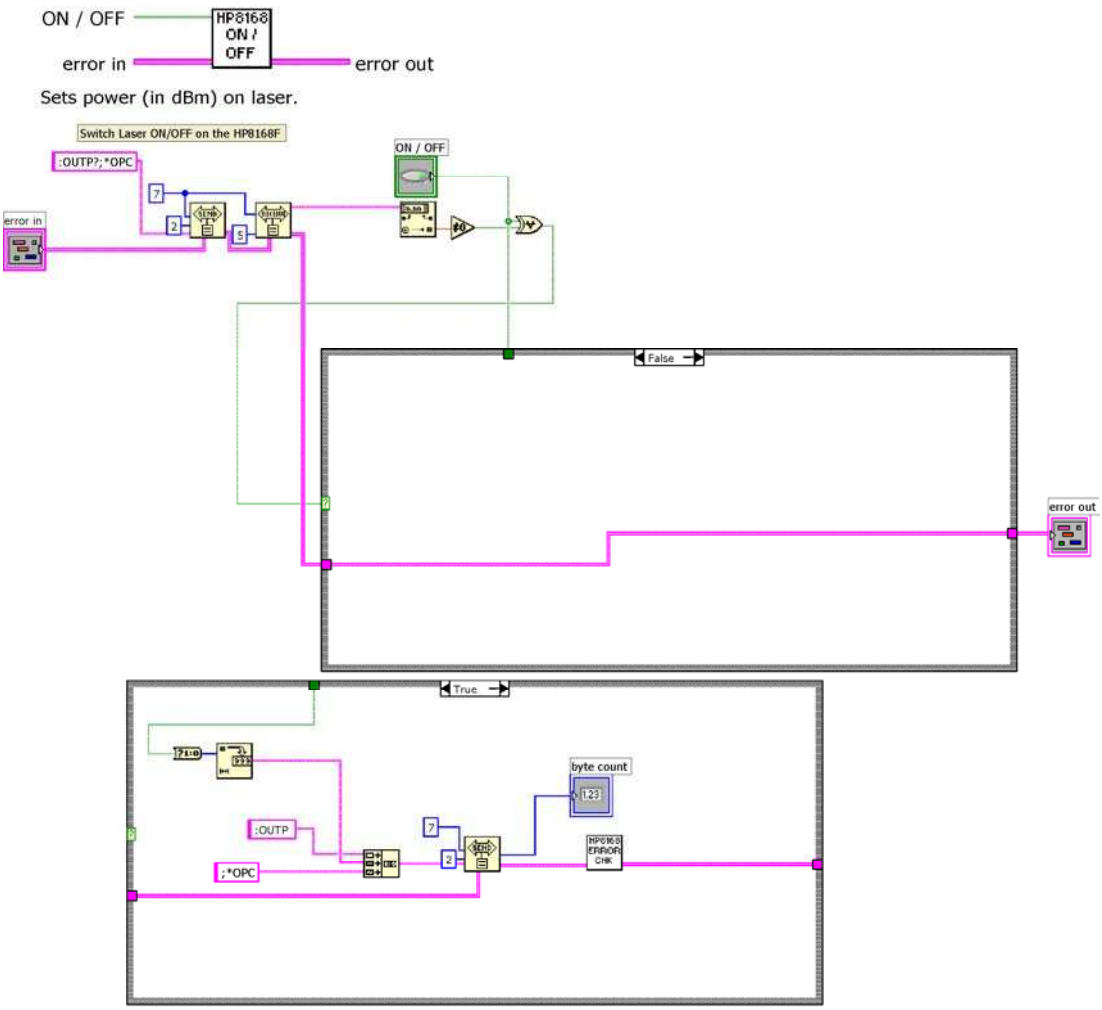

CarrePSI.vi
C:\Program Files\National Instruments\LabVIEW 8.0\user.lib\MEAS PSI\CarrePSI.vi
Last modified on 13/11/2006 at 14:51
Printed on 04/08/2009 at 15:45